

Modeling of Zinc-Air Batteries Using Theoretical and Empirical Approach



A Dissertation Submitted in Partial Fulfillment of the Requirements
for the Degree of Doctor of Engineering in Chemical Engineering
Department of Chemical Engineering
FACULTY OF ENGINEERING
Chulalongkorn University
Academic Year 2020
Copyright of Chulalongkorn University

การพัฒนาแบบจำลองของแบตเตอรี่สังกะสี-อากาศโดยใช้วิธีการเชิงทฤษฎีและเชิงประจักษ์



วิทยานิพนธ์นี้เป็นส่วนหนึ่งของการศึกษาตามหลักสูตรปริญญาวิศวกรรมศาสตรดุษฎีบัณฑิต

สาขาวิชาวิศวกรรมเคมี ภาควิชาวิศวกรรมเคมี

คณะวิศวกรรมศาสตร์ จุฬาลงกรณ์มหาวิทยาลัย

ปีการศึกษา 2563

ลิขสิทธิ์ของจุฬาลงกรณ์มหาวิทยาลัย

Thesis Title Modeling of Zinc-Air Batteries Using Theoretical and
 Empirical Approach
By Mr. Woranunt Lao-atiman
Field of Study Chemical Engineering
Thesis Advisor Associate Professor SOORATHEP KHEAWHOM, Ph.D.

Accepted by the FACULTY OF ENGINEERING, Chulalongkorn University in
Partial Fulfillment of the Requirement for the Doctor of Engineering

Dean of the FACULTY OF
ENGINEERING
(Professor SUPOT TEACHAVORASINSKUN, D.Eng.)

DISSERTATION COMMITTEE

----- Chairman
(Assistant Professor Pornchai Bumroongsri, D.Eng.)
----- Thesis Advisor
(Associate Professor SOORATHEP KHEAWHOM, Ph.D.)
----- Examiner
(Assistant Professor PIMPORN PONPESH, Ph.D.)
----- Examiner
(Assistant Professor AMORNCHAI ARPORNWICHANOP,
D.Eng.)
----- Examiner
(Professor BUNJERD JONGSOMJIT, Ph.D.)


จุฬาลงกรณ์มหาวิทยาลัย
CHULALONGKORN UNIVERSITY

วรรณที่ เส้าอดิมาน : การพัฒนาแบบจำลองของแบตเตอรี่สังกะสี-อากาศโดยใช้วิธีการเชิงทฤษฎีและเชิงประจักษ์. (Modeling of Zinc-Air Batteries Using Theoretical and Empirical Approach) อ.ที่
 ปริญญาหลัก : รศ. ดร.สุรเทพ เชี่ยวหอม

ในปัจจุบันนี้ระบบกักเก็บพลังงานได้รับความสนใจในด้านงานวิจัยอย่างกว้างขวาง แบตเตอรี่สังกะสีอากาศเป็นหนึ่งในตัวเลือกที่มีแนวโน้มการใช้เป็นระบบกักเก็บพลังงานเนื่องจากแบตเตอรี่สังกะสีอากาศมีความหนาแน่นพลังงานสูงแต่มีค่าใช้จ่ายต่ำ แม้ว่าแบตเตอรี่สังกะสีอากาศจะได้รับการวิจัยในหลากหลายด้านแต่การวิจัยในด้านการพัฒนาแบบจำลองยังคงไม่เพียงพอ ดังนั้นงานวิจัยนี้จึงมุ่งศึกษาการพัฒนาแบบจำลองของแบตเตอรี่สังกะสีอากาศโดยใช้วิธีการเชิงทฤษฎีและเชิงประจักษ์ เริ่มแรกระบบแบตเตอรี่สังกะสีอากาศถูกวิเคราะห์ด้วยวิธีการเชิงทฤษฎี โดยระบบที่ใช้ศึกษาคือระบบร่วมระหว่างแบตเตอรี่สังกะสีอากาศแบบไหลกลับอิเล็กโทรไลต์ของสังกะสีแบบจำลองทางคณิตศาสตร์ศูนย์มิติถูกพัฒนาขึ้นโดยใช้โปรแกรมเม็ทแล็บและตรวจสอบเทียบกับข้อมูลจากการทดลอง แบบจำลองถูกใช้ในการตรวจสอบพารามิเตอร์ 3 อย่างได้แก่ ความเข้มข้นของโพแทสเซียมไฮดรอกไซด์ ความเข้มข้นเริ่มต้นของไอออนซิงค์แคต และอัตราการไหลของอิเล็กโทรไลต์ ปฏิกริยาการเกิดแก๊สไฮโดรเจนถูกบรรจุไว้ในแบบจำลองด้วย ดังนั้นประสิทธิภาพเชิงกระแสไฟฟ้าจากการเกิดแก๊สไฮโดรเจนของระบบจะสามารถคำนวณได้ ผลลัพธ์แสดงให้เห็นว่าการเพิ่มขึ้นของความเข้มข้นของโพแทสเซียมไฮดรอกไซด์ทำให้พลังงานการคายประจุของแบตเตอรี่สูงขึ้น แต่ก็ทำให้แก๊สไฮโดรเจนเกิดมากขึ้นเช่นกัน จากการทดลองพบว่าความเข้มข้นของโพแทสเซียมไฮดรอกไซด์ที่เหมาะสมอยู่ที่ 6-7 โมลาร์ การเพิ่มความเข้มข้นเริ่มต้นของไอออนซิงค์แคตทำให้ประสิทธิภาพเชิงกระแสไฟฟ้าเพิ่มขึ้นเนื่องจากการเกิดแก๊สไฮโดรเจนลดลง สำหรับอัตราการไหลของอิเล็กโทรไลต์ที่สูงขึ้นจะช่วยรักษาความเข้มข้นของสารในระบบให้คงที่ แต่อัตราการไหลที่สูงก็ส่งผลเสียต่อสมรรถนะของแบตเตอรี่เช่นกัน ต่อไปเป็นการศึกษาพฤติกรรมเชิงพลวัตของแบตเตอรี่สังกะสีอากาศโดยใช้แบบจำลองเชิงประจักษ์ แบบจำลองพารามิเตอร์ผันแปรเชิงเส้นถูกเสนอเพื่อใช้ในการตรวจสอบพฤติกรรมที่ไม่เป็นเชิงเส้นของแบตเตอรี่สังกะสีอากาศ โดยแบบจำลองนี้สร้างจากชุดของแบบจำลองเชิงเส้นที่ไม่ขึ้นกับเวลา ข้อมูลที่ใช้สร้างแบบจำลองและสอบเทียบถูกวัดค่ามาจากแบตเตอรี่สังกะสีอากาศแบบเดิมได้ที่ประกอบขึ้นเอง จากผลลัพธ์พบว่าแบบจำลองพารามิเตอร์ผันแปรเชิงเส้นสามารถทำนายพฤติกรรมที่ไม่เป็นเชิงเส้นของแบตเตอรี่นี้ได้ และความสามารถในการทำนายของแบบจำลองนี้มีความแม่นยำเท่ากับแบบจำลองที่ไม่เป็นเชิงเส้นอีกด้วย สุดท้ายคือการศึกษาระเบียบสภาวะของประจุของแบตเตอรี่สังกะสีอากาศ แบบจำลองพารามิเตอร์ผันแปรเชิงเส้นถูกใช้เป็นตัวประเมินสภาวะของประจุ่มร่วมกับอัลกอริทึมตัวกรองคาลมานแบบขยาย ข้อมูลที่ใช้ทดสอบได้มาจากแบตเตอรี่สังกะสีอากาศแบบไหลที่มีสามขั้ว พารามิเตอร์ปรับแต่งที่ผันแปรกับความถูกต้องในการเดาค่าเริ่มต้นของสภาวะของประจุถูกใช้เป็นสถานการณ์จำลองในการทดสอบ ผลลัพธ์เผยว่าตัวประเมินสภาวะของประจุ่มที่พัฒนาขึ้นสามารถที่จะประเมินค่าสภาวะของประจุ่มจริงที่ต่อเมื่อสภาวะของประจุเข้าใกล้ศูนย์เนื่องจากว่าแบตเตอรี่แบบไหลนั้นมีรูปแบบโปรไฟล์แรงดันที่ค่อนข้างเรียบ อย่างไรก็ตามตัวประเมินสภาวะของประจุ่มนี้สามารถติดตามค่าสภาวะของประจุ่มจริงได้ในการดำเนินการระยะยาวที่มีการอัด-คายของประจุหลายรอบ ผลงานงานวิจัยนี้สร้างความเข้าใจเชิงลึกเกี่ยวกับแบตเตอรี่สังกะสีอากาศมากยิ่งขึ้นและยังขยายขอบเขตความรู้เกี่ยวกับแบตเตอรี่สังกะสีอากาศในแง่ของการพัฒนาแบบจำลอง

CHULALONGKORN UNIVERSITY

สาขาวิชา วิศวกรรมเคมี
 ปีการศึกษา 2563

ลายมือชื่อนิสิต
 ลายมือชื่อ อ.ที่ปรึกษาหลัก

6071438621 : MAJOR CHEMICAL ENGINEERING

KEYWORD: Zinc-air battery, Linear parameter-varying model, modeling

Woranunt Lao-atiman : Modeling of Zinc-Air Batteries Using Theoretical and Empirical Approach. Advisor: Assoc. Prof. SOORATHEP KHEAWHOM, Ph.D.

Nowadays, an energy storage system (ESS) is attracting widespread research interest. Zinc-air battery (ZAB) is a promising candidate for ESS owing to its high energy density at low cost. Although ZAB has been researched in various aspects, the modeling aspect is still insufficient. Therefore, this work aims to study the modeling of ZAB using both theoretical and empirical approaches. At first, the ZAB system was analyzed using a theoretical approach. The studied system was an integrated system of zinc-air flow battery (ZAFB) and zinc electrolyzer. The zero-dimensional mathematical model was developed in MATLAB and validated against experimental data. The model was used to investigate 3 parameters: potassium hydroxide (KOH) concentration, zincate ion initial concentration and electrolyte flowrate. Hydrogen evolution reaction (HER) was contained in the model therefore the current efficiency based on HER of the system can be calculated. The result showed that increasing KOH concentration improved the discharge energy of the battery, but it also promoted HER. An optimal KOH concentration of 6-7 M was obtained from the simulation result. Increasing zincate ion initial concentration improved the current efficiency of the system as it reduced HER. For electrolyte flowrate, the higher flowrate helped maintain the concentration of the active species in the battery; however, the higher flowrate also provided a negative effect on the battery performance. Next, ZAB dynamic behavior was investigated by empirical modeling. A linear parameter-varying model was proposed to examine the nonlinear behavior of ZAB. The LPV model was created from a set of linear time-invariant models. The data used to identify and validate the model in this study was measured from a homemade refuellable ZAB. As a result, it was found that the LPV model was able to predict the nonlinear behavior of the battery and its performance was comparable to the nonlinear model. Finally, the SOC estimation of ZAB was studied. The LPV model integrated with the extended Kalman filter algorithm was proposed as SOC estimator. The data used to test in this case were obtained from a laboratory-made tri-electrode ZAFB. The tested scenarios include varied tuning parameters and the correctness of the initial SOC guess. The result revealed that the developed estimator was able to estimate true SOC value only when SOC approached zero due to the flat voltage profile of the flow battery. Nevertheless, the SOC estimator was capable of true SOC tracking in the long-term operation with multiple charge-discharge cycles. The results of this research provide a better comprehension and extended knowledge boundary of modeling of ZAB.

Field of Study: Chemical Engineering

Academic Year: 2020

Student's Signature

Advisor's Signature

ACKNOWLEDGEMENTS

First of all, I would like to show my appreciation to my thesis advisor, Assoc. Prof. Soorathep Kheawhom, for his advice and support throughout my doctoral course. His suggestion greatly improved my work and research insight. Without his assistance, the completion of this work would have been impossible.

I would like to thank the Dusadeepipat scholarship for research fund and scholarship throughout the course of my doctoral degree. I thank to Government of France/Campus France under Franco-Thai Cooperation Programme in Higher Education and Research/Franco-Thai Mobility Programme/PHC SIAM for funds and the opportunity in doing research in France.

I am gratefully acknowledged Prof. Bunjerd Jongsomjit Asst. Prof. Pimporn Ponpesh Asst. Prof. Amornchai Arpornwichanop and Asst. Prof. Pornchai Bumroongsri, who are the thesis committee member for their comments and recommendations. I would like to thank the staff of the department of chemical engineering who provide assistance to my work especially Mr.Kijchai Karnkajanaparakul. He greatly provided technical assistance to my thesis experiment. I also would like to show my appreciation to Prof. Sorin Olaru from the Laboratory of Signals and Systems, CentraleSupélec, France for comments, recommendations, and collaboration in research.

I would like to thank my father and mother for everything they have given to me. Without their support, life would not come this far. Next, I would like to acknowledge my family for their support especially my aunt who support me with funds for living throughout the course of my doctoral degree.

I would like to express my thankfulness to my friends who contributed to me while I was studying for the doctoral degree. My colleagues from the process control and life cycle engineering laboratory have played an important role in my graduate pursuit of sharing knowledge and attitude.

Finally, I would like to show my gratefulness to Miss Nutthakarn Phumkokrux for friendship, advice, care, and encouragement.

Woranunt Lao-atiman

TABLE OF CONTENTS

	Page
.....	iii
ABSTRACT (THAI)	iii
.....	iv
ABSTRACT (ENGLISH).....	iv
ACKNOWLEDGEMENTS.....	v
TABLE OF CONTENTS.....	vi
LIST OF FIGURES	xi
LIST OF TABLES.....	xvi
CHAPTER 1 INTRODUCTION.....	1
1.1 Background.....	1
1.2 Objectives	4
1.3 Scopes of research	4
1.4 Research benefit	5
CHAPTER 2 THEORIES AND LITERATURE REVIEWS	6
2.1 Introduction to Zinc-air Technology	6
2.2 Cell Configurations	7
2.2.1 Zn electrode.....	8
2.2.2 Air electrode	8
2.2.3 Electrolyte	9
2.2.4 Separator.....	9
2.3 Working Principle and Electrochemistry	9
2.4 Focuses, Progresses and Challenges.....	10
2.4.1 Zn electrode.....	11
2.4.2 Air electrode	12
2.4.3 Electrolyte	13

2.4.4 Model-based engineering	14
2.4.5 Battery State Estimation	16
2.5 Theoretical Cell Modeling	17
2.5.1 Continuity of species	17
2.5.2 Mass transport in electrolyte	17
2.5.3 Electrode kinetics	18
2.5.4 Cell potential	19
2.5.5 Cell performance evaluation	20
2.5.5.1 Open Circuit Cell Potential	20
2.5.5.2 Overpotential / Potential losses and Polarization curve	20
A) Activation Overpotential	21
B) Ohmic Overpotential	22
C) Concentration Overpotential	22
2.5.5.3 Current Density and Power Density	23
2.5.5.4 Efficiency of the Electrochemical cell	23
2.6 Empirical Dynamic Modeling	24
2.6.1 State Space Model	24
2.6.2 Linear Parameter Varying model	24
2.6.3 Hammerstein-Weiner model	25
2.7 SOC estimation techniques	25
2.7.1 Direct measurement	25
2.7.2 Coulomb counting	26
2.7.3 Kalman filter	26
2.7.4 Extended Kalman filter	27
2.8 Literature Reviews	28
2.8.1 Zinc-air cell	28
2.8.2 Regeneration of Zn	31
2.8.3 Modeling of zinc-air battery	35

CHAPTER 3 Model-based Analysis of an Integrated Zinc-Air Flow Battery/ Zinc Electrolyzer System	39
3.1 Preface	39
3.2 Abstract.....	39
Keywords:.....	40
3.3 Introduction	40
3.4 Zinc-air Flow Battery and Zinc Electrolyzer.....	43
3.5 Experimental Setup	44
3.6 Mathematical Models	46
3.6.1 Species Balances	46
3.6.2 Rates of Reactions	47
3.6.3 Volume Change.....	48
3.6.4 Cell Potential	48
3.6.5 Activation Loss.....	49
3.6.6 Ohmic Loss.....	51
3.7 Results and Discussion	52
3.7.1 Model Validation.....	52
3.7.2 Battery Performance	53
3.7.3 Electrolyzer Performance	56
3.7.4 Integrated System	58
3.8 Conclusion	60
3.9 Nomenclature	61
CHAPTER 4 Discharge Performance and Dynamic Behavior of Refuellable Zinc-Air Battery.....	64
4.1 Preface	64
4.2 Abstract.....	64
4.3 Background & Summary	65
4.4 Methods	66
4.4.1 Chemical and materials	66
4.4.2 Battery fabrication and operation	68

4.4.3 Measurement and data collection	69
4.5 Data Records	70
4.6 Technical Validation	71
4.7 Usage Notes	73
4.8 Code Availability	73
CHAPTER 5 Linear Parameter-varying Model for a Refuellable Zinc-air Battery	74
5.1 Preface	74
5.2 Abstract	74
5.3 Introduction	76
5.4 Battery Description and experimental data	79
5.5 Methodology	80
5.5.1 Linear state-space model	82
5.5.2 LPV model	82
5.5.3 Nonlinear model	84
5.6 Results and Discussion	87
5.6.1 Linear state-space model	87
5.6.2 LPV model	88
5.7 Conclusion	92
CHAPTER 6 Charge-discharge Behavior Prediction and State of Charge estimation for a Tri-electrode Zinc-air Flow Battery Using Linear Parameter-varying Model integrated with Extended Kalman Filter	93
6.1 Preface	93
6.2 Abstract	93
6.3 Introduction	93
6.4 Description of Tri-electrode ZAFB and experimental data	95
6.5 Methodology	97
6.5.1 LPV Model	97
6.5.2 Extended Kalman filter (EKF)	99
6.6 Results and Discussion	101
6.6.1 LPV modeling of Tri-electrode ZAFB	101

6.6.2 SOC estimation.....	105
6.6.2.1 Parameter tuning.....	105
6.6.2.2 Initial SOC guess	107
6.6.2.3 Charge-discharge combined model and continuous scenario.....	110
6.7 Conclusion.....	113
CHAPTER 7 Conclusion	115
7.1 Conclusions	115
7.2 Limitation of this research.....	117
7.3 Recommendations and further studies.....	117
REFERENCES	119
Appendix A Supplementary Material Model-based Analysis of an Integrated Zinc-Air Flow Battery/ Zinc Electrolyzer System.....	132
Appendix B Supplementary Material Linear Parameter-varying Model for a Refuellable Zinc-air Battery	143
Appendix C Supplementary Material Charge-discharge Behavior Prediction and State of Charge estimation for a Tri-electrode Zinc-air Flow Battery Using Linear Parameter-varying Model integrated with Extended Kalman Filter	156
VITA.....	162

LIST OF FIGURES

	Page
Figure 2.1 Schematic diagram of zinc-air flow battery	10
Figure 3.1 Schematic diagram of zinc-air flow battery and zinc electrolyzer.	44
Figure 3.2 Schematic diagram of zinc-air flow battery integrated with zinc electrolyzer.....	44
Figure 3.3 Validation of the proposed models: (A) polarization characteristic of ZAFB (B) anode and cathode overpotential of ZAFB (C) polarization characteristic of Zn electrolyzer and (D) anode and cathode overpotential of Zn electrolyzer.....	52
Figure 3.4 Effects of KOH concentration on ZAFB using zincate ion initial concentration 0.2 M and discharge current density of 100 mA/cm ² : (A) current efficiency as a function of space velocity and (B) discharge energy as a function of space velocity.....	53
Figure 3.5 Effects of zincate ion initial concentration on ΔE_{ZH} as a function of KOH concentration.....	55
Figure 3.6 Effects of zincate ion initial concentration on ZAFB using 8 M KOH at discharge current density of 100 mA/cm ² : (A) current efficiency as a function of space velocity and (B) discharge energy as a function of space velocity.....	55
Figure 3.7 Effects of zincate ion initial concentration on zinc electrolyzer using 8 M KOH at charge current density of 100 mA/cm ² : (A) current efficiency as a function of space velocity and (B) charge energy as a function of space velocity.....	57
Figure 3.8 Effects of KOH concentration on zinc electrolyzer using different zincate ion initial concentration (0.2 M (dotted line) and saturated zincate ion (solid line)) at discharge current density of 100 mA/cm ² : (A) current efficiency as a function of space velocity and (B) charge energy as a function of space velocity.....	57
Figure 3.9 Effects of zincate ion initial concentration using 8 M KOH at charge and discharge current density of 100 mA/cm ² : (A) current efficiency as a function of space velocity (B) discharge efficiency as a function of space velocity (C) charge efficiency as a function of space velocity and (D) energy efficiency as a function of space velocity.....	59
Figure 3.10 Effects of KOH concentration using 0.2 M zincate ion initial concentration at charge and discharge current density of 100 mA/cm ² : (A) current efficiency as a function of space velocity (B) discharge efficiency as a function of space velocity (C) charge efficiency as a function of space velocity and (D) energy efficiency as a function of space velocity.	60

Figure 4.1 Digital photographic images of a homemade zinc-air battery. (A) Fabricated tubular zinc-air battery, (B) stainless steel mesh cylinder as a supporting structure, (C) stainless-steel mesh tube (the anode current collector), (D) the air cathode, (E) the separator, and (F) zinc pellets used as the anode active material.....	67
Figure 4.2 cell structure and cell dimension of a homemade zinc-air battery.	70
Figure 4.3 Linear sweep voltammograms of the zinc plate (scanned from OCV to -0.5 V vs. Hg/HgO), and stainless-steel mesh (scanned from -1.5 V to -0.5 V vs. Hg/HgO) with a scan rate of 5 mV/s.....	71
Figure 4.4 Linear sweep voltammogram of the Ni foam with scan rate of 5 mV/s. (A) Scanned from 0 to -0.7 V vs. Hg/HgO, and (B) scanned from OCV to -0.7 V vs. Hg/HgO.....	73
Figure 5.1 Schematic diagram of experimental ZAB.	80
Figure 5.2 Electrical equivalent circuit diagram of potential loss of battery: first-order RC model	83
Figure 5.3 Block diagram of Hammerstein-Wiener model	85
Figure 5.4 Comparison of response between measured data (blue lines) and predicted data from linear models: a) Matching conditions with current step from 0 to 100 mA b) Different conditions with current step from 0 to 100 mA and c) Multiple current steps from 0 to 100 , 450 and 900 mA.....	88
Figure 5.5 Correlations of state space model parameters as functions of current levels: a) Parameter A b) Parameter D and c) Parameter BC	89
Figure 5.6 Comparison of fit percentage of model prediction between various models and data. Fit % indicates how well the model prediction fits the estimation data and expressed as: $100(1 - \frac{y - \hat{y}}{\text{mean}(y)})$	90
Figure 5.7. Comparison of response between measured data (dark blue lines), predicted data from linear model (red line), LPV model (green line) and nonlinear models: a) Multiple current steps from 0 to 100 , 450 and 900 mA and b) Various current steps	91
Figure 6.1 Schematic diagram of laboratory-made Tri-electrode ZAFB	96
Figure 6.2 Electrical equivalent circuit diagram of battery: second-order RC model	99
Figure 6.3 Schematic scheme of an EKF algorithm.	100
Figure 6.4 Correlations of parameters of LPV model for discharging	102
Figure 6.5 Correlations of parameters of LPV model for charging	102

Figure 6.6 Correlations between V_{OC} and SOC for (A) discharging and (B) charging	103
Figure 6.7 Comparison of fit percentage of model prediction between various models and data for (A) discharging and (B) charging. Fit % expressed as: $100 \times 1 - \frac{\text{mean}(y) - \text{mean}(\hat{y})}{\text{mean}(y)}$.	104
Figure 6.8 Comparison of response between measured data, predicted data from LPV model and linear model: (A) multiple discharge current steps and (B) multiple charge current steps.	104
Figure 6.9 Comparison of the reference scenario between response of measure data (MULTI A) and response predicted from the proposed algorithm: (A) cell voltage and (B) SOC	106
Figure 6.10 Comparison of normalized mean absolute error of estimation between various tuning parameters scenario using data MULTI A: (A) cell voltage and (B) SOC.	106
Figure 6.11 Comparison of SOC estimation between different initial covariance P_3 for correct initial guess scenario using data MULTI A.	107
Figure 6.12 Comparison of SOC estimation between different initial covariance P_3 for incorrect initial SOC guess scenario using data MULTI A: (A) guess initial SOC of 0.8 true initial SOC of 1 (B) guess initial SOC of 1 true initial SOC of 0.8064.	108
Figure 6.13 Comparison of SOC estimation between different initial covariance P_3 for incorrect initial SOC guess scenario using data CMULTI: (A) guess initial SOC of 0.2 true initial SOC of 0 (B) guess initial SOC of 0.1 true initial SOC of 0.3011.	109
Figure 6.14 Comparison of the multi-cycle scenario between response of measure data (COMBINE) and response predicted from the proposed algorithm: (A) cell voltage and (B) SOC.	111
Figure 6.15 Comparison of SOC estimation between different initial covariance P for incorrect initial SOC guess scenario using data COMBINE: (A) guess initial SOC of 0.2 true initial SOC of 0 (B) guess initial SOC of 0.5 true initial SOC of 0.	112
Figure 6.16 Comparison of SOC estimation between different covariance Q_4 and initial covariance P for incorrect initial SOC guess scenario using data COMBINE: guess initial SOC of 0.5 true initial SOC of 0.	113
Figure A1 Example of dynamic behavior of ZAFB/ ZE integrated system with initial KOH and zincate ion concentration of 8 and 0.2 M, respectively: (A) cell voltage, (B) moles of Zn, (C) hydroxide ion concentration, (D) zincate ion concentration, (E) instant current efficiency and (F) HER current density	140

Figure A2 Example of dynamic behavior of ZAFB/ ZE integrated system with initial zincate ion concentration and space velocity of 0.2 M and 0.01 s ⁻¹ , respectively: (A) zincate ion concentration and (B) instant current efficiency	141
Figure A3 Inflection occurred in the current efficiency curve of ZAFB/ ZE integrated system	142
Figure A4 Example of dynamic behavior of ZAFB/ ZE integrated system with initial KOH and zincate ion concentration of 8 and 0.2 M, respectively: (A) zincate ion concentration and (B) instant current efficiency.....	142
Figure B1 Response signals for data 0T100 including (a,c,e) current and (b,d,f) potential loss vs time.....	146
Figure B2 Response signals for data 0T450 including (a,c,e) current and (b,d,f) potential loss vs time.....	147
Figure B3 Response signals for data 0T900 including (a,c,e) current and (b,d,f) potential loss vs time.....	148
Figure B4 Response signals for data 100T0 including (a,c,e) current and (b,d,f) potential loss vs time.....	149
Figure B5 Response signals for data 450T0 including (a,c,e) current and (b,d,f) potential loss vs time.....	150
Figure B6 Response signals for data 900T0 including (a,c,e) current and (b,d,f) potential loss vs time.....	151
Figure B7 Response signals for data 400T500R including (a) current and (b) potential loss vs time.....	152
Figure B8 Response signals for data 500T1000R including (a) current and (b) potential loss vs time.....	152
Figure B9 Response signals for data MULTI including (a) current and (b) potential loss vs time.....	152
Figure B10 Response signals for data VARIOUS including (a) current and (b) potential loss vs time.....	153
Figure B11 Full graphical comparison of response between measured data (blue lines) and predicted data from linear models: a) Matching conditions with current step from 0 to 100 mA b) Matching condition with current step from 100 to 0 mA c) Different conditions with current step from 0 to 100 mA d) Different conditions with current step of 0 to 900 mA e) Repeating current steps between 500 to 1000 mA and f) Multiple current steps from 0 to 100, 450 and 900 mA.....	154

Figure B12 Full graphical comparison of response between measured data (dark blue lines), predicted data from linear model (red line), LPV model (green line) and nonlinear models: a) Current step from 0 to 100 mA b) Current step from 0 to 900 mA c) Repeating current steps between 400 to 500 mA d) Repeating current steps between 500 to 1000 mA e) Multiple current steps from 0 to 100, 450 and 900 mA and f) Various current steps.....	155
Figure C1 Response signals for data DSOC500A including (A) current and (B) cell voltage vs time.	158
Figure C2 Response signals for data DSOC1000A including (A) current and (B) cell voltage vs time.	158
Figure C3 Response signals for data DSOC1500A including (A) current and (B) cell voltage vs time.	158
Figure C4 Response signals for data DSOC2000A including (A) current and (B) cell voltage vs time.	159
Figure C5 Response signals for data MULTI A including (A) current and (B) cell voltage vs time.	159
Figure C6 Response signals for data MULTI B including (A) current and (B) cell voltage vs time.	159
Figure C7 Response signals for data CSOC500A including (A) current and (B) cell voltage vs time.	160
Figure C8 Response signals for data CSOC1000A including (A) current and (B) cell voltage vs time.	160
Figure C9 Response signals for data CSOC1500A including (A) current and (B) cell voltage vs time.	160
Figure C10 Response signals for data CSOC2000A including (A) current and (B) cell voltage vs time.	161
Figure C11 Response signals for data CMULTI including (A) current and (B) cell voltage vs time.	161

LIST OF TABLES

	Page
Table 1.1 List of studied operating parameter	5
Table 2.1 Properties of various metals used in metal-air batteries	7
Table 2.2 Performance of zinc-air cells in literatures	30
Table 2.2 (cont.) Performance of zinc-air cells in literatures	31
Table 2.3 Literature reviews of Zn regeneration	34
Table 2.3 (cont.) Literature reviews of Zn regeneration	35
Table 2.4 Summary of literature reviews for modeling of zinc-air battery	38
Table 4.1 Summary of cell components	68
Table 4.2 Summary of cell parameters	69
Table 4.3. Metadata of discharge and response test.....	70
Table 5.1 Nomenclature.....	75
Table 5.1 (cont.) Nomenclature	76
Table 5.2 Summary of experimental data used for identification and validation of models.....	81
Table 5.3 Summary of conditions for identification of the model used in this work ..	86
Table 6.1 list of names and descriptions of data used in this work	97
Table 6.2 Function used to fit the model parameter correlations	101
Table 6.3 Reference values of tuning parameters for EKF.....	105
Table 6.4 Reference values of tuning parameters for combined model estimator.....	111
Table A1 Designed parameters and operating conditions.	132
Table A1(cont.) Designed parameters and operating conditions.....	133
Table A2 Initial conditions at $t = 0$ s used in the simulation.	134
Table A3 Validation of the ZAFB model (from Fig. 3.3A and 3.3B)	137
Table A4 Validation of the zinc electrolyzer model (from Fig. 3.3C and 3.3D).....	137
Table A4 (cont.) Validation of the zinc electrolyzer model (from Fig. 3.3C and 3.3D)	138
Table B1 The location of the data used in this work.	143
Table B2 Parameter values of linear state space models	144

Table B3 Parameter values of nonlinear Hammerstein-Wiener model	144
Table B4 Correlations for parameters of LPV model	145
Table B5 Fit % values ¹ of model predictions relating to Figure 5.4, 5.6 and 5.7	145
Table C1 Correlations for parameters of LPV model	156
Table C1(cont.) Correlations for parameters of LPV model	157
Table C2 Fit % values ¹ of model predictions according to Figure 6.7	157
Table C3 Normalized mean absolute error ¹ of SOC estimation according to Figure 6.10.....	157



CHAPTER 1

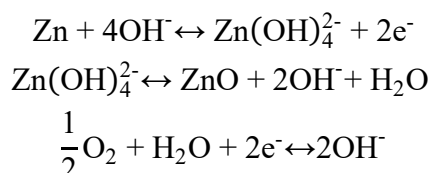
INTRODUCTION

1.1 Background

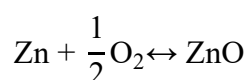
Recently, renewable energy technologies have been enthusiastically researched and developed owing to the rise of energy demand and crucial environmental crisis. Various sources of renewable energies such as solar and wind possess the capability to achieve the requirement. Nevertheless, the intermittent characteristic of renewable energy contributes to several operational problems such as an imbalance between energy demand and supply. For instance, a wind turbine can convert wind energy to electricity. The performance of wind turbines depends on wind speed which is highly unstable resulting in fluctuation in electricity generation. A reliable energy storage system (ESS) can efficiently diminish the drawback of renewable energy. In addition, the ESS is a key to effectively utilize the renewable energy sources

Metal-air batteries are a promising ESS that obtains widespread research interest. Among them, zinc-air battery demonstrates strong potential and has a great possibility to attain commercialization. In recent years, zinc-air battery performance has been actively improved, and their energy density can reach up to 837 Wh/kg (Yan et al., 2018). An anodic active material of this battery is zinc (Zn) which is non-toxic, harmless, plentiful, and low-cost. Besides, zinc-air cell exhibits exceptional reliability, recyclability, and rechargeability (Zhu et al., 2016).

A zinc-air cell can charge and discharge electricity through the electrochemical reaction of Zn and oxygen. During the discharge process, oxidation of Zn and reduction of oxygen are involved. At the negative electrode, Zn is oxidized into zincate ion and later precipitates to zinc oxide (ZnO). At the positive electrode, oxygen reduction reaction (ORR) proceeds. Vice versa, the backward reactions occur during the recharge process. Zincate ion is reduced to Zn at the negative electrode. At the positive electrode, oxygen evolution reaction (OER) takes place instead of ORR. The reactions are shown as followed:



The overall reaction is shown as followed:



The zinc-air cell has been developed in various types and designs. Primary (non-rechargeable) cells are the most developed type and already commercialized.

This type of zinc-air cell is typically fabricated in button cell format which is exclusively used in hearing aid devices or some other small medical devices. Same as button cells, flexible batteries (Suren and Kheawhom, 2016) and cable-type batteries (Park et al., 2015) are also developed to use in small-scale applications. The button cells have very good performance but suffer from difficulty in scaling up. Prismatic design can address the scale-up problem via stacking the cell. Examples of applications of medium-scale primary zinc-air batteries are the power source of navigation instruments, marker lights, or railway signals. It is also selected to use in the military due to its non-explosive property. The flow batteries (Hosseini et al., 2018a, Hosseini et al., 2018b) can be used in large-scale applications such as grid storage systems. The flow batteries have much higher power and capacity. The flow electrolyte provides the advantage in a higher power. Moreover, scaling the capacity up can be done independently by increasing the active material storage tank size. Regarding various benefits for large-scale applications, flow batteries exhibit greater potential than other types of batteries.

Lately, secondary (rechargeable) cells have gained widespread interest and tend to be commercialized in the near future. Several challenges have to be addressed such as dendrite formation. As regards electrical recharge, the formation of dendritic zinc occurs at the zinc electrode. The dendrite can penetrate thru the separator and cause an electrical short-circuit. Additionally, the air electrode decomposed due to oxygen bubbles growth and carbon corrosion during recharge. These problems limit the cycle life of rechargeable zinc-air batteries. Using a mechanical recharge approach can avoid these mentioned issues. Active zinc can be refueled directly to the cell. By this approach, dendrite formation, oxygen bubble growth, and carbon corrosion are completely avoided because zinc is not regenerated inside the cell.

Zinc-air battery can be developed in various aspects. Among them, the model-based engineering is one of the effective approaches which can support the development of zinc-air battery. Modeling and simulation can be applied to examine the phenomena inside the battery or modify the battery structure. For instance, Sunu and Bennion (1980) developed the continuum model of a porous zinc electrode in an alkaline zinc battery which was able to predict the transient behavior and analyze its failure. Later, Mao and White (1992) modified the previous model of Sunu and Bennion which had been extended to comprise the separator, the air electrode, and the precipitation of solid zinc oxide and potassium zincate. Deiss et al. (2002) investigated modeling of a rechargeable zinc-air battery which focused on the redistribution of zinc during the battery cycling and the concentration gradient in the cell. Schröder and Krewer (2014) introduced the zero-dimensional model of secondary zinc-air battery. This model is used to analyze the effect of air composition

including relative humidity, carbon dioxide, and oxygen content. Recently, a mathematical model of zinc electrolyzer with flow electrolyte was developed by Dundálek et al. (2017). Their model comprised the role of hydrogen evolution reaction (HER) therefore the influence of HER on the efficiency and zinc morphology was able to be analyzed. Mostly, the mentioned works of literature were used a theoretical modeling approach to study the phenomena inside the battery.

There are other modeling types that were used to study other battery types but lack for zinc-air battery such as the empirical model. The equivalent circuit model is an empirical model which can clarify the electrochemical behavior via an electrical circuit. According to various literature, equivalent circuit models were used to predict the dynamic behavior of batteries. For example, the dynamic behavior of lithium-ion battery was analyzed using an equivalent circuit model in many works of literature. Stroe et al. (2017) proposed a second-order equivalent circuit model to determine suitability for various applications. This model was also used to investigate zinc-nickel battery. For example, Yao et al. (2017) build an equivalent circuit model of a single-cell zinc-nickel flow battery with 300 Ah. Another example type of model is the linear parameter varying (LPV) model which contains the varying parameters inside the model. Hu and Yurkovich (2011) developed an LPV battery model and proposed a subspace identification algorithm. The proposed LPV model was able to describe the dynamic of the battery under various operating conditions.

A practical application of the dynamic model is the battery state estimation such as the state of charge (SOC) estimation. The estimation of the SOC of the battery is important for the operation of every battery type including zinc-air battery. For instance, Tang et al. (2011) proposed the algorithm for parameter estimation of lithium-ion battery including open circuit voltage and SOC using an equivalent circuit model. Akbar et al. (2015) developed a dynamic model with a constant charging current for lead-acid batteries and used it to compute open circuit voltage and corresponding SOC. Hu and Yurkovich (2012) developed an LPV model of a battery and used the model with a state observer to estimate the SOC of a lithium-ion battery. The dynamic model was also regularly used to estimated other battery states such as state of health (SOH) which reflects the remaining lifetime of the battery. Nevertheless, the study of state estimation still requires more consideration for applying in ZAB.

This thesis is written as a research paper-based thesis which includes 3 published research papers and a manuscript prepared for publishing in the future. All papers are part of the dissertation publication for graduation. The content of this thesis comprises 3 main parts: Model-based analysis of zinc-air flow battery, investigation of the dynamic behavior of the battery, and SOC estimation.

The first part aims to apply the modeling to investigate and improve the operability of zinc-air battery. The type of model used in the first part is a zero-dimensional theoretical model. The mathematical model is developed and implemented in MATLAB. Some model parameters are estimated from the experimental data. The experimental data with various conditions is used to verify the model validity. The model-based analysis is adopted to investigate various operating parameters including electrolyte flowrate, electrolyte concentration, and zincate ion concentration. The optimal parameters are determined using the proposed model. Furthermore, the developed model can be used to study the control and operational strategy for the battery. The second part of this work is to examine the dynamic behavior of zinc-air battery using empirical modeling. The empirical models are identified and implemented in order to predict, monitor, and control the dynamic behavior of battery. The model parameters of empirical models are identified with the experimental dynamic response. Finally, in the last part, the estimation of SOC is studied using the proposed empirical model from the previous part. Extended Kalman filter as state estimation methods integrating with the developed models is employed and compared.

1.2 Objectives

This work can be separated into 3 parts: Model-based analysis, investigation of dynamic behavior, and SOC estimation. For the first part, the model-based analysis aims to develop mathematical models, examine the effect of operating parameters and develop the control and operation strategies of a zinc-air battery system.

The second part is the investigation of the dynamic behavior of the zinc-air battery. The objective of this part is to examine the dynamic behavior of zinc-air battery using an empirical model. Various types of empirical models are used to identify the dynamic behavior of the battery.

The objective of the third part, SOC estimation of zinc-air battery, is to study the SOC estimation for zinc-air battery using the developed model integrated with the SOC estimation method.

1.3 Scopes of research

As regards the first part of this work, model-based analysis, modeling, and simulation of this part are performed in MATLAB. Zero-dimension theoretical model is developed. The developed model is validated with the experimental data measured from a laboratory-made zinc-air flow battery. The flow battery is set up as a plate and frame cell with a stack arrangement of zinc anode separator and an air cathode. The data used to validate are the current density-potential (IV) curve and polarization data

of the battery. The studied parameters include electrolyte flowrate, initial KOH concentration, and initial zincate ion concentration. The values of studied parameters are listed in table 1.1.

For the second part, the dynamic models are also developed using MATLAB. The types of the model used in this part are the state-space model, linear parameter-varying model, and Hammerstein-Weiner model. The dynamic models are identified by parameter fitting. The parameters of the model are fitted using the data measured from a laboratory-made refuellable zinc-air battery. The design of the battery is a tubular cell using zinc pellets as anode active material. The measured data include discharge profile and step response at various current values. The method used to fit the parameter is the minimization of error between measured and predicted data. The validity and accuracy of the model are compared. The dynamic behavior between different current levels is investigated.

The last part, SOC estimation, is conducted with the aid of models developed from the previous part. The methods of SOC estimation include coulomb counting and an extended Kalman filter. The experimental data are obtained from the laboratory-made tri-electrode zinc-air flow battery. The obtained data are used to validate the proposed model and test the performance of the estimation. The tested scenarios in this part are based on varying tuning parameters and the correctness of the initial SOC guess.

Table 1.1 List of studied operating parameter

Parameter	Values	Unit
Electrolyte space velocity	10^{-3} to 10^3	s^{-1}
Initial KOH concentration	2 to 12	M
Initial Zincate ion concentration	0.4 to 1.0	M

1.4 Research benefit

This research provides knowledge of model-based engineering in zinc-air battery research. The first part, Model-based analysis, provide the better insight of zinc-air battery from the theoretical point of view. The proposed model and idea from this part can also be applied in other battery types or other study fields. The second and third parts, investigation of dynamic behavior and state estimation, develop a more practical approach for a battery management system for the zinc-air battery.

CHAPTER 2

THEORIES AND LITERATURE REVIEWS

2.1 Introduction to Zinc-air Technology

Metal-air technology has been developed for several decades. Originally, the purpose of this technology is to use as a power source for small portable devices. Nevertheless, there are numerous attempts to improve this technology into other levels of application. Metal-air batteries work by utilizing electrochemical coupling of a metal anode and air cathode with an appropriate electrolyte. Various types of metal can be used in these batteries. Table 2.1 presents the comparison of properties of metals used in metal-air batteries. Lithium (Li) shows the highest theoretical specific energy and voltage, but it suffers from difficulties in operation. Li is also very dangerous and has limited supply amount. Other metals such as aluminum (Al), magnesium (Mg) or zinc (Zn) are also good candidates. Although Zn has low theoretical specific energy, voltage and capacity compared to other metals, the zinc-air battery is the most developed and nearly successful to commercialize. The difference between theoretical and practical specific energy of Zn is smaller than other metals. Zn also has higher stability and reversibility compared with Al and Mg. For Al-air and Mg-air batteries, corrosion of Al and Mg is extremely unfavorable. This phenomenon makes the actual open circuit voltage (OCV) and practical specific energy of both batteries enormously lower than their theoretical values. Therefore, Al and Mg are suggested to be used with saline electrolyte instead of alkaline electrolyte in order to lower the corrosion effect. As regards zinc-air battery, the properties of Zn are well balance (Zhu et al., 2016). The corrosion resistance of Zn in the alkaline electrolyte is adequate. Moreover, the regeneration of the Zn discharge product is not difficult since Zn electrodeposition in an aqueous electrolyte is feasible. In contrast, Al-air and Mg-air are not electrically rechargeable therefore the recycling process of Al and Mg discharge products is more problematic than that of Zn. This reason truly makes Zn gain an advantage over other candidates. Lately, the practical energy density of zinc-air system has reached 837 Wh/kg in academic research (Yan et al., 2018) and 350 Wh/kg in the industry (Energizer). These numbers already exceed the specific energy density of the market-dominating Li-ion battery (100 to 250 Wh/kg).

Zinc-air battery was first invented unintentionally when the cathode of the Leclanché cell was exposed to atmospheric oxygen. The Leclanché cell is a battery invented by the French scientist Georges Leclanché in 1866 (Leclanché, 1867). This battery consists of a zinc anode coupling with a mixture of manganese dioxide (MnO_2) and carbon as a cathode and ammonium chloride electrolyte. The cathode of

the Leclanché cell was accidentally exposed to the air leading to the three-phase reaction and the change in battery performance. In 1878, a porous platinized carbon air cathode was first introduced to the zinc-air battery by Maiche (1878). In 1932, the primary zinc-air batteries were commercially launched by the National Carbon Company (Heise, 1933). The primary cells have high energy density but low power output (Zhang et al., 2019a). The most widespread application of these cells is a medical application such as hearing aid device or cardiac telemetry. Other applications are also currently seen such as traffic signals. In the last few decades, zinc-air batteries have been revisited as rechargeable batteries. There are two major applications for the commercialization of zinc-air batteries: power sources for electrical vehicles and grid-scale energy storage systems. In 1999, Electric Fuel Ltd. (EFL) developed an electrical vehicle utilizing refuellable zinc-air batteries as power sources (Goldstein et al., 1999). These refuellable batteries were designed as constructible cells. Zn anodes were replaceable cassettes that can be mechanically replaced at the refueling station. In 2012, the first commercialized rechargeable zinc-air batteries for grid storage were introduced by NantEnergy (formerly Fluidic Energy). This technology utilized ionic liquid contained sulfonate anions in zinc-air battery and was able to obtain 5000 charge-discharge cycles (Wolfe et al., 2012). EOS is another company that successfully commercialized the zinc-air energy storage system. EOS proposed the tri-electrode cell with a horizontal structure and near-neutral electrolyte and was able to obtain 2700 cycles (Amendola et al., 2013).

Table 2.1 Properties of various metals used in metal-air batteries

Metal	Theoretical OCV (V)	Actual OCV (V)	Theoretical specific energy (kWh/kg)	Practical specific energy (kWh/kg)	Specific capacity (Ah/g)	Widely used electrolyte type
Li	3.4	2.4	13.0	0.9-5	3.86	non-aqueous
Ca	3.4	2.0	4.6	n.d.	1.34	non-aqueous
Mg	3.08	1.7	6.8	0.4-0.7	2.2	saline
Al	2.70	1.2	8.1	0.4-1.8	2.98	saline
Zn	1.65	1.3	1.3	0.35-0.9	0.82	alkaline
Fe	1.3	1.0	1.2	0.6-0.8	0.96	alkaline

2.2 Cell Configurations

Generally, zinc-air cell consists of 2 electrodes: Zn electrode and air electrode. Both electrodes are separated by electrolyte and separator.

2.2.1 Zn electrode

Negative electrode is Zn metal which serves as fuel for the battery. The requirements for Zn electrode are large surface area, high electrical conductivity and low self-discharge (Pei et al., 2014b). The surface area can be increased by adjusting porosity and particle size. The higher surface area is preferred because it can provide higher discharge current. However, self-corrosion is also higher as a trade-off.

The Zn electrode can have many shapes depending on the design of the battery. For example, the primary cell design usually uses Zn paste as anode while the secondary cell uses Zn coated on current collector. The current collector of Zn electrode can be made of material with high electrical conductivity and high corrosion resistance, e.g., nickel and stainless steel (Sapkota and Kim, 2009).

Morphology of Zn can highly affect the operation of zinc-air cell and is a key factor that should be considered carefully. For instance, dendrite morphology provides large active surface area but also greatly suffers by the corrosion. Thus, this morphology is regularly used in high power cell such as zinc-air fuel cell (Goldstein et al., 1999). On the other hand, low surface area morphologies, such as granular powder form, have lower kinetic activity but have higher corrosion resistance than dendrite form. These morphologies are preferred in long time and low power storage cell such as button cell.

2.2.2 Air electrode

As regards air electrode, the reactant of positive electrode is oxygen in the air. The air electrode should be air breathable, leak-proof and high electrically conductive (Pei et al., 2014b). Air electrode can be composed of 3 layers: current collector, gas diffusion layer (GDL) and catalytic layer. The current collector for air electrode is typically made of porous carbon or metal such as nickel foam. The porous electrode provides large surface area which oxygen can attach on. To improve surface area for oxygen adhering, GDL is implemented. GDL is normally fabricated with porous carbon structure which allows oxygen to diffuse through. The air electrode requires a catalyst for oxygen reduction reaction (ORR) which naturally has sluggish kinetics. Typically, manganese oxide is the most widely used catalyst type for ORR in zinc-air battery (Neburchilov et al., 2010, Gu et al., 2017). This catalyst is notably inexpensive but provides decent catalytic activity. The noble metal catalysts such as silver (Ag) are also interesting candidates, but their economical values have been overcome by the low-cost manganese oxide. Another property that is important to the air electrode is hydrophobicity. ORR in zinc-air system can be considered as a three-phase reaction. Oxygen in the air is gas phase. Electrolyte is generally liquid phase. The last is solid phase which is the catalyst. The balance between three phases can be optimized by

configuring hydrophobicity of the electrode. The hydrophobic polymer such as polytetrafluoroethylene (PTFE) is used as binder for catalyst or GDL in order to link the particle together and provide the hydrophobicity. Some works used PTFE membrane to provide the hydrophobic layer instead of using normal GDL (Ma et al., 2014, Li et al., 2016, Xu et al., 2018).

2.2.3 Electrolyte

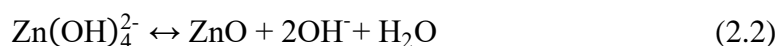
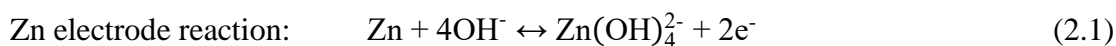
Electrolyte is ionic conducting medium that filled inside the cell chamber and transport ion between negative and positive electrodes. The requirement for the electrolyte is high ionic conductivity. For zinc-air system, various type of electrolyte can be adopted; i.e. alkaline, neutral or non-aqueous. The most commonly used electrolyte for zinc-air cell is potassium hydroxide (KOH) which is alkaline electrolyte (Xu et al., 2015, R. Mainar et al., 2016).

2.2.4 Separator

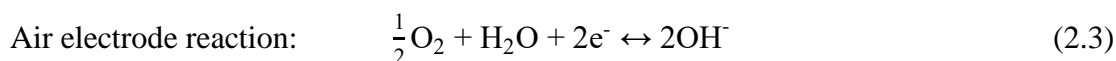
The function of separator is to prevent contacting between negative and positive electrodes. The separator should selectively allow the ions to transfer across. The basic requirements are stable in electrolyte, electrical insulation, high ionic conductivity and capability to store electrolyte. The commonly used separator is organic porous membranes such as polypropylene membrane.

2.3 Working Principle and Electrochemistry

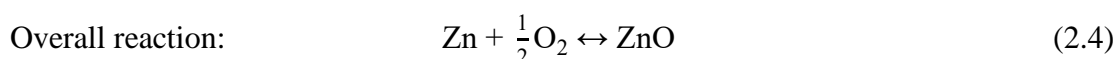
Zinc-air batteries are electrochemical cells which store energy via electrochemical reaction. The schematic diagram of zinc-air battery is shown in Fig. 2.1. While discharge, the batteries act as galvanic cells. At negative (Anode) electrode, oxidation of Zn or Zn dissolution is proceeded. Zn reacts with hydroxide ions and converts to tetrahydroxo-zincate ion ($\text{Zn}(\text{OH})_4^{2-}$) or zincate ion. Electrons are also produced from this reaction. When the electrolyte becomes saturated with zincate ion, the precipitation of zinc oxide (ZnO) occurs.



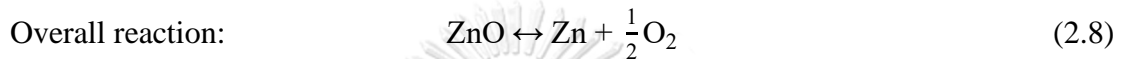
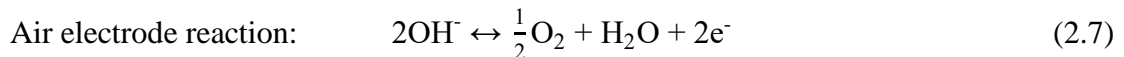
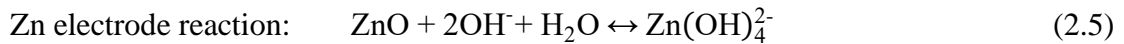
At positive (cathode) electrode, oxygen receives electrons release from Zn dissolution and ORR takes place.



The overall reaction can be basically expressed as Zn reacts with oxygen and forms ZnO. The theoretical standard cell potential is 1.65 volt.



During recharge process, the batteries become electrolysis cell and the reactions are proceeded backward. At negative (cathode) electrode, zincate ion is reduced into Zn metal. The reaction is the same as electrodeposition of Zn. At positive (anode) electrode, oxygen is generated via oxygen evolution reaction (OER). The reaction of recharge process can be rearranged from equation (2.1) to (2.4) as followed:



At the negative electrode, hydrogen evolution reaction (HER) arises as parasitic reaction (equation (2.9)). HER can combine with Zn dissolution resulting in Zn corrosion reaction as expressed in equation (2.10). Zn corrosion occurs when Zn contacts with aqueous electrolyte. It consumes Zn and generates hydrogen and heat. Consequently, the life of battery is shortened. During recharge, HER competes with Zn electrodeposition hence the recharge efficiency is lower.

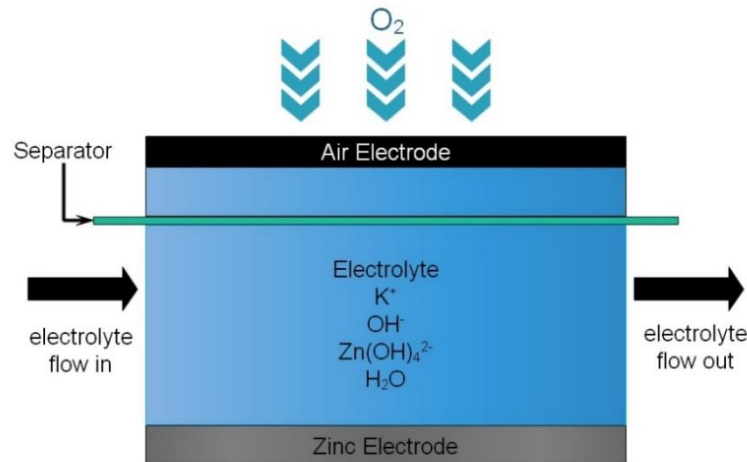
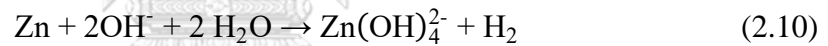


Figure 2.1 Schematic diagram of zinc-air flow battery

2.4 Focuses, Progresses and Challenges

Zinc-air batteries have been research and developed in various aspects. This section provides perspective of focuses, progresses and challenges of zinc-air battery research.

2.4.1 Zn electrode

Development of Zn electrode is one of the most focused topics of zinc-air battery in recent years. The studies of Zn electrode are about overcoming the 4 main problems of Zn electrode: passivation, corrosion (hydrogen evolution), shape change and dendrite formation. These problems have limited the lifetime of zinc-air batteries. Neutralization of these problems can extend the lifespan of the batteries to exceed the commercialization threshold.

Passivation is occurred when the battery discharges. The local concentration of zincate ion exceeds the saturation limit resulting in the formation of ZnO film over the electrode surface. Consequently, the transportation of active species and the active surface area of the electrode are reduced. When the oxide film grows too large, the electrode is totally passivated and inactive. ZnO passivation is considered to have 2 types: type I and type II (Bockelmann et al., 2017, Bockelmann et al., 2018). Type I ZnO is a white porous layer which precipitate over the electrode surface. This type does not fully passivate the electrode and it can be reversed. Another type of ZnO is type II which is black dense film. This type is directly grown on the surface of Zn. It totally blocks the electrode surface and cannot be reversed spontaneously. Type II ZnO is formed due to the exceeding local discharge current. Passivation can be reduced by flow electrolyte or adding some additive such as silicate ion (SiO_3^{2-}).

As regards Zn corrosion, HER can thermodynamically proceed because its potential is greater than Zn electrode potential. This reaction happens on the surface of Zn. It consumes Zn and generate hydrogen gas resulting in capacity loss, electrolyte concentration change and pressure build up. During recharge, HER shares the charge current with the Zn electrodeposition led to charging efficiency loss. To suppress the corrosion, the simplest approach is interfering the reaction equilibrium by increasing zincate ion concentration or adding ZnO into the electrolyte (Einerhand et al., 1988, Sharifi et al., 2009). This method aims to reduce the activity of water and slows down the Zn dissolution as well as Zn corrosion. In addition, some inhibitor such as mercury (Hg) or bismuth (Bi) were doped into the electrode in order to increase the overpotential of HER (Lee et al., 2013). Electrolyte organic additives such as succinic acid was also used to reduce the corrosion (Lee et al., 2006b). Using alternative electrolyte is also a way to address this problem. Besides the alkaline electrolyte, near-neutral electrolyte or non-aqueous electrolyte has also been developed to use in zinc-air battery. The example of saline electrolyte is near-neutral chloride-based electrolyte which has been investigated by many researchers (Sumboja et al., 2016, Clark et al., 2019). The non-aqueous electrolyte has also been interesting since its non-corrosive property can absolutely prevent the corrosion.

For secondary zinc-air battery, shape and morphology change is a phenomenon that can cause the battery failure. The causes of this problem are non-uniform charge current density distribution and concentration gradient in the electrolyte. The shape of recharged Zn is changed from its original design shape resulting in changing of porosity and active area, capacity loss and battery deterioration from undesired morphology. The morphology of Zn is the performance affecting factor of Zn electrode. Different morphologies have different properties and have been used in different application. Shape change into the unfavored morphology can cause degradation in the cell performance. In some case, the morphology of Zn can be changes into the lower porosity morphology. It is called densification. The most unwanted morphology for secondary battery is dendrite which can cause the internal short-circuit and destroy the cell.

Dendritic formation is one type of morphology changing phenomenon. It happens when the charging process is diffusion controlled (Jing et al., 2017). At the high charge current density range, the concentration of zincate ion at surface is become very low and its concentration gradient is large. This causes the dendritic formation which has penetrating structure. It can damage the cell by penetration through the separator and cause short-circuit between two electrodes. The dendritic growth has been addressed by adding electrolyte additive, using alternative electrode design, and charging with pulse current. Additionally, mechanical recharge can completely avoid the short circuit caused by dendritic formation (Smedley and Zhang, 2009).

2.4.2 Air electrode

Air electrode is the most performance affected part in term of cell power. Due to the sluggish kinetic of ORR, the reaction of air cathode is relatively slow and is considered to be a bottle neck for battery discharge. Therefore, the development of air electrode substantially improves the cell power of zinc-air battery. Most of research focus on the improvement of catalyst and composition of electrode. The research of ORR catalyst concentrates on the crystalline structure, synthesis, and fabrication procedure. Development of bi-functional catalyst that is good for both ORR and OER is also a very challenging topic. Furthermore, the ORR needs three-phase boundary as active site thus balancing hydrophobic and hydrophilic composition is also concerned.

Optimization of hydrophobicity of air electrode is crucial for the operation of zinc-air cell. The imbalance of hydrophobicity can cause air electrode flooding or drying (Pei et al., 2014b, Xu et al., 2015). For air electrode flooding, the electrolyte penetrates the GDL because the electrode hydrophobicity is too low. Consequently, oxygen diffusion resistance is increased, and ORR rate is decreased. As regards air electrode drying, water in electrolyte evaporates too fast when humidity in the

ambient air is very low. Accordingly, the active site is dry and reaction rate is decreased. For the cell with small amount of electrolyte such as button cell, electrolyte can be drying out from the entire cell. The air electrode flooding or drying can also be prevented by humidity management.

Electrical recharge can cause detrimental effects to the air electrode, i.e., oxygen bubble growth and electrode corrosion. When the battery is charged, OER is proceeded, and oxygen is formed at the air electrode. The oxygen formation builds the pressure up and lead to mechanical degradation of air electrode. Charging process also induce the corrosion of electrode. Carbon and catalyst in air electrode can be corroded as a result of charging with high current density. Both oxygen bubble growth and electrode corrosion reduce the cycle life of the secondary battery. These phenomena can be avoided by using mechanical recharge or tri-electrode configuration.

Another problem of air electrode is carbonation at air electrode or carbon dioxide (CO₂) poisoning which relates with alkaline electrolyte. CO₂ in the air can easily dissolve and react with alkaline solution. At first, CO₂ reacts with hydroxide ions to forms carbonate ion (CO₃²⁻). When carbonate ion reaches solubility limit, potassium carbonate (K₂CO₃) salt is precipitated. The product of carbonation can be precipitate inside the pore of air electrode resulting in pore plugging and active site blocking. Moreover, the concentration of electrolyte is changed as well as its ionic conductivity (Schröder and Krewer, 2014). For that reason, the CO₂ management must be concerned.

2.4.3 Electrolyte

Recent studies interested on various types of electrolyte ranging from aqueous electrolytes to non-aqueous electrolyte. Aqueous electrolytes include alkaline and near-neutral electrolyte. As mentioned in previous section, alkaline electrolyte is the most widely studied since it provides higher ionic conductivity and superior kinetic for Zn than other electrolytes. Thus, the development of electrolyte mostly conducted to reduce and prevent the problems existing in alkaline electrolyte. The problems of alkaline electrolyte have connection with the other parts of zinc-air battery, i.e., Zn corrosion, electrolyte carbonation, electrolyte drying out, electrolyte leakage, etc.

The other types of electrolytes have also gotten widespread interest as alternative electrolyte. The main reason is that alkaline electrolyte exhibits higher hydrogen evolution than any other electrolyte. Aqueous near-neutral electrolytes such as zinc sulphate (ZnSO₄) and zinc chloride (ZnCl₂) solutions are already well known in Zn electroplating process. Besides the corrosion, neutral electrolyte has two more advantages over alkaline electrolyte. Firstly, neutral electrolyte can completely avoid the CO₂ poisoning because CO₂ absorption in neutral pH is very low. Secondly,

dendrite formation in neutral electrolyte is lower than in alkaline electrolyte due to the lower Zn solubility in neutral electrolyte. The most common near-neutral electrolyte is zinc chloride/ammonium chloride ($\text{ZnCl}_2\text{-NH}_4\text{Cl}$), which has been used in LeClanché cell.

Non-aqueous electrolyte has been on the spotlight because it can eliminate various critical problem of alkaline aqueous electrolyte. There are 3 types of non-aqueous electrolyte that have been investigated in zinc-air battery (Mainar et al., 2018): solid polymer electrolytes (SPEs), gel polymer electrolytes (GPEs) and room temperature ionic liquids (RTILs). SPEs are ionic conductive solids that contain dissolved salts. These electrolytes have good mechanical strength and are easy to handle. The corrosion and battery leakage problems can be mitigated by SPEs. However, SPEs suffer from low ionic conductivity and passivation between polymer-electrode interface. The most widely studied SPEs are poly (ethylene oxide)-based electrolytes.

GPEs are polymer gels containing liquid electrolyte. These electrolytes are usually immersed in liquid electrolyte such as KOH solution. Consequently, GPEs have acceptably high ionic conductivity. It was reported that polyvinyl alcohol / poly (acrylic acid) soaked in 32% KOH can provide ionic conductivity with the same order of magnitude as conventional KOH electrolyte (Zhang et al., 2014). Unfortunately, GPEs also confront the limit of zinc ion solubility and formation of passive layer resulting in limitation of rechargeability. These make GPEs is still not appropriate for secondary batteries.

RTILs gain considerable studies in recent years and are considered as promising candidate for zinc-air cell. RTILs has been developed in various names including molten salt, liquid organic salt or ionic liquid. RTILs are salts that have liquid form in room temperature. The advantages of RTILs are non-volatile, wide electrochemical window, no HER, no carbonation and no dendrite formation. Nonetheless, the ionic conductivity of RTILs is limited and it required high purity. Furthermore, the production and purification of RTILs are high cost and emit pollution. Later, deep eutectic solvents (DESs) are developed as cheaper and greener alternatives to RTILs (Mainar et al., 2018).

2.4.4 Model-based engineering

Modeling and simulation can be adopted in zinc-air batteries research for many purposes. These procedures can help to clarify the complicated phenomena inside the batteries and aid in optimization of cell design and configuration. Modeling can also be applied on material development level ranging from electrode material to electrolyte. For instance, the development of catalyst can be assisted by density functional theory (DFT) which utilizes quantum mechanics to predict electronic

structure in atomic level (Sholl and Steckel, 2009). DFT can also assist to investigate electrode material such as the precipitation of Li_2O_2 in Li-air battery (Hummelshøj et al., 2010, Hummelshøj et al., 2013). Another example is equilibrium thermodynamic model which can be used in determining the suitability of electrolyte. This model can also be used to construct Pourbiac diagram or Potential-pH diagram (Beverkog and Puigdomenech, 1997, R. Mainar et al., 2016).

Typically, the most useful and widely used modeling method is theoretical continuum model. This procedure can use in simulation of battery including evaluation of cell performance or investigation of transport phenomena inside the cells. At the beginning, the continuum model was developed to investigate Zn electrode and the precipitation of ZnO (Sunu and Bennion, 1980). This prototype model was further developed to one-dimensional model for zinc-air battery (Mao and White, 1992, Deiss et al., 2002). Most of the continuum models highlight on the principle of Zn electrode and considering the effect of ZnO precipitation. For example, Stamm et al. (2017) proposed the study of nucleation and growth of ZnO during battery discharge by using one-dimensional model. Other than that, the influence of air composition on the cell cycle performance was examined by using zero-dimensional continuum model (Schröder and Krewer, 2014). Due to the rise of attention to alternative electrolyte, the modeling framework for near-neutral electrolyte system in zinc-air battery was recently proposed by Clark et al. (2017). As regards Zn regeneration, various works utilized the continuum model to investigate the phenomena in the regeneration process. Wang et al. (2014) studied morphology control of Zn regeneration by computational fluid dynamic analysis. Dundálek et al. (2017) proposed model-based analysis of alkaline Zn electrodeposition with respect to the role of HER.

Empirical model has been used in various type of batteries, but it still lacks in the field of zinc-air battery. Empirical model usually uses to predict the dynamic behavior of the battery system. Regularly, the complexity of empirical model is lesser than that of theoretical continuum model. The most commonly used empirical model for battery research is an equivalent circuit model (ECM). The ECM can simplify the electrochemical characteristic of battery and describe it via the theoretical circuit. This type of model has been frequently used to express various types of battery such as Li-ion battery (Tang et al., 2011, Samadani et al., 2015, Li et al., 2017b, Stroe et al., 2017), lead-acid battery (Mauracher and Karden, 1997, Buller et al., 2003, Jantharamin and Zhang, 2008, Akbar et al., 2015) or Zn-Ni battery (Li et al., 2014, Yao et al., 2017). Zinc-air battery also received little investigation by using ECM (Şanal et al., 2015).

2.4.5 Battery State Estimation

In order to utilize battery effectively, Battery Management System (BMS) is adopted in various application. BMS can optimize the used energy of battery and prevent the battery damaging from inappropriate operation (Pop et al., 2008). Moreover, this system is typically used for battery monitoring and control. The state of battery is an important parameter for BMS and battery users. The battery state can indicate how to use battery properly and helps develop the control strategy (Chang, 2013).

The most significant state parameter is state of charge (SOC) which represents the remaining charge inside a battery. SOC is usually defined as the percentage or ratio of the current capacity to the nominal capacity of a battery. State of health (SOH) is another important parameter that indicate the remaining lifetime of the battery. SOH reflects the battery aging and capacity fading. SOH is normally defined as the ratio of present maximum capacity to initial maximum capacity. The accurate state estimation can protect the battery from unsuitable usage, prevent overcharge and overdischarge and prolong the life of battery.

For SOC, the simple estimation can be done via direct measurement or book-keeping method. The direct measurement method relies on the relationship between the SOC and measurable properties such as OCV. This method can be done easily but the measurement requires long rest time which is problem for estimating in dynamic condition. The book-keeping method, such as coulomb counting, utilizes applied current data to estimate SOC. This method is simple but not robust. The error can be accumulated by the time thus, the estimation becomes inaccurate. The SOH can also be easily estimated via the physical analysis and direct impedance measurement techniques. Physical measurement techniques, such as Raman spectroscopy or X-ray diffraction (XRD), can obviously observe the physical change of battery but they are impossible to conduct in real-time estimation. The impedance measurement is also difficult for real-time SOH estimation. As regards advance method, the model-based estimation can be used to estimate various type of battery state including SOC and SOH. This advance method contains correction algorithm which can adapt the parameters dynamically. Consequently, the model-based estimation is very accurate, robust and suitable for the real-time estimation.

Generally, the model-based estimation consists of a system model and an adaptive filter. The empirical model such as ECM is commonly used as the battery model because it is not too complicated (Wei et al., 2018). Nevertheless, the theoretical model has been tried but the model is too complicate to use with adaptive process. The widely used adaptive filters are various types of Kalman filter. This filter can update the model parameter associated with the measurement data therefore the real-time estimation becomes more robust.

2.5 Theoretical Cell Modeling

As regards theoretical continuum model of battery, this section is divided into 5 parts including continuity of species, electrode kinetics, mass transport in electrolyte, cell potential and evaluation of cell performance.

2.5.1 Continuity of species

Mass and charge balances of battery cell can be done via the continuity equations. The mass continuity, equation (2.11), is developed by mass balance over the control volume. In this case, it describes the transport of chemical species k in porous electrode. For charge continuity, equation (2.12) describes charge conservation via the assumption of electroneutrality. The general equations of mass and charge continuity are expressed as followed:

$$\frac{\partial \varepsilon C_k}{\partial t} = -\vec{\nabla} \cdot \vec{J}_k + R_i \quad (2.11)$$

$$0 = -\vec{\nabla} \cdot \vec{i} + \sum_i n_k F R_i \quad (2.12)$$

Both continuity equations require the expression of electrolyte transport and electrochemical reactions to be completed.

2.5.2 Mass transport in electrolyte

Mass transport of species k in electrolyte can be expressed by Nernst-Planck equation:

$$\vec{J}_k = -\left[D \vec{\nabla} C_k - C_k \vec{V} + \frac{n_k F}{RT} D_k C_k (\vec{\nabla} \phi_e) \right] \quad (2.13)$$

Where \vec{J}_k is mass flux of species k which combines diffusion, convection and migration fluxes. $-D \vec{\nabla} C_k$ represents diffusion flux (\vec{J}_k^{diff}). $C_k \vec{V}$ denotes convective flux (\vec{J}_k^{conv}). $-\frac{n_k F}{RT} D_k C_k (\vec{\nabla} \phi_e)$ designates migration flux (\vec{J}_k^{mig}). The model components shown in equation (2.13) are universal form of electrolyte transport. Theoretically, electrolyte transport equation can be expressed by 2 different forms based on ionic strength and pH of the electrolyte, i.e. dilute solution theory and concentrated solution theory (Clark et al., 2018). As regards low ionic strength electrolyte, dilute solution theory can be applied. On the other hand, concentration solution theory can be used in the high ionic strength system which zinc-air battery typically is.

Dilute Solution Theory:

$$\vec{J}_k^{diff} = -D \vec{\nabla} C_k \quad (2.14)$$

$$\vec{J}_k^{mig} = -\frac{n_k F}{RT} D_k C_k (\vec{\nabla} \phi_e) \quad (2.15)$$

Concentrated Solution Theory:

$$\vec{J}_k^{diff,mig} = -D \vec{\nabla} C_k - \frac{t_k}{n_k F} \vec{i} \quad (2.16)$$

$$\vec{i} = -\kappa \vec{\nabla} \phi_e + \frac{\kappa}{F} \sum_k \frac{t_k}{n_k} \frac{\partial \mu_k}{\partial C_k} \vec{\nabla} C_k \quad (2.17)$$

2.5.3 Electrode kinetics

The rate of electrochemical reaction depends on the charge or discharge current. Thus, the electrochemical reaction rate is directly proportional to the applied current. As regards faraday's law, the charge transfer rate is described as:

$$I = \frac{dQ}{dt} \quad (2.18)$$

Where I is the current, Q is charge and t is time. The electrochemical reaction produces electron equivalent to charge transfer per time or electrical current. Rate of electrochemical reaction in the unit of mole per time can be calculated as:

$$R_i = \frac{dN}{dt} = \frac{i}{n_i F} \quad (2.19)$$

Let consider an electrochemical reaction as followed:



The rate of this reaction can be written in traditional kinetic form as:

$$R = k_{red} a_{ox} - k_{ox} a_{red} \quad (2.21)$$

This reaction rate can be written in the net current form as followed:

$$i = nF(k_{red} a_{ox} - k_{ox} a_{red}) \quad (2.22)$$

Conventionally, the reaction rate constant depends on temperature, activation energy and natural characteristic of the reaction and can be described via Arrhenius equation:

$$k = A \exp\left(\frac{-E_a}{RT}\right) \quad (2.23)$$

For electrochemical reaction, the activation energy can be inserted as applied potential:

$$k_{red} = A_{red} \exp\left(\frac{\Delta G_{red}}{RT}\right) \exp\left(\frac{\alpha_{red} nF (E - E_{eq})}{RT}\right) \quad (2.24)$$

$$k_{ox} = A_{ox} \exp\left(\frac{\Delta G_{ox}}{RT}\right) \exp\left(\frac{-\alpha_{ox} nF (E - E_{eq})}{RT}\right) \quad (2.25)$$

These can be reduced to the simple forms:

$$k_{red} = k_{red}^0 \exp\left(\frac{\alpha_{red} nF (E - E_{eq})}{RT}\right) \quad (2.26)$$

$$k_{ox} = k_{ox}^0 \exp\left(\frac{-\alpha_{ox} nF (E - E_{eq})}{RT}\right) \quad (2.27)$$

Inserting equation (2.22) and (2.23) into equation (2.20) gives:

$$i = nF \left[k_{red}^0 a_{ox} \exp\left(\frac{\alpha_{red} nF (E - E_{eq})}{RT}\right) - k_{ox}^0 a_{red} \exp\left(\frac{-\alpha_{ox} nF (E - E_{eq})}{RT}\right) \right] \quad (2.28)$$

Considering dynamic equilibrium case, net current is zero. The oxidation and reduction currents are equals to each other. Both rate constants are also considered to be equal so that $k_{red}^0 = k_{ox}^0 = k^0$. Equation (2.28) can be further rearranged:

$$i = nFk^0 \left[a_{ox} \exp\left(\frac{\alpha_{red}nF(E-E_{eq})}{RT}\right) - a_{red} \exp\left(\frac{-\alpha_{ox}nF(E-E_{eq})}{RT}\right) \right] \quad (2.29)$$

$$i = i_0 \left[a_{ox} \exp\left(\frac{\alpha_{red}nF(E-E_{eq})}{RT}\right) - a_{red} \exp\left(\frac{-\alpha_{ox}nF(E-E_{eq})}{RT}\right) \right] \quad (2.30)$$

The equation (2.30) is one form of the Butler-Volmer equation. This equation describes the relation of electrochemical reaction rate and the potential applied. a_{ox} and a_{red} can be changed into different forms depending on the reaction system. For the standard state, the most common form of Butler-Volmer equation is shown in equation (2.31).

$$i = i_0 \left[\exp\left(\frac{\alpha_{red}nF(E-E_{eq})}{RT}\right) - \exp\left(\frac{-\alpha_{ox}nF(E-E_{eq})}{RT}\right) \right] \quad (2.31)$$

2.5.4 Cell potential

The equilibrium electromotive force (E_{emf}) of battery is obtained at zero current state. As regards half-cell reaction, the equilibrium E_{emf} denotes the standard electrode potential (E^0). The E_{emf} is equivalent with the standard Gibbs free energy change (ΔG^0) of the reaction and can be calculated as followed:

$$E_{emf} = E^0 = \frac{-\Delta G^0}{nF} \quad (2.32)$$

From the thermodynamics data of Gibbs energy, the equation (2.32) can be used to calculate E^0 of any electrochemical reaction in standard state. For non-standard state, the electrode potential deviates from the E^0 . To calculate the electrode potential at any state, Nernst equation is applied to express the effect of temperature and activity of reactant. This equation gives a result as Nernst potential of electrode (E_{eq}). Then, the equilibrium electrode potential of each electrode can be used to calculate the equilibrium cell potential ($E_{eq,cell}$) or Nernst potential of the cell or OCV.

$$E_{eq} = E^0 - \frac{RT}{nF} \ln\left(\frac{a_{red}}{a_{ox}}\right) \quad (2.33)$$

$$E_{eq,cell} = E_{eq}^{positive} - E_{eq}^{negative} \quad (2.34)$$

Where a_{red} and a_{ox} are the activity of reduced and oxidized form of reactant, respectively. E is electrode potential. Superscript 0 stands for standard state. Subscript eq stands for equilibrium.

$$E_{cell} = E_{eq,cell} - \eta_{activation} - \eta_{ohmic} - \eta_{concentration} \quad (2.35)$$

Furthermore, when battery discharges or charges, the cell voltage is different from the equilibrium potential. In order to calculate cell potential, potential losses must be accounted, i.e., activation loss, ohmic loss and concentration loss. The details of potential losses are given in section 2.5.5.

2.5.5 Cell performance evaluation

2.5.5.1 Open Circuit Cell Potential

The OCV is defined as the equilibrium potential of battery cell measuring at zero current state. For zinc-air battery, the theoretical OCV calculating from standard electrode potential is 1.65 V. However, the actual OCV measuring from an actual cell is practically less than 1.65 V and is about 1.2 to 1.4 V. This happens because the actual OCV already includes some potential losses. Specifically, the activation overpotential of air electrode is very impactful even at open circuit condition. Another loss that reduces the OCV is Zn corrosion. If the corrosion is high, the equilibrium potential is shifted lower. For example, the theoretical OCV of Al-air battery in alkaline system is about 2.7 V but the actual OCV of this battery is only about 1.2 V due to high corrosion and sluggish ORR.

The theoretical OCV can be calculated as shown above in equations (2.33) and (2.34). These equations can be adapted into zinc-air battery as in equations (2.36) and (2.37). The parameters affected OCV are temperature and activity of the reactant.

$$E_{eq}^{air} = E^{0,air} - \frac{RT}{nF} \ln \left(\frac{(P_{O_2}/P^{ref})^{0.5}}{(C_{OH^-}^{air}/C^{ref})^2} \right) \quad (2.36)$$

$$E_{eq}^{zinc} = E^{0,zinc} - \frac{RT}{nF} \ln \left(\frac{(C_{Zn(OH)_4^{2-}}^{zinc}/C^{ref})}{(C_{OH^-}^{zinc}/C^{ref})^4} \right) \quad (2.37)$$

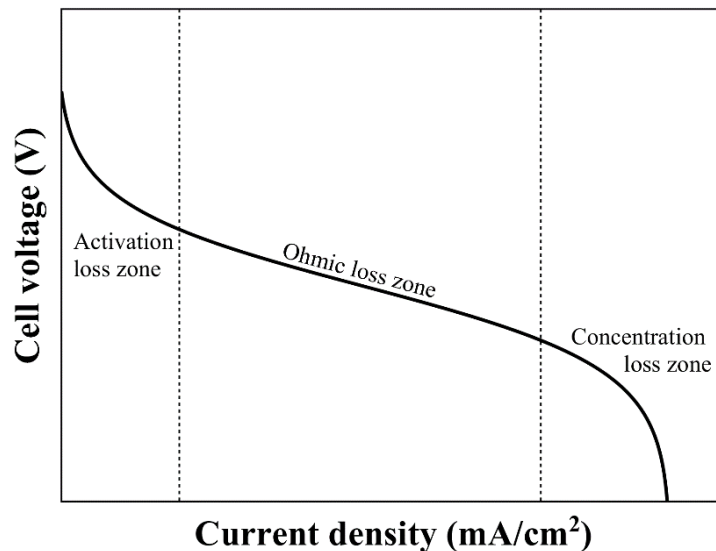


Figure 2.2 example of polarization curve of a zinc-air battery

2.5.5.2 Overpotential / Potential losses and Polarization curve

As mentioned before in section 2.5.4, the potential losses or overpotentials are used to calculate the cell potential. The overpotential is defined as the energy loss when the

electrochemical cell operates. Generally, the overpotential and cell performance are monitored by polarization curve. Polarization curve or current-potential curve shows the cell potential in the function of applied current. Fig. 2.2 illustrates the example of polarization curve of the battery. Each different region of the curve represents different overpotential dominating in each region. Regularly, 3 types of overpotential can be depicted in the curve, i.e., activation overpotential, ohmic overpotential and concentration overpotential.

A) Activation Overpotential

An electrochemical reaction thermodynamically requires activation energy to be proceed. The activation overpotential refers to that activation energy in term of potential losses. This overpotential directly relates to the current rate. The higher current requires the higher overpotential. From Fig. 2.2, activation overpotential dominates over the initial-middle zone of the polarization curve ranging from OCV to the origin of region with constant slope. In zinc-air battery, the activation overpotentials involves in the charge transfer reactions of Zn and air electrode as shown in equations (2.1) and (2.3). The Butler-Volmer approach can be used to describe the activation overpotentials as shown in equations (2.38) and (2.39).

$$i_{Zn} = i_0^{zinc} \cdot \left[\exp\left(\frac{\alpha_{zinc} n_e F}{RT} \eta_{act}^{zinc}\right) - \exp\left(-\frac{(1-\alpha_{zinc}) n_e F}{RT} \eta_{act}^{zinc}\right) \right] \quad (2.38)$$

$$i_{air} = i_0^{air} \cdot \left[\exp\left(\frac{\alpha_{air} n_e F}{RT} \eta_{act}^{air}\right) - \exp\left(-\frac{(1-\alpha_{air}) n_e F}{RT} \eta_{act}^{air}\right) \right] \quad (2.39)$$

The equations (2.38) and (2.39) are derived from equation (2.31). $E - E_{eq}$ is replace with the η_{act} . These equations express the relationship between the activation overpotential and the current density of each electrode. In most cases, symmetric electron transfer is assumed resulting in $\alpha = 0.5$. The equation (2.31) can be simplified to the form of inverse hyperbolic sine as shown in equation (2.40).

$$\eta_{act} = \frac{2RT}{nF} \sinh^{-1}\left(\frac{i}{2i_0}\right) \quad (2.40)$$

When the overpotential goes very large, one of the exponential terms inside the bracket can be diminished due to its very low value. Therefore, the equation (2.31) can become the Tafel equation:

$$\eta_{act} = \frac{RT}{\alpha nF} \ln\left(\frac{i}{i_0}\right) \quad (2.41)$$

$$\eta_{act} = \frac{RT}{\alpha nF} \ln(i) - \frac{RT}{\alpha nF} \ln(i_0) \quad (2.42)$$

The term $\frac{RT}{\alpha nF}$ is called Tafel slope which can be determined from Tafel plot ($\ln|i|$ vs η_{act} or $\log|i|$ vs η_{act}). The Tafel slope expresses the relationship of overpotential and reaction rate. The Tafel plot can also be used to determine the

information of electrochemical reaction such as corrosion potential, open circuit potential, charge transfer coefficient or exchange current density.

The activation overpotential generally depends on the natural characteristic of each electrochemical reaction. For example, the ORR in zinc-air battery is very sluggish reaction led to very high activation overpotential. Meanwhile, Zn dissolution is always faster than ORR resulting in lower activation overpotential. Furthermore, the activation overpotential is also affected by temperature and the activity of reactant same as other chemical reaction.

B) Ohmic Overpotential

The ohmic overpotential denotes the potential loss to the internal resistance of cell components, i.e., electrode, electrolyte, etc. It is the dominant overpotential of the middle region with constant slope. In most case, ohmic overpotential is linearly increased with the current according to Ohm's law. It is simply expressed as equation (2.43).

$$\eta_{ohmic} = I^{cell} R_{ohmic} \quad (2.43)$$

Where I^{cell} is total current applied. R_{ohmic} is internal resistance from the cell components. R_{ohmic} can be affected various parameters. For instance, change of KOH concentration contributes to change of ionic conductivity of electrolyte. Formation of ZnO reduces the electrical conductivity of Zn electrode.

C) Concentration Overpotential

The concentration overpotential is also sometimes called diffusion loss or mass transport loss. This overpotential occurs due to the limit of mass transport. The reaction becomes a state called mass transfer control or diffusion control. Therefore, the concentration overpotential dominates the high current region of the polarization curve. For discharge process of zinc-air battery, diffusion limit of oxygen at air cathode contributes the concentration overpotential. In this region, increasing current further results in potential drop rapidly. For charge process, mass transport limit of zincate ion can cause the rise of parasitic reaction.

The concentration overpotential from the oxygen diffusion limit can be calculated via the limiting current density (i_{lim}). The limiting current density is derived from Fick's law of diffusion as shown in equation (2.44). Then, the limiting current density is used to calculate concentration overpotential in equation (2.45). If we manage to know oxygen concentration at catalyst surface, it can also be used to compute concentration loss instead of limiting current density as shown in equation (2.46).

$$i_{lim} = \frac{Z_{e,O_2} F D_{O_2, GDL}}{\delta_{GDL}} \cdot C_{O_2} \quad (2.44)$$

$$\eta_{conc} = \frac{RT}{n_{e,O_2}F} \ln \left(1 - \frac{i^{cell}}{i_{lim}} \right) \quad (2.45)$$

$$\eta_{conc} = \frac{RT}{n_{e,O_2}F} \ln \left(\frac{C_{O_2,CS}}{C_{O_2,bulk}} \right) \quad (2.46)$$

2.5.5.3 Current Density and Power Density

For the electrochemical cell, current is equivalent to the rate of reaction. In order to compare the performance of batteries, the current density is regularly used to report the performance of batteries instead of current. As regards zinc-air battery, current density is typically normalized with the active surface area of air electrode because the area of air electrode is practically constant. Moreover, the air electrode is the bottle neck limit of the system in case of discharging.

$$\text{current density } (i) = \frac{\text{current}}{\text{Active area of air electrode}} = \frac{I}{A_{air}} \quad (2.47)$$

Same as current, the cell power also needs to be normalized to the active area of electrode. The normalized cell power is called power density.

$$\text{power density} = \frac{\text{cell power}}{\text{Active area of air electrode}} = i_{cell} E_{cell} \quad (2.48)$$

To compare the performance between different batteries reported in literature, the peak (maximum) power density and the current density at peak are usually used.

2.5.5.4 Efficiency of the Electrochemical cell

The performance of battery usually evaluates in the term of efficiency. Different types of efficiency indicate different aspect of cell performance. Current efficiency or coulombic efficiency of the rechargeable battery is the ratio between extracted electrical charge and the total input charge based on a full charge-discharge cycle.

$$\text{current efficiency} = \frac{Q_{discharging}}{Q_{charging}} \quad (2.49)$$

As regards parasitic reaction, the current efficiency for charging process can be defined as the ratio of Zn electrode current density to the total applied current density. The current efficiency of discharging process can be defined as the ratio of the actual discharge current density to the total Zn electrode current density.

$$\text{Charge current efficiency} = \frac{i^{Zn}}{i^{cell}} \quad (2.50)$$

$$\text{Discharge current efficiency} = \frac{i^{cell}}{i^{Zn}} \quad (2.51)$$

Current efficiency can express the quantity of the useful charge. This efficiency does not include the quality of charge respect to cell power. Therefore, the energy efficiency is another performance index for the rechargeable battery. It is the ratio of discharged energy to charged energy based on a full charge-discharge cycle. This efficiency indicates both quality and quantity of the applied charge.

$$Energy = IEt \quad (2.52)$$

$$energy\ efficiency = \frac{Discharged\ Energy}{Charged\ Energy} \quad (2.53)$$

2.6 Empirical Dynamic Modeling

Generally, the purpose of empirical modeling of battery is to predict the behavior and some significant parameters of the battery with fast and less effort of computation since it typically applied on the real-time operation such as monitoring and control. Herein, this work includes 3 selected types of empirical model: state space model, linear varying parameter model and Hammerstein-Weiner model.

2.6.1 State Space Model

State space model is a linear time-invariant (LTI) model. In this work, this model is the representative of the linear model. The model describes the system of input, output and state variables by first-order differential equations as followed:

$$\dot{X}(t) = AX(t) + Bu(t) \quad (2.54)$$

$$Y(t) = CX(t) + Du(t) \quad (2.55)$$

Where u , X and Y are input vector, state vector and output vector, respectively. A , B , C and D are state matrix, input matrix, output matrix and feed through matrix, respectively.

The above equations are written in the continuous-time domain. The state space model can also be expressed in the discrete representation as followed:

$$X(k+1) = AX(k) + Bu(k) \quad (2.56)$$

$$Y(k) = CX(k) + Du(k) \quad (2.57)$$

2.6.2 Linear Parameter Varying model

Linear parameter varying (LPV) model is a time-variant model and it still possesses linear behavior. However, some model parameters vary with other parameters called scheduling parameters. Therefore, LPV model can be used to predict nonlinear behavior which related to the scheduling parameter. By applying LPV representation to the state space model, the model parameters are expressed as a function of scheduling parameter $p(k)$:

$$A = A(p(k)), B = B(p(k)), C = C(p(k)) \text{ and } D = D(p(k)) \quad (2.58)$$

Consequently, the equations (2.56) and (2.57) becomes

$$X(k+1) = A(p(k))X(k) + B(p(k))u(k) \quad (2.59)$$

$$Y(k) = C(p(k))X(k) + D(p(k))u(k) \quad (2.60)$$

2.6.3 Hammerstein-Weiner model

Hammerstein-Weiner (HW) model is a block-oriented model which has linear and nonlinear functions as separated blocks. In this work, this model is a representative of nonlinear model. The block diagram of HW model is shown in Fig. 2.3. The model is oriented as three function blocks connected in series. The first block is a nonlinear block called ‘Hammerstein block’ and is expressed by function f . The input signal is transformed by this block. The transformed signal sequentially goes to the linear block.

$$w(k) = f[u(k)] \quad (2.61)$$

where $u(k)$ and $w(k)$ are the input and output of nonlinear block f , respectively.

The linear block is designated as B/F and is derived from an output error (OE) model.

$$x(k) = (B/F)w(k - n_k) \quad (2.62)$$

where n_k is an input delay. B and F are polynomials in a linear output-error model with respect to the delay operator z^{-1} and expressed as followed:

$$B(z) = b_1 + b_2z^{-1} + \dots + b_{n_b}z^{-n_b+1} \text{ for } B \text{ order} = n_b \quad (2.63)$$

$$F(z) = 1 + f_1z^{-1} + \dots + f_{n_f}z^{-n_f} \text{ for } F \text{ order} = n_f \quad (2.64)$$

The last nonlinear block h is called ‘Wiener block’. the output signal of the linear block is transformed by this block:

$$y(k) = h[x(k)] \quad (2.65)$$

where $y(k)$ is the output of the nonlinear block h and the output of HW model.

The output of the HW model can be written as followed:

$$y(k) = h[(B/F)f[u(k)]] \quad (2.66)$$

2.7 SOC estimation techniques

2.7.1 Direct measurement

The simplest way to estimate SOC is the direct measurement. This group of methods takes advantage from the measurable physical properties such as OCV or terminal voltage and estimate SOC by constructing the correlation between the measured properties and SOC. For example, the OCV method estimate SOC from the OCV-SOC correlations (Danko et al., 2019).

$$V_{OC} = A \cdot SOC + B \quad (2.67)$$

This example correlation is the linear correlation which has been implemented in lead-acid battery. For other types of battery, the correlations are different. Because measurement of some physical properties takes long time, the direct measurement method is difficult to use in real-time estimation.

2.7.2 Coulomb counting

The coulomb counting (CC) method estimates SOC by counting the change of capacity of a battery. Mathematically, discharging / charging current is integrated over time resulting in capacity change. To estimate the SOC, the capacity change together with previous estimated SOC values and nominal capacity (C_n) are used in the calculation, as followed:

$$SOC(t) = SOC(t - 1) + \int_{t-1}^t \frac{I_{cell}(t)}{C_n} dt \quad (2.68)$$

Or it can be written in discrete time domain as:

$$SOC(k) = SOC(k - 1) + \frac{\Delta t}{C_n} \cdot I_{cell}(k) \quad (2.69)$$

These two equations are common form of CC method for the ideal system that has current efficiency of 1; however, the efficiency is always less than 1. Therefore, modification is applied to the CC method, as expressed:

$$SOC(t) = SOC(t - 1) + \int_{t-1}^t \frac{\varepsilon \cdot I_{cell}(t)}{C_n} dt \quad (2.70)$$

$$SOC(k) = SOC(k - 1) + \frac{\Delta t}{C_n} \cdot \varepsilon \cdot I_{cell}(k) \quad (2.71)$$

Where ε is the current efficiency

Nonetheless, the accuracy of CC method can be affected by various factors (Moo et al., 2007), i.e., temperature, battery aging, current level, cycle life and efficiency. Another drawback of CC method is the error accumulation when it applies in long-time operation.

2.7.3 Kalman filter

Kalman filter (KF) is a recursive state estimation algorithm which can estimate the inner states of any dynamic system (Murnane and Ghazel). As regards state estimation of battery, the battery pack is observed as dynamic system which has cell current as input and terminal voltage as output (Rivera-Barrera et al., 2017). Moreover, this technique is also capable of real-time estimation (Chang, 2013).

KF takes advantage from the estimated states from previous time and the measurement from current time. The errors of the system are assumed to be Gaussian. Typically, KF is designed to estimate state linear system. For example, the linear model can be written as:

$$X_{k+1} = AX_k + Bu_k + q_k^X \quad (2.72)$$

$$Y_k = CX_k + r_k^X \quad (2.73)$$

Where q_k^X and r_k^X are stochastic noise. These equations are equivalent to the linear state-space model. The algorithm of KF is described as following equations:

Prediction

Estimated state prediction: $\hat{X}_{k+1}^- = AX_k + Bu_k$ (2.74)

Estimated covariance prediction: $P_{k+1}^- = AP_k^+ A^T + Q^X$ (2.75)

Output estimation: $\hat{Y}_k = C\hat{X}_{k+1}^-$ (2.76)

Correction

Optimal Kalman gain: $K_k = P_{k+1}^- C^T (CP_{k+1}^- C^T + R^X)^{-1}$ (2.77)

State update: $\hat{X}_{k+1}^+ = \hat{X}_{k+1}^- + K_k(Y_k - \hat{Y}_k)$ (2.78)

Estimated covariance update: $P_{k+1}^+ = (1 - K_k C)P_{k+1}^-$ (2.79)

Where variables with superscript + means that variables are corrected and variables with superscript – means that variables are predicted. \hat{X}_k and \hat{Y}_k represent estimated state and output, respectively. P is estimated covariance. Q and R are covariances of process noise and measurement noise, respectively.

2.7.4 Extended Kalman filter

The EKF is the nonlinear variant of KF. EKF utilizes the linearization to handle the nonlinear system (Julier and Uhlmann, 2004). The nonlinear model used with EKF can be written as:

$$X_{k+1} = f(X_k, u_k) + q_k^X \quad (2.80)$$

$$Y_k = g(X_k, u_k) + r_k^X \quad (2.81)$$

Where $f(X_k, u_k)$ and $g(X_k, u_k)$ are nonlinear function. q_k^X and r_k^X are stochastic noise. The procedure of EKF is defined as following equations:

Prediction

Estimated state prediction: $\hat{X}_{k+1}^- = f(\hat{X}_k^+, u_k)$ (2.82)

Estimated covariance prediction: $P_{k+1}^- = \hat{F}_k P_k^+ \hat{F}_k^T + Q^X$ (2.83)

Output estimation: $\hat{Y}_k = g(\hat{X}_{k+1}^-, u_k)$ (2.84)

Correction

Optimal Kalman gain: $K_k = P_{k+1}^- \hat{G}_k^T (\hat{G}_k P_{k+1}^- \hat{G}_k^T + R^X)^{-1}$ (2.85)

State update: $\hat{X}_{k+1}^+ = \hat{X}_{k+1}^- + K_k(Y_k - \hat{Y}_k)$ (2.86)

Estimated covariance update: $P_{k+1}^+ = (1 - K_k \hat{G}_k) P_{k+1}^-$ (2.87)

Where \hat{F}_k and \hat{G}_k are Jacobian matrices of state and output functions, respectively, which can be defined as:

$$\hat{F}_k = \frac{\partial f(\hat{X}_k^+, u_k)}{\partial \hat{X}_k^+} \quad (2.88)$$

$$\hat{G}_k = \frac{\partial g(\hat{X}_{k+1}^-, u_k)}{\partial \hat{X}_{k+1}^-} \quad (2.89)$$

The EKF also has some drawbacks. The first drawback is the difficulty in the Jacobians calculation for some model. The computational cost might be high based on

the Jacobians calculation. Next, EKF only works with the differentiable model. Lastly, the highly nonlinear system might be difficult to find the optimal state by EKF.

2.8 Literature Reviews

2.8.1 Zinc-air cell

The development of ZAB tried to address the battery problem and improve the cell performance and stability of the battery. In previous literature, the most widely used methods were material study and configuration of the cell parameters.

Flow battery is a battery configuration that can improve the performance of battery significantly. For example, Appleby and Jacquier (1976) from Laboratories de Marcoussis (C.G.E.) proposed a circulating zinc-air battery using as a vehicle power source. The discharging unit was designed to be separated with the charging unit. The discharging unit consisted of many tubular cells. The charging unit was an electrolysis cell. The electrolyte and zinc were mixed together and were stored in reservoir. The proposed system was capable of 110 Wh/kg with the power rate of 80 W/kg for an urban vehicle and was able to scale up to 125 Wh/kg for heavy duty purpose. The lifetime of this system was two times higher than that of lead acid battery. Recharge efficiency of this system was about 40% which was relatively low.

A zinc-air flow battery with packed bed anode was studied by Lawrence Berkeley Laboratory (Huh et al., 1992, Savaskan et al., 1992). The cell was fabricated as a plate cell with zinc particle packed in the anode channel. The area of cathode was 76 cm². The electrolyte was 45% KOH solution. The battery exhibited peak power density of 185 mW/cm² with current density of 200 mA/cm² at temperature of 45 °C. They further studied the regeneration of zinc particles and electrolyte using fluidized bed electrodeposition (Huh et al., 1992). The electrolyte was also 45% KOH solution. The suitability of various electrode material and the effect of current density and zincate concentration on cell performance were investigated. After optimizing the material, the result showed that the energy consumption was 1.92 kWh per kg of zinc at 1000 A/m² and 2.08 kWh per kg of zinc at 2000 A/m². Combining both parts of studies, the round-trip energy efficiencies of 50% and 46% were exhibited.

In the past century, there is an adaptation of zinc-air flow battery which is zinc-air fuel cell or refuelable battery. This configuration attracts widespread interest because of its continuous operation. For instance, Sapkota and Kim (2010) proposed a zinc-air fuel cell using metal oxide catalyst and polymer separator. The cell was designed as a plate cell with 3 degrees taper end. Air cathode, separator and electrolyte were examined. For air cathode, cathode fabrication with catalyst mixture of MnO₂ and CeO₂ showed the best performance. Nylon net was the best separator in

the comparison. The electrolyte was compared between NaOH and KOH with concentration of 4, 8 and 16 M. 8 M KOH was exhibited to be the optimal condition for electrolyte. For maximum performance, this cell provided 70 mA/cm² at 1 volt.

Jiratchayamaethasakul et al. (2014) investigate anode orientation and flow channel design in refuelable zinc-air fuel cell. The cell was designed as plate and frame type with 3.5 × 3.5 of active area. Active zinc slurry was fed into the cell by pumping. The effect of anode orientation and flow pattern on cell performance was examined. It was found that the anode-bottom orientation provided higher performance than top orientation due to the effect of gravity. As regards the effect of flow pattern, serpentine flow channel performed better than parallel flow channel. The maximum performance of this cell was 240 mW/cm² of peak power density at 500 mA/cm².

Pei et al. (2014a) proposed high performance ZAFC stack. Bipolar plate used as anode current collector and for stacking cell. MnO₂ was used as cathode catalyst. The 5 cells stack was characterized the polarization curve. The third cell in the stack provided highest performance due to the highest temperature spot in the stack. The effects of location, filled state of zinc, contact resistance and flow state of electrolyte and air were investigated by 2 cells stack. The optimal performance was obtained from the second cell of the stack with type Y chamber and cleaned nickel foil. Its peak power density was able to reach 435 mW/cm² at 0.86 V and 510 mA/cm².

Recently, Oh et al. (2018) developed the flexible tubular zinc-air fuel cells with single-layer cathode. This cell was designed as tubular cell. Zinc gel mixed with 8.5 M KOH was used as flow electrolyte. The cathode was fabricated as single-layer electrode. The result showed that the electrochemical performance of the cell with single-layer cathode was superior to that of double-layer cathode. The effects of PTFE content, ball milling duration and cathode thickness were further investigated

Electrical recharging was also a key method to recharge zinc-air battery. There are now 2 solutions for electrical charging of zinc-air battery: bifunctional electrode and tri-electrode configuration. Ma et al. (2014) proposed electrically rechargeable ZAB stack consisting of 3 cells in series. A novel bipolar plate was developed as anode current collector. A-MnO₂ and LaNiO₃ were used as bifunctional catalyst. The polarization characteristic of a single cell showed peak power density of 60.4 mW/cm² at 80 mA/cm². The total peak power of cell stack was 4500 mW. After 100 charge-discharge cycles, the stability testing result showed that the charging voltage increased by 1.56 % which exhibited excellent stability performance. The electrochemical impedance spectra showed the charge transfer resistance increased from 1.57 to 2.21 Ω for air cathode and 0.21 to 0.34 Ω for zinc electrode after 100 charge-discharge cycles.

Bockelmann et al. (2016) studied electrically rechargeable zinc-oxygen batteries with tri-electrode configuration. A 2 cm² Copper foam was used as substrate for zinc electrode. A silver-based oxygen depolarized cathode was used as oxygen electrode. A 5 cm² nickel foam was used as third electrode. 30% KOH solution with 2% ZnO was used as electrolyte. The electrolyte flowrate was 0.4 L/min. Pure oxygen was supplied to oxygen electrode with flowrate of 0.2 L/min. The cell was able to charge and discharge with current density up to 600 mA/cm². Discharge peak power density was able to reach 270 mW/cm². The cell was able to operate up to 600 cycles.

Table 2.2 Performance of zinc-air cells in literatures

Description	Performance / Remarkable conclusion	References
Circulating zinc-air flow battery for using as vehicle power source	Specific energy of 110 Wh/kg Specific power of 80 W/kg	Appleby and Jacquier (1976)
Zinc-air cell with packed bed anode	Peak power density of 185 mW/cm ² at 20 mA/cm ² 45°C	Savaskan et al. (1992)
A regenerative ZAFC	12 cell stacks a 1.8 kW. Net power output of 1.1 kW for 24h	Smedley and Zhang (2007)
ZAFC with MnO ₂ catalyst and polymer separator	Current density of about 70 mA/cm ² at 1 Volt	Sapkota and Kim (2010)
ZAFC with flowing gelled electrolyte	Current of about 370 mA at 1 Volt	Puapattanakul et al. (2013)
ZAFC with circulation electrolyte	Current density of about 70 mA/cm ² at 1 Volt	Kim et al. (2013)
Rechargeable ZAB stack	Peak power density of 64 mW/cm ² at 80mA/cm ² Total peak power of 4.5 W	Ma et al. (2014)
ZAFC with serpentine and parallel anode flow channel	Peak power density of 240 mW/cm ² at 500 mA/cm ² with 4 ml/h flowrate	Jiratchayamaethasakul et al. (2014)
High performance ZAFC stack with MnO ₂	Peak power density of 435 mW/cm ² at 510 mA/cm ² 0.86V	Pei et al. (2014a)
ZAFC with inhibitor coated zinc	Novel coating method is proposed. Inhibitor coating can suppress HER.	Kim et al. (2015b)
ZAFC used to study effect of KOH concentration and depth of discharge	Current density of 102 mA/cm ² at 1 Volt	Li et al. (2015)

Table 2.2 (cont.) Performance of zinc-air cells in literatures

Description	Performance / Remarkable conclusion	References
ZAFC with calcium hydroxide	Ca(OH) ₂ can remove zincate ion. Electrolyte capacity is increased.	Zhu et al. (2015)
Rechargeable zinc-oxygen flow battery	Peak power density of 270 mW/cm ² at 460 mA/cm ²	Bockelmann et al. (2016)
ZAFC with N and S co-doped hierarchically porous carbon as electrocatalyst	Peak power density of 516.3 mW/cm ² at 800 mA/cm ² with 5 mg/cm ² catalyst loading	Tang et al. (2017)
Studying air supply effect using commercial 48 Ah primary prismatic ZAB	Rated capacity of 48 Ah, 53 Wh at 1 A discharge	Larsson et al. (2017)
Flexible tubular ZAFC with single layer cathode	1.06 V at 50 mA/cm ² / Nominal voltage maintaining for 45 h	Oh et al. (2018)
Parameter optimization for rechargeable zinc-air battery	Air electrode / cell configuration / Cycling operation are optimized.	Wang et al. (2018)

2.8.2 Regeneration of Zn

Zn regeneration or charging is an important process for Zn-based battery. The most common regeneration method related to zinc-air battery is electrodeposition in alkaline solution which have been researched for many years. Generally, current efficiency and morphology of Zn are the performance index of the regeneration process. Many studies focused on the effects of various parameter on the efficiency and morphology.

For example, the deposition of electrolytic Zn from alkaline zincate solution was investigated by Sharifi et al. (2009). Three parameters were studied in this work including current density, zincate concentration and KOH concentration. Current efficiency, Zn morphology and specific surface area were observed. For the effect of current density, it was observed that current efficiency tended to increase when increasing current density. The morphology became more dendritic with higher surface area when using higher current density. For effect of electrolyte concentration, increasing zincate concentration or decreasing KOH concentration provided increasing in current efficiency and decreasing in surface area.

Gavrilović-Wohlmuther et al. (2015) studied the effect of electrolyte concentration, temperature, flow velocity and current density on Zn deposition morphology. A polished carbon composite with no additive was used as substrate for

Zn deposit. The used electrolyte was 8 M KOH solution with 0.1, 0.2 and 0.5 M zincate concentration. The tests were conducted on the homemade design flow cell. The result showed that the higher zincate concentration provided the higher current efficiency and mossy morphology. Increasing current density promoted dendrite formation. The maximum current efficiency of 87 to 93% was observed at the optimal condition (8 M KOH with 0.5 M ZnO, elevated temperature of 50 to 70 °C, current density of 100 mA/cm² and flow velocity higher than 6.7 cm/s).

The morphology control was also focused in many works. Popov et al. (1978) studied the electrodeposition of Zn on copper by constant and pulsating overpotential from alkaline zincate solution. In constant overpotential, the transformation of morphology from spongy to dendrite was observed. The smooth morphology was obtained from pulsating overpotential. Later, Simičić et al. (2000) examined the Zn morphology control using low direct and pulsating overpotential in alkaline electrolyte. This work considered the mechanism of spongy Zn formation. The experiment was Zn electrodeposition onto copper wire in 1 M KOH with 0.1 M zincate. It was found that square wave pulsating overpotential was able to deliver less particle agglomerate than direct overpotential. The higher pulse-to-pulse ratio provided the stronger effect.

Morphology control of Zn regeneration was also investigated by Wang et al. (2014). Shape change and morphology control during charging were investigated. 3D model of Zn regeneration was developed with COMSOL software. Direct and pulse current were also examined. The result showed that flowing electrolyte, surface roughness, electrode structure, charging current and mode provided the effects on morphology change. The uniform morphology was able to be obtained from low pulsating current or flowing electrolyte. Discrete columnar electrode with high current and flowing electrolyte was able to provide granular morphology. Wang, Pei et al. (2015) further inspected dendrite growth in recharging process of ZAB using phase-field model. It was observed that the dendrite growth was dependent on diffusion control of zinc ions.

Hydrogen evolution was also a detrimental problem in Zn electrodeposition. Hydrogen generation during Zn electrodeposition in alkaline solution was studied by Einerhand et al. (1988). Rotating ring disc electrode technique was used in this experiment. The result pointed that the hydrogen evolution during electrodeposition was very small at 8 M KOH with 1 M zincate. It was concluded that hydrogen was mainly produced from corrosion of Zn electrode.

Saleh et al. (1995), (Saleh et al., 1997) studied electrowinning of Zn at flow-through porous electrode. The mathematical model was proposed including simultaneous hydrogen evolution. The result revealed that the hydrogen gas bubbles

promoted the nonuniform distribution of the reaction by increasing the effective resistance of gas-electrolyte dispersion. The optimum current was also influenced by the hydrogen gas bubble.

There were some researches trying to gain insight of the morphology change and dendrite formation. The relationship between morphology change and the process parameter was figured out. Ito et al. (2012) proposed an indicator of Zn morphology change in flowing alkaline electrolyte. Effects of zincate concentration, flow velocity and current density on the morphology change were experimentally examined. It was found that Zn morphology was able to be determined from the ratio of effective current density and limiting current density (current density ratio). Mossy and porous morphology occurred when the ratio was below 0.4. The dominant morphology in the ratio between 0.4 and 0.9 was a mixture of mossy and crystalline structure. Zn became crystalline and compact when the ratio exceeded 0.9.

Later, Dundálek et al. (2017) investigated role of hydrogen evolution in Zn electrodeposition from flowing alkaline zincate electrolyte. Mathematical approach was implemented with the experimental data. The idea of current density ratio was adopted from the work of Ito et al. (2012). The result showed that the hydrogen bubble gas caused the mixing of diffusion layer and disturbed the mass transport of zincate ion. This work also showed that current density ratio was not suitable for using as morphology indicator because the overall current density also involved with hydrogen evolution current. However, they proposed the modify current density ratio which was the ratio between Zn electrodeposition current density and limiting current density. This proposed current density ratio was able to be used to predict morphology change from mossy to crystalline and to dendrite.

Besides the conventional electroplating, the novel Zn regeneration procedures attracted widespread interest and have been investigated. Fluidized bed electrodeposition of Zn was studied (Huh et al., 1992). This process was used to regenerate Zn particle and electrolyte. The effects of current density and zincate concentration on cell performance were investigated. 45 % KOH zincate solution was used as electrolyte. The result showed that the minimum energy consumption was 1.92 kWh/kg of Zn at superficial current density of 1000 A/m².

After that, Jiricny et al. (2000) proposed spout bed Zn electrolysis cell. The experiment was carried out on the laboratory scale electrolysis cell with spout bed cathode. The operability for production of Zn particle range from 0.4 to 1 mm was determined. Suitable material for using as diaphragm was also identified.

Wen et al. (2009) conducted preliminary study on Zn electrolysis with propanol oxidation as counter electrode. A cadmium-plated nickel sheet was used as substrate which was able to prevent dendrite growth and HER effectively. When

charge time was increased, Zn granular became larger but still dense. Changing cell configuration from 'gas introducing' to 'cavity-opening' increased discharge voltage about 100 mV due to the enhance in kinetic. The feasibility of Zn electrolysis with propanol oxidation as a counter electrode was also studied.

Zn regeneration process was able to integrate with zinc-air cells. A regenerative ZAFC was proposed by Metallic Power (Smedley and Zhang, 2007). This work combined the electrolyzer with the ZAFC. The electrolyzer was designed as discrete particle electrolyzer which was able to regenerate Zn in the dense particle form. It was found that the particle size produced was 0.5 to 0.6 mm.

Table 2.3 Literature reviews of Zn regeneration

Description	Performance / remarkable conclusion	Reference
Regeneration of Zn and electrolyte fluidized bed electrodeposition	Lowest energy consumption of 1.92 kWh/kg of Zn at 1000 A/m ²	Huh et al. (1992)
Zn deposition with low direct and pulsating overpotential	Morphology was less agglomerated in pulsating overpotential	Simičić et al. (2000)
Zn electrolysis cell with spout bed electrode	Particle range 0.4 to 1 mm regeneration rate of 10 kg per day	Jiricny et al. (2000)
Electrolysis cell with bipolar nickel electrode	Energy consumption of about 1.8 Wh/kg, cell voltage of 4.2 V, current density < 1 kA/m ²	Cooper and Krueger (2006)
Electrical recharging process in ZAFC with additives	Cellulose and lead oxide partially reduce dendrite growth and hydrogen.	Lee et al. (2006a)
Discrete particle electrolyzer integrated with regenerative ZAFC	0.5-0.6 mm dense Zn particle.	Smedley and Zhang (2007)
Deposition of electrolytic Zn from alkaline solution	Effect of current density and electrolyte concentration on morphology, surface area and C.E.	Sharifi et al. (2009)
Zn electrolysis with propanol oxidation as counter electrode	The highest Organic-electro-synthesis efficiency of 82% at propanol up to 1 M	Wen et al. (2009)

Table 2.3 (cont.) Literature reviews of Zn regeneration

Description	Performance / remarkable conclusion	Reference
an indicator of Zn morphology change in flowing alkaline electrolyte	Current density ratio was proposed as morphology change indicator. The morphology change from mossy to crystalline was able to be predicted.	Ito et al. (2012)
Study effect of current density, temperature, flow velocity and concentration	Highest C.E. of 87 – 93 % at 0.5M ZnO in 8 M KOH, 50-70 °C, 100 mA/cm ²	Gavrilović-Wohlmuther et al. (2015)
Study role of HER in Zn electrodeposition from flowing alkaline solution	Diffusion layer of zincate ion was mixed by the disturbance of hydrogen bubble gas. The dendrite formation was able to be predicted from the modify current density ratio.	Dundálek et al. (2017)

2.8.3 Modeling of zinc-air battery

As mentioned in section 2.4.4, the continuum model is the most commonly used model type for studying zinc-air battery. The previous work of Sunu and Bennion (1980) developed the one-dimensional continuum model of porous Zn electrode. This work established the modeling framework of Zn electrode for several consecutive research works. This model adopted the concentrated solution theory to describe the mass transport and was used to predicted electrode behavior during galvanostatic operation. Another main feature of this model is ZnO precipitation and the change of electrode porosity. The result revealed that the reaction was highly non-uniform and had very thin reaction zone located near electrode surface. Consequently, electrolyte depletion occurred inside the porous electrode causing the electrode failure. Moreover, the charge and discharge reactions distributed unevenly resulting in shape change of Zn electrode.

The porous Zn electrode model developed by Sunu and Bennion (1980) was further extended to the one-dimensional model of primary ZAB by Mao and White (1992). The separator, air cathode and precipitation of solid species were added into the model therefore the model was able to use to investigate the battery design. The developed model was validated with the experimental data provided by MATSI.inc. The result predicted that depletion of OH⁻ concentration limited the Zn utilization. It was observed that thickness of electrode showed insignificant effect on the utilization, but the material loading provided a great effect on the utilization. Increasing material

loading decreased the utilization and capacity. Increasing the thickness of separator provided higher utilization but decreased cell voltage.

Later, Deiss et al. (2002) developed a one-dimensional model for secondary ZAB and simulated charge-discharge cycling. This model adopted the dilute solution theory instead. This model showed good agreement with their experiment. The result suggested that OH^- depletion was a limiting factor for high current discharge. The redistribution of anode material was observed in charge-discharge cycling. It was found that the redistribution per cycle is reduced as the cycle proceeded.

Jung et al. (2016) presented the analysis of Zn utilization in primary ZAB using a one-dimensional model. The model included all cell component which allowed to perform full-cell scale simulation. The model validity was verified by comparing the predicted discharge curve with their experimental data. The model was used to find the optimal values for key parameters. As a result, the maximum Zn utilization of 97% was obtained at the optimal studied parameters. The optimal values for thickness of anode and separator were 0.61 mm and 0.11 mm, respectively.

Schröder and Krewer (2014) studied the effect of air composition using zero-dimensional model of ZAB. The zero-dimensional continuum model was developed and included all necessary cell component. Three studied parameters of air component were O_2 , CO_2 and humidity. As regards effect of O_2 , it affected the limiting current of the battery. The higher concentration of O_2 provide higher limiting current and cell performance. For the effect of CO_2 , it was noted that CO_2 affected the electrolyte concentration via the carbonation reaction. As the cycle proceeded, electrolyte concentration was changed resulting in decreasing of cell voltage. Lastly, the humidity contributed to electrode flooding and drying. The optimal relative humidity was reported. The relative humidity above the optimal value causes the electrode flooding. Vice versa, the electrode drying was occurred when the relative humidity was lower than the optimal value.

Recently, Stamm et al. (2017) proposed modeling and simulation of primary ZAB based on VARTA button cell. This work included the modeling of nucleation and growth of ZnO and investigated its effect on discharge curve. Furthermore, carbonation in electrolyte was also included. The simulation revealed the inhomogeneous precipitation of ZnO and dissolution of Zn. The addition of ZnO into anode was able to improve the rechargeability; however, the initial discharge capacity was reduced. It was also found that CO_2 absorption in alkaline electrolyte limited the battery lifetime.

As regards the dynamic behavior of zinc-air battery, little model-based research was done in the past. For instance, the cell parameters of zinc-air cells for a BMS were determined by electrotechnical investigation (Şanal et al., 2015). This

work analyzed a zinc-air cell with capacity of 50 Ah and presented a battery test bench. The test bench is used to investigate cell parameters including OCV, cell resistance and cell capacity. The result showed that OCV and cell resistance exhibited the relationship with SOC. Therefore, this relationship was able to be used to estimate the SOC.

It can be clearly seen that this study of the dynamic behavior of zinc-air battery is still lack in recent times. In contrast, the other battery types have been received relatively higher research interest. The decent examples are the Li-ion battery and lead-acid battery. The research on dynamic behavior, BMS and state estimation of these batteries has superior progress. For Li-ion battery, many works were focusing on the dynamic model (Docimo et al., 2014, Akbar et al., 2015, Stroe et al., 2017, Krewer et al., 2018, Nam et al., 2018). Most of these works aimed to develop the dynamic model for use in battery state estimation. Furthermore, the state estimation algorithm was also a popular topic for Li-ion battery (Li et al., 2017b, Tran et al., 2017, Wei et al., 2018).

For instance, Hu and Yurkovich (2011) developed an LPV model for the prediction dynamic voltage of the lithium-ion battery and proposed a subspace identification method. The dynamics of the battery under various operating conditions were able to be predict by the proposed model. Further, the LPV technique was developed for the SOC estimation of a battery cell (Hu and Yurkovich, 2012). The model was applied with a state observer to estimate the SOC. The proposed technique provided good performance with guaranteed stability.

Table 2.4 Summary of literature reviews for modeling of zinc-air battery

Description	remarkable conclusion	Source
One-dimensional model of porous Zn electrode in alkaline electrolyte	The reaction was highly non-uniform and had thin active zone. Limitation of Zn electrode came from electrolyte depletion.	Sunu and Bennion (1980)
Two-dimensional model of porous Zn electrode for investigation of material redistribution.	Non uniform current and concentration distribution contributed to redistribution of Zn and ZnO	Isaacson et al. (1990)
One-dimensional model of primary ZAB for investigation of the battery behavior with respect to design	Zn utilization is limited by depletion of hydroxide ions. Material loading provide a significant effect on Zn utilization.	Mao and White (1992)
One-dimensional model of rechargeable ZAB for analysis of galvanostatic experiment.	OH ⁻ depletion was predicted to be limiting factor for high-current discharge. Zn redistribution per cycle was reduced with increasing number.	Deiss et al. (2002)
Zero-dimensional model of secondary ZAB for studying effect of air composition.	O ₂ contributed to limiting current. Air humidity caused electrode flooding or drying. CO ₂ affected OH ⁻ concentration and operation lifetime.	Schröder and Krewer (2014)
Analysis of O ₂ bubble growth in ZAB recharging process using computation fluid dynamic.	Using flowing electrolyte and partial insulation electrode could prevent oxygen bubble coalescence. Two type of tri electrode configuration were compared.	Wang et al. (2015a)
Investigation of morphology control in Zn regeneration using computation fluid dynamic.	Dendrite growth can be reduced by pulsating current and flowing electrolyte. Morphology of Zn depends on rates of reaction and mass transfer.	Wang et al. (2015b)
One-dimensional model of GDL in ZAB with moving gas-liquid interface.	Pulse-current operation and electrode flooding were investigated. The parameters affecting O ₂ distribution was also studied.	Schröder et al. (2016)
One-dimensional model of ZAB considering the effect of anode and separator thickness on Zn utilization	The optimal thickness of anode and separator was reported. (97 % Zn utilization with compact anode, 0.61 mm for anode and 0.11 mm for separator)	Jung et al. (2016)
Study of ZnO nucleation and growth using multi-phase one-dimensional ZAB model	Inhomogeneous deposition and dissolution of Zn/ZnO were detected. Rechargeable capacity was improved by adding ZnO to the electrode, but it reduced initial discharge capacity.	Stamm et al. (2017)

CHAPTER 3

Model-based Analysis of an Integrated Zinc-Air Flow Battery/ Zinc Electrolyzer System

3.1 Preface

First author: Woranunt Lao-atiman

Advisor: Soorathep Kheawhom

Affiliation: Department of Chemical Engineering, Faculty of Engineering, Chulalongkorn University, Bangkok

Journal: Frontiers in Energy Research

Published: 22 February 2019

Volume: 7

Article: 15

Citation: Lao-atiman W, Bumroongsil K, Arpornwichanop A, Bumroongsakulsawat P, Olaru S and Kheawhom S (2019) Model-Based Analysis of an Integrated Zinc-Air Flow Battery/Zinc Electrolyzer System. *Front. Energy Res.* 7:15. doi: 10.3389/fenrg.2019.00015

This research paper is a part of dissertation publication for graduation and is already published in the journal 'Frontiers in Energy Research' on 22 February 2019. The publication also includes supplementary material which can be found online at: <https://www.frontiersin.org/articles/10.3389/fenrg.2019.00015/full#supplementary-material> and is also provided in Appendix A of this thesis.

3.2 Abstract

This work aims at analyzing an integrated system of a zinc-air flow battery with a zinc electrolyzer for energy storage application. For efficient utilization of inherently intermittent renewable energy sources, safe and cost-effective energy storage systems are required. A zinc-air flow battery integrated with a zinc electrolyzer shows great promise as an electricity storage system due to its high specific energy density at low cost. A mathematical model of the system was developed. The model was implemented in MATLAB and validated against experimental results. The validation of the model was verified by the agreement between the simulation and experimental polarization characteristic. The behavior and performance of the system were then examined as a function of different operating parameters: the flow rate of the electrolyte, the initial concentration of potassium hydroxide (KOH) and the initial concentration of zincate ion. These parameters significantly affected the performance

of the system. The influence of the hydrogen evolution reaction (HER) on the performance of the system was investigated and discussed as it significantly affected the coulombic efficiencies of both the zinc-air flow battery and the zinc electrolyzer. Optimal KOH concentration was found to be about 6–7M. Whilst increased KOH concentration enhanced the discharge energy of the battery, it also increased HER of both the battery and the electrolyzer. However, higher initial concentration of zincate ion reduced HER and improved the coulombic efficiency of the system. Besides, a higher flow rate of electrolyte enhanced the performance of the system especially at a high charge/discharge current by maintaining the concentration of active species in the cell. Nevertheless, the battery suffered from a higher rate of HER at a high flow rate. It was noted that the model-based analysis provided better insight into the behavioral characteristics of the system leading to an improved design and operation of the integrated system of zinc-air flow battery with the zinc electrolyzer.

Keywords: zinc-air battery, zinc electrolyzer, simulation, energy storage, flow battery

3.3 Introduction

Nowadays, renewable energy has captured the public interest and has been extensively explored due to the increment in energy demand and stringent climate change targets (Li and Dai, 2014, Jing et al., 2017). Renewable energy sources, therefore, such as solar and wind have a strong potential to fulfill the need. Nevertheless, their practical employment has been limited by their variability and intermittent nature. Thus, a reliable and cost-effective energy storage system (ESS) is required for efficient utilization of renewable energy sources (Zhang, 2013). Besides, ESS can play a significant role to enhance stability and flexibility of a power grid in both supply and demand (Dunn et al., 2011).

Zinc-air batteries are a promising ESS because of their high practical specific energy, up to 700 Wh/kg (Li et al., 2013). Zinc (Zn) is also an attractive anodic active material because it is non-toxic, safe, abundant and low-cost (Lao-atiman et al., 2017). Besides, Zn exhibits high stability and reversibility during charge-discharge cycle (Zhu et al., 2016). Zn-air batteries generate electricity through the electrochemical reaction of Zn and oxygen. During discharge of the battery, Zn anode is oxidized and produces zincate and later changes to zinc oxide whilst, at the cathode, oxygen from the atmosphere undergoes reduction. As the cathodic active material is not enclosed in the cell, Zn-air batteries exhibit very high energy density. Zn-air batteries have been fabricated in various forms and shapes such as flexible batteries (Fu et al., 2016, Suren and Kheawhom, 2016, Wang et al., 2017), cable-type batteries (Park et al., 2015), and flow batteries (Bockelmann et al., 2016, Hosseini et al.,

2018b, Wang et al., 2018). Flow batteries have a wide power range and much higher capacity ratings. In addition, they can independently scale the power and capacity by storing active materials outside the cell. In other words, flow batteries allow for independent scale-up of power and capacity specifications (Escalante Soberanis et al., 2018). Thus, regarding cost, system flexibility, quick response and safety concerns for large-scale applications, flow batteries exhibit significant advantages over other types of battery.

Zn-air batteries can be recharged by two approaches: electrical recharge and mechanical recharge (Xu et al., 2015, Mainar et al., 2018). An electrically rechargeable Zn-air battery is recharged by supplying electricity directly to the cell. During recharge, oxygen is generated at the air electrode whilst Zn metal is electrochemically regenerated at the Zn electrode. A significant problem of the Zn electrode is the formation of dendritic Zn during recharge. Moreover, during recharge, the air electrode rapidly deteriorates due to the growth of oxygen bubbles and the air electrode corrosion (Pei et al., 2014b). These issues are a critical life cycle-limiting factor for rechargeable Zn-air batteries. These problems can be avoided by using a mechanical recharging approach. A mechanically rechargeable Zn-air battery (also known as a Zn-air fuel cell) can be recharged by directly refueling active Zn anode into the cell. Zn serving as fuel is stored in a storage tank and fed to the cell. In this configuration, dendritic Zn formation inside the cell is avoided because Zn is regenerated in other places such as an electrolyzer. Further, the air electrode of the battery does not suffer from oxygen bubbles erosion and carbon corrosion. As Zn is regenerated outside the cell, the mechanically rechargeable Zn-air battery is typically fabricated as a flow battery such that the discharge product can be circulated out of the cell.

Zn can be regenerated by various methods. Yet, the most appropriate procedure to use with Zn-air flow batteries is electrochemical regeneration or electrolysis. The discharge product of the batteries can be directly used as reactant of the electrolysis cell or electrolyzer. The outlet stream of a flow battery containing zincate and zinc oxide is fed to an electrolyzer to regenerate Zn. The regenerated Zn is then refueled back into the battery. The zinc-air flow battery integrated with an electrolyzer can be operated as an ESS. Technologies based on mechanically rechargeable Zn-air flow batteries and Zn regeneration have been developed progressively. Smedley and Zhang (2007) proposed an integrated system of Zn-air fuel cells and electrolyzers which was designed to serve as a source of an emergency power backup system. The 12-cell-stacks system was able to provide a power output of 1.8 kW for 12 h. Recently, the ESS based on Zn-air flow batteries was developed by Amunátegui et al. (2018). A 1 kW, 4 kWh Zn-air flow battery pilot plant was

demonstrated having 40% round-trip efficiency and 2000 cycles, respectively. It was observed that the coulombic efficiency was reduced by 18% because of shunt current phenomenon.

Previously, mathematical models for different types of Zn-air batteries were proposed to study the influence of various parameters. Mao and White (1992) developed a model of a primary Zn-air battery to investigate the behavior of the battery concerning several design parameters. Their results showed that the utilization of Zn was restricted by the depletion of hydroxide ion (OH⁻) and significantly depended on the Zn loading in the electrode. Deiss et al. (2002) proposed a one-dimensional mathematical model of a rechargeable Zn-air battery and indicated that the redistribution and shape change of Zn and ZnO leads to a non-uniform Zn electrode. The shape change proceeded as the battery cycle progressed forward. Nevertheless, the redistribution rate slowed down when the number of cycles increased. Schröder and Krewer (2014) introduced a mathematical model for a secondary Zn-air battery to examine the impact of air composition under isothermal operation.

Significant performance evaluations of Zn electrolysis include the morphology of Zn and the coulombic efficiency of the process (Savaskan et al., 1992, Simičić et al., 2000, Lee et al., 2006a, Sharifi et al., 2009, Gavrilović-Wohlmuther et al., 2015). Wang et al. (2015a) also proposed an electrochemical phase field model for the simulation of Zn dendritic growth. The results showed that dendrite growth could be controlled by manipulating the concentration gradient of Zn ion. Moreover, dendrite growth could be suppressed by pulsed-current charging and flowing electrolyte (Garcia et al., 2017). Besides, the growth of oxygen bubbles during recharge of the Zn-air battery was studied. It was found that the oxygen bubble coalescence could be inhibited by the flowing electrolyte.

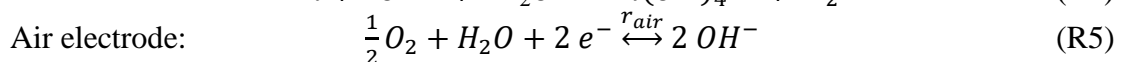
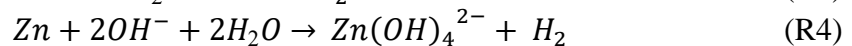
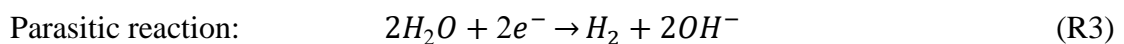
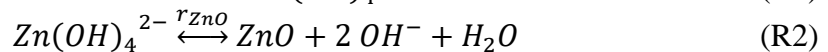
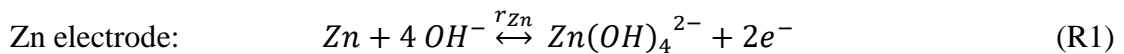
Zn-air batteries are preferably operated using an alkaline electrolyte. One crucial issue that occurs in alkaline Zn-air cells is corrosion of the Zn anode due to hydrogen evolution reaction (HER). This is known as self-corrosion of the Zn anode (Wongrujipairoj et al., 2017). Moreover, this reaction consumes the electrolyte and decreases the utilization efficiency of Zn. In other words, hydrogen evolution contributes to the coulombic efficiency loss during both charging and discharging processes. Saleh et al. (1997) developed a model of alkaline Zn electro-winning considering HER to study the effects of different operating parameters. Besides, Dundálek et al. (2017) proposed a model of Zn electrodeposition from a flowing alkaline electrolyte by considering HER and limiting current density of Zn reduction. The model was used to examine the relationship between HER and the morphology of

Zn deposited. Nevertheless, HER has not been addressed previously in a mathematical model of a Zn-air flow battery.

This work aims to develop a mathematical model of a Zn-air flow battery integrated with an electrolyzer. Hydrogen evolution reaction as a parasitic reaction is also considered in the model. The developed model was implemented in MATLAB and validated against the experimental data. Then, simulation was performed to examine the dynamic behavior of the battery system. The study consists of the following: (1) a brief overview of the Zn-air flow battery and Zn electrolyzer (2) experimental setup of the system for model validation (3) model development and validation of the model (4) simulation of the system and the effects of various parameters (5) final summary.

3.4 Zinc-air Flow Battery and Zinc Electrolyzer

A Zn-air flow battery (ZAFB) consists of two electrodes: a Zn anode and an air cathode, as shown in Fig. 3.1A. The anode and cathode are separated by a separator allowing ions to transfer across the cell. Potassium hydroxide (KOH) aqueous solution is used as an electrolyte. At the anode (negative electrode), Zn reacts with hydroxide ions (OH^-) and forms zincate ions ($\text{Zn}(\text{OH})_4^{2-}$) as shown in R1. When the concentration of zincate ion reaches its solubility limit, zinc oxide (ZnO) precipitation reaction proceeds, as presented in R2. Hydrogen evolution reaction (HER) is also considered as a parasitic reaction on the Zn electrode. Water receives electrons and converts to hydrogen (H_2) and hydroxide ions, as shown in R3. HER combined with Zn dissolution reaction results in Zn corrosion, as shown in R4. At the cathode (positive electrode), oxygen reduction reaction (ORR) consumes oxygen (O_2) and water and produces hydroxide ions as described in R5. As the battery discharges, electrons are released from reaction R1 and received by reaction R5. Both reactions proceed and generate electricity.



The Zn electrolyzer, as shown in Fig. 3.1B, consists of a Zn regeneration electrode (negative electrode) and an air electrode (positive electrode). The charge current is supplied to the electrolyzer inducing the reverse reactions of ZAFB to proceed: zincate ions as a reactant are converted back to Zn and hydroxide ions at the negative electrode (a reversion of R1). HER (R3) also significantly affects

performance of the electrolyzer because water in the electrolyte can receive electrons directly from the charge current. At the positive electrode, oxygen evolution reaction (OER; a reversion of R5) converts hydroxide ions into oxygen and water.

ZAFB integrated with the Zn electrolyzer can be used as an energy storage system. In Fig. 3.2, the integrated system of ZAFB connecting with Zn electrolyzer is illustrated. The electrolyte circulates between the battery and the electrolyzer. During discharge, ZAFB consumes Zn and produces zincate ion. The effluent from ZAFB, containing a high concentration of zincate ion, is fed into the electrolyzer. The electrolyzer consumes electricity in order to regenerate Zn. Zincate ions are then converted to Zn. In comparison, the effluent from the electrolyzer, containing a lower concentration of zincate ion, is fed into ZAFB. Besides, Zn regenerated from the electrolyzer is mechanically transferred to the ZAFB.

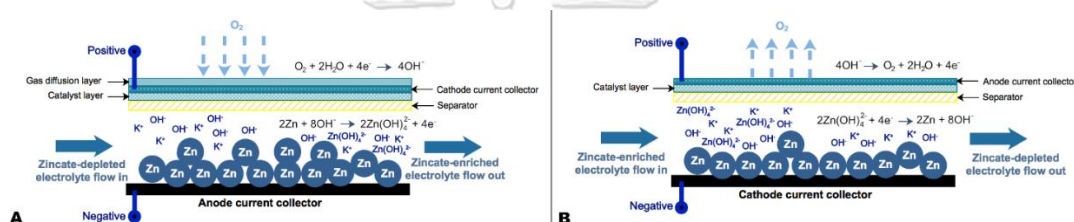


Figure 3.1 Schematic diagram of zinc-air flow battery and zinc electrolyzer.

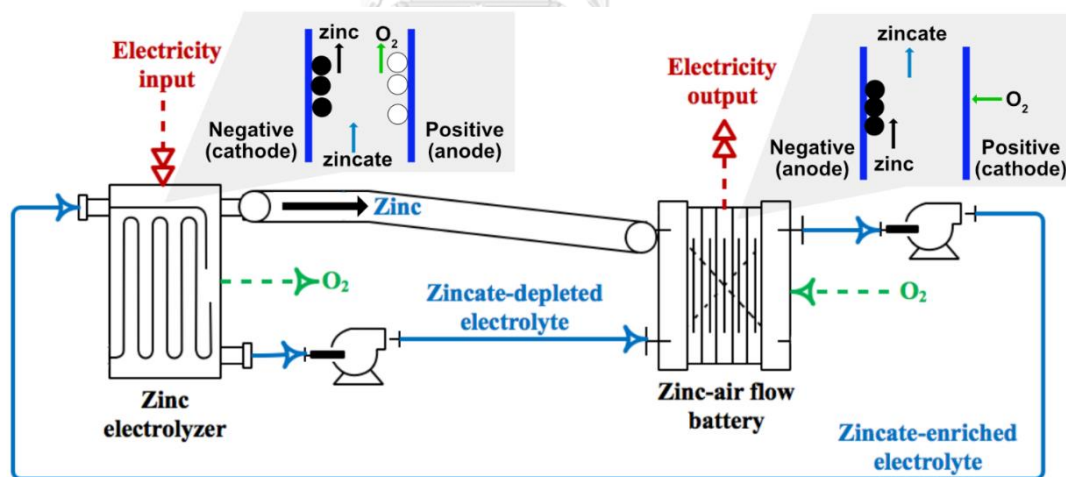


Figure 3.2 Schematic diagram of zinc-air flow battery integrated with zinc electrolyzer.

3.5 Experimental Setup

The model developed in this work was validated against experimental data obtained from a Zn-air flow battery and a Zn electrolyzer. The experimental setup of the battery included a stack arrangement with a Zn anode plate, a separator and an air cathode. The Zn anode consisted of 10 g Zn granules with an average diameter of 0.8

mm loaded inside a 100-mesh stainless steel pouch functioning as a current collector. The area of the current collector was 10 cm². The separator was prepared by casting 2 g of 24 wt.% poly(vinyl acetate) (PVAc) aqueous solution over both sides of a filter paper and then dried in an oven at 55 °C for 10 min. The air cathode plate consisted of three layers: namely, a gas diffusion layer, a cathode current collector and a catalyst layer. Nickel foam (0.5 mm thick with 100 PPI) was employed as the cathode current collector. The gas diffusion layer was fabricated by casting a slurry mixture of 4 g carbon black, 4 g PTFE powder and 2 g glucose in 50 ml ethanol on one side of the nickel foam. The coated nickel foam was then heat-pressed at 350 °C for 15 min using a manual hot press machine. Then, the catalyst layer was fabricated on the other side of the nickel foam by adding a slurry mixture of 3 g MnO₂ and 7 g carbon black in the binder dissolved solvent. The solvent was prepared by dissolving 1 g poly styrene-co-butadiene (4% butadiene, Sigma Aldrich) as a binder in 50 ml toluene. The catalyst coated cathode was then annealed at 110 °C in an oven. The gas diffusion layer exhibited good hydrophobicity. The hydrophobicity of the gas diffusion layer prevents leakage of the electrolyte and water flooding in the cathode. This layer also allows oxygen gas from the atmosphere to permeate through the cell. The active area of the cathode was 10 cm². KOH aqueous solution (7 M) was used as the electrolyte. The electrolyte with a total volume of 150 mL was fed through the cell at a circulation rate of 50 mL/min using a peristaltic pump.

The experimental setup of the electrolyzer is similar to the battery. The electrolyzer included a stack arrangement with a cathode plate, a separator and an anode. The cathode plate is made of stainless steel with an active area of 10 cm². The separator was prepared by casting 2 g of 24 wt.% PVAc aqueous solution over both sides of a filter paper and then dried in an oven at 55 °C for 10 min. The anode was made of nickel foam (0.5 mm thick with 100 PPI) with an area of 10 cm².

To validate the mathematical models of ZAFB and Zn electrolyzer, the polarization characteristic of ZAFB was examined. The cell voltage and current were measured by a BA500 battery analyzer using BA500WIN software. The current input can be adjusted manually and cell voltage is measured at the selected current continuously. The data of cell voltage was collected every second. For one current value, the voltage data had been collected for 10 seconds and 10 voltage values were used to calculate the average cell voltage. After that, the current value was changed to the next value. To measure the overpotential of the electrodes, a mercury / mercury oxide electrode was used as a reference electrode. The overpotential was calculated from the difference of potential between the reference electrode and the equilibrium potential of each electrode.

3.6 Mathematical Models

In this section, mathematical models of ZAFB and the Zn electrolyzer are described. The models were developed based on the following assumptions:

- Temperature variations are negligible: an isothermally operation at 298.15K is assumed. Operation of both ZAFB and the Zn electrolyzer are carried out at room temperature.
- Zero-dimensional space: all variables and parameters inside the cell are independent of the location. The concentration gradient inside the cell is very small and can be neglected. This assumption is valid because the reactions are sufficiently slow; electrode reaction rate is relatively slower than mass transfer rate. Hence, homogenous concentrations in each cell are assumed. In previous literature, a similar assumption was also considered. For instance, Schröder and Krewer (2014) proposed a zero-dimensional zinc-air battery model which was used to investigate the effect of air-composition on cell performance. Dundálek et al. (2017) published a zero-dimensional model of zinc electrodeposition with flowing electrolyte.
- Negligible distance between the cells: the effluent of the electrolyzer immediately affects the ZAFB. In the same manner, the effluent of the ZAFB instantly affects the electrolyzer.
- Constant physical properties, electrode areas and thickness: material properties are assumed to be constant because the state of temperature and pressure is constant. The electrode area and thickness were also assumed to be constant as the cell design.
- Zn oxidation / reduction taking place at the Zn electrode and ORR / OER taking place at the air electrode: no reaction occurred outside the reaction area.
- The capacitive effects are negligible: the system is assumed to be a quasi-electroneutrality condition.
- Ideal gas behavior: ideal gas law is applied as the system is operated at ambient pressure.
- Binary mass diffusion: the diffusion rate is determined by Fick's law.

3.6.1 Species Balances

The molar concentration balance of species k , including OH^- , $\text{Zn}(\text{OH})_4^{2-}$ and H_2O , is expressed as in Equation (3.1). Superscript j represents the electrode or position referring to Zn electrode ($j = \text{zinc}$) and air electrode ($j = \text{air}$):

$$\frac{dC_k^j}{dt} = \frac{1}{V_{\text{electrolyte}}^j} \cdot \left[F_{k,in} - F_{k,out} + J_k + \sum_i v_{k,i} \cdot r_i - C_k^j \frac{dV_{\text{electrolyte}}^j}{dt} \right] \quad (3.1)$$

where C_k is concentration of species k , $V_{\text{electrolyte}}$ is electrolyte volume, F_k is molar flowrate of species k , $\nu_{k,i}$ is stoichiometric coefficient of species k in reaction i , r_i is rate of reaction i (mol/s). J_k is molar transfer rate crossing between Zn and air electrodes of species k including diffusion (diff), migration (mig) and convection (conv) and can be calculated as in Equation (3.2):

$$J_k = J_k^{\text{diff}} + J_k^{\text{mig}} + J_k^{\text{conv}} \quad (3.2)$$

where:

$$J_k^{\text{diff}} = D_k \cdot \frac{(C_k^{\text{air}} - C_k^{\text{zinc}})}{\delta_{\text{sep}}} \cdot \varepsilon_{\text{sep}} \cdot A_{\text{sep}}$$

$$J_k^{\text{mig}} = \frac{t_k}{z_k^{\pm} F} \cdot i^{\text{cell}} \cdot \varepsilon_{\text{sep}} \cdot A_{\text{sep}}$$

$$J_k^{\text{conv}} = F_{\text{conv}} \cdot C_k^{\text{zinc}}$$

where D_k is diffusivity of species k , ε_{sep} is porosity of separator, A_{sep} is area of separator, δ_{sep} is thickness of separator, t_k is transference number of ion k , z_k^{\pm} is ion number of species k , F is Faraday constant, i^{cell} is current density, F_{conv} is convective volume flow crossing between Zn and air electrodes.

$$F_{\text{conv}} = \sum_k J_k \cdot \bar{V}_k \quad (3.3)$$

From the zero-dimensional space assumption, the outlet molar flowrate of species k ($F_{k,\text{out}}$) can be calculated as in Equation (3.4). The electroneutrality conditions are applied to an ionic species charge balance, as shown in Equation (3.5):

$$F_{k,\text{out}} = C_k^{\text{zinc}} \cdot V_{\text{electrolyte}}^{\text{zinc}} \cdot SV \quad (3.4)$$

$$\sum_k z_k^{\pm} C_k^j = 0 \quad (3.5)$$

where SV is space velocity.

The accumulation of ZnO is expressed by the molar balance with reaction R2. Solid Zn is calculated in the same way with reaction R1:

$$\frac{dN_{\text{ZnO}}}{dt} = \nu_{\text{ZnO},2} \cdot r_{\text{ZnO}} \quad (3.6)$$

$$\frac{dN_{\text{Zn}}}{dt} = \nu_{\text{Zn},1} \cdot r_{\text{Zn}} \quad (3.7)$$

where N_{ZnO} is moles of ZnO, N_{Zn} is moles of Zn.

3.6.2 Rates of Reactions

The reaction rates of reaction R1, R3 and R5 are modeled by Faradaic reaction approach as expressed in Equations (3.8), (3.9) and (3.10), respectively:

$$r_{\text{Zn}} = \frac{i_{\text{Zn}} \cdot A_{\text{zinc}}}{n_e F} \quad (3.8)$$

$$r_{\text{H}} = \frac{i_{\text{H}} \cdot A_{\text{zinc}}}{n_e F} \quad (3.9)$$

$$r_{\text{air}} = \frac{i_{\text{air}} \cdot A_{\text{air}}}{n_e F} \quad (3.10)$$

where r_{Zn} , r_H and r_{air} are rates of reaction R1, R3 and R5, respectively. i_{Zn} , i_H and i_{air} are current density related to reaction R1, R3 and R5, respectively. n_e is number of exchange electrons involved in the reaction.

For ZnO precipitation reaction (Equation R2), the rate of reaction is expressed by a saturation approach (Sunu and Bennion, 1980):

$$r_{ZnO} = k_s (C_{Zn(OH)_4^{2-}} - C_{Zn(OH)_4^{2-}}^{sat}) \quad (3.11)$$

where r_{ZnO} is rate of reaction R2, k_s is rate constant of reaction R2 and $C_{Zn(OH)_4^{2-}}^{sat}$ is saturation limit concentration of $Zn(OH)_4^{2-}$

3.6.3 Volume Change

The solid electrode volume change can be expressed as follows:

$$\frac{dV_{solid}^{zinc}}{dt} = \frac{dN_{Zn}}{dt} \cdot \bar{V}_{Zn} + \frac{dN_{ZnO}}{dt} \cdot \bar{V}_{ZnO} \quad (3.12)$$

The electrolyte volume change can be calculated accordingly:

$$\frac{dV_{electrolyte}^{zinc}}{dt} = \sum_k \left(V_{electrolyte}^{zinc} \cdot \frac{dC_k^{zinc}}{dt} + C_k^{zinc} \cdot \frac{dV_{electrolyte}^{zinc}}{dt} \right) \cdot \bar{V}_k \quad (3.13)$$

$$\frac{dV_{electrolyte}^{air}}{dt} = -F_{conv} + r_{air} \sum_k \nu_{k,air} \cdot \bar{V}_k \quad (3.14)$$

$$\varepsilon = 1 - \frac{V_{solid}^{zinc}}{\delta_{zinc} A_{elecZn}} \quad (3.15)$$

where \bar{V}_k is specific molar volume of species k, ε is porosity of Zn electrode, V_{solid}^{zinc} is volume of solid Zn electrode, δ_{zinc} is thickness of the Zn electrode and A_{elecZn} is surface area of the Zn electrode.

3.6.4 Cell Potential จุฬาลงกรณ์มหาวิทยาลัย

The cell potential (E_{cell}) can be calculated from Nernst potential ($E_{0,cell}$) minus with overpotentials as expressed in Equation (3.16). The included overpotentials are Zn activation overpotential (η_{act}^{zinc}), air activation overpotential (η_{act}^{air}) and ohmic overpotential (η_{ohmic}):

$$E_{cell} = E_{0,cell} - \eta_{act}^{zinc} - \eta_{act}^{air} - \eta_{ohmic} \quad (3.16)$$

$$E_{0,cell} = E^{air} - E^{zinc} \quad (3.17)$$

where E^{air} is potential of air electrode and E^{zinc} is potential of the Zn electrode.

$$E^{air} = E_0^{air} + \frac{RT}{n_e \cdot F} \ln \left(\frac{(P_{O_2}/P^{ref})^{0.5}}{(C_{OH^-}^{air}/C^{ref})^2} \right) \quad (3.18)$$

$$E^{zinc} = E_0^{zinc} + \frac{RT}{n_e \cdot F} \ln \left(\frac{(C_{Zn(OH)_4^{2-}}^{zinc}/C^{ref})}{(C_{OH^-}^{zinc}/C^{ref})^4} \right) \quad (3.19)$$

where E_0^{air} is standard electrode potential of air electrode, E_0^{zinc} is standard electrode potential of the Zn electrode, P_{O_2} is partial pressure of oxygen, P^{ref} is reference state pressure and C^{ref} is reference state concentration.

3.6.5 Activation Loss

The activation loss of Zn electrode ($\eta_{\text{act}}^{\text{zinc}}$) can be calculated from the total current at Zn electrode including Zn dissolution or regeneration (i_{Zn}) and HER (i_{H}), as described in Equations (3.20) to (3.25):

$$\frac{d\eta_{\text{act}}^{\text{zinc}}}{dt} \cdot C_{\text{DL}}^{\text{zinc}} = i^{\text{cell}} - (i_{\text{Zn}} + i_{\text{H}}) \quad (3.20)$$

$$i_{\text{Zn}} = i_0^{\text{zinc}} \cdot \left[\exp\left(\frac{\alpha_{\text{zinc}} n_e F}{RT} \eta_{\text{act}}^{\text{zinc}}\right) - \left(\frac{C_{\text{Zn(OH)}_4^{2-},s}}{C_{\text{Zn(OH)}_4^{2-},b}}\right) \exp\left(-\frac{(1-\alpha_{\text{zinc}}) n_e F}{RT} \eta_{\text{act}}^{\text{zinc}}\right) \right] \quad (3.21)$$

$$i_{\text{H}} = i_0^{\text{H}} \cdot \left[\exp\left(\frac{\alpha_{\text{H}} n_e F}{RT} \eta_{\text{H}}\right) - \exp\left(-\frac{(1-\alpha_{\text{H}}) n_e F}{RT} \eta_{\text{H}}\right) \right] \quad (3.22)$$

where $C_{\text{DL}}^{\text{zinc}}$ is double layer capacitance of the Zn electrode, i_0^{zinc} is exchange current density of the Zn electrode, i_0^{H} is exchange current density of HER, α is charge transfer coefficient, $C_{\text{Zn(OH)}_4^{2-},s}$ is concentration of zincate ion at the electrode surface, $C_{\text{Zn(OH)}_4^{2-},b}$ is concentration of zincate ion in the bulk electrolyte and η_{H} is overpotential of HER at the Zn electrode which can be calculated from Equations (3.23) to (3.25).

$$\eta_{\text{H}} = \eta_{\text{act}}^{\text{zinc}} + \Delta E_{\text{ZH}} \quad (3.23)$$

$$\Delta E_{\text{ZH}} = E^{\text{zinc}} - E^{\text{H}} \quad (3.24)$$

$$E^{\text{H}} = E_0^{\text{H}} - \frac{RT}{n_e F} \ln\left(\frac{C_{\text{OH}}^{\text{zinc}}}{C^{\text{ref}}}\right) \quad (3.25)$$

where ΔE_{ZH} is potential difference between the Zn electrode reaction and HER, E^{H} is electrode potential of HER, E_0^{H} is standard electrode potential of HER. The exchange current density (i_0^{zinc}) of the Zn electrode can be calculated from Equations (3.26) to (3.29). The reference exchange current density ($i_0^{\text{Zn,ref}}$) can be calculated from a correlation between exchange current density and concentration of OH^- fitted with experimental data by Dirkse and Hampson (1972) as determined in Equation (3.26):

$$i_0^{\text{Zn,ref}} = 0.0281 + 0.0613 C_{\text{OH}^-} - 0.0041 C_{\text{OH}^-}^2 \quad (3.26)$$

$$X_{\text{zinc}} = \frac{V_{\text{solid,Zn}}^{2/3}}{V_{\text{solid,Zn}}^{2/3} + V_{\text{solid,ZnO}}^{2/3}} \quad (3.27)$$

$$a_s = a_0 \left(\frac{1-\varepsilon}{1-\varepsilon_0}\right)^{2/3} \quad (3.28)$$

$$i_0^{\text{zinc}} = i_0^{\text{ref,zinc}} a_s X_{\text{zinc}} \quad (3.29)$$

where X_{Zninc} is active surface fraction of Zn in solid phase, $V_{\text{solid},k}$ is volume of solid species k, a_s is solid-solution interface area per unit volume, a_0 is initial solid-solution interface area per unit volume and ε_0 is initial porosity of the Zn electrode. Equation (3.21) expressed the current of Zn electrode including both oxidation and reduction. For electrolyzer, the term $\left(\frac{C_{\text{Zn(OH)}_4^{2-},s}}{C_{\text{Zn(OH)}_4^{2-},b}}\right)$ refers to the diffusion limit of zincate ion in Zn reduction reaction (Ito et al., 2012, Dundálek et al., 2017). The concentration of zincate ion at the electrode surface ($C_{\text{Zn(OH)}_4^{2-},s}$) and bulk electrolyte ($C_{\text{Zn(OH)}_4^{2-},b}$) can be described as in Equations (3.30) and (3.31):

$$\frac{dC_{\text{Zn(OH)}_4^{2-},s}}{dt} = \frac{1}{V_{\text{electrolyte}}} \cdot \left[r_{\text{Zn}} - D_{\text{Zn(OH)}_4^{2-},\text{elec}} \frac{(C_{\text{Zn(OH)}_4^{2-},s} - C_{\text{Zn(OH)}_4^{2-},b})}{\delta_{\text{Zn(OH)}_4^{2-},\text{diff}} A_{\text{elecZn}}} + C_{\text{Zn(OH)}_4^{2-},s} \frac{dV_{\text{electrolyte}}}{dt} \right] \quad (3.30)$$

$$\frac{dC_{\text{Zn(OH)}_4^{2-},b}}{dt} = \frac{1}{V_{\text{electrolyte}}} \cdot \left[F_{\text{Zn(OH)}_4^{2-},\text{in}} - F_{\text{Zn(OH)}_4^{2-},\text{out}} - r_{\text{ZnO}} + D_{\text{Zn(OH)}_4^{2-},\text{elec}} \frac{(C_{\text{Zn(OH)}_4^{2-},s} - C_{\text{Zn(OH)}_4^{2-},b})}{\delta_{\text{Zn(OH)}_4^{2-},\text{diff}} A_{\text{elecZn}}} + C_{\text{Zn(OH)}_4^{2-},b} \frac{dV_{\text{electrolyte}}}{dt} \right] \quad (3.31)$$

where $D_{\text{Zn(OH)}_4^{2-},\text{elec}}$ is diffusivity of zincate ion in electrolyte. The thickness of the zincate ion diffusion layer ($\delta_{\text{Zn(OH)}_4^{2-},\text{diff}}$) can be calculated as in Equations (3.32) to (3.35):

$$\delta_{\text{Zn(OH)}_4^{2-},\text{diff}} = \frac{d_h}{Sh} \quad (3.32)$$

$$Sh = 1.85 \left(\frac{d_h}{L} Re Sc \right)^{1/3} \quad (3.33)$$

$$Re = \frac{d_h v \rho_{\text{elec}}}{\mu} \quad (3.34)$$

$$Sc = \frac{\mu}{D_{\text{Zn(OH)}_4^{2-},\text{elec}} \rho_{\text{elec}}} \quad (3.35)$$

where $D_{\text{Zn(OH)}_4^{2-},\text{elec}}$ is the diffusion coefficient of zincate in electrolyte, $C_{\text{Zn(OH)}_4^{2-},b}$ is concentration of zincate in bulk electrolyte, $\delta_{\text{Zn(OH)}_4^{2-},\text{diff}}$ is the thickness of zincate ion diffusion layer, d_h is hydraulic diameter, Sh is Sherwood number, Re is Reynolds number, Sc is Schmidt number, v is electrolyte velocity, μ is viscosity of electrolyte and ρ_{elec} is density of electrolyte.

The activation loss of air electrode ($\eta_{\text{act}}^{\text{air}}$) can be calculated accordingly:

$$\frac{d\eta_{\text{act}}^{\text{air}}}{dt} \cdot C_{\text{DL}}^{\text{air}} = i_{\text{cell}} - i_{\text{air}} \quad (3.36)$$

$$i_{\text{air}} = i_0^{\text{air}} \cdot \left[\left(\frac{C_{\text{O}_2,s}}{C_{\text{O}_2,\text{atm}}} \right) \exp \left(\frac{\alpha_{\text{air}} n_e F}{RT} \eta_{\text{act}}^{\text{air}} \right) - \exp \left(- \frac{(1-\alpha_{\text{air}}) n_e F}{RT} \eta_{\text{act}}^{\text{air}} \right) \right] \quad (3.37)$$

where C_{DL}^{air} is double layer capacitance of air electrode, i_{air} is current density respecting to air electrode reaction, $C_{O_2,atm}$ is concentration of oxygen in the atmosphere. The exchange current density of air electrode (i_0^{air}) is expressed as in Equation (3.38). The oxygen concentration at catalyst surface ($C_{O_2,s}$) can be calculated by using molar concentration balance as described in Equation (3.39).

$$i_0^{air} = i_0^{air,ref} a_c \delta_{active} \quad (3.38)$$

$$\frac{dC_{O_2,s}}{dt} = \frac{1}{V_{electrolyte}} \cdot \left[-0.5r_{air} - D_{O_2,air} \frac{(C_{O_2,s} - C_{O_2,atm})}{\delta_{GDL} A_{air}} + C_{O_2,s} \frac{dV_{electrolyte}^{air}}{dt} \right] \quad (3.39)$$

where $D_{O_2,air}$ is diffusivity of oxygen in air electrode, δ_{GDL} is thickness of gas diffusion layer of air electrode and A_{air} is active surface area of air electrode.

3.6.6 Ohmic Loss

The ohmic loss (η_{ohmic}) is expressed by Ohmic's law. The total ohmic resistance (R_{ohmic}) is calculated from the conductivity and resistivity of the chemical species and cell components involved. Anode conductivity is accounted for by the solid species conductivity and mole fraction in solid electrode.

$$\eta_{ohmic} = i^{cell} \cdot A_{cell} \cdot R_{ohmic} \quad (3.40)$$

$$R_{ohmic} = \frac{\delta_{zinc}}{\sigma_{anode} A_{zinc}} + \frac{\delta_{electrolyte}}{\sigma_{electrolyte} A_{electrolyte}} + \frac{\delta_{air}}{\sigma_{cathode} A_{air}} + R_{comp} \frac{\delta_{comp}}{A_{cell}} \quad (3.41)$$

$$\sigma_{anode} = \left(\frac{N_{Zn}}{N_{Zn} + N_{ZnO}} \sigma_{Zn} + \frac{N_{ZnO}}{N_{Zn} + N_{ZnO}} \sigma_{ZnO} \right) \cdot (1 - \varepsilon) + \sigma_{electrolyte} \varepsilon \quad (3.42)$$

where δ_{zinc} , $\delta_{electrolyte}$ and δ_{air} are thickness of the Zn electrode, electrolyte channel and air electrode, respectively. σ_{anode} , $\sigma_{electrolyte}$ and $\sigma_{cathode}$ are conductivity of Zn electrode, electrolyte channel and air electrode, respectively. R_{comp} and δ_{comp} are resistivity and equilibrium thickness of other cell components. σ_{Zn} and σ_{ZnO} are conductivity of Zn and zinc oxide, respectively.

The developed model was implemented and simulated in MATLAB. The designed parameters and operating conditions are given in Table A1 in supplementary material. The initial conditions at $t = 0$ s are listed in Table A2 in supplementary material.

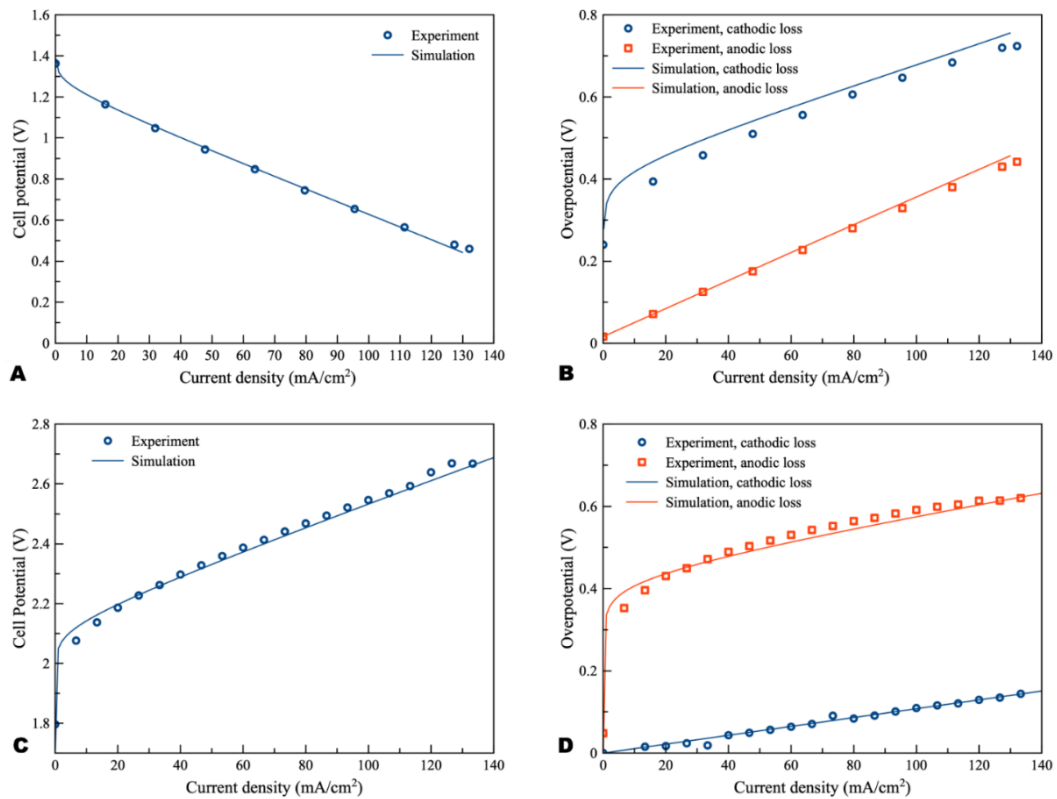


Figure 3.3 Validation of the proposed models: (A) polarization characteristic of ZAFB (B) anode and cathode overpotential of ZAFB (C) polarization characteristic of Zn electrolyzer and (D) anode and cathode overpotential of Zn electrolyzer.

3.7 Results and Discussion

3.7.1 Model Validation

As regards validation of the ZAFB and the electrolyzer model, two parameters, including the thickness of the active air electrode (δ_{active}) and the resistance of other cell components (R_{comp}), were manually adjusted to fit the model prediction with the experimental data. The fitted values of δ_{active} and R_{comp} were 30 μm and 5 $\Omega\cdot\text{cm}$, respectively. Fig. 3.3A shows the comparison of the polarization curve between simulation and experimental data of the ZAFB. It was observed that there was good agreement between the model prediction and the experimental data. The comparison of total overpotential of the electrodes between the model prediction and experimental data is displayed in Fig. 3.3B. The overpotential of each electrode is a combination of electrode activation overpotential and the ohmic loss. It was assumed that the ohmic loss from the cathode contributes to half of the total ohmic loss of the cell. The ohmic loss from the anode also contributes to half of the total ohmic loss of the cell. The comparison was acceptable for Zn overpotential. In the case of the air electrode, a small offset was observed. This offset might have arisen from the ohmic loss which

arbitrarily adds to the activation overpotential. The measured overpotential of the electrodes from the experiment included some part of the ohmic overpotential which cannot be distinguished from the activation overpotential. The model simulated the activation overpotential and ohmic overpotential separately. Therefore, the measured overpotentials were found to be different from the simulated overpotentials. Furthermore, the differentiation of the air electrode was reported (Schröder et al., 2016). However, this differentiation was not included in the model herein. On the part of the Zn electrolyzer, Figs. 3.3C and 3.3D show the comparison of the cell potential and the absolute overpotential of the electrodes between simulation and experiment. Acceptable validity between the simulation and experimental data was observed. A small offset was still shown in the overpotential of air electrode. When charging, it was noted that the growth of oxygen bubbles at the air electrode can affect the behavior of the air electrode (Wang et al., 2015b). Nevertheless, this model does not consider the effects of oxygen bubbles.

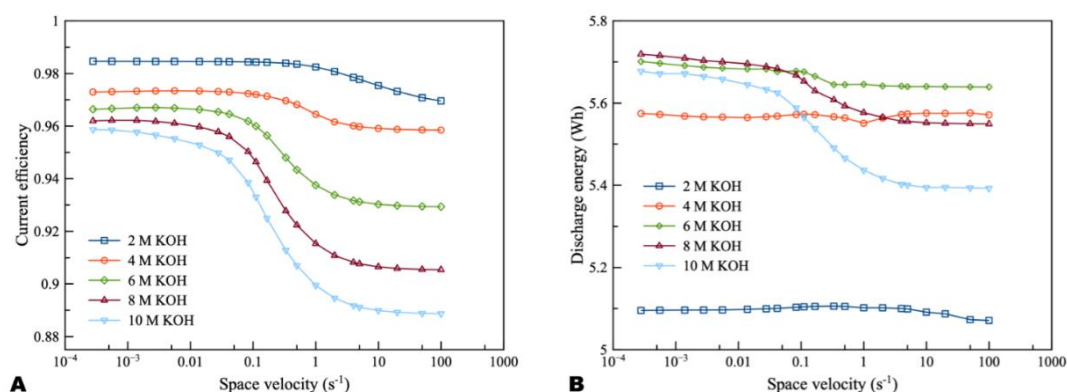


Figure 3.4 Effects of KOH concentration on ZAFB using zincate ion initial concentration 0.2 M and discharge current density of 100 mA/cm²: (A) current efficiency as a function of space velocity and (B) discharge energy as a function of space velocity.

3.7.2 Battery Performance

The ZAFB with 10 g of initial Zn (0.1538 mole of Zn) was simulated to analyze performance as functions of space velocity, KOH concentration and zincate ion initial concentration. The discharge current density was 100 mA/cm². The simulation was carried out until depletion of Zn. The performance of ZAFB was evaluated from its current efficiency and discharge energy at the end of the simulation. The current efficiency of ZAFB is defined as the ratio of the total discharge current to the electrochemical equivalent current of the Zn electrode. In this case, the current efficiency was calculated as follows:

$$\text{Current efficiency of ZAFB} = \frac{i^{\text{cell}} A_{\text{elecZn}} t_f}{2F(N_{\text{Zn},0} - N_{\text{Zn},f})} \quad (3.43)$$

and the discharge energy is given by:

$$\text{Discharge energy (Wh)} = \frac{\sum_{t=0}^{t_f} (E_{\text{cell}}) \cdot (i^{\text{cell}} \cdot A_{\text{elecZn}} \cdot t_f)}{3600} \quad (3.44)$$

where t_f is the total operating time in sec, $N_{\text{Zn},0}$ is initial mole of Zn and $N_{\text{Zn},f}$ is final mole of Zn.

As shown in Fig. 3.4, the current efficiency and discharge energy of ZAFB were examined as functions of KOH concentration and space velocity. Fig. 3.4A shows that the higher KOH concentration provided lower efficiency than the lower KOH concentration. It indicated that corrosion of the Zn electrode increased when the concentration of KOH increased. The corrosion was greater at higher KOH concentration because the reversible potential difference between the Zn electrode reaction and HER (ΔE_{ZH}) was negatively larger at higher KOH concentration, as shown in Fig. 3.5. ΔE_{ZH} contributes to HER overpotential (η_{H}) and drives the current of HER, as shown in Equations (3.23) and (3.22), respectively. The effect of KOH concentration on Zn corrosion was also investigated by other researchers using different methods (Muralidharan and Rajagopalan, 1978, Ravindran and Muralidharan, 1995, El-Sayed et al., 2012). Muralidharan and Rajagopalan (1978) studied corrosion of zinc in sodium hydroxide solution with steady state and transient Tafel extrapolation. Ravindran and Muralidharan (1995) determined the hydrogen evolution rate by gasometric method and examined the behavior of zinc in alkaline electrolyte. El-Sayed et al. (2012) proposed the corrosion study of Zn in alkaline solution by Tafel plot and electrochemical impedance spectroscopy (EIS). The research as mentioned above is in full agreement with the result concerning the effect of KOH concentration on hydrogen evolution. However, when KOH concentration increased, it had a different effect on the discharge energy, as shown in Fig. 3.4B. Consequently, when concentration of KOH reached about 6 M, it provided maximum exchange current density of Zn dissolution and maximum ionic conductivity. Using KOH concentration more or less than 6 M decreased the energy discharge of ZAFB. Thus, at 6 M KOH concentration, the maximum performance for ZAFB was achieved.

As regards the effect of flowrate, the increasing space velocity of the electrolyte provided lower current efficiency because the higher electrolyte flowrate maintained a higher concentration of KOH which contributed to higher corrosion. However, the flowrate exhibited less effect at lower KOH concentration.

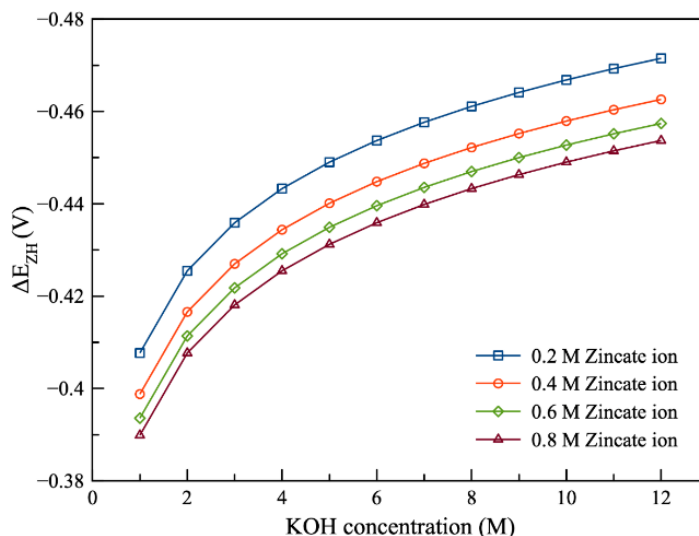


Figure 3.5 Effects of zincate ion initial concentration on ΔE_{ZH} as a function of KOH concentration.

Fig. 3.6 presents the effect of zincate ion concentration on the performance of ZAFB. The results showed that increasing the concentration of zincate ion tended to increase the current efficiency and discharge energy of the battery. This was because hydrogen evolution was affected by the zincate ion concentration. Previously, Fig. 3.5 shows the relation between ΔE_{ZH} and concentration of zincate ion. When zincate ion concentration increased, ΔE_{ZH} reduced due to the decrease in the reversible Zn electrode potential (E^{zinc}). According to the previous work of Shivkumar et al. (1995), it was reported that adding ZnO reduced hydrogen evolution and Zn dissolution. The previous work came to the same conclusion as the result herein.

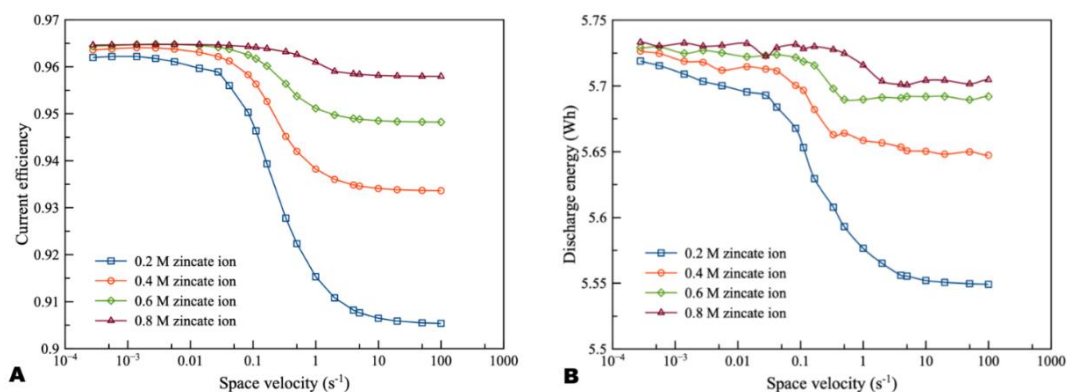


Figure 3.6 Effects of zincate ion initial concentration on ZAFB using 8 M KOH at discharge current density of 100 mA/cm^2 : (A) current efficiency as a function of space velocity and (B) discharge energy as a function of space velocity.

3.7.3 Electrolyzer Performance

In the case of the electrolyzer, simulation was performed in order to examine the effects of space velocity, KOH concentration and zincate ion concentration using a charge current density of 100 mA/cm². The target amount of regenerated Zn was 10 g. The simulation was terminated when it reached the target amount of Zn. The current efficiency of the electrolyzer is the ratio of the equivalent current for Zn regeneration to the total applied current. The current efficiency and charge energy of electrolyzer is expressed by:

$$\text{Current efficiency of electrolyzer} = \frac{2F(N_{Zn,f} - N_{Zn,0})}{i^{\text{cell}} A_{\text{elecZn}} t_f} \quad (3.45)$$

$$\text{Charge energy (Wh)} = \frac{\sum_{t=0}^{t_f} (E_{\text{cell}}) \cdot (-i^{\text{cell}} \cdot A_{\text{elecZn}} \cdot t_f)}{3600} \quad (3.46)$$

The performance of the Zn electrolyzer was evaluated by the current efficiency and the charge energy, as shown in Fig. 3.7. It was found that the flow of the electrolyte had a significant effect on the performance of the electrolyzer. Increasing space velocity increased the current efficiency but decreased charge energy. The high flowrate was preferred because increasing flowrate reduced the diffusion film thickness of the zincate ion. Consequently, Zn reduction was promoted and HER was suppressed. As regards the effect of zincate ion concentration, current efficiency increased and charge energy decreased when the concentration of zincate ion increased. The higher zincate ion concentration provided greater driving force of the diffusion and thereby enhanced the Zn reduction reaction. Increasing zincate ion concentration also reduced ΔE_{ZH} of HER which also suppressed the corrosion of Zn electrode. Many previous works have reached the same conclusion about the effect of zincate ion on Zn electrodeposition, as the result put forward herein (Einerhand et al., 1988, Sharifi et al., 2009, Dundálek et al., 2017). Einerhand et al. (1988) reported that the high concentration of zincate ion promoted ZnO layer formation on Zn electrode surface which protected Zn against corrosion. Dundálek et al. (2017) also highlighted the relation between Zn deposition morphology, electrolyte condition and HER and concluded that high flowrate and zincate ion concentration were preferred for Zn electrodeposition with low HER.

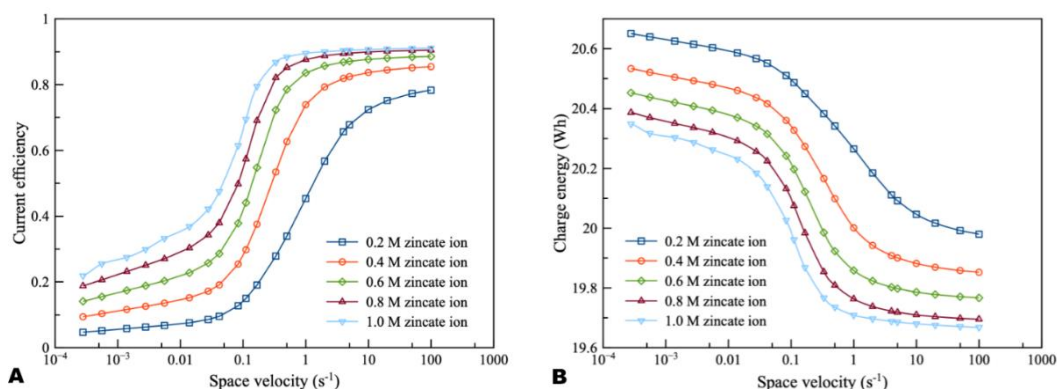


Figure 3.7 Effects of zincate ion initial concentration on zinc electrolyzer using 8 M KOH at charge current density of 100 mA/cm^2 : (A) current efficiency as a function of space velocity and (B) charge energy as a function of space velocity.

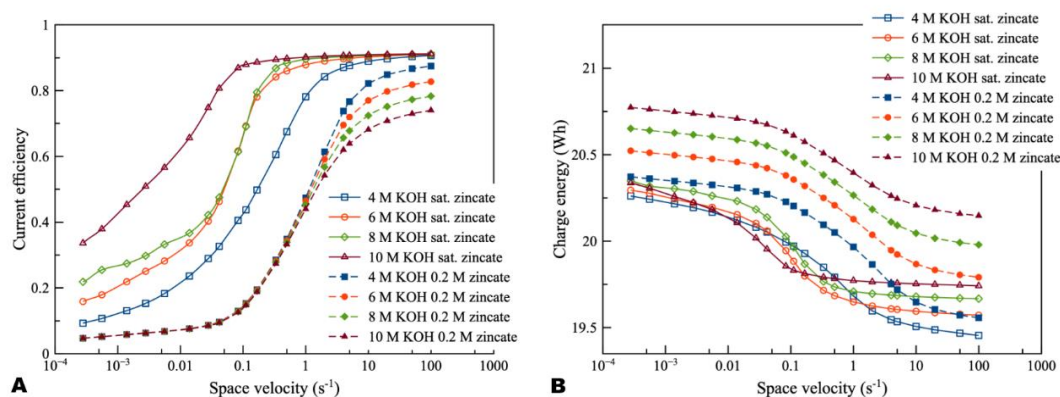


Figure 3.8 Effects of KOH concentration on zinc electrolyzer using different zincate ion initial concentration (0.2 M (dotted line) and saturated zincate ion (solid line)) at discharge current density of 100 mA/cm^2 : (A) current efficiency as a function of space velocity and (B) charge energy as a function of space velocity.

Regarding the effect of KOH concentration, as illustrated in Fig. 3.8, it was observed that KOH concentration had a complicated effect on current efficiency and charge energy. KOH concentration had a connection with the saturation limit of zincate ion. When zincate ion was not saturated, KOH concentration had little effect on current efficiency in the low flowrate region. However, a different trend was observed in the high flowrate region (space velocity above 1 per second). In the high flowrate region, increasing KOH concentration provided lower current efficiency due to increasing ΔE_{ZH} . As for the effect on charge energy, the higher KOH concentration needed higher charge energy because of the higher Nernst potential ($E_{0, \text{cell}}$). Sharifi et al. (2009) also studied zinc electrolysis using various KOH concentration and approached to the same conclusion. When the zincate ion was saturated, the effect on current efficiency and charge energy was different from that of non-saturated zincate ion. KOH concentration had less effect in the high flowrate region, but it had a direct

effect in the low flowrate region. When KOH concentration increased, efficiency tended to increase due to the saturation limit of zincate ion. The saturation limit increased due to the increase in KOH concentration. The effect of the saturation limit showed a similar trend with the effect of zincate ion concentration, as in Fig. 3.7. The higher saturation limit provided higher efficiency.

3.7.4 Integrated System

The operation having an equal charge-discharge current density of 100 mA/cm² was simulated. The initial Zn in ZAFB was 10 g (0.1538 mole of Zn). Zn depletion in ZAFB was the termination criterion. The current efficiency of the integrated system is defined as the ratio of the total amount of Zn regenerated to the total amount of Zn utilized, as in Equation (3.47). The other performance evaluation is energy efficiency which is expressed as the ratio of discharge energy to charge energy, as described in Equation (3.48):

$$\text{Current efficiency of the integrated system} = \frac{N_{\text{Zn},f}^{\text{electrolyzer}} - N_{\text{Zn},0}^{\text{electrolyzer}}}{N_{\text{Zn},0}^{\text{battery}} - N_{\text{Zn},f}^{\text{battery}}} \quad (3.47)$$

$$\text{Energy efficiency} = \frac{\text{Discharge energy (Wh)}}{\text{Charge energy (Wh)}} \quad (3.48)$$

Then, the performance of the integrated system was examined by considering various operating parameters i.e. space velocity, KOH concentration and zincate ion concentration.

The current efficiency and energy efficiency of the integrated system are as shown in Fig. 3.9. It was observed that the efficiency trends of the integrated system were comparable with the charge efficiency trends of the electrolyzer, as illustrated in Figs. 3.9A, 3.9B and 3.9C. It can be inferred that the efficiency of the integrated system is dominated by the electrolyzer. The results showed that increasing flowrate enhanced the current efficiency except at low zincate ion concentration. At low zincate concentration, the inflection point occurred at space velocity range 0.1 to 1 s⁻¹ and especially at 0.2 M zincate concentration. The condition at the bottom of the curve is the condition such that the total amount of zincate ion transferring to the electrode surface is minimum compared to the adjacent condition. The increasing flowrate had a positive effect on the energy efficiency of the system. In the case of the comparison of effect of zincate ion concentration, the higher zincate ion concentration provided better performance throughout the range of space velocity. Increasing zincate ion concentration was able to suppress HER and increase the current efficiency for both discharging and charging. At space velocity, approximately below 0.1 s⁻¹, increasing zincate ion concentration improved energy efficiency. In contrast, at space velocity above 1 s⁻¹, increasing zincate ion concentration provided an adverse effect on energy efficiency.

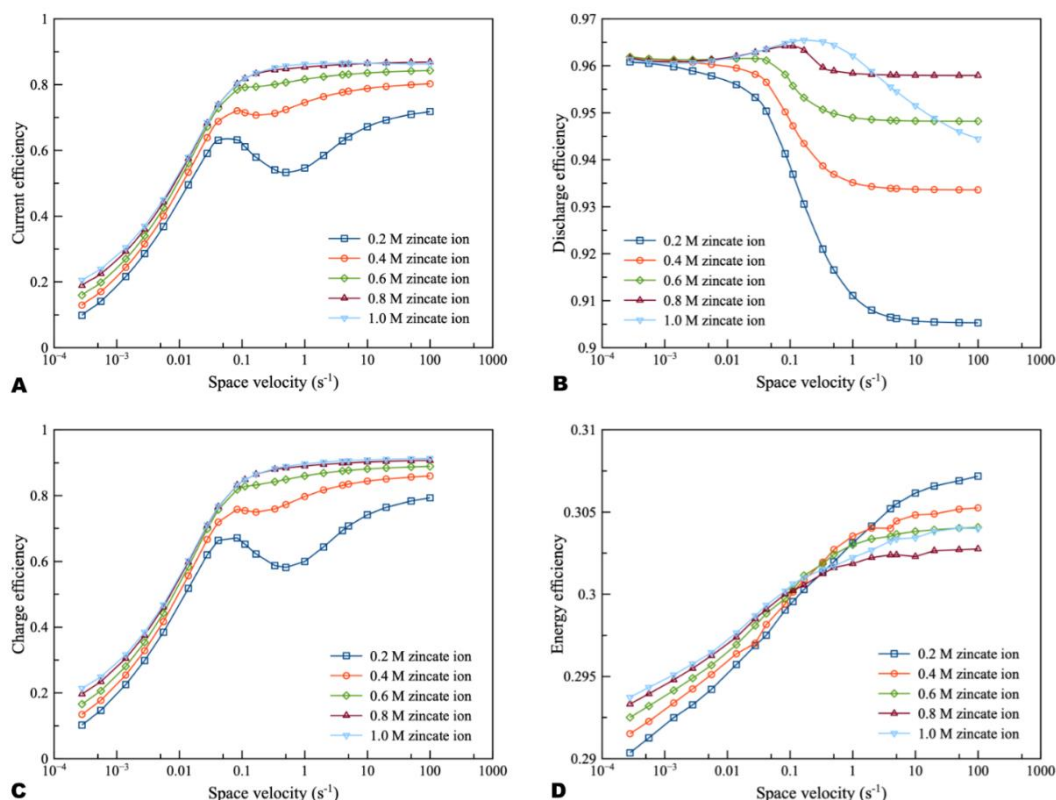


Figure 3.9 Effects of zincate ion initial concentration using 8 M KOH at charge and discharge current density of 100 mA/cm^2 : (A) current efficiency as a function of space velocity (B) discharge efficiency as a function of space velocity (C) charge efficiency as a function of space velocity and (D) energy efficiency as a function of space velocity.

In Fig. 3.10, the performance of the integrated system was examined: namely, from 2 to 10 M KOH concentration. It was observed that the efficiency curve could be divided into 2 regions: the region before and after the inflection point. For the region before the inflection point, efficiency increased as KOH concentration increased. Zincate ion was saturated herein. Subsequently, when KOH concentration increased, the saturation limit of zincate ion increased. Therefore, zincate ion diffusion also improved. On the other hand, efficiency decreased as KOH concentration increased for the region after the inflection point. Zincate ion was not saturated in this region. Thus, the concentration of zincate ion was not much different between the various KOH concentration. However, HER still intensified as KOH concentration increased. It is evident that 8 M KOH concentration provided maximum energy efficiency. This was followed by 6 M KOH concentration. Energy efficiency was dominated by the performance of the discharge process which was influenced mainly by optimal KOH concentration. As mentioned previously in the section of battery performance, concentration of about 6 to 7 M KOH provided maximum exchange current density of the Zn electrode reaction and maximum ionic conductivity. Consequently, in the case

of the integrated system, 6 and 8 M KOH concentration exhibited optimal performance.

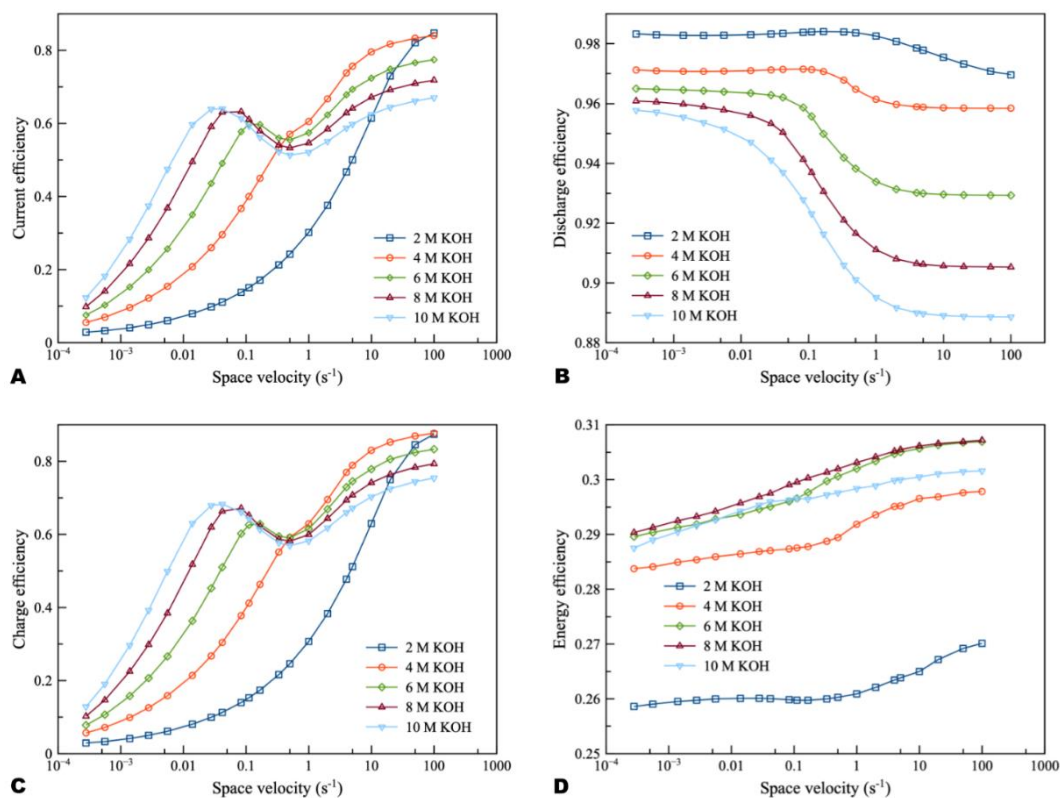


Figure 3.10 Effects of KOH concentration using 0.2 M zincate ion initial concentration at charge and discharge current density of 100 mA/cm^2 : (A) current efficiency as a function of space velocity (B) discharge efficiency as a function of space velocity (C) charge efficiency as a function of space velocity and (D) energy efficiency as a function of space velocity.

3.8 Conclusion

In this work, a mathematical model of a Zn-air flow battery integrated with a Zn electrolyzer including the model of HER was developed to evaluate the system performance. Thereby, the following parameters were investigated: electrolyte flowrate, potassium hydroxide (KOH) concentration and zincate ion initial concentration. Besides, the influence of the hydrogen evolution reaction (HER) on the performance of the Zn-air energy storage system was examined. Upon investigation, it was found that KOH concentration had a significant effect on the performance of the battery. Further, it was noted that increasing KOH concentration enhanced HER and reduced the current efficiency. However, the optimal KOH concentration, which was about 6-7 M, provided maximum discharge energy. Increasing zincate ion initial concentration was able to suppress the HER and increase the current efficiency of the battery because of the lessening of reversible potential difference between the Zn

electrode reaction and HER. As regards the electrolyzer, the results showed that the performance of the electrolyzer was dominated by zincate ion initial concentration and electrolyte flowrate. When zincate ion initial concentration increased together with the flowrate, current efficiency significantly increased. Further, the charge energy was reduced due to the enhancement of zincate ion diffusion to the electrode surface. Yet, increasing KOH concentration did not directly improve electrolyzer performance but contributed to the increment of saturation limit of zincate ion which enhanced the electrolyzer performance. For the overall integrated system, it was observed that the current efficiency of the integrated system was dominated by the electrolyzer. Therefore, increasing zincate ion initial concentration and electrolyte flowrate had a beneficial effect on the current efficiency of the integrated system. On the other hand, the energy efficiency of the integrated system was essentially influenced by the discharging cell. Maximum energy efficiency was obtained by the optimal concentration of KOH similar to the discharge energy of the flow battery. The results of this work described the role that HER contributed towards the performance of the integrated system of Zn-air flow battery and Zn electrolyzer. Overall, it was found that HER had a detrimental effect on the performance of the integrated system. To conclude, it can be seen that control of the operating conditions was found to be an effective way to diminish HER and extract optimal performance out of the integrated system.

3.9 Nomenclature

a_0	initial solid-solution interface area per unit volume, dm^2/dm^3
a_c	specific surface area of catalyst per unit volume, dm^2/dm^3
a_s	solid-solution interface area per unit volume, dm^2/dm^3
A_{zinc}	active surface area of Zn electrode, dm^2
A_{air}	active surface area of air electrode, dm^2
A_{sep}	area of separator, dm^2
C^{ref}	reference state concentration, mol/dm^3
$C_{\text{DL}}^{\text{zinc}}$	double layer capacitance of Zn electrode, F/dm^2
$C_{\text{DL}}^{\text{air}}$	double layer capacitance of air electrode, F/dm^2
C_k^j	concentration of specie k at electrode j , mol/cm^3
D_k	diffusivity/ diffusion coefficient of specie k , dm^2/s
$E_{0,\text{cell}}$	Nernst potential/ standard electrode potential, V
E_{cell}	cell voltage, V
E^{zinc}	reversible potential of Zn electrode, V
E^{air}	reversible potential of air electrode, V

E^H	reversible potential of hydrogen evolution reaction, V
F	Faraday constant, C/mol
F_{conv}	convective volume flow, dm ³ /s
$F_{k,\text{in}}$	inlet molar flowrate of specie k , mol/s
$F_{k,\text{out}}$	outlet molar flowrate of specie k , mol/s
I	electrical current, A
i^{cell}	current density, A/dm ²
i_0	exchange current density, A/dm ²
i_0^{ref}	reference exchange current density, A/dm ²
J_k	molar transfer rate between electrodes, mol/s
j_k^{conv}	convective molar flow rate, mol/s
j_k^{diff}	diffusion molar flow rate, mol/s
j_k^{mig}	migration molar flow rate, mol/s
k_s	rate constant of ZnO precipitation reaction, dm ³ /s
n_e	number of exchange electron involved in the reaction
N_k^j	moles of specie k at electrode j , mol
p^{ref}	reference pressure, atm
P_{O_2}	partial pressure of oxygen, atm
r_i	rate of reaction i , mol/s
R	gas constant, J/mol · K
R_{comp}	resistivity of cell component, $\Omega \cdot \text{dm}$
R_{ohmic}	total ohmic resistance, Ω
SV	space velocity, s ⁻¹
t	time, s
t_k	transference number of ion k
T	temperature, K
$V_{\text{electrolyte}}^j$	volume of electrolyte at electrode j , dm ³
$V_{\text{solid}}^{\text{zinc}}$	volume of solid Zn electrode, dm ³
$V_{\text{solid},k}$	volume of solid specie k , dm ³
\bar{V}_k	specific molar volume of specie k , dm ³ /mol
X_{zinc}	active surface fraction of Zn in solid phase
z_k^{\pm}	ion number of specie k
Greek symbol	
α	charge transfer coefficient
δ_{air}	thickness of air electrode, dm
$\delta_{\text{electrolyte}}$	thickness of electrolyte, dm

δ_{zinc}	thickness of Zn electrode, dm
δ_{active}	thickness of active reaction zone, dm
δ_{sep}	thickness of separator, dm
δ_{GDL}	thickness of gas diffusion layer, dm
ΔE_{ZH}	potential difference between Zn and hydrogen electrode, V
ε	porosity of Zn electrode
ε_0	initial porosity of Zn electrode
ε_{sep}	porosity of separator
$\eta_{\text{act}}^{\text{zinc}}$	activation loss/ activation overpotential of Zn electrode, V
$\eta_{\text{act}}^{\text{air}}$	activation loss/ activation overpotential of air electrode, V
$\eta_{\text{ionic}}^{\text{sep}}$	ionic separator loss, V
η_{ohmic}	ohmic loss/ ohmic overpotential, V
σ_{anode}	total conductivity of anode, S/dm
σ_{cathode}	total conductivity of cathode, S/dm
σ_k	conductivity of specie k , S/dm
$\sigma_{\text{electrolyte}}$	conductivity of electrolyte, S/dm
$\nu_{k,i}$	stoichiometric coefficient of specie k in reaction i

CHAPTER 4

Discharge Performance and Dynamic Behavior of Refuellable Zinc-Air Battery

4.1 Preface

First author: Woranunt Lao-atiman

Advisor: Soorathep Kheawhom

Affiliation: Department of Chemical Engineering, Faculty of Engineering,
Chulalongkorn University, Bangkok

Journal: Scientific Data

Published: 9 September 2019

Volume: 6

Article: 168

Citation: Lao-atiman, W., Olaru, S., Arpornwichanop, A. et al. Discharge performance and dynamic behavior of refuellable zinc-air battery. *Sci Data* 6, 168 (2019). <https://doi.org/10.1038/s41597-019-0178-3>

Data citation: Kheawhom, S. Discharge Performance of Zinc-air Battery. *Open Science Framework*. <https://doi.org/10.17605/OSF.IO/FDQCP> (2019).

This paper is a part of dissertation publication for graduation and is already published in the journal ‘Scientific Data’ on 9 September 2019. This article is published as a data descriptor along with the dataset. The data are available separately at the directory designated above.

4.2 Abstract

Zinc-air batteries (ZABs) are considered a promising energy storage system. A model-based analysis is one of the effective approaches for the study of ZABs. This technique, however, requires reliable discharge data as regards parameter estimation and model validation. This work, therefore, provides the data required for the modeling and simulation of ZABs. Each set of data includes working time, cell voltage, current, capacity, power, energy, and temperature. The data can be divided into three categories: discharge profiles at different constant currents, dynamic behavior at different step changes of discharge current, and dynamic behavior at different random step changes of discharge current. Constant current discharge profile data focus on the evolution of voltage through time. The data of step changes emphasize the dynamic behavior of voltage responding to the change of discharge current. Besides, the data of random step changes are similar to the data of step

changes, but the patterns of step changes are random. Such data support the modeling of a zinc-air battery for both theoretical and empirical approaches.

4.3 Background & Summary

Global warming and climate change become aggravated as a result of excessive consumption of fossil fuels. Thus, renewable energy technologies have been actively developed and implemented. Unfortunately, renewable energy sources exhibit inherent intermittent attributes. The innate, erratic nature of renewable energy causes operational difficulties i.e., an unexpected imbalance between energy demand and supply, and lowered power quality. However, the disadvantages of intermittency can be effectively mitigated using an energy storage system (Zhang, 2013, Chen et al., 2019b).

In recent years, metal-air batteries, as a promising energy storage system, have received widespread research interest. As regards the various types of metal-air batteries, zinc-air battery (ZAB) technology shows great potential and is near commercialization.

ZAB exhibits high energy density up to 700 Wh/kg (Li et al., 2013). Zinc is a low-cost metal and is abundant (Chen et al., 2019a, Yang et al., 2019). Moreover, it is safe, non-toxic, and environmentally friendly. A zinc-air battery can be fabricated in various designs: namely, a primary cell (Guo, 2003, Arlt et al., 2014, Fu et al., 2016, Suren and Kheawhom, 2016), an electrically rechargeable cell (Appleby and Jacquier, 1976, Amendola et al., 2013), and a mechanically rechargeable or refuellable cell (Clark et al., 2018, Hosseini et al., 2018a, Hosseini et al., 2018b, Oh et al., 2018). ZAB was commercialized only as a primary cell for lower current application such as in a hearing aid device. For other applications, however, this battery needs to be developed in a variety of facets.

Model-based engineering is one of the effective approaches which can facilitate the development of ZAB. Modeling and simulation can be applied to investigate the phenomena in a battery, monitor its state, optimally operate or assist in designing battery structure (Bonnick and Dahn, 2012). The developed models need to be validated on a variety of real-world configurations. Therefore, reliable experimental data for such validation are necessary. For instance, Mao and White (1992) proposed a primary ZAB model which included precipitation of solid zinc oxide and potassium zincate. Their work used the experimental discharge data provided by MATSI, Inc. to verify the validity of their model. Deiss et al. (2002) conducted a discharge and cycle experiment and used the relevant data to verify their own proposed ZAB model. Furthermore, the experimental data was also used to verify the mathematical model proposed by Schröder and Krewer (2014). Recently,

Lao-atiman et al. (2019a) introduced a mathematical model of an integrated system of a zinc-air flow battery and zinc electrolyzer in order to investigate the effect of operating parameters on the efficiency of the system related to hydrogen evolution reaction. The validated data were obtained from the experiment using a homemade zinc-air flow battery and zinc electrolyzer.

Knowledge of ZAB in the model-based engineering aspect is still in the early stages and can be improved considerably. In the aforementioned studies of different battery types, there are missing elements with respect to the ZAB operation, such as dynamic behavior analysis. For example, according to the literature, equivalent circuit models were used to estimate the dynamic behavior of batteries and developed thereby. The equivalent circuit model is an empirical model which can simplify the complexity of the electrochemical model. This type of model often needs low-order approximations to fit the model parameters (Docimo et al., 2014). Stroe et al. (2017) proposed a second order equivalent circuit model and used a current pulse technique to parameterize the dynamic model of a lithium-ion battery. A zinc-nickel battery was also investigated along with the equivalent circuit model (Li et al., 2014, Yao et al., 2017). The dynamic model was also able to be used to estimate the state of charge of the battery (Tang et al., 2011, Akbar et al., 2015). The estimation of the state of charge of the battery is crucial for the application of all types of batteries including ZAB. Both the continuum model and the empirical model require reliable experimental data for validation and parameter estimation.

The purpose of this work is to provide the experimental data for ZAB including discharge profiles at different constant discharge currents, dynamic behavior at different step changes of discharge current, and dynamic behavior at different random step changes of discharge current. All testing data were measured from the home-made tubular ZAB. Discharge profile data were tested within a current density range of 100 mA to 1000 mA. Response data were tested applying various step currents. The data provided can be used to validate the mathematical model of ZAB or estimate the parameters for the empirical model.

4.4 Methods

4.4.1 Chemical and materials

Nickel (Ni) foams (purity: 99.97%, pores per inch: 100 and thickness: 1 mm) were purchased from Qijing Trading Co., Ltd and were used as cathode current collect. Stainless steel mesh (30 mesh, SUS 304) was purchased from Alikafeii Trading Co., Ltd. and was used as anode current collector and cell chamber structure. Zinc pellets (20 mesh, 99.99% purity) were active material for the battery and were purchased from Sirikul Engineering Ltd., Part. Potassium hydroxide (KOH) pellets (99% purity)

purchased from CT Chemical Co., Ltd. was used for preparation of electrolyte. Chemical and materials for preparing cathode consisted of manganese dioxide (MnO_2 , self-synthesized), D-glucose (UNIVAR), acetylene black (AB-50, POLIMAXX, IRPC Public Co., Ltd.), carbon black (BP-2000, Cabot Corporation) and poly(tetrafluoro-ethylene) (PTFE powder, 1 μm , Sigma-Aldrich). Poly (styrene-co-butadiene) was used as a binder. Ethanol and Toluene were used as a solvent. Whatman filter paper No. 4 and poly (vinyl acetate) (24 wt.%, TOA Paint Public Co., Ltd.) were used to prepare the separator. All chemicals were used as received without any further purification.

The synthesis of MnO_2 was modified from the method published by Pang et al. (2012). The aqueous solutions of potassium permanganate (KMnO_4 ; prepared from KMnO_4 , UNIVAR) and manganese sulfate (MnSO_4 ; prepared from $\text{MnSO}_4 \cdot \text{H}_2\text{O}$, QRec) was gently mixed at ambient temperature and pressure. The reaction product was collected by filtration and washed with ethanol. The solid residue was then dried in a vacuum oven at 60 $^\circ\text{C}$ and 50 mbar.

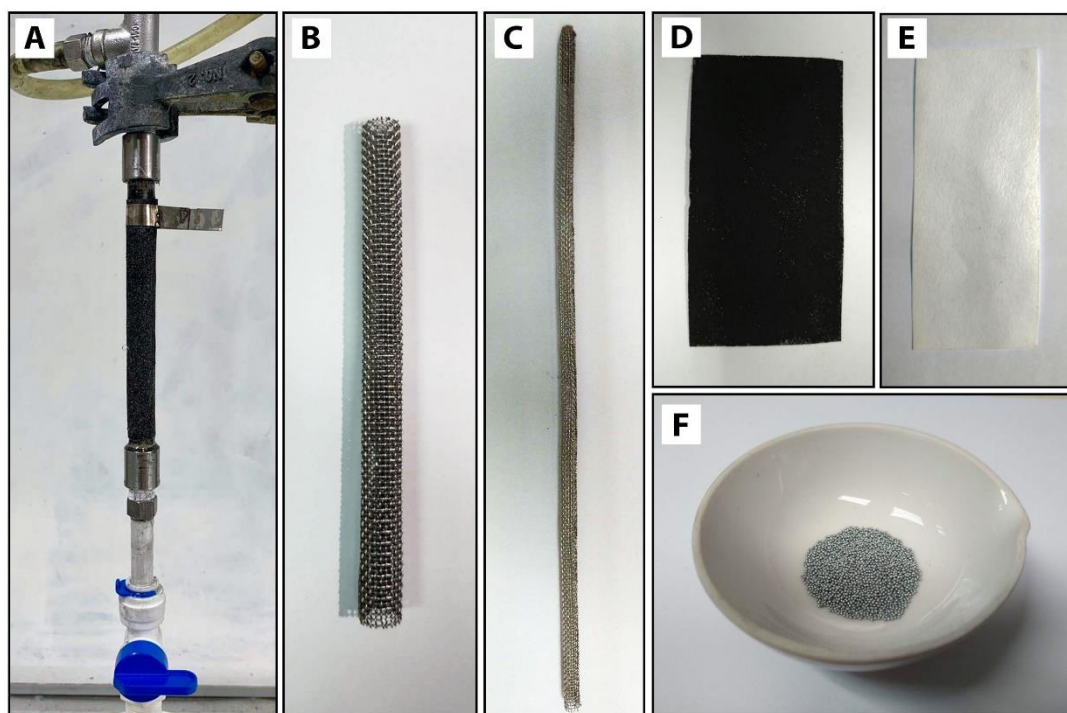


Figure 4.1 Digital photographic images of a homemade zinc-air battery. (A) Fabricated tubular zinc-air battery, (B) stainless steel mesh cylinder as a supporting structure, (C) stainless-steel mesh tube (the anode current collector), (D) the air cathode, (E) the separator, and (F) zinc pellets used as the anode active material.

4.4.2 Battery fabrication and operation

Homemade zinc-air batteries were designed and fabricated as a tubular cell, as shown in Fig. 4.1A. The digital photographic images of each cell component are shown in Fig. 4.1B-F. The cell structure (supporting structure) was made of stainless-steel mesh rolled into a cylindrical form (Fig. 4.1B). The cylinder was wrapped with a separator. Whatman filter paper (No.4) coated with 24 wt.% poly (vinyl acetate) solution was used as the separator (Fig. 4.1E). After that, the cell was covered with the air cathode on the outer layer.

Table 4.1 Summary of cell components

Components	Material
Anode Current Collector	5 mm-diameter tube made of 30 mesh stainless-steel mesh
Cathode current collector	Nickel foam (1 mm thick)
Separator	Whatman filter paper (No.4) coated with 24 wt.% Poly (vinyl acetate) solution
Anode active material	20 mesh zinc pellets packed inside current collector tube
Cathode active material	Oxygen in the atmospheric air
Gas diffusion layer	Mixture of 40 wt.% AB-50 / 40 wt.% Polytetrafluoroethylene / 20 wt.% Glucose
Catalytic layer	Mixture of 70 wt.% BP-2000 / 30 wt.% MnO ₂ (catalyst loading of 3 mg/cm ²) Poly (styrene-co-butadiene) as binder by the amount of 5 wt.% of dry-basis mixture
Electrolyte	8 M Potassium hydroxide solution

To prepare the air cathode, nickel foam was used as the cathode current collector and substrate for the gas diffusion layer (GDL) and ORR catalyst layer. The active area of the cathode was 29.83 cm². The GDL mixture was composed of 40 wt.% AB-50, 40 wt.% PTFE powder and 20 wt.% glucose. Ethanol was used as a solvent for the GDL mixture. This layer was coated on one-side of the Ni foam and then taken to the hot press for 15 min at 350 °C. After that, the catalyst layer was coated on the other side. The catalyst layer consisted of 70 wt.% BP-2000 carbon black and 30 wt.% manganese oxide. Then, poly (styrene-co-butadiene) was used as a binder, and 5 wt.% of dry-basis catalyst mixture was added. Toluene was used as a solvent for the catalyst mixture. Next, the coated cathode was annealed at 110 °C for 15 min. After annealing, the electrode was pressed by a roll pressing machine until the electrode thickness equaled 1 mm. The finished cathode, as shown in Fig. 4.1D, had

catalyst loading of 3 mg/cm^2 . Finally, after the cathode was finished, it was taken to wrap around the cell by means of facing the catalyst side towards the separator. Before putting the anode inside, the cell was filled with 8 M KOH solution and held for 24 h in order to saturate the separator and be ready for use.

The anode was placed in the center of the tubular cell. A 5 mm-diameter tube made of 30 mesh stainless-steel mesh was used as anode current collector. 6 g of 20 mesh zinc pellets were packed inside the current collector tube as anode active material. 8 M KOH solution was used as the electrolyte and was poured into the anode chamber. A summary of cell components and parameters is shown in Tables 4.1 and 4.2. The battery was fabricated, as shown in Fig. 4.2.

Table 4.2 Summary of cell parameters

Parameters	Values
KOH concentration	8 M
Separator thickness	0.1 mm
Cathode thickness	1 mm
Cathode length	9.5 cm
Cathode active surface area	29.83 cm^2
Catalyst loading	3 mg cm^{-2}
Amount of zinc	6 g
Electrolyte volume	15 cm^3
Anode current collector diameter (stainless-steel mesh tube)	5 mm
Anode current collector full length	20.5 cm
Zinc pellets bed length (equivalent of 6 g of zinc pellet)	13.5 cm
Anode chamber diameter (stainless-steel mesh cylinder)	10 mm

4.4.3 Measurement and data collection

After battery fabrication, cell voltage and current were measured by a BA500 battery analyzer using BA500WIN software. The discharge current can be adjusted manually, and cell voltage can be measured at the selected current continuously. Data logging time can also be selected. The output files of the collecting data were.csv files. The data were rearranged, and the file type was changed into.xlsx. The data file contains various information, including working time, cell voltage, discharge current, discharge capacity, discharge power, discharge energy, and temperature. A discharge profile test was executed by discharging the battery at selected values of discharge current and measuring the evolution of cell voltage until the battery was exhausted. The measurement of discharge profile test was terminated when the discharge current was lower than the setpoint current. As for the step discharge test, the voltage was measured when the discharge current was step-changed. The random discharge test is

similar to the step discharge test except that the patterns of the step changes are more random in each test. Data logging time was 1 sec for the step and random discharge test and 5 sec for the discharge profile test.

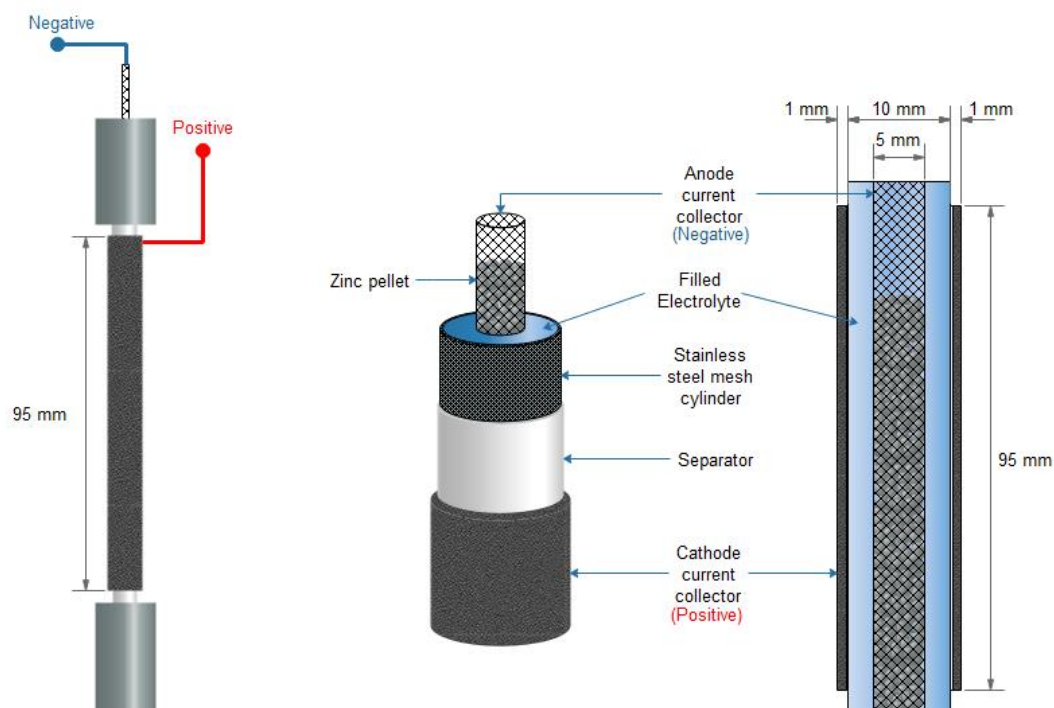


Figure 4.2 cell structure and cell dimension of a homemade zinc-air battery.

Table 4.3. Metadata of discharge and response test

Data	Unit	Description
Total time	S	Total operating time
Voltage	V	Measured voltage of the battery
Current	mA	Measured current of the battery
Result	mAh	Calculated capacity of the battery
Power	W	Calculated power of the battery
Energy	Wh	Calculated energy of the battery
Temp	°C	Room temperature

4.5 Data Records

The data provided can be divided into three categories: discharge profiles at different constant discharge currents, dynamic behavior at different step changes of discharge current, and dynamic behavior at different random step changes of discharge current. Three dataset categories can be separately found in the DischargeProfiles.xlsx, RandomDischarge.xlsx, and StepDischarge.xlsx. These datasets are available at the

repositories (Kheawhom, 2019). In Table 4.3, metadata which provide the description for each data column are presented.

4.6 Technical Validation

In the experiment, data were collected from different batteries. Every time a new test was carried out, the anode and electrolyte were changed. Thereby, a deviation in the data set was apparent and affected battery capacity. It represents a usual phenomenon which should be accounted for in future large mass production. Besides, the deviation might also have affected the voltage, but this was less than the effect on the capacity. For all data, the erroneous data point of voltage was removed and smoothed. It was noted that such incorrect data occurred at a lower current range or near the OCV range. Such errors caused the voltage values to be higher than the real values. The method used to remove the erroneous data is the interpolation between non-error points.

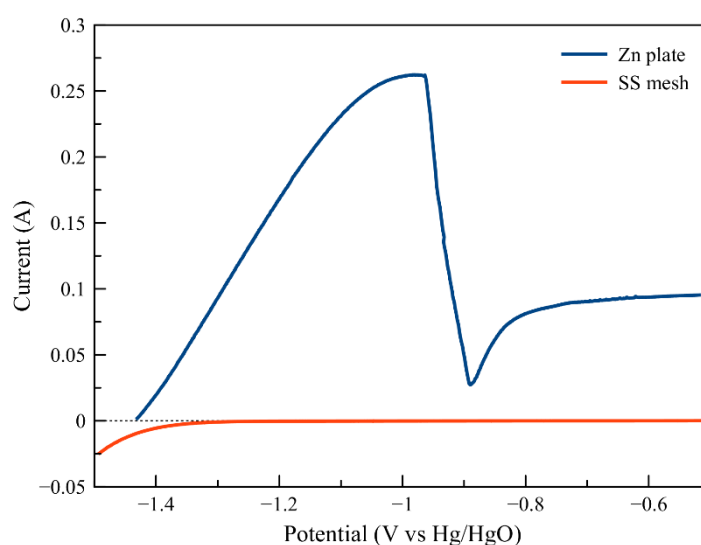


Figure 4.3 Linear sweep voltammograms of the zinc plate (scanned from OCV to -0.5 V vs. Hg/HgO), and stainless-steel mesh (scanned from -1.5 V to -0.5 V vs. Hg/HgO) with a scan rate of 5 mV/s.

To check the electrochemical compatibility of the materials used in the battery, the electrochemical characteristic was examined by linear sweep voltammetry (LSV). The LSV was performed by a potentiostat/galvanostat (AMETEK, VersaSTAT 3). Three electrodes configuration was used with platinum as the counter electrode and mercury/mercury oxide (Hg/HgO) as the reference electrode. The electrolyte used in all tests was 8 M KOH solution. The linear sweep voltammograms of the zinc plate and stainless-steel mesh are depicted in Fig. 4.3. The dimension of zinc plate was 1×1 cm². The test of the zinc plate scanned from the open circuit voltage (OCV) to

-0.5 V vs. Hg/HgO with a scan rate of 5 mV/s. The OCV of zinc plate was 1.44 V vs. Hg/HgO. As the potential scanning proceeded, the current positively increased, which is known as oxidation current. The oxidation of zinc increased until reaching the peak at -0.98 V vs. Hg/HgO. Scanning further caused decreasing in current due to the passivation of zinc surface, and the depletion of hydroxide ion at the surface of the electrode (Li et al., 2017a, Mainar et al., 2018, Stock et al., 2019). Because stainless-steel mesh was used as the anode current collector, the electrochemical characteristic of stainless-steel mesh has to be checked in the same potential range as the zinc. The dimension of stainless-steel mesh was also 1×1 cm². The stainless-steel mesh was scanned from -1.5 to -0.5 V vs. Hg/HgO with a scan rate of 5 mV/s. The small negative current was detected at the potential about -1.5 to -1.3 V vs. Hg/HgO. The negative current is the reduction reaction, which is contributed to a hydrogen evolution reaction. Nonetheless, the potential range of -1.2 to -0.5 V vs. Hg/HgO showed almost no current. It means that stainless-steel mesh was stable and did not oxidize in this potential window. The result showed that the zinc is compatible with stainless-steel mesh in the operation potential of the battery. At the OCV, the stainless-steel mesh conducted a small amount of hydrogen evolution, which can promote corrosion of zinc. However, it was observed that the hydrogen evolution current of stainless-steel mesh was minimal compared with the zinc oxidation current.

Because nickel foam was used as the cathode current collector, the electrochemical characterization in the potential range of air cathode reaction must be checked. The LSV of nickel foam is presented in Fig. 4.4. As regards Fig. 4.4A, the 1×1 cm² nickel foam was scanned from 0 to -0.7 V vs. Hg/HgO with a scan rate of 5 mV/s. Before the test, the electrolyte was purged with nitrogen gas for 30 min in order to reduce the effect of dissolved oxygen. Small oxidation current was noticed at the potential range of 0 to about -0.25 V vs. Hg/HgO. This oxidation current might come from the oxidation of nickel. At the potential range of -0.25 to -0.7 V vs. Hg/HgO, small reduction current was observed. The reduction current might come from the reduction of remain dissolved oxygen in the electrolyte and the nickel oxide on the nickel surface. To focus on the reduction reaction, nickel foam was scanned from OCV to -0.7 V vs. Hg/HgO, as shown in Fig. 4.4B. It was found that the order of magnitude of the current of nickel foam was very low. It can be inferred that the reduction of nickel metal slightly occurred in the test potential range. Therefore, the reaction of nickel metal does not interfere the oxygen reduction reaction of the air cathode.

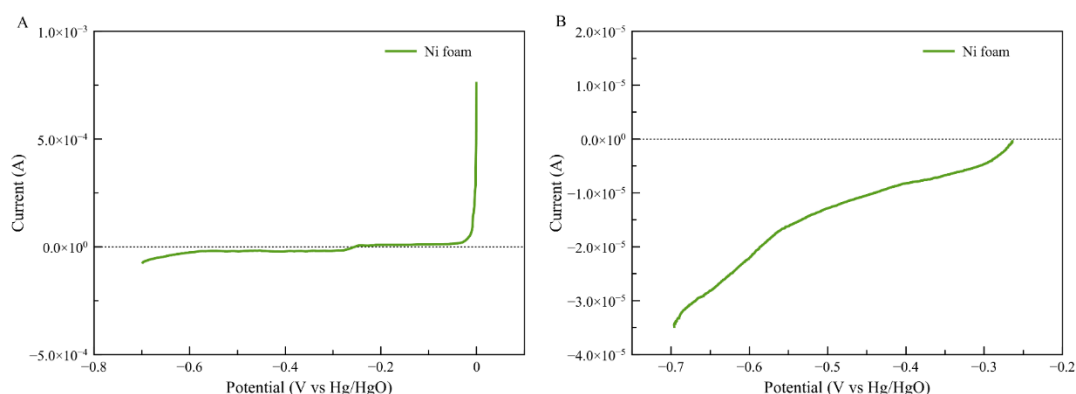


Figure 4.4 Linear sweep voltammogram of the Ni foam with scan rate of 5 mV/s. (A) Scanned from 0 to -0.7 V vs. Hg/HgO, and (B) scanned from OCV to -0.7 V vs. Hg/HgO.

4.7 Usage Notes

The data provided herein has been useful in assisting model-based engineering for a zinc-air battery. Thus, the data can be employed to validate the result of the theoretical model or fit the parameters of the empirical model. It should be noted that this data was collected from the home-made battery, as shown in Fig. 4.1. For this type of cell structure, battery behavior, and phenomena might be unique. It is difficult to compare the data as mentioned above to the data as measured from the batteries having different structures.

4.8 Code Availability

The reported data were generated from experiments, and not relevant to any computer codes.

CHAPTER 5

Linear Parameter-varying Model for a Refuellable Zinc-air Battery

5.1 Preface

First author: Woranunt Lao-atiman

Advisor: Soorathep Kheawhom

Affiliation: Department of Chemical Engineering, Faculty of Engineering, Chulalongkorn University, Bangkok

Journal: Royal Society Open Science

Published: 9 December 2020

Volume: 7

Issue: 12

Citation: Lao-atiman Woranunt, Olaru Sorin, Diop Sette, Skogestad Sigurd, Arpornwichanop Amornchai, Cheacharoen Rongrong and Kheawhom Soorathep 2020 Linear parameter-varying model for a refuellable zinc–air battery. *R. Soc. open sci.* **7**: 201107. <http://doi.org/10.1098/rsos.201107>

This paper is a part of dissertation publication for graduation and is already published in the journal ‘Royal Society Open Science’ on 9 December 2020. The experimental data used in this article are obtained from previously published data as described in chapter 4. This publication also includes supplementary material which has been uploaded to The Open Science Framework at <https://osf.io/mnbpq/>, and the DOI is 10.17605/OSF.IO/MNBPG. The supplementary material can also be found in Appendix B of this thesis.

5.2 Abstract

Due to the increasing trend of using renewable energy, the development of an energy storage system (ESS) attracts great research interest. A zinc–air battery (ZAB) is a promising ESS due to its high capacity, low cost and high potential to support circular economy principles. However, despite ZABs' technological advancements, a generic dynamic model for a ZAB, which is a key component for effective battery management and monitoring, is still lacking. ZABs show nonlinear behaviour where the steady-state gain is strongly dependent on operating conditions. The present study aims to develop a dynamic model, being capable of predicting the nonlinear dynamic behaviour of a refuellable ZAB, using a linear parameter-varying (LPV) technique. The LPV model is constructed from a family of linear time-invariant models, where

the discharge current level is used as a scheduling parameter. The developed LPV model is benchmarked against linear and nonlinear model counterparts. Herein, the LPV model performs remarkably well in capturing the nonlinear behaviour of a ZAB. It significantly outperforms the linear model. Overall, the LPV approach provides a systematic way to construct a robust dynamic model which well represents the nonlinear behaviour of a ZAB.

Table 5.1 Nomenclature

A	State matrix in state space model
B	Input matrix in state space model
BC	Combined parameter between parameters B and C
B/F	Linear block in HW model
$B(z)$	Numerator polynomial function of linear block in HW model
b_{nb}	Polynomial coefficient of B(z)
C	Output matrix in state space model
C_P	Capacitance in RC loop, F
D	Feedthrough matrix in state space model
$E_{0,air}$	Standard electrode potential of air electrode, 0.401 V vs SHE
$E_{0,cell}$	Standard cell potential or theoretical OCV, V
$E_{0,zn}$	Standard electrode potential of Zn electrode, -1.26 V vs SHE
F	Faraday constant, 96485.3329 A·s / mol
$F(z)$	Denominator polynomial function of linear block in HW model
f	Input nonlinear block
f_{nf}	Polynomial coefficient of F(z)
h	Output nonlinear block
I_{cell}	Discharge current, A
k	Discrete time, sec
n	Number of states = 1
n_b	Order of B(z) polynomial
n_e	Number of electron transfer in the reaction
n_f	Order of F(z) polynomial
n_k	Input delay of linear block in HW model
p	Scheduling parameter
R	Gas constant, 8.3145 J / mol·K
R_C	Resistance in RC loop, Ω
R_0	Ohmic resistance, Ω
T	Temperature, K
T_s	Sampling time, s
u	Input vector of state space model and HW model

Table 5.1 (cont.) Nomenclature

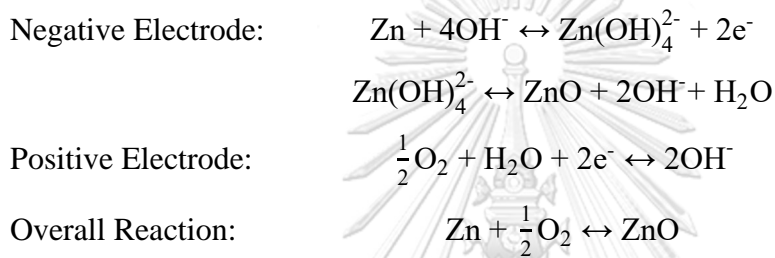
V_{OC}	Open circuit potential, V
V_{RC}	Potential loss, V
V_{RCR}	Potential drop across RC loop, V
w	Input of linear block in HW model
X	State vector in state space model
x	Output of linear block in HW model
Y	Output vector of state space model
y	Output of HW model
z	Delay operator in output-error model
α	Coefficient of two-term exponential function
β	Coefficient of two-term exponential function
γ	Coefficient of two-term exponential function
δ	Coefficient of two-term exponential function
μ	Coefficient of third-order polynomial function
ξ	Model parameter estimated from correlations

5.3 Introduction

Renewable energy has great potential to sustain global energy security. Nevertheless, renewable energy is very intermittent and highly erratic, resulting in fluctuation in energy production. An energy storage system (ESS) can stabilize such fluctuation and effectively support energy management and integration. Recently, ESS has become an immensely focused topic in energy research. An ESS can enhance the efficiency and stability of various energy systems (Zhang, 2013, Luo et al., 2015)

Of the various types of ESS, zinc–air batteries (ZABs) prove to be the most promising, providing excellent specific capacity. ZAB technology has made substantial research progress and is approaching commercialization (Amunátegui et al., 2018, Hosseini et al., 2018a, Hosseini et al., 2018b). ZABs use the electrochemical reaction between zinc (Zn) and oxygen (O₂) to store and release electricity. ZABs characteristically have high energy density but low power. It is reported that ZABs are able to deliver peak power density up to 430 mW cm⁻² and energy density up to 837 W h kg⁻¹ (Yan et al., 2018). These values have already exceeded the specific energy of commercialized lithium ion batteries (LIBs) many times. Moreover, Zn is abundant on Earth; therefore, its cost is quite low (Lao-atiman et al., 2017, Kao-ian et al., 2019, Khamsanga et al., 2019). In addition, Zn is safe, environmentally friendly and highly stable. Zinc oxide (ZnO), which is the discharge product, can be easily recycled. O₂, supplied from atmospheric air, is also quasi-free and virtually unlimited. Thus, ZABs present great potential and feasibility in providing a decent ESS on a large scale.

Generally, a ZAB consists of two electrodes: a Zn electrode (negative electrode) and an air electrode (positive electrode). The most common electrolyte for a ZAB is an aqueous alkaline electrolyte such as potassium hydroxide (KOH) solution. As regards discharging, Zn serves as an electron donor at the negative electrode. Zn reacts with hydroxide ions (OH^-) producing zincate ions ($\text{Zn}(\text{OH})_4^{2-}$) and electrons (e^-). Zincate ions remain in the electrolyte and can precipitate to form ZnO. At the positive electrode, O_2 from the ambient air acts as an electron acceptor. Oxygen reduction reaction (ORR) proceeds and provides OH^- as the product. The overall reaction of a ZAB is the redox reaction of Zn and O_2 , thereby producing ZnO. The overall reactions that occur in the battery are described as follows (Lee et al., 2011, Li and Dai, 2014):



The theoretical open circuit voltage (OCV) is approximately 1.65 V (Lee et al., 2011), which can be calculated from the following equation:

$$E_{0,\text{cell}} = \left(E_{0,\text{air}} + \frac{RT}{n_e F} \ln \frac{[\text{O}_2]^{0.5}}{[\text{OH}]^2} \right) - \left(E_{0,\text{Zn}} + \frac{RT}{n_e F} \ln \frac{[\text{Zn}(\text{OH})_4^{2-}]}{[\text{OH}]^4} \right) \quad (5.1)$$

where $E_{0,\text{cell}}$ is the standard cell potential or theoretical OCV, $E_{0,\text{air}}$ is the standard electrode potential of the air electrode (corresponding to ORR) which is 0.401 V vs standard hydrogen electrode (SHE), $E_{0,\text{Zn}}$ is the standard electrode potential of Zn electrode (corresponding to Zn oxidation reaction) which is -1.26 V vs SHE, R is gas constant, T is temperature, n_e is the number of electron transfers in the reaction, F is faraday constant. This equation uses the concentration of the reactants to calculate the standard cell potential.

However, the practical OCV obtained from laboratory prototypes is about 1.4 V (Wang et al., 2003, Zhu et al., 2011, Larsson et al., 2017). Charging can be done in a rechargeable ZAB by applying a potential higher than the theoretical OCV. When charging, the reactions proceed backwards and regenerate Zn and O_2 .

The development of a ZAB encompasses many aspects (Lao-atiman et al., 2019a, Poolnapol et al., 2020, Hosseini et al., 2019, Abbasi et al., 2019). In the past decade, the focus has been on improving the performance and stability of the battery such as development of ORR catalyst or battery electrolyte. It is noted that the performance of a ZAB has been improved by optimizing battery parameters (Wang et

al., 2018). The development of battery operation i.e. pulse-current charging has also been investigated. Pulse-current charging is a technique developed to prevent the growth of dendritic zinc when charging the battery (Wang et al., 2014, Zhu et al., 2016, Zhang et al., 2019b). While most research concentrates on the improvement of material and battery design, management and monitoring tools for a ZAB have received less attention and clearly represent an incomplete field of study. Management systems can improve the performance of batteries and protect batteries from inappropriate operations (Pop et al., 2008, Zelger et al., 2019). For instance, when ZABs are charged with excessive voltage, both the detrimental dendritic formation as well as hydrogen evolution reaction (HER) occur. Management systems require precise prediction of dynamic behavior and state of the battery, which is typically achieved via modeling. Some types of modeling have been used in ZAB researches. As such, theoretical continuum models have been carried out and used to examine phenomena occurring inside the battery (Wang et al., 2014, Stamm et al., 2017, Schmitt et al., 2019).

The dynamic behavior of a battery focuses on the discharge current and voltage of the battery, which is considered as being the input and output of the system. Thus, empirical modeling has regularly been preferred, due to its simplicity in computation. For example, an equivalent circuit model (ECM) is the most commonly used empirical model in the investigation of battery dynamics. An ECM describes the dynamic behavior of the battery via simple electrical elements that are comparable to the electrochemical characteristics of the battery (Krewer et al., 2018). This type of model has been used in various batteries, such as LIBs (Samadani et al., 2015, Pei et al., 2018, Madani et al., 2019), Zn-Ni batteries (Li et al., 2014, Yao et al., 2017) or lead-acid batteries (Jantharamin and Zhang, 2008). However, only a few works on a ZAB have utilized ECM to predict battery behavior (Şanal et al., 2015), although electrochemical impedance spectroscopy (EIS) has frequently been applied. For a more empirical approach, a state space model has been developed. This model is normally used with both state and parameter estimation algorithms (Krewer et al., 2018).

Although the dynamic behavior of a ZAB is strongly nonlinear, previous studies have centered on the development of empirical linear models. Nonlinear behavior can be realized by invoking first principles-based models or nonlinear empirical modeling techniques. However, it is acknowledged that nonlinear models are less flexible than comparable linear models and the mathematical tools are lacking for nonlinear systems. Alternatively, nonlinear behavior can be captured via an LPV model, which approximates a nonlinear system with high accuracy (Mohammadpour Velni and Scherer, 2012, Schoukens and Tóth, 2018).

LPV models have been applied in various systems, but only a few works have employed this technique in a battery system (Hu and Yurkovich, 2011, Hu and Yurkovich, 2012, Remmlinger et al., 2013). For instance, a subspace method has been introduced for the identification of an LPV battery model for LIBs, where state of charge (SOC) estimation was done using LPV techniques (Hu and Yurkovich, 2011, Hu and Yurkovich, 2012). Results indicated that this technique provides good and stable performance and is easy to tune compared with other algorithms. In another example, LPV modeling has been used to assist in monitoring the state of health (SOH) for a LIB cell (Remmlinger et al., 2013). This model combined with a nonlinear Kalman filter proved capable of online estimating SOC and SOH. The model was validated via measurement data and provided good validation results.

Herein, an LPV model is developed to account for all nonlinearities within a ZAB directly. Nonlinear ZAB characteristics, therefore, are empirically exhibited in the form of change in parameters of the underlying LTI models, with respect to a reference condition. The LPV model is seen to combine the varying parameters into a single model. Besides, it proved capable of effectively predicting battery nonlinear behavior over a wide range of conditions. Furthermore, the LPV model adopted the linear characteristic of the LTI model. Hence, it possessed considerable robustness. This work proposes to use LPV models for predicting the input-output discharge behavior of a ZAB. Data employed in this scheme were obtained from an in-house refuellable ZAB (Lao-atiman et al., 2019b). The underlying linear models obtained at different conditions are then combined into a single LPV model, where the discharge current level is used as a scheduling parameter. As regards validation, the developed LPV model is used to predict various sets of response data. A nonlinear model was further implemented to compare results between the nonlinear and LPV model.

5.4 Battery Description and experimental data

Battery response data previously published by Lao-atiman et al. (Lao-atiman et al., 2019b) have been implemented for parameter estimation and model validation. As shown in Fig. 5.1, such data were acquired from a tubular refuellable ZAB, designed in-house. The cylindrical structure of the cell was made of stainless-steel mesh. The active material for the anode was 6 g of 20 mesh Zn pellets packed into another stainless-steel mesh tube. The cathode current collector was comprised of nickel (Ni) foam coated with ORR catalyst (MnO_2) and a gas diffusion layer. The cell contained 8 M KOH aqueous solution as the electrolyte.

After battery fabrication, both the discharge current and voltage of the battery were measured by BA500 battery analyzer (Battery Metric, Toronto, ON, Canada). Sampling time was 1 second. Then, the discharge current setpoint was set.

Subsequently, the battery was forced to discharge in accordance with the setpoint. Next, both the actual discharge current and voltage were measured and recorded along with the selected sampling time. The set of data used for model identification contained a time-series of discharge current (as input) and discharge voltage (as output). The discharge voltage was measured at the specified discharge current. Step response data, including the discharging current steps from 0 to 100 mA, 0 to 450 mA, and 0 to 900 mA, were used to identify linear models. With respect to validation, response data with increased variability and complexity were examined. All data used in this work, including data names and descriptions, are summarized in Table 5.2. Graphical representation for each data set can be found in Figs. B1-B10 in the supplementary file.

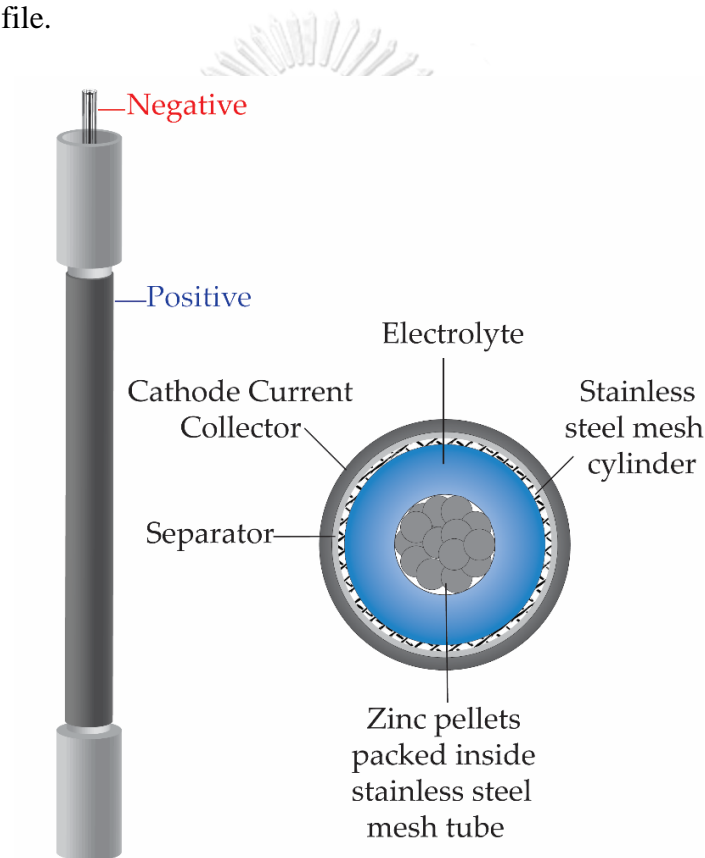


Figure 5.1 Schematic diagram of experimental ZAB.

5.5 Methodology

The LPV model is a collection of LTI state-space models whose parameters vary, as a function of scheduling parameters. In the case of a ZAB, discharge current is considered to be the scheduling variable, which is available for measurement. More importantly, the discharge current is the signal which directly enables modifications of a ZAB's dynamic behavior to occur.

In terms of methodology, this approach follows a classical operation mode: namely, a certain number of points in the scheduling space were selected. Thus, an

LTI model was constructed and assigned to each point, representing the dynamics in the local vicinity of that point. The dynamics at scheduling locations in between the specified grid points were acquired by interpolation of LTI models at neighboring points.

In addition, a nonlinear model was constructed to benchmark the LPV model in terms of precision and complexity of the prediction.

Table 5.2 Summary of experimental data used for identification and validation of models

Data name	Description	Description
0T100	Current step from 0 to 100 mA	StepDischarge.xlsx (Lao-atiman et al., 2019b) Sheet: 100STEP0-100-0
100T0	Current step from 100 to 0 mA	StepDischarge.xlsx (Lao-atiman et al., 2019b) Sheet: 100STEP0-100-0
0T450	Current step from 0 to 450 mA	StepDischarge.xlsx (Lao-atiman et al., 2019b) Sheet: 450STEP0-450-0
450T0	Current step from 450 to 0 mA	StepDischarge.xlsx (Lao-atiman et al., 2019b) Sheet: 450STEP0-450-0
0T900	Current step from 0 to 900 mA	StepDischarge.xlsx (Lao-atiman et al., 2019b) Sheet: 900STEP0-900-0
900T0	Current step from 900 to 0 mA	StepDischarge.xlsx (Lao-atiman et al., 2019b) Sheet: 900STEP0-900-0
400T500R	Repeating current step between 400 to 500 mA	StepDischarge.xlsx (Lao-atiman et al., 2019b) Sheet: 100STEP400-500
500T1000R	Repeating current step between 500 to 1000 mA	StepDischarge.xlsx (Lao-atiman et al., 2019b) Sheet: 500STEP500-1000
MULTI	Multiple current step from 0 to 100, 450 and 900 mA	Supplementary.xlsx ^a Sheet: MULTI
VARIOUS	Various current step with random pattern	Supplementary.xlsx ^a Sheet: VARIOUS

^aThe data are located in the supplementary file.

5.5.1 Linear state-space model

The LPV model uses local LTI models: the choice being made here is to represent these models in a discrete domain, taking into account that available data is inherently obtained on a discrete timescale after sampling. Trajectories of a state vector (X) and output vector (Y) are commonly measured and tracked as they move through time. The LTI model, at each local operation point, is expressed as in Eqs. (5.2) and (5.3):

$$X(k+1) = AX(k) + Bu(k) \quad (5.2)$$

$$Y(k) = CX(k) + Du(k) \quad (5.3)$$

where u is an input vector. As for a single-input, single-output case:

$$A \in \mathbb{R}^{n \times n}, B \in \mathbb{R}^{n \times 1}, C \in \mathbb{R}^{1 \times n} \text{ and } D \in \mathbb{R}$$

A , B , C and D matrices are estimated from the experimental data ($Y(k)$, $u(k)$) via least square regression.

In this case, the input and output of the experimental data are discharge current and cell voltage, respectively. For convenience of computation, Y represents the deviation of cell voltage from the OCV (potential loss). Then, u represents the discharge current. This change of coordinate ensures that both Y and u is expressed in the absence of excitation and have a fixed point at 0, according to the LTI model, as shown in Eqs. (5.2) and (5.3).

5.5.2 LPV model

As regards the LPV model, system dynamics are represented as a linear state space model having parameters expressed in terms of functions of r scheduling variables (Lovera et al., 2013). The case of a single-input, single-output system is denoted as follows:

$$A: \mathbb{R}^r \rightarrow \mathbb{R}^{n \times n}, B: \mathbb{R}^r \rightarrow \mathbb{R}^{n \times 1}, C: \mathbb{R}^r \rightarrow \mathbb{R}^{1 \times n} \text{ and } D: \mathbb{R}^r \rightarrow \mathbb{R}$$

The LPV model is a generalization of the LTI structure, building on the principles that dynamic properties vary with respect to the functioning conditions (represented by exogenous or internal signals) or parameters. Explicitly, model parameters are a function of the scheduling vector of parameters p which in turn is time-varying:

$$A = A(p(k)), B = B(p(k)), C = C(p(k)) \text{ and } D = D(p(k)) \quad (5.4)$$

Accordingly, the state space model becomes:

$$X(k+1) = A(p(k))X(k) + B(p(k))u(k) \quad (5.5)$$

$$Y(k) = C(p(k))X(k) + D(p(k))u(k) \quad (5.6)$$

For simplicity of notation, in time, the time dependence of the parameter will be dropped. With respect to ZAB modeling, given the fact that the experiments are

conducted at constant external temperature, it is therefore assumed that the parameters are concentrated in the discharge current.

An important remark related to the particular single-input single-output form is that parametric dependence in both B and C has a certain degree of redundancy, as long as it relates to the input-output gain in Eqs. (5.2) and (5.3) and can lead to non-unicity problems. To solve this issue and simplify Eqs. (5.5) and (5.6), the coefficients of the matrix C are assumed to be time-independent and considered constant through an appropriate change of coordinate leading to the form, as shown in Eqs. (5.7) and (5.8):

$$X(k+1) = A(p)X(k) + B(p)u(k) \quad (5.7)$$

$$Y(k) = CX(k) + D(p)u(k) \quad (5.8)$$

The state space model becomes more useful as the number of parameters are reduced. This form of model can also be interpreted as first-order resistor-capacitor (RC) model, as illustrated in Fig. 5.2.

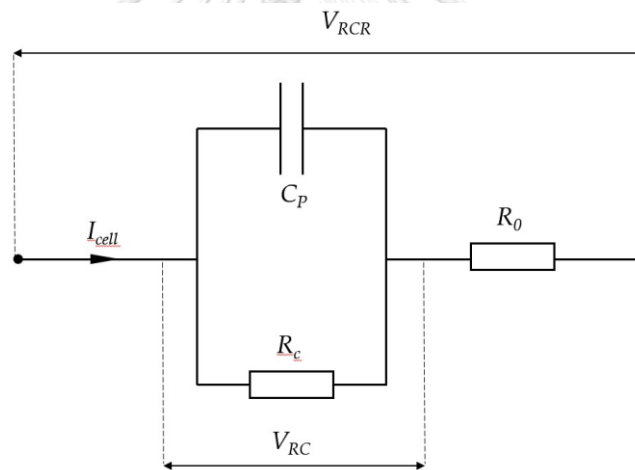


Figure 5.2 Electrical equivalent circuit diagram of potential loss of battery: first-order RC model

In the circuit, there is a resistor–capacitor (RC) loop (R_c and C_P) connected with another resistor (R_0). In a comparison between the state space model and the equivalent circuit, it was found that the input, u , is equivalent to the discharge current (I_{cell}). Output, Y , is equivalent to V_{RCR} which is potential loss of battery. The state variable, X , can be interpreted as the potential drop across the RC loop (V_{RC}). Parameter A is equivalent to $-T_s/R_c C_P$. Parameters B and D are T_s/C_P and R_0 , respectively. Parameter C equals to 1 which agrees with the assumption previously made. The state space model can be rewritten as ECM, as follows:

$$V_{RC}(k+1) = \left(1 - \frac{T_s}{R_c C_P}\right) V_{RC}(k) + \frac{T_s}{C_P} I_{cell}(k) \quad (5.9)$$

$$V_{RCR}(k) = V_{RC}(k) + R_0 I_{cell}(k) \quad (5.10)$$

For physical interpretation, ECM is normally used for investigating battery behavior via EIS. Herein, the RC loop contributed to potential loss due to the electrochemical reactions: so-called activation overpotential. This overpotential is the potential required to drive the reactions viz. Zn oxidation and ORR for discharging the ZAB. Several researches have suggested that the overpotential strongly depends on the discharge current level and can be theoretically described by the Butler-Volmer approach (Schröder and Krewer, 2014, Stamm et al., 2017, Lao-atiman et al., 2019a). Next, R_0 contributed to the potential loss to internal resistance: so-called ohmic overpotential. This loss increases proportionally with the current drawn from the battery.

As regards battery modeling, scheduling parameters can be chosen from various parameters. In this work, input-output behavior depends on the level of discharge current. Therefore, the sets of parameters used for constructing the LPV model were obtained from the data having different discharge current conditions.

As regards model parameters, the correlation between the model parameters (coefficients of the matrices in Eqs. (5.7) and (5.8)) and discharge current was estimated via such forms as quadratic polynomial or exponential function:

$$\text{Quadratic Polynomial:} \quad \xi = \mu_1 p^2 + \mu_2 p + \mu_3 \quad (5.11)$$

$$\text{Two-term Exponential:} \quad \xi = \alpha e^{\beta p} + \gamma e^{\delta p} \quad (5.12)$$

where ξ denotes the estimated parameter. μ_1 , μ_2 and μ_3 are the parameters acquired from the curve fitting. α , β , γ and δ are the coefficients of the exponential function obtained from the curve fitting.

The parameters of the linear model from the previous section were used to build the correlations with respect to after-stepping current levels, as scheduling parameters. From the experimental data, the conditions of current levels used for constructing the correlations were 0, 100, 450, and 900 mA. The correlations of parameters A , B and C were estimated by a second-order polynomial function. For parameter C , a linear function was used. An exponential function was used to fit the correlation of parameter BC . Correlations for parameters of the LPV model are provided in Table B4 of the supplementary file.

5.5.3 Nonlinear model

The nonlinear model used for comparison in this work was Hammerstein-Wiener (HW) model. The HW model is a block-oriented model which contains nonlinear functions and a linear block separately (Wills et al., 2013, Shokrollahi et al., 2018). As shown in Fig. 5.3, the HW model is depicted as a series of three connected blocks.

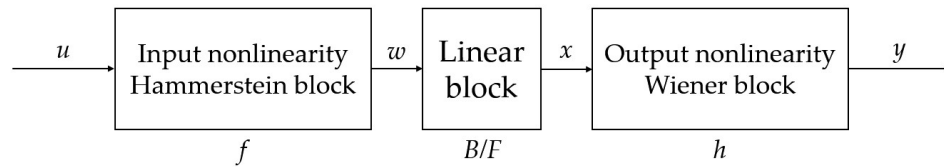


Figure 5.3 Block diagram of Hammerstein-Wiener model

The first and last blocks are nonlinear functions which transform the input and output signals, respectively. The second block located between the two nonlinear blocks is the linear block. The first nonlinear block is called “Hammerstein block” and is represented by function f , as shown in Eq. (5.13). This nonlinear block transforms the input signal before entering the linear block:

$$w(k) = f[u(k)] \quad (5.13)$$

where $u(k)$ and $w(k)$ are the input and output of nonlinear block f , respectively.

The next block is the linear block and is denoted by B/F . The linear block is derived from an output-error (OE) model and transfers input $w(k)$ to output $x(k)$, as in Eq. (14):

$$x(k) = (B/F)w(k-n_k) \quad (5.14)$$

where n_k is an input delay. B and F are polynomials in a linear output-error model with respect to the delay operator z^{-1} and defined, as follows in Eqs. (5.15) and (5.16):

$$B(z) = b_1 + b_2z^{-1} + \dots + b_{n_b}z^{-n_b+1} \text{ for } B \text{ order} = n_b \quad (5.15)$$

$$F(z) = 1 + f_1z^{-1} + \dots + f_{n_f}z^{-n_f} \text{ for } F \text{ order} = n_f \quad (5.16)$$

The last nonlinear block h is called “Wiener block”. This block transforms the output signal of the linear block, as in Eq. (5.17):

$$y(k) = h[x(k)] \quad (5.17)$$

where $y(k)$ is the output of the nonlinear block h and the output of HW model. The output of the HW model $y(k)$ can be rewritten as a function of $u(k)$, as in Eq. (5.18):

$$Y(k) = h[(B/F)f[u(k)]] \quad (5.18)$$

For this study, only the Hammerstein nonlinear block was used. The HW model, therefore, is reduced to Hammerstein model.

In contrast with the linear model, the nonlinear models were identified from the data with multiple steps under varying conditions. In Table 5.3, model identification data for all developed models are tabulated.

Table 5.3 Summary of conditions for identification of the model used in this work

Model name	Model type	Identification data ^a	Identifying condition
SS0T100A	Linear model	0T100A	First-order model with feedthrough and 1 sec sampling time Number of states (n) = 1
SS0T100B	Linear model	0T100B	
SS0T100C	Linear model	0T100C	
SS100T0A	Linear model	100T0A	
SS100T0B	Linear model	100T0B	
SS100T0C	Linear model	100T0C	
SS0T450A	Linear model	0T450A	
SS0T450B	Linear model	0T450B	
SS0T450C	Linear model	0T450C	
SS450T0A	Linear model	450T0A	
SS450T0B	Linear model	450T0B	
SS450T0C	Linear model	450T0C	
SS0T900A	Linear model	0T900A	
SS0T900B	Linear model	0T900B	
SS0T900C	Linear model	0T900C	
SS900T0A	Linear model	900T0A	
SS900T0B	Linear model	900T0B	
SS900T0C	Linear model	900T0C	
LPV	LPV model	Linear models: SS0T100A, SS0T100B, SS0T100C, SS100T0A, SS100T0B, SS100T0C, SS0T450A, SS0T450B, SS0T450C, SS450T0A, SS450T0B, SS450T0C, SS0T900A, SS0T900B, SS0T900C, SS900T0A, SS900T0B, SS900T0C	Curve fitting: A: second-order polynomial B: second-order polynomial C: second-order polynomial D: linear function BC: two-term exponential
Nonlinear A	Nonlinear HW model	MULTI	Input nonlinearity: third-order polynomial Output nonlinearity: unit gain (absent) OE model order: $n_b = 2, n_f = 1, n_k = 0$
Nonlinear B	Nonlinear HW model	VARIOUS	Input nonlinearity: third-order polynomial Output nonlinearity: unit gain (absent) OE model order: $n_b = 2, n_f = 1, n_k = 0$

^a The data location is tabulated in Table B1 in supplementary file.

5.6 Results and Discussion

In Table B2 of the supplementary file, the LTI model parameters are shown. From these LTI models, the LPV model was developed. The correlations of the model parameters were constructed via curve fitting. The nonlinear models were identified from the multiple step and various step data (Lao-atiman et al., 2019b). A third-order polynomial function was selected for the Hammerstein block. The model order of the OE model was $n_b = 2$, $n_f = 1$ and $n_k = 0$. In Table 5.3, the identifying conditions are summarized. In addition, parameter values estimated in this work are provided in Table B3 of the supplementary file.

In the following sections, the graphical highlights of validation and comparison results are displayed. Full graphical results of the linear model and the LPV model are shown in Figs. B11 and B12 of the supplementary file, respectively. In Table B5 of the supplementary file, the fit percentage values of the prediction results are tabulated.

5.6.1 Linear state-space model

The linear models were identified as first-order state space models. The number of states (n) was 1. Model parameters were estimated using one set of experimental data. To validate the models, different sets of experimental data were applied. In Fig. 5.4, validation results for the linear models are shown. Fig. 5.4a shows the validation results with the same conditions (current steps) as used in the estimation (0 to 100 mA). Results demonstrate that the models were able to accurately predict individual response data.

Fig. 5.4b highlights the results when the models were validated at different conditions (different current steps). It was found that the models could predict accurately only the data used to identify the models' parameters. The models poorly estimated other data. The gain of the models significantly deviated. Results suggested that the linear model was only accurate locally.

Fig. 5.4c provides an example by displaying a comparison between model predictions and measured data in the context of multiple step current discharges. Results clarified the dependency between gain and current level. Thus, from the results shown, the linear models were able to accurately predict the responses if the current level corresponded with the models. Nevertheless, most of the battery data contain more than one current level. Consequently, the linear model cannot be applied in most cases. In this situation, the LPV model proved to offer the level of flexibility necessary for adapting to the LTI responses.

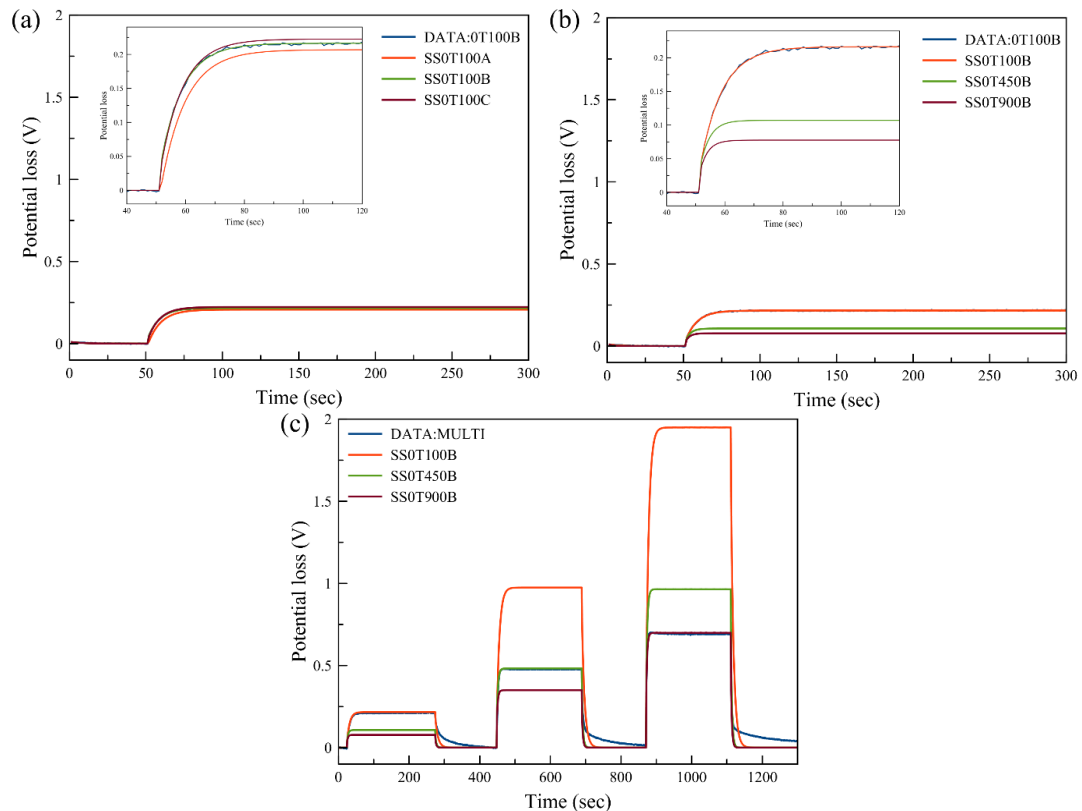


Figure 5.4 Comparison of response between measured data (blue lines) and predicted data from linear models: a) Matching conditions with current step from 0 to 100 mA b) Different conditions with current step from 0 to 100 mA and c) Multiple current steps from 0 to 100, 450 and 900 mA

5.6.2 LPV model

As previously stated, the LPV model was developed from linear state space models. Consequently, the models with different current level conditions were combined into one model. For this model, the conditions of current level included: 0 mA, 100 mA, 450 mA and 900 mA. Each condition, with respect to the final current level, provided a different set of model parameters. For instance, the state space model estimated from the current step of 0 to 100 mA provided the values of model parameters at the 100 mA current level. At each current level, three data sets of the same condition were used. For validation, the LPV model was then used to predict the various response data.

As shown in Fig. 5.5, correlations between model parameters and current levels were fitted in accordance with Eqs. (5.5) and (5.6). In Figs. 5.5a and 5.5b, the correlation of model parameters A and D was able to be fitted using a second-order polynomial function as well as a linear function, respectively. Parameters A and D showed consistent trends with respect to current levels. However, parameters B and C were found to be inconsistent in their trends. Moreover, the values of B and C

contained both positive and negative values which can cause discrepancy in prediction. To address this issue, C was fixed at $C=1$, whilst B and C were multiplied together, resulting in the parameter BC which proved to be more consistent, as described in Eqs. (5.7) and (5.8). Accordingly, the LPV model becomes:

$$X(k+1) = A(p)X(k) + BC(p)u(k) \quad (5.19)$$

$$Y(k) = X(k) + D(p)u(k) \quad (5.20)$$

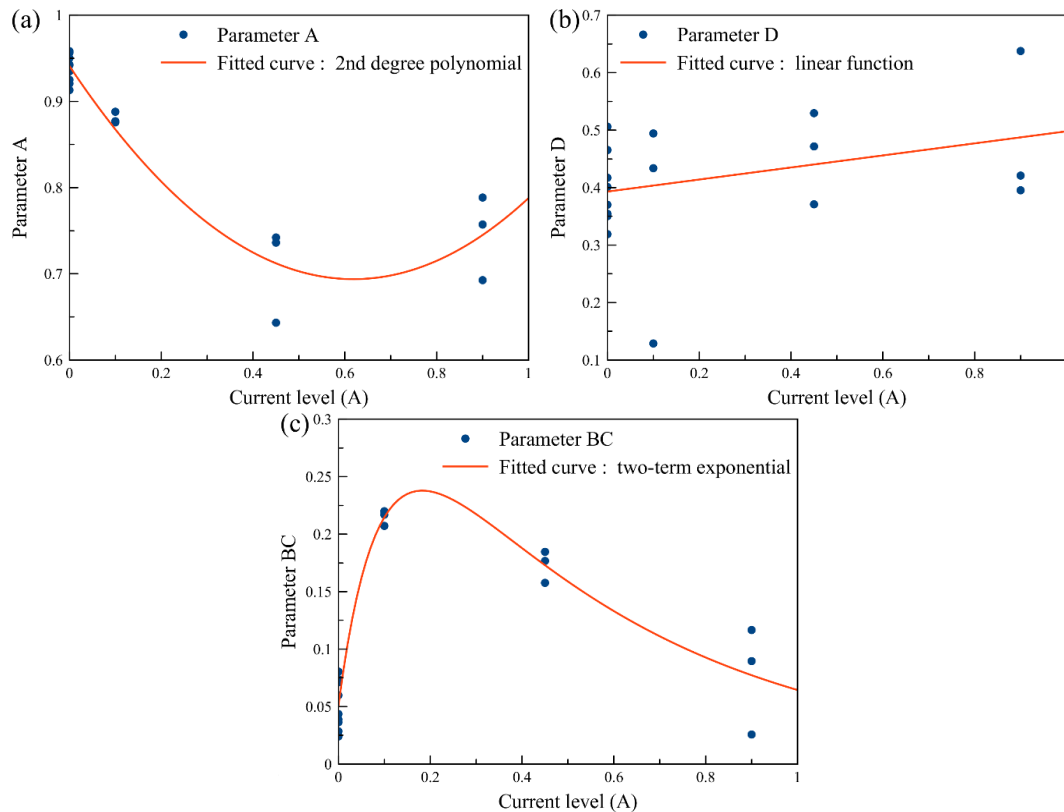


Figure 5.5 Correlations of state space model parameters as functions of current levels: a) Parameter A b) Parameter D and c) Parameter BC

The trend of parameter BC exhibited good consistency and was able to be fitted via a two-term exponential function, as shown in Fig. 5.5c. For physical interpretation, Eqs. (5.19) and (5.20) are equivalent to the ECM as expressed in Eqs. (5.9) and (5.10). Parameter D was expressed as a linear function having a small slope. This indicated that the discharge current level had little effect on R_0 . Parameters A and BC were fitted with a polynomial and exponential function, respectively. As the RC loop represented the activation loss, these correlations agreed with the nonlinear trend of the activation loss.

As regards validation, the developed LPV model was used to predict the same response data as used previously in section 5.1. A comparison of the fit percentage between various model predictions is shown in Fig. 5.6. As for the single step

responses (0T100A and 0T900A), results demonstrated good agreement between measured data and predicted data. Compared with the linear model, however, the LPV model proved to be slightly less accurate due to the error in correlation fitting. Yet, the LPV model performed much better globally because the models used for constructing this LPV model were estimated from data measured directly. In addition to the LPV model, two nonlinear models, nonlinear A and nonlinear B (Table 5.3), were identified and compared for response prediction. Results showed that the LPV model performed better than the nonlinear models in this case. The nonlinear models, identified from the data, were seen to have high complexity. Thereby, the models were found to be less robust (especially nonlinear model B).

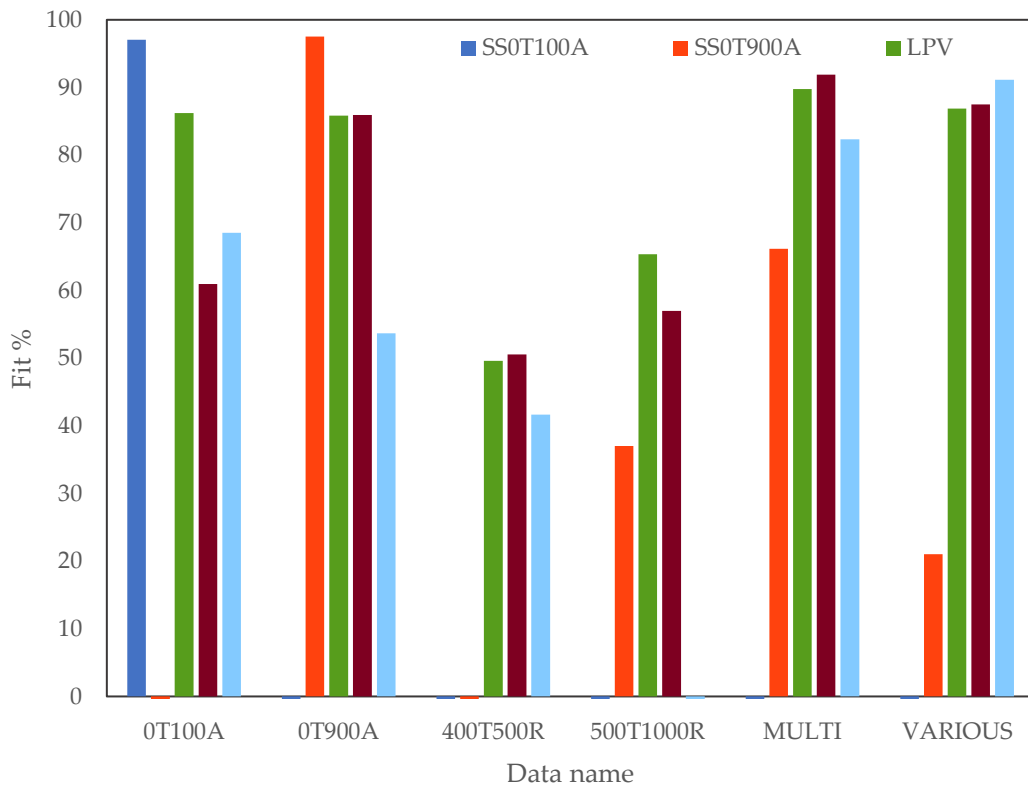


Figure 5.6 Comparison of fit percentage of model prediction between various models and data. Fit % indicates how well the model prediction fits the estimation data and expressed as: $100 \left(1 - \frac{\|y-\hat{y}\|}{\|y-\text{mean}(y)\|} \right)$.

As regards multiple step responses (MULTI), prediction results of the multiple step responses are displayed in Fig. 5.7a. Results highlighted the benefit of the LPV model revealing that the LPV model was able to predict multiple step responses with acceptable agreement. In comparison with the linear model, the LPV model confirmed improvement in prediction. In addition, when the current level changed, the

LPV model was able to predict cell voltage more accurately than the linear model. The gain of the LPV model prediction was able to adapt to current level change. The LPV model proved to be comparable with that of the nonlinear model identified from the matching data (nonlinear A). However, the nonlinear model identified from the other condition (nonlinear B) indicated less accurate prediction.

For validation purposes, the LPV model was tested further, using the different sets of data that had not been used for estimation of the coefficients in the underlying LTI models. The measured data with the repeating step currents: 400 to 500 mA (400T500R) and 500 to 1000 mA (500T1000R) were used for validation. A comparison of the fit percentages found that all the proposed models including the LPV model and nonlinear models were less accurate than the other data sets in predicting the responses. As shown in Fig. S12, the response comparison revealed two limitations of the LPV model: the effect of SOC and the input range of the underlying LTI models.

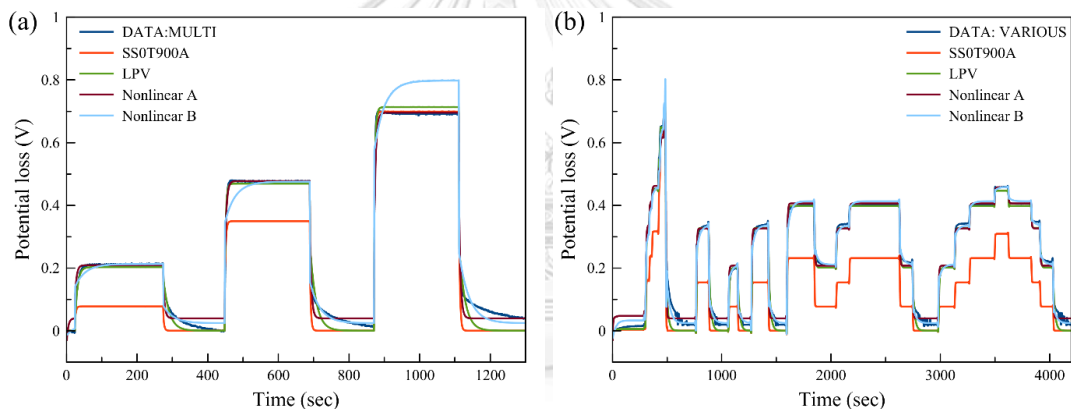


Figure 5.7. Comparison of response between measured data (dark blue lines), predicted data from linear model (red line), LPV model (green line) and nonlinear models: a) Multiple current steps from 0 to 100, 450 and 900 mA and b) Various current steps

Regarding the effect of SOC, the error of prediction increased as time passed because cell voltage is also a function of SOC (Larsson et al., 2017). As the battery discharged over time, cell voltage dropped because of the decrease in SOC. However, in this model, the effect of SOC on cell voltage was not considered. Another limitation shown is regarding the input range of the underlying LTI model. For instance, the upper bound of the current level of the underlying LTI models was 900 mA. For the current level higher than 900 mA, the correlation of the model parameters was found to be incorrect; less accurate values were obtained from extrapolation. Thus, this indicated that the LPV model was not precise in predicting conditions which are out of the input range of the underlying LTI models.

In Fig. 5.7b, prediction results of the various step responses (VARIOUS) are displayed, verifying the models against more complicated data. Limitation of the model appeared the same as in a previous test where cell voltage is dependent on SOC. Nonetheless, the LPV model exhibited superior performance when compared with the linear model and its performance was comparable to that of the nonlinear model. This result revealed the feasibility of using the LPV model. The LPV approach sets out to prove its significance as a modelling tool for the nonlinear behaviour of a ZAB. Herein, the discharge current level is demonstrated as the effective scheduling parameter for predicting the nonlinear behaviour of a ZAB. For some large-scale refuellable ZABs, the influence of SOC is less concerned. Hence, the management system having only discharge current scheduling might be viable over a wide range of operations. To improve the LPV model, the model may have to be developed further by including other scheduling parameters such as SOC or temperature. Moreover, it might be feasible to study the LPV model in a rechargeable ZAB, as the charging process of this battery also adopts the nonlinear characteristic.

5.7 Conclusion

In this work, an LPV model was developed to predict the nonlinear dynamic behavior of a ZAB. LTI models were used as the basis to construct the LPV model. The experimental data acquired from an in-house designed tubular refuellable ZAB were used for identification purposes and validation. By comparing model accuracy based on normalized root mean square error, results showed that the linear model, identified at each local point, was able to predict the behavior of a ZAB but only at the local vicinity of that point. However, it was unable to capture the nonlinear behavior of the ZAB where the gain intensely varied with the discharge current levels. In contrast, the LPV model could well predict battery response. Further, the LPV model was found to be more robust than two other nonlinear models. The LPV model sets out to prove its worth as a dynamic modeling approach for a ZAB.

CHAPTER 6

Charge-discharge Behavior Prediction and State of Charge estimation for a Tri-electrode Zinc-air Flow Battery Using Linear Parameter-varying Model integrated with Extended Kalman Filter

6.1 Preface

This manuscript is an unpublished paper, but it is prepared to publish soon. This paper is the last part of this dissertation which is battery state estimation.

6.2 Abstract

This work intended to use the linear parameter varying (LPV) model to predict the dynamic behavior of tri-electrode zinc-air flow battery (ZAFB) and to estimate the state of charge (SOC) of the battery by integrating with an extended Kalman filter (EKF). The battery response data used to identify the model was measured from the laboratory-made tri-electrode ZAFB. The used data included charge and discharge step response at various current levels and SOC. The LPV model was established from multiple linear time-invariant (LTI) models with battery current and SOC as scheduling parameters. The prediction result of the LPV model is comparable with the linear model for the local accuracy; however, the LPV model outperformed the linear model in the case of global accuracy. The effect of different currents and SOC can be predicted by the developed LPV model. Then, the SOC estimation of ZAFB was investigated by the integration between the developed models and EKF. It was observed that the response data of ZAFB possesses an exceptionally flat profile related to SOC change. The dynamic differentiation only occurred at nearly depleted SOC. For this reason, the estimation of SOC converges to the true value when the SOC is near depletion. The performance of estimation also depends on the initial guess SOC values and the tuning parameters of EKF. By appropriate tuning, the SOC estimation performance of the LPV model combined with EKF is acceptably good. This result revealed the SOC estimation capability of the LPV model integrated with EKF and the feasibility to use it in the BMS.

6.3 Introduction

The energy storage system (ESS) is currently in the research spotlight as it can support the application of renewable energy. Renewable energy such as solar and wind energy has a discontinuous characteristic which contributes to inconsistency in

power generation. ESS is a key technology to neutralize this issue as it can make the system more stable. Zinc-air battery (ZAB) has great potential as ESS for renewable energy due to its high energy density and low cost (Mainar et al., 2018).

In recent years, the technologies related to ZAB have been progressively developed in various aspects. The most concentrated aspect is material development in order to improve the performance and stability of ZAB. For instance, the development of ORR catalyst and air cathode is the main focused topic for tackling the power and stability issues (Alfaruqi et al., 2015, Li et al., 2016, Wu et al., 2019). A zinc electrode has been developed to improve the cyclability of ZAB (Kim et al., 2015a, Kim et al., 2015b, Zhu et al., 2016). Battery design and operation have also been received a lot of attention in the past decade (Pei et al., 2014b, Larsson et al., 2017, Wang et al., 2018). For example, flow electrolyte configuration has been applied with ZAB in order to solve various problems and improve the stability and performance associated with the zinc electrode (Wang et al., 2015a, Dundálek et al., 2017). Tri-electrode configuration is another design developed to avoid the issues related to charging with air electrodes (Hong et al., 2016). However, management and monitoring systems are still underdeveloped. A battery management system (BMS) is widely investigated in battery research as it can improve the safety and operability of the battery (Pop et al., 2008).

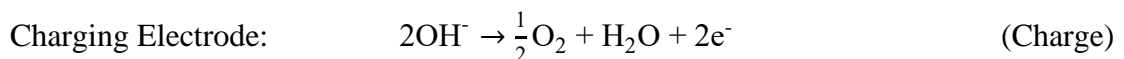
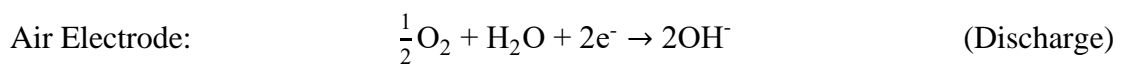
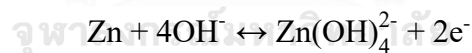
Modeling is one of the research topics involving the development of BMS. Battery modeling can be done in various approaches. For example, the simulation using a theoretical continuum model has been conducted to analyze the phenomena occurring inside the battery (Mao and White, 1992, Deiss et al., 2002, Schröder and Krewer, 2014, Wang et al., 2014). The empirical model has also been studied for using in BMS in various types of battery because this type of model is suitable for online prediction due to its speed and simplicity in the calculation. In recent times, a linear parameter-varying model was proposed to predict the discharge behavior of ZAB (Lao-atiman et al., 2020). It was found that the nonlinear behavior based on the discharge current level of ZAB can be addressed using the proposed technique. One important feature of BMS which must be established is battery state estimation especially SOC estimation (Chang, 2013). As regards SOC estimation, the empirical model has also been used with various adaptive filters such as state observer (Hu and Yurkovich, 2012) or Kalman filter-based estimator (Cai et al., 2017, Wei et al., 2018, Wassiliadis et al., 2018). Nevertheless, studies of empirical models and SOC estimation are still deficient in ZAB research.

This work aims to develop the LPV model and use it to predict the dynamic behavior of tri-electrode zinc-air flow battery (ZAFB). Furthermore, the developed model is integrated with the extended Kalman filter (EKF) state estimator to estimate

the SOC of the battery. The battery data used for dynamic identification and validation were measured from the laboratory-made tri-electrode ZAFB. Linear state-space models identified from different conditions were used to create an LPV model which has discharge current level and SOC as scheduling parameters. After that, the LPV model was tested for validity using battery data from different experimental batches. Then, the developed model was combined with EKF and examined for the ability of SOC estimation. Various scenarios of battery data were compared.

6.4 Description of Tri-electrode ZAFB and experimental data

ZAB is an energy storage device that can store and release energy via an electrochemical reaction. Commonly, a ZAB is comprised of 2 electrodes: zinc electrode (negative) and air electrode (positive). However, the tri-electrode configuration was employed in this work therefore there is one more electrode which is the charging electrode (positive when charging). Potassium hydroxide (KOH) solution with zinc oxide (ZnO) is the most common electrolyte. When the battery discharges, the zinc electrode is connected to the air electrode. Zinc oxidation occurs at the zinc electrode generating electrons and zincate ions as products. When the electrolyte becomes saturated with zincate ions, the ion converts to ZnO. The electrons generated at the zinc electrode transfer to the air electrode and the oxygen reduction reaction (ORR) occurs. When the battery charges, the zinc electrode is connected to the charging electrode. The reduction of zincate ions occurs at the zinc electrode instead. At the charging electrode, the oxygen evolution reaction (OER) takes place. The reactions that occurred are summarized as followed: Zinc Electrode:



For the overall reaction, zinc reacts with oxygen and forms ZnO while discharging. While charging, the reverse reaction proceeds. The theoretical cell potential of ZAB is 1.65 V. Nonetheless, the practical values of open circuit voltage (OCV) are different from the theoretical value. When the battery discharges, the OCV is about 1.4 V. When the battery charges, the OCV is about 1.7 V.

The laboratory made ZAB in this work was designed as a tubular cylinder cell, as shown in Fig. 6.1. This cell configuration was a tri-electrode flow battery that has three electrodes including air cathode, zinc anode and charging electrode. The

cylinder support structure was made of poly vinyl chloride (PVC). The cell is circulated with an electrolyte which is an 8 M potassium hydroxide solution with 0.5 M ZnO. The anode active material is Zn electroplated on the current collector which is nickel (Ni) foam. Cathode active material is oxygen in the air. The ORR occurred at the cathode current collector which is Ni foam coated with catalytic layer and gas diffusion layer. For the charging process, the charging electrode was made of Ni foam.

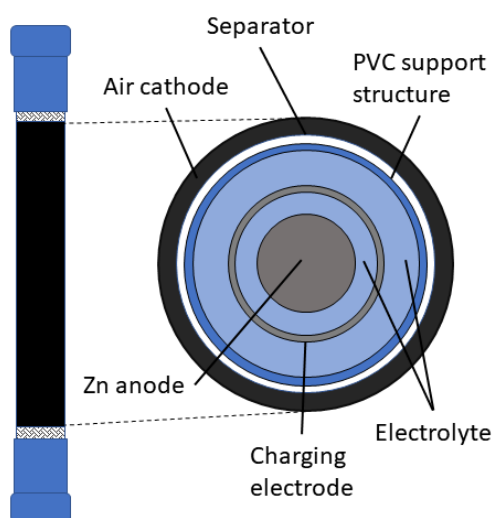


Figure 6.1 Schematic diagram of laboratory-made Tri-electrode ZAFB

To obtain the experimental data, cell voltage and current were measured by battery testing equipment (NEWARE, CT-4008-5V20mA, Neware Technology Ltd., Shenzhen, China). All experiment was conducted at ambient temperature. The circulation rate of electrolyte was maintained at 100 ml/min by a peristaltic pump. The sampling time was 1 s.

The used data are battery response data with current as input and voltage as output. For the dynamic identification, the pattern of the used profile was charge / discharge for 50 mAh alternating with rest for 5 min. The procedure was repeated until the voltage cutoff of 0.5 V was met for discharging or the capacity reached 500 mAh for charging. The applied current values were 500, 1000, 1500 and 2000 mA. For example, the data named DSOC500A has contained discharge steps with a current of 500 mA for 50 mAh alternating with rest for 5 min. As regards model validation, the pattern was more random and was separated between charge and discharge. The data names and descriptions are summarized in table 6.1. More details of the data used can be found in supplementary data in Appendix C.

Table 6.1 list of names and descriptions of data used in this work

Data name	Description
DSOC500A	Discharge step of 500 mA alternating with rest step
DSOC1000A	Discharge step of 1000 mA alternating with rest step
DSOC1500A	Discharge step of 1500 mA alternating with rest step
DSOC2000A	Discharge step of 2000 mA alternating with rest step
MULTI A	Discharge step of multiple current alternating with rest step
MULTI B	Discharge step of multiple current alternating with rest step
CSOC500A	Charge step of 500 mA alternating with rest step
CSOC1000A	Charge step of 1000 mA alternating with rest step
CSOC1500A	Charge step of 1500 mA alternating with rest step
CSOC2000A	Charge step of 2000 mA alternating with rest step
CMULTI	Charge step of multiple current alternating with rest step
COMBINE	Multiple charge-discharge cycle data

6.5 Methodology

In this section, the LPV model and identification procedure are described. In addition, the EKF state estimator is also explained. Regarding the procedure, linear state space models were identified using data with different current levels and SOC. After that, the parameter correlations of the LPV model were created from the set of model parameters identified at different current levels and SOC. As a result, the parameter correlations were functions of the current level and SOC which were scheduling parameters. Then, the LPV model was validated with measured data from a different experimental batch. Subsequently, the LPV model was used with EKF to test for state estimation. Several scenarios of tuning parameter set and assessed data were compared.

6.5.1 LPV Model

LPV model is a time-variant model of which parameters are varied as function of scheduling parameters (p). Herein, LPV model was constructed from a set of state space model. The model was expressed in discrete form as followed:

$$X(k+1) = A(p(k))X(k) + B(p(k))u(k) \quad (6.1)$$

$$Y(k) = C(p(k))X(k) + D(p(k))u(k) \quad (6.2)$$

Where u , X and Y are input vector, state vector and output vector, respectively. A , B , C and D are state matrix, input matrix, output matrix and feed through matrix, respectively.

Herein, this model contains 3 states including V_{RC1} , V_{RC2} and SOC . V_{RC1} and V_{RC2} represent the overpotential of the zinc electrode and counter electrode (air or

charging), respectively. *SOC* represents the state of charge of the battery. *SOC* is included as a state because the model is used with a state estimator to estimate *SOC* in the next part. To make the LPV model more practical, the model was interpreted with an equivalent circuit second-order RC model, as illustrated in Fig.6.2. From the interpretation, the LPV model can be written as followed:

$$\begin{bmatrix} V_{RC1}(k+1) \\ V_{RC2}(k+1) \\ SOC(k+1) \end{bmatrix} = \begin{bmatrix} A_1 & 0 & 0 \\ 0 & A_2 & 0 \\ 0 & 0 & 1 \end{bmatrix} \begin{bmatrix} V_{RC1}(k) \\ V_{RC2}(k) \\ SOC(k) \end{bmatrix} + \begin{bmatrix} B_1 \\ B_2 \\ \frac{\Delta t}{3600 \cdot C_n} \end{bmatrix} I_{cell}(k) \quad (6.3)$$

$$V_{cell}(k) = V_{oc} + [1 \quad 1 \quad 0] \begin{bmatrix} V_{RC1}(k) \\ V_{RC2}(k) \\ SOC(k) \end{bmatrix} + D \cdot I_{cell}(k) \quad (6.4)$$

Where A_1 , A_2 , B_1 , B_2 and D are state space parameters. V_{cell} , V_{oc} and I_{cell} are cell voltage, open circuit voltage and cell current, respectively. Δt and C_n are sampling time and nominal capacity, respectively.

The calculation of *SOC* in Eq. 6.3 is based on the coulomb counting (CC) method. Including of V_{oc} in Eq. 6.4 make the model able to calculate cell voltage, V_{cell} . I_{cell} and *SOC* were also selected as scheduling parameters therefore A_1 , A_2 , B_1 , B_2 and D were functions of I_{cell} and *SOC*:

$$A_1(SOC, I), A_2(SOC, I), B_1(SOC, I), B_2(SOC, I) \text{ and } D(SOC, I)$$

However, there are some arbitrary assumptions that have been made in order to adapt the model with the scenarios of battery data. Firstly, for discharging, when *SOC* decreased, Zn at the electrode is depleted. Therefore, V_{RC1} is affected and V_{RC2} is not affected by *SOC* change. This makes A_2 and B_2 become functions of only the current level for discharging. The next assumption is that the *SOC* effect on the overpotential is less significant for both electrodes when the battery is charged. This assumption makes B_1 and B_2 become functions of the current level for charging. The last assumption made is that the internal resistance of the system does is independent of current (Larsson et al., 2017, Zhong et al., 2021). As interpreted from Fig. 6.2, D is equivalent to R_0 which is related to ohmic resistance. Thus, D is assumed to be a function of only *SOC* for both discharging and charging.

For discharging: $A_2(I)$, $B_2(I)$ and $D(SOC)$

For charging: $B_1(I)$, $B_2(I)$ and $D(SOC)$

Regarding varying model parameters, the correlations between model parameters and scheduling parameters were constructed from the identified model parameters. For instance, the model parameters identified from the discharge step data with a discharge current of 1000 mA and starting *SOC* of 0.5 had their scheduling current level and *SOC* as 1 A and 0.5, respectively. After the correlations were

created, the LPV model was validated with the various dataset including the data obtained from a different batch of the experiment.

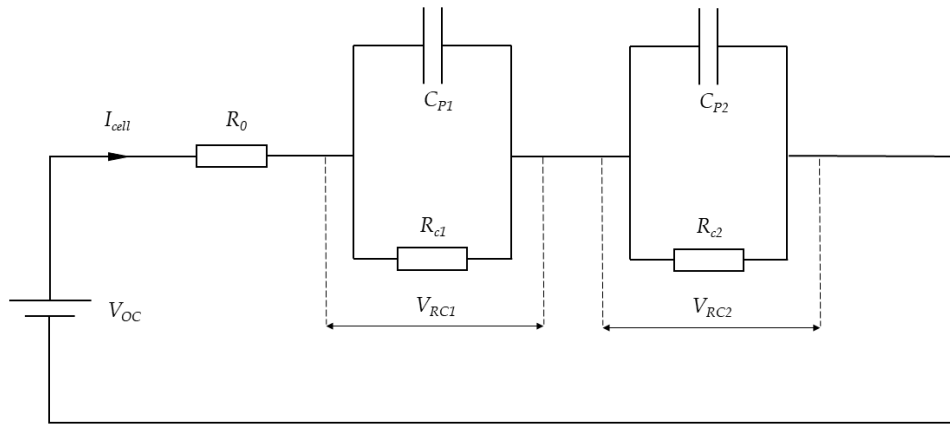


Figure 6.2 Electrical equivalent circuit diagram of battery: second-order RC model

For comparison purpose, the linear state space model was introduced. The expression of the linear model is same as Eqs. (6.3) and (6.4) but the model parameters are not varied with scheduling parameters. The details of model parameters of linear model can be found in supplementary data in Appendix C.

6.5.2 Extended Kalman filter (EKF)

Kalman filter (KF) is a model-based state estimation algorithm that can estimate the inner states of any dynamic system (Murnane and Ghazel). Typically, KF is capable of state estimation for linear systems only. EKF is the extension of KF designed to estimate the state of the nonlinear system (Julier and Uhlmann, 2004).

Regarding this work, EKF is used with the LPV model developed for ZAFB. For simplicity, the battery model can be written as:

$$X_{k+1} = f(X_k, u_k) + q_k^X \quad (6.5)$$

$$Y_k = g(X_k, u_k) + r_k^X \quad (6.6)$$

Where $f(X_k, u_k)$ and $g(X_k, u_k)$ are nonlinear function which is equivalent to Eqs. (6.3) and (6.4) of LPV model, respectively. q_k^X and r_k^X are stochastic noise.

The algorithm of EKF is shown in Fig.6.3 and described in following equations:

Prediction

$$\text{Estimated state prediction: } \hat{X}_{k+1}^- = f(\hat{X}_k^+, u_k) \quad (6.7)$$

$$\text{Estimated covariance prediction: } P_{k+1}^- = \hat{F}_k P_k^+ \hat{F}_k^T + Q^X \quad (6.8)$$

$$\text{Output estimation: } \hat{Y}_k = g(\hat{X}_{k+1}^-, u_k) \quad (6.9)$$

Correction

$$\text{Optimal Kalman gain: } K_k = P_{k+1}^- \hat{G}_k^T (\hat{G}_k P_{k+1}^- \hat{G}_k^T + R^X)^{-1} \quad (6.10)$$

$$\text{State update: } \hat{X}_{k+1}^+ = \hat{X}_{k+1}^- + K_k (Y_k - \hat{Y}_k) \quad (6.11)$$

$$\text{Estimated covariance update: } P_{k+1}^+ = (1 - K_k \hat{G}_k) P_{k+1}^- \quad (6.12)$$

Where variables with superscript + mean that variables are corrected and variables with superscript – means that variables are predicted. \hat{X}_k and \hat{Y}_k represent estimated state and output, respectively. P is estimated covariance. Q and R are covariances of process noise and measurement noise, respectively. \hat{F}_k and \hat{G}_k are Jacobian matrices of state and output functions, respectively, which can be defined as:

$$\hat{F}_k = \frac{\partial f(\hat{X}_k^+, u_k)}{\partial \hat{X}_k^+} \quad (6.13)$$

$$\hat{G}_k = \frac{\partial g(\hat{X}_{k+1}^-, u_k)}{\partial \hat{X}_{k+1}^-} \quad (6.14)$$

Herein, there are 3 tuning parameters of EKF including initial P , Q and R . R is fixed at 5×10^{-3} as obtained from equipment accuracy. P is specified for confidence in values of initial states. Q is specified for confidence in the model. Both P and Q are diagonal matrices containing 3×3 elements which the number of diagonal entries equal to the number of states.

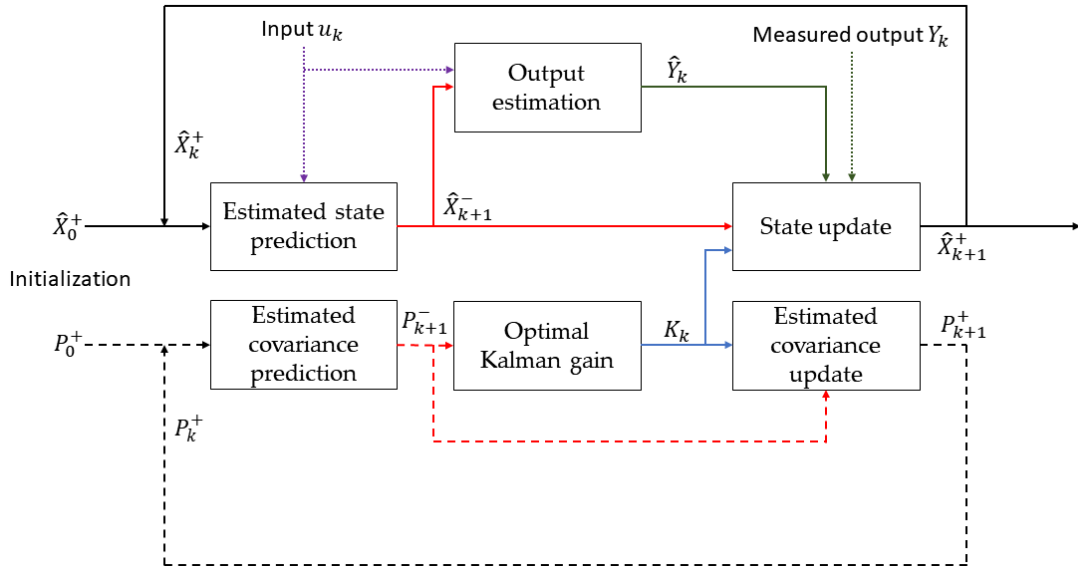


Figure 6.3 Schematic scheme of an EKF algorithm.

Various scenarios were set to test the performance of the estimator. LPV model and linear model were compared. Some tuning parameters are varied. Guess of initial SOC was also studied. Comparison between right guess and wrong guess of initial SOC was conducted.

6.6 Results and Discussion

In this section, there are 2 sub-sections including the LPV modeling and SOC estimation. For the first sub-section, the result of LPV model creation is shown. The correlations of model parameters are included for both charging and discharging. The validation results of the LPV model are also contained. For the second sub-sections, the result of SOC estimation using the developed model integrated with EKF is displayed.

6.6.1 LPV modeling of Tri-electrode ZAFB

As mentioned previously, the LPV model for Tri-electrode ZAFB was developed from the state space model as a based linear time-invariant (LTI) model. The state space parameters of the identified model were fitted to make the correlation with the scheduling parameters. From Eqs. (6.3) and (6.4), there were 5 parameters which have to be made the correlations: A_1 , A_2 , B_1 , B_2 and D . There were 2 scheduling parameters including current level and SOC hence the fitted correlations were surface functions. Nevertheless, there are some model parameters that are functions of only one scheduling parameter according to the assumption made in the previous section. Additionally, V_{OC} has also varied with SOC therefore the correlation of V_{OC} was also made. The list of the function used to fit the correlations for both discharging and charging are tabulated in table 6.2. The graphical correlations of LPV model parameters are illustrated in Figs. 6.4 and 6.5. The correlations of V_{OC} for discharging and charging are shown in Fig. 6.6.

Table 6.2 Function used to fit the model parameter correlations

Fitting function	parameter
Discharging	
$\alpha \exp(\beta(SOC) + \gamma(I_{cell})) + \delta \exp(\varepsilon(I_{cell}) + \theta(SOC)) + \vartheta$	A_1
$\alpha \exp(\beta(SOC) + \gamma(I_{cell})) + \delta \exp(\varepsilon(I_{cell}) + \theta(SOC))$	B_1
$\alpha \exp(\beta(I_{cell})) + \gamma \exp(\delta(I_{cell}))$	A_2, B_2
$\alpha \exp(\beta(SOC)) + \gamma \exp(\delta(SOC))$	D
Charging	
$\mu_{00} + \mu_{10}(SOC) + \mu_{01}(I_{cell}) + \mu_{11}(SOC)(I_{cell}) + \mu_{02}(I_{cell})^2$	$A1, A2$
$\alpha \exp(\beta(I_{cell})) + \gamma \exp(\delta(I_{cell}))$	$B1, B2$
$\alpha \exp(\beta(SOC)) + \gamma \exp(\delta(SOC))$	D
Open Circuit Voltage	
$\alpha \exp(\beta(SOC)) + \gamma \exp(\delta(SOC))$	V_{OC}

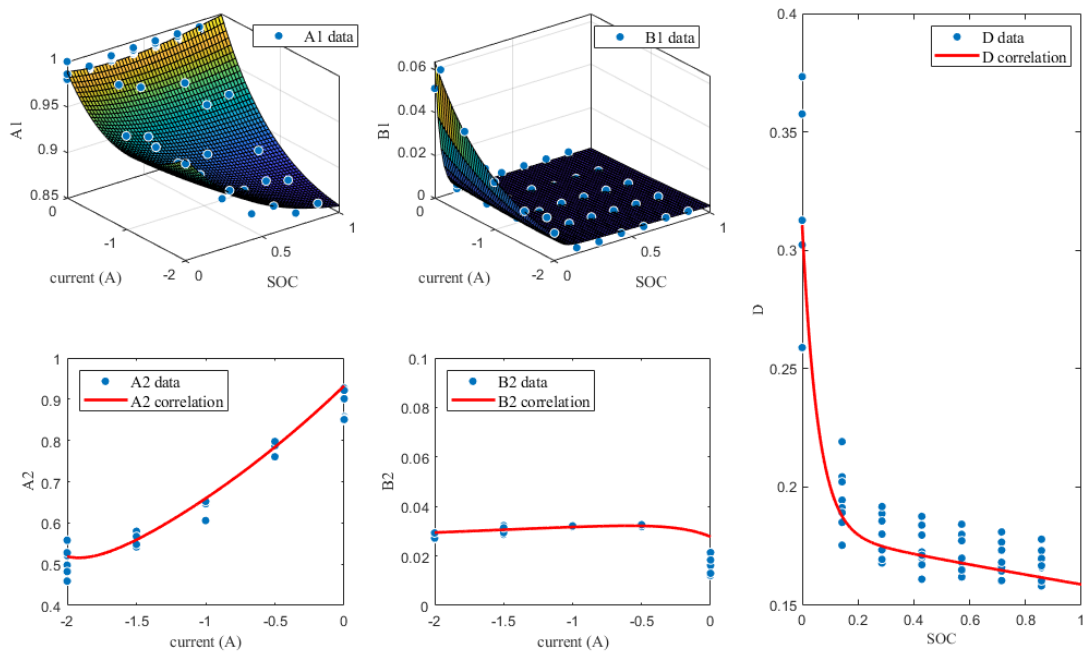


Figure 6.4 Correlations of parameters of LPV model for discharging

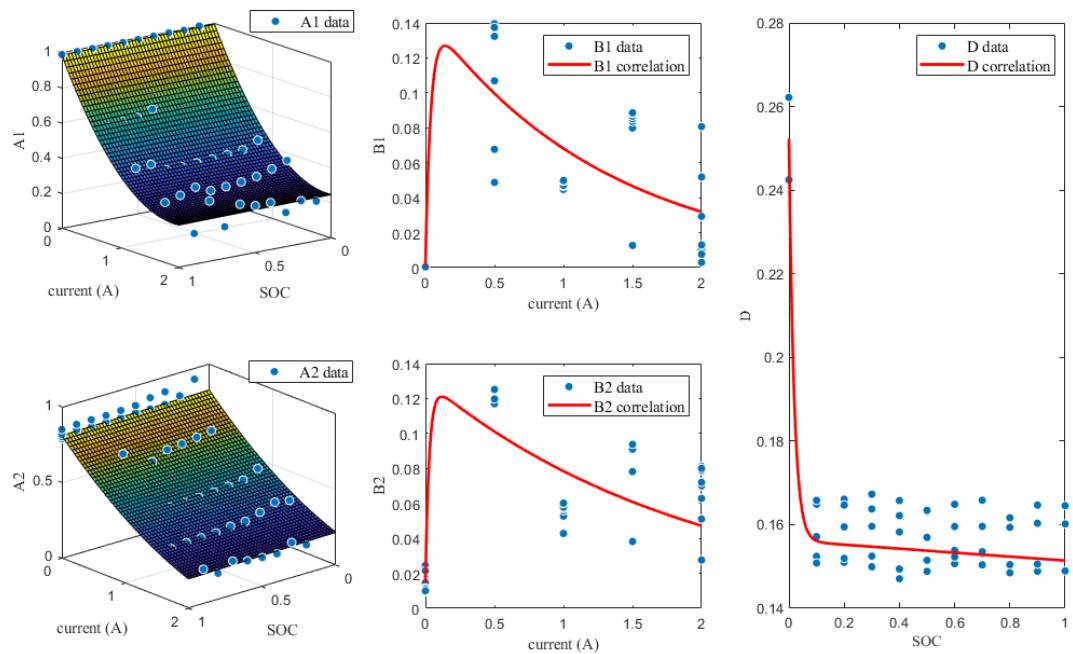


Figure 6.5 Correlations of parameters of LPV model for charging

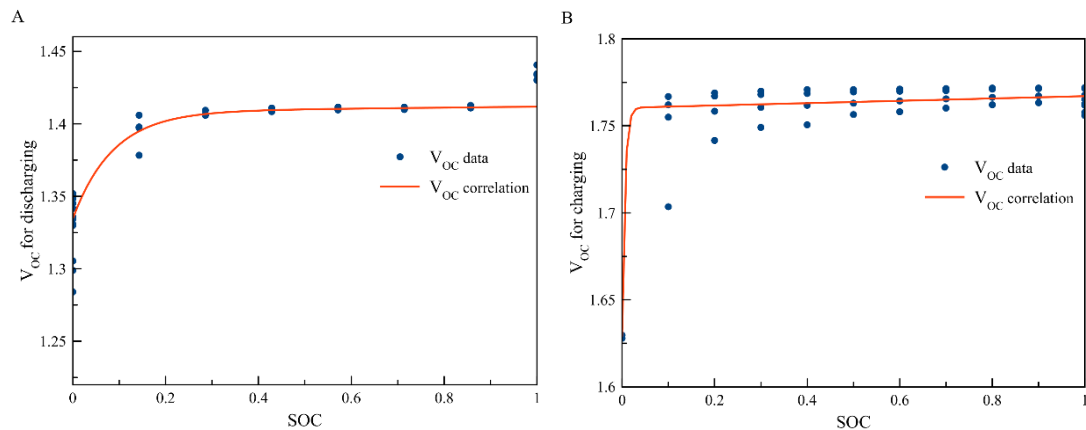


Figure 6.6 Correlations between V_{OC} and SOC for (A) discharging and (B) charging

Regarding validation of the LPV model, the model was tested by predicting various response data. The testing data included the same data used to identify the based LTI model and the data obtained from a different batch of the experiment. The fit percentages of the prediction of the LPV model and linear model are shown in Fig. 6.7. The result revealed that the LPV model was more accurate than the linear model in most cases for both discharging and charging. The main reason was that the effect of SOC change was implemented in the LPV model. This made the LPV model more accurate than the linear model in a wider range of SOC. For further validation, the model was tested with data obtained from a different batch of the experiment including the data named MULTI A and MULTI B for discharging and CMULTI for charging. From Fig. 6.7, it was observed that the fit percentage of LPV model prediction was acceptably high although the data were obtained from a different batch of the experiment. The Graphical prediction results for data MULTI A and CMULTI are displayed in Fig. 6.8. From Fig. 6.8A, for data MULTI A, prediction errors were still observed at some current level. The highest error was occurred at discharging near the battery depletion zone. Besides, the LPV model acceptably performed in predicting the response at the resting zone. As regards data CMULTI, a high error occurred at the beginning range of the predicted response. The error might come from the mismatch between the V_{oc} correlation of the model and the resting voltage of this data. Totally, the LPV model was adequately accurate as it was able to address the effect of different current and SOC changes. This showed the potential of the LPV model to use in SOC estimation with a model-based state estimation algorithm.

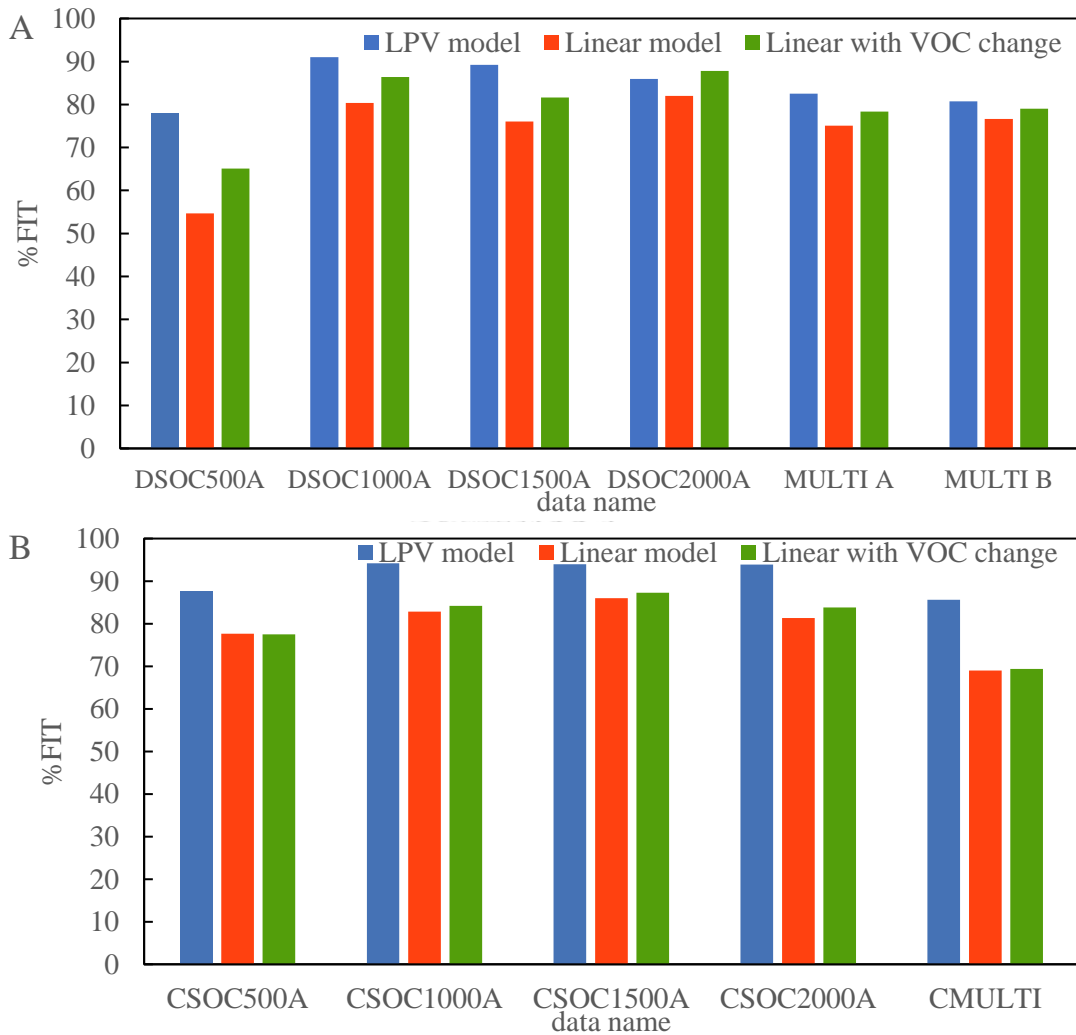


Figure 6.7 Comparison of fit percentage of model prediction between various models and data for (A) discharging and (B) charging.

$$\text{Fit \% expressed as: } 100 \times \left(1 - \frac{\text{mean}|y-\hat{y}|}{\text{mean}|y-\text{mean}(y)} \right).$$

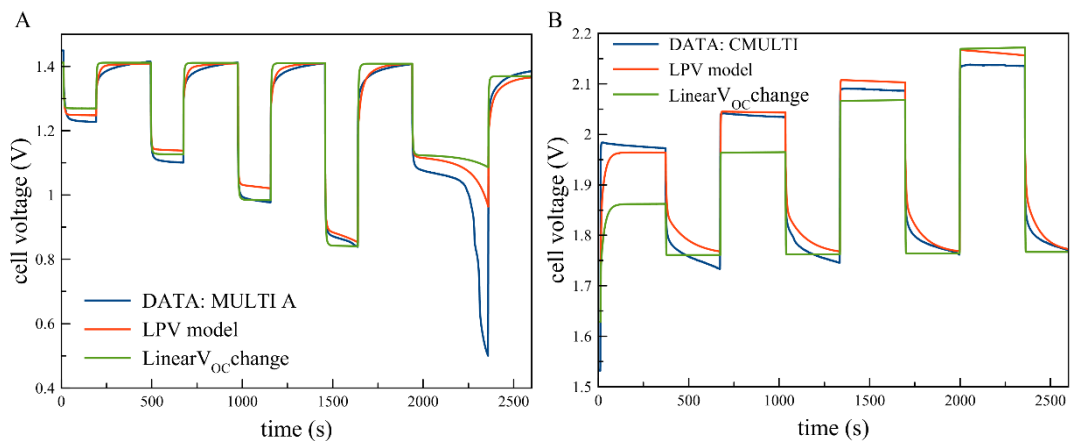


Figure 6.8 Comparison of response between measured data, predicted data from LPV model and linear model: (A) multiple discharge current steps and (B) multiple charge current steps.

6.6.2 SOC estimation

Regarding SOC estimation of Tri-electrode ZAFB, the developed model was integrated with the EKF state estimator. Several scenarios were conducted in order to test the performance of the developed SOC estimator. Some tuning parameters and the correctness of the initial guess were considered.

Table 6.3 Reference values of tuning parameters for EKF

Tuning parameter	Description	Value
P	Initial state estimate covariance	$\begin{bmatrix} P_1 & 0 & 0 \\ 0 & P_2 & 0 \\ 0 & 0 & P_3 \end{bmatrix} = \begin{bmatrix} 10^{-6} & 0 & 0 \\ 0 & 10^{-6} & 0 \\ 0 & 0 & 10^{-6} \end{bmatrix}$
Q	Process noise covariance	$\begin{bmatrix} Q_1 & 0 & 0 \\ 0 & Q_2 & 0 \\ 0 & 0 & Q_3 \end{bmatrix} = \begin{bmatrix} 10^{-6} & 0 & 0 \\ 0 & 10^{-6} & 0 \\ 0 & 0 & 10^{-6} \end{bmatrix}$
R	Measurement noise covariance	5×10^{-3}

6.6.2.1 Parameter tuning

As described in the EKF sub-section, there were 3 tuning parameters including P , Q and R . R was fixed at 5×10^{-3} according to the accuracy of testing equipment. P and Q were left to be tuned. P relates with confidence in initial state values while Q relates with confidence in the used model. High confidence in the initial state and model, which means low P and Q , was selected as a reference scenario. Hence, every element of P and Q were equal to 1×10^{-6} as reference values for tuning parameters. The reference values were tabulated in Table 6.3. Two models used with EKF including the LPV model and linear model with V_{OC} change were also compared.

The reference scenario is depicted in Fig. 6.9. The data used in this scenario was MULTI A. In Fig 6.9A, some errors were still observed in the estimated cell voltage of the reference scenario since the estimator was tuned to trust the model. Nevertheless, the estimated result was closer to the measured data compared to the prediction using the models without EKF, as observed from Fig. 6.8A. As regards SOC estimation, the SOC values estimated by the estimators were approximate to the values from the CC method, as shown in Fig. 6.9B. The CC method is commonly used as a standard method for comparison of SOC estimation; however, this method does not consider the effect of SOC loss such as the low charging efficiency of the battery. Therefore, the CC tends to be erroneous as time pass. Some differences between the CC method and the proposed estimator occurred. For the LPV model, a high difference between the estimated value and CC value was observed in the middle

of the response. Nonetheless, the estimated value converged to the CC value at the end of the response near-zero value because the estimator detected the depletion of the battery from the voltage data. On the other hand, the linear model with V_{OC} change estimated a little different value from the LPV model because V_{OC} is the only parameter related to SOC for the linear model. The linear model estimator showed a higher difference than the LPV model at the end of the response.

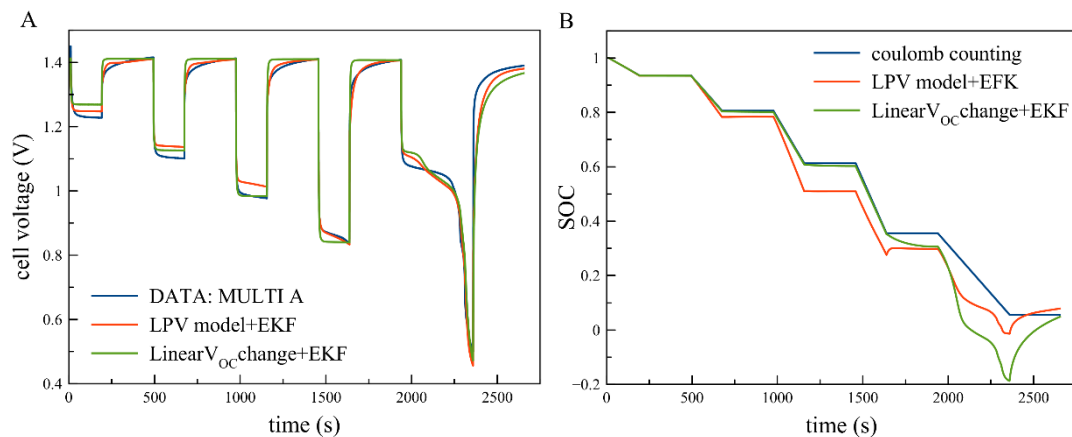


Figure 6.9 Comparison of the reference scenario between response of measure data (MULTI A) and response predicted from the proposed algorithm: (A) cell voltage and (B) SOC

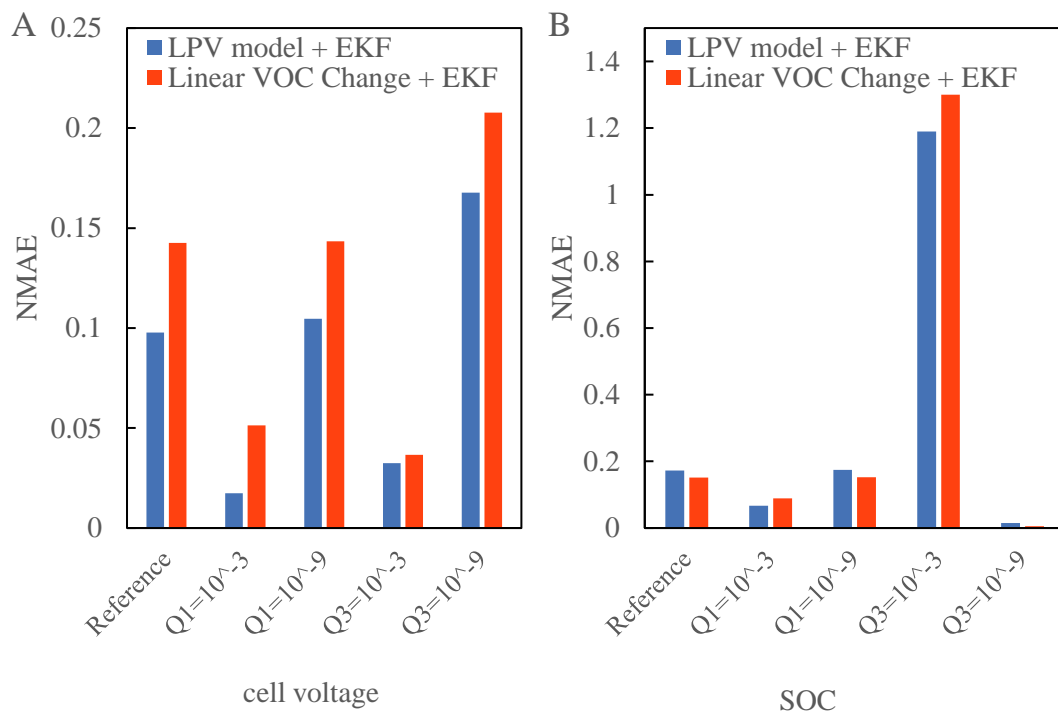


Figure 6.10 Comparison of normalized mean absolute error of estimation between various tuning parameters scenario using data MULTI A: (A) cell voltage and (B) SOC.

To study parameter tuning, some tuning parameters were adjusted and compared. The result was compared by normalized mean absolute error, as shown in Fig. 6.10. Changing confidence in the model for V_{RCI} was tested by tuning covariances Q_1 and Q_3 . At first, Q_1 was changed from 1×10^{-6} to 1×10^{-3} and 1×10^{-9} . The result showed that increasing Q_1 increased the accuracy of cell voltage prediction while the error in SOC estimation was slightly affected. On the contrary, decreasing Q_1 further from 1×10^{-6} provided only an insignificant effect on the error of both cell voltage and SOC because Q_1 of 1×10^{-6} was already a high confidence value. Another scenario tested was adjusting confidence in the model for SOC therefore Q_3 was changed from 1×10^{-6} to 1×10^{-3} and 1×10^{-9} . Increasing Q_3 made the error in SOC estimation greatly increased but the error in voltage estimation is reduced. Conversely, reducing Q_3 made estimated SOC values approach the CC values. However, the error in cell voltage estimation was also increased as if the EKF did not involve. Increasing the confidence in the model for SOC made the estimation result approach the prediction result of the model without EKF.

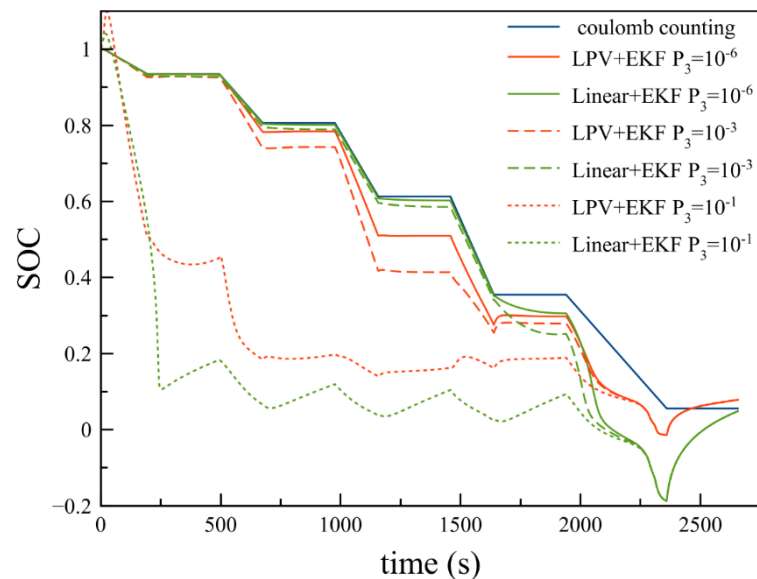


Figure 6.11 Comparison of SOC estimation between different initial covariance P_3 for correct initial guess scenario using data MULTI A.

6.6.2.2 Initial SOC guess

The next test was the correctness of the initial SOC guess. The scenarios were conducted by adjusting the initial guess values into the wrong values and observing the performance of estimation. The confidence in the initial SOC value can be tuned by adjusting the initial covariance P_3 . At first, tuning of P_3 was examined with the correct initial guess scenario using data MULTI A, as shown in Fig. 6.11. The result showed that increasing P_3 from 1×10^{-6} to 1×10^{-3} provided an insignificant difference

in the estimation but adjusting P to a high enough value (1×10^{-1}) made the estimation become false. Nonetheless, SOC estimation in every case compared in Fig. 6.11 converged to the same values near the end of the response as the estimation algorithm was able to detect the depletion of the battery.

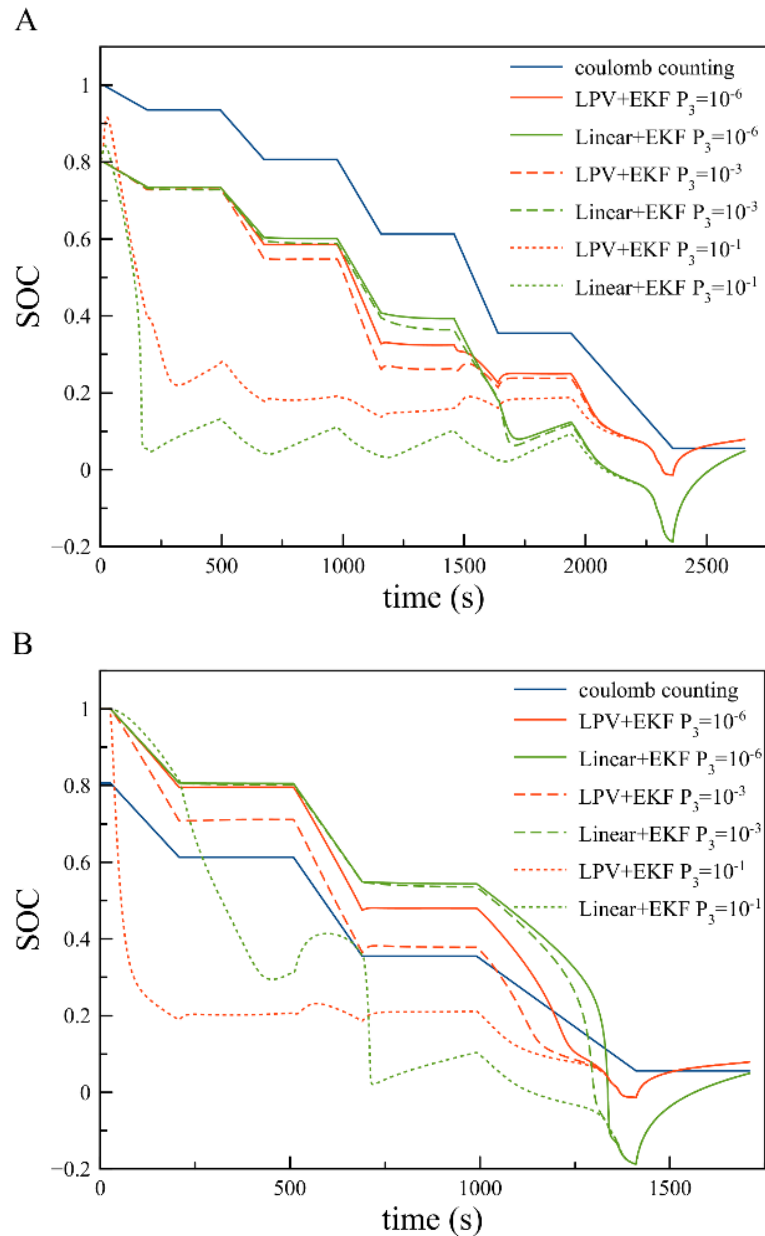


Figure 6.12 Comparison of SOC estimation between different initial covariance P_3 for incorrect initial SOC guess scenario using data MULTI A: (A) guess initial SOC of 0.8 true initial SOC of 1 (B) guess initial SOC of 1 true initial SOC of 0.8064.

To test the performance of SOC estimation of the proposed estimator, incorrect initial guess scenarios were conducted. The data MULTI A was used in this test for discharging, as displayed in Fig. 6.12. Fig. 6.12A showed the SOC estimation

result with initial guess SOC of 0.8 while the true SOC was 1. Covariance P_3 was also varied in the scenario test. It was found that the estimated SOC was converged to the CC value only at the battery depletion zone. In other zones, the estimator could not estimate the expected SOC value even though P_3 was varied from 1×10^{-6} to 1×10^{-1} . The same result occurred in another scenario, as shown in Fig. 6.12B. 6.12B showed the SOC estimation result with initial guess SOC of 1 while the true SOC was 0.8064. The proposed estimator could only track the expected SOC value when SOC reached 0. The reason was that ZAB has extremely flat voltage behavior (Lan et al., 2006, Hosseini et al., 2018b), especially ZAFB. Therefore, the estimator was unable to distinguish the difference in the voltage response except only when SOC approached 0. The battery depletion zone is the only zone that the differentiation of voltage dynamic was obvious for ZAFB.

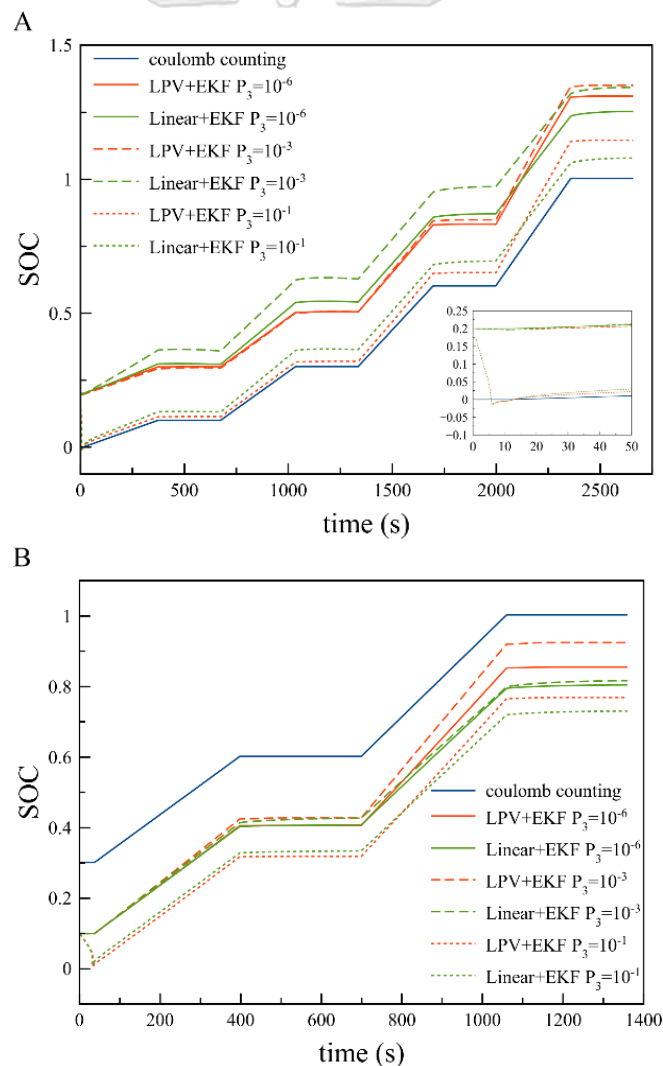


Figure 6.13 Comparison of SOC estimation between different initial covariance P_3 for incorrect initial SOC guess scenario using data CMULTI: (A) guess initial SOC of 0.2 true initial SOC of 0 (B) guess initial SOC of 0.1 true initial SOC of 0.3011.

As regards charging, the data CMULTI was used, as presented in Fig. 6.13. Fig. 6.13A shows the SOC estimation result with initial guess SOC of 0.2 while the true SOC was 0. The result was different from the previous discharge scenario as the estimator was able to track the true SOC value from the beginning of the response with P_3 of 1×10^{-1} . On the contrary, the convergence to the true SOC did not happen for another case which was the initial guess SOC of 0.1 as the true SOC was 0.3011, as illustrated in Fig. 6.13B. The former scenario in Fig. 6.13A contained the point that SOC was 0 therefore the estimated SOC converged to the CC value at the beginning, as shown in the small figure of Fig. 6.13A. On the other hand, the latter scenario in Fig. 6.13B did not include the zero SOC thus the estimator was unable to estimate true SOC value at any point of the response.

6.6.2.3 Charge-discharge combined model and continuous scenario

According to the incorrect initial guess test, the SOC value was able to be estimated correctly only if the depleted SOC was included in the battery operation. In order to investigate SOC estimation for the multi-cycle operation, a multi-cycle scenario was proceeded by connecting the sequential charge-discharge cycle into one multi-cycle data. Then, the multi-cycle scenario was used to test for SOC estimation. Because the multi-cycle data included both charge and discharge processes, the LPV model used with EKF had to include both charge and discharge mode. Accordingly, the charge-discharge combined LPV model was proposed as followed:

$$\begin{bmatrix} V_{RC1}(k+1) \\ V_{RC2}(k+1) \\ V_{RC3}(k+1) \\ SOC(k+1) \end{bmatrix} = \begin{bmatrix} A_1 & 0 & 0 & 0 \\ 0 & A_2 & 0 & 0 \\ 0 & 0 & A_3 & 0 \\ 0 & 0 & 0 & 1 \end{bmatrix} \begin{bmatrix} V_{RC1}(k) \\ V_{RC2}(k) \\ V_{RC3}(k) \\ SOC(k) \end{bmatrix} + \begin{bmatrix} B_1 \\ B_2 \\ B_3 \\ \frac{\Delta t}{3600 \cdot CN} \cdot \varepsilon \end{bmatrix} I_{cell}(k) \quad (6.15)$$

$$V_{cell}(k) = V_{oc} + [1 \quad C_2 \quad C_3 \quad 0] \begin{bmatrix} V_{RC1}(k) \\ V_{RC2}(k) \\ V_{RC3}(k) \\ SOC(k) \end{bmatrix} + D \cdot I_{cell}(k) \quad (6.16)$$

The combined LPV model was almost similar to the Eqs. (6.3) and (6.4); however, the new model was extended to 4 states which include one more V_{RC} . For Eq. (6.15), V_{RC1} , V_{RC2} and V_{RC3} represent the overpotential of zinc electrode, air electrode and charging electrode, respectively. With the new LPV model, the overpotential of the air electrode and charging electrode can be computed separately. Regarding model parameters including A_1 , A_2 , A_3 , B_1 , B_2 , B_3 , D and V_{OC} , the current direction is also involved as another scheduling parameter used for switching between charge and discharge. ε is the efficiency factor which indicated the inequality SOC changing rate between charge and discharge. Parameters C_2 and C_3 act as switching functions for the output matrix:

For discharging: $\varepsilon = 1, C_2 = 1, C_3 = 0$

For charging: $\varepsilon = \text{charging efficiency}, C_2 = 0, C_3 = 1$

Where charging efficiency depends on each battery. For the following test, charging efficiency was equal to 0.772. The efficiency factor was also implemented in the linear model.

The test of the multi-cycle scenario was proceeded using reference tuning parameters, as specified in Table 6.4, and correct initial guess, as depicted in Fig. 6.14. It was found that the combined LPV model with EKF was able to estimate cell voltage and SOC accurately. Some errors occurred during the discharge cycle. On the other hand, the linear model with V_{OC} change was very inaccurate for estimating cell voltage but the estimated SOC from the linear model with V_{OC} change was very similar to the value from the CC method.

Table 6.4 Reference values of tuning parameters for combined model estimator

Tuning parameter	Description	Value
P	Initial state estimate covariance	$\begin{bmatrix} P_1 & 0 & 0 & 0 \\ 0 & P_2 & 0 & 0 \\ 0 & 0 & P_3 & 0 \\ 0 & 0 & 0 & P_4 \end{bmatrix} = \begin{bmatrix} 10^{-6} & 0 & 0 & 0 \\ 0 & 10^{-6} & 0 & 0 \\ 0 & 0 & 10^{-6} & 0 \\ 0 & 0 & 0 & 10^{-6} \end{bmatrix}$
Q	Process noise covariance	$\begin{bmatrix} Q_1 & 0 & 0 & 0 \\ 0 & Q_2 & 0 & 0 \\ 0 & 0 & Q_3 & 0 \\ 0 & 0 & 0 & Q_4 \end{bmatrix} = \begin{bmatrix} 10^{-6} & 0 & 0 & 0 \\ 0 & 10^{-6} & 0 & 0 \\ 0 & 0 & 10^{-6} & 0 \\ 0 & 0 & 0 & 10^{-6} \end{bmatrix}$
R	Measurement noise covariance	5×10^{-3}

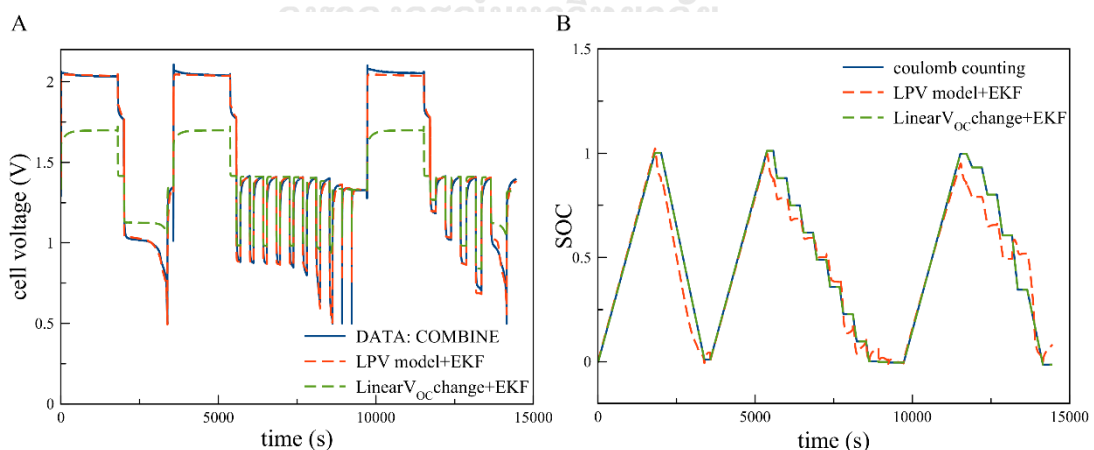


Figure 6.14 Comparison of the multi-cycle scenario between response of measure data (COMBINE) and response predicted from the proposed algorithm: (A) cell voltage and (B) SOC

The incorrect initial guess scenario was conducted with the data COMBINE, as illustrated in Fig. 6.15. The covariance for initial SOC was also varied. The case of

guess initial SOC of 0.2 with the true initial SOC of 0 is shown in Fig. 6.15A. The result revealed that the LPV model with EKF estimator was able to track the true SOC value after the first charging cycle (starting of discharge cycle). Increasing P_4 did not provide significant improvement for the SOC estimation. At P_4 of 1×10^{-1} , the estimated value oscillated at the starting point but did not converge to the true value. On the contrary, the linear model with EKF was unable to estimate the true value at any point because the mismatch between the implemented data and the linear model was exceedingly high, as shown in Fig. 6.14A. When the error of cell voltage prediction was too large, the EKF was unable to estimate the appropriate value of SOC. For another example, the guess initial SOC value was 0.5 while the true value was 0 (Fig. 6.15B). The same result was obtained as the true SOC was able to be tracked by the LPV model with EKF estimator after the first discharge cycle. The higher error in the initial guess value made the SOC tracking slightly slower. The result of the linear model with EKF was also the same as it could not track the true SOC.

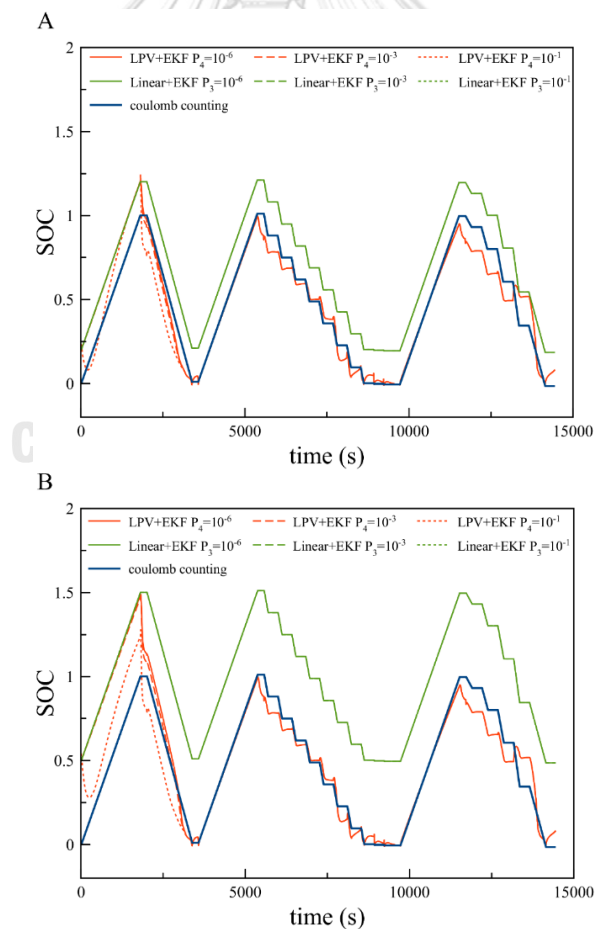


Figure 6.15 Comparison of SOC estimation between different initial covariance P for incorrect initial SOC guess scenario using data COMBINE: (A) guess initial SOC of 0.2 true initial SOC of 0 (B) guess initial SOC of 0.5 true initial SOC of 0.

The accuracy of SOC estimation of LPV model using with EKF was able to be improved further by adjusting covariance Q_4 which is the confidence in the model for SOC, as exhibited in Fig. 6.16. From Fig. 6.16, adjusting Q_4 to 1×10^{-9} ($P_4 = 1 \times 10^{-6}$) made the estimator unable to track SOC (green line in Fig. 6.16). However, the SOC estimation became highly accurate after tuning of P_4 to 1×10^{-3} . Using Q_4 of 1×10^{-9} and P_4 of 1×10^{-3} (high confidence in SOC model / lower confidence in initial SOC) contributed to the higher accuracy at discharge cycle than the reference values. This result indicated that the LPV model using EKF with the appropriate tuning parameters possesses great potential as a SOC estimator for a tri-electrode ZAFB. Furthermore, it shows the feasibility to use the proposed technique with other types of batteries.

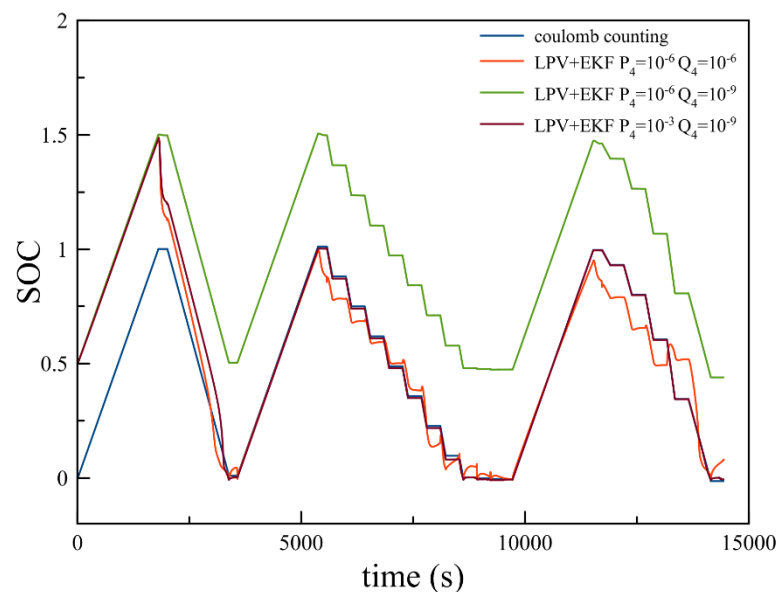


Figure 6.16 Comparison of SOC estimation between different covariance Q_4 and initial covariance P for incorrect initial SOC guess scenario using data COMBINE: guess initial SOC of 0.5 true initial SOC of 0.

6.7 Conclusion

The LPV model for a tri-electrode ZAFB was proposed and applied with EKF in order to estimate the SOC of the battery. The parameters of the LTI model at various current and SOC values were used to construct the correlations for the LPV model. The experimental data used for dynamic identification and validation were obtained from the laboratory-made tri-electrode ZAFB. From the validation result, the LPV model was able to predict the behavior of ZAFB and the LPV model was more accurate than the linear model based on the comparison using normalized mean absolute error. The proposed LPV model was also able to handle the effect of SOC change as the SOC was one of the scheduling parameters of the model. Subsequently,

the LPV model was implemented with the EKF algorithm for using as a SOC estimator. The proposed estimator was able to track the true SOC value only if the depleted SOC was reached. Consequently, the LPV model integrated with EKF was capable of SOC tracking in the scenario which contained multiple charge-discharge cycles. It should be noted that the developed algorithm was applicable only in the current range of the data used to construct the LPV model. The estimation might be inaccurate when the current input was out of range. The overall result showed that the LPV model integrated with EKF is verified to be a promising SOC estimator for a tri-electrode ZAFB.



CHAPTER 7

Conclusion

7.1 Conclusions

This research aims to investigate the modeling of zinc-air battery (ZAB) using theoretical and empirical approach. This work can be divided into 3 parts: model-based analysis of zinc-air flow battery (ZAFB), investigation of the dynamic behavior of the battery, and state of charge (SOC) estimation.

The first part is the model-based analysis of ZAFB. The theoretical mathematical model was developed to analyze the integrated system of ZAFB and zinc electrolyzer. Hydrogen evolution reaction (HER) was also implemented in the developed model therefore the current efficiency was able to be calculated. There were 3 studied parameters including electrolyte flowrate, potassium hydroxide (KOH) concentration, and zincate ion initial concentration. Regarding the result of the flow battery, it was found that KOH concentration played an important role in the performance of the battery as increasing KOH concentration promoted HER and decreased the current efficiency. Nevertheless, 6-7 M of KOH concentration was found to be optimal concentration. Zincate ion acted as an HER prohibitor since increasing zincate ion concentration lowered the reversible potential difference between the reaction of zinc (Zn) electrode and HER. For the result of zinc electrolyzer, zincate ion initial concentration and electrolyte flowrate had a significant influence on the performance of the electrolyzer as increasing zincate ion initial concentration and electrolyte flowrate substantially increased the current efficiency. KOH concentration did not provide a direct effect on the electrolyzer performance but affected the saturation limit of zincate ions. As regards the integrated system, the result showed that zinc electrolyzer predominated the current efficiency of the integrated system. Thus, increasing zincate ion initial concentration and electrolyte flowrate also provided an advantageous effect on the performance of the integrated system. Though, the energy efficiency of the integrated system was dominated by the discharging instead. Hence, the optimal concentration of KOH provided the maximum energy efficiency of the integrated system as well as the ZAFB. Totally, this result indicated the effect of HER on the performance of the integrated system of ZAFB and zinc electrolyzer and suggested that optimal performance can be obtained by control the operating condition.

For the second part, the dynamic behavior of the ZAB was investigated using the empirical model. The empirical model used in this study included the linear state-space model, the linear parameter-varying (LPV) model, and Hammerstein-Weiner

(HW) model. The state-space model is represented as the linear time-invariant (LTI) model. LPV model was constructed using the parameter sets of LTI model as the based model parameters and selecting discharge current level as scheduling parameter. HW model was representative of the nonlinear model which was included for comparison reasons. The data used for identification and validation were obtained from a homemade ZAB designed as a tubular refuellable cell. The result showed that ZAB possessed the nonlinear behavior in discharge current level. The LTI model was accurate only at the local discharge current level while it was unable to accurately predict the battery response at other current levels. On the contrary, this nonlinear behavior was able to be captured by the LPV model because the effect of different current levels was implemented in the LPV model. The prediction accuracy of the LPV model was comparable with the nonlinear HW model. Nonetheless, it was observed that the LPV model occupied more robustness than the nonlinear model. The LPV model developed in this part possessed limitations regarding the effect of SOC and range of input current. Therefore, the model was applicable in the current range included in the based data and in the high SOC range that the dynamics of the battery did not change much. Overall, this result pointed out that the LPV model is a favorable dynamic model for the prediction of ZAB behavior.

Regarding the third part, SOC estimation of ZAB was investigated using the LPV model integrated with the extended Kalman filter (EKF) algorithm. LPV model was constructed with the same technique used in the previous part. The data used for this study was acquired from a laboratory-made ZAFB. The battery configuration was a tri-electrode cell with flowing electrolyte. The correlations of model parameters were created using the current level and SOC as scheduling parameters. For the model validation result, the LPV model provides acceptable validity and was able to capture the effect of SOC change for both charge and discharge. Then, the SOC estimator was established by integrating the developed model with EKF algorithm and was used to estimate and track the SOC of ZAFB. The test of SOC estimation was conducted by applying various scenarios. The studied scenario included the varying tuning parameters and the correctness of the initial SOC guess. The result showed that the proposed estimator was able to track the true SOC value only when the SOC reached 0 because the voltage dynamic of ZAFB was highly different at this zone. Subsequently, the LPV model was modified to be capable of predicting both charge and discharge mode. The estimator used the modified LPV model was able to track the SOC in the scenario that contained multiple charge-discharge cycles. However, the applicable current range of the model and the estimator depended on the current boundary of the based data. Utilizing the model and the estimator out of the applicable range led to a fault in estimation. Finally, the SOC estimator integrating

between LPV model and EKF is proved to be viable in SOC estimation for a tri-electrode ZAFB.

7.2 Limitation of this research

For the first part of the research, HER was the main phenomenon that affected the current efficiency of the battery system. In fact, there are other phenomena that can be affected the efficiency of the ZAB such as zinc morphology change. This makes the research scope limits to the only effect of HER on the current efficiency. Another limitation of the model of this part is the model dimension which was zero-dimensional. This assumption simplified the model and made it easy to study the battery operation. However, this assumption also limited the scope of this study.

Regarding the second part, the range of data is the limitation for this part. This limitation makes the developed LPV model only viable on the range of the data. Prediction of the battery response at the condition that out of correlation bounds was very inaccurate. Another limitation of this part is that the effect of SOC did not include. However, this limitation was already fixed in the last part of the research.

As regards the SOC estimation part, the main limitation is the behavior of the ZAB itself. ZAB possesses a very flat voltage profile, especially the flow battery. The estimator used in this study tracked the SOC using the change in voltage dynamic. If the dynamic profile is very flat, the estimator cannot track the true SOC value. The true SOC can only be tracked at the near-zero SOC.

7.3 Recommendations and further studies

The modeling of ZAB was studied using theoretical and empirical approach.

1. For theoretical approach, the developed model can be further included some other parameters such as temperature. Some phenomena should also consider such as Zn morphology change.
2. Zero dimension limits the scope of research. Develop the higher dimension model can expand the scope of study further.
3. The developed model should apply with more testing scenario or other application such as the multiple cell scenario or the renewable energy storage scenario.
4. As regards empirical approach, the LPV model can be further include some other scheduling parameter such as temperature.

5. Besides state space model, LPV modeling can be applied in other LTI model such as equivalent circuit model.
6. LPV modeling technique can be implemented in other type of battery.
7. For the SOC estimation, the other type of model can also be tried using the proposed algorithm.
8. Besides EKF, the other type of model-based state estimation algorithm such as state observer or unscented Kalman filter can also be tried.
9. Besides SOC, other states of battery should also be tried and studied with the proposed estimation technique.



REFERENCES

- ABBASI, A., HOSSEINI, S., SOMWANGTHANAROJ, A., MOHAMAD, A. A. & KHEAWHOM, S. 2019. Poly(2,6-Dimethyl-1,4-Phenylene Oxide)-Based Hydroxide Exchange Separator Membranes for Zinc–Air Battery. *International Journal of Molecular Sciences*, 20, 3678.
- AKBAR, N., ISLAM, M., AHMED, S. S. & HYE, A. A. Dynamic model of battery charging. TENCON 2015 - 2015 IEEE Region 10 Conference, 1-4 Nov. 2015. 1-4.
- ALFARUQI, M. H., GIM, J., KIM, S., SONG, J., PHAM, D. T., JO, J., XIU, Z., MATHEW, V. & KIM, J. 2015. “A Layered δ -MnO₂ Nanoflake Cathode with High Zinc-storage Capacities for Eco-friendly Battery Applications”. *Electrochem. Commun.*, 60, 121.
- AMENDOLA, S., JOHNSON, L., BINDER, M., KUNZ, M., BLACK, P. J., OSTER, M., STEFANIE SHARP-GOLDMAN, E., CHCIUK, T. & JOHNSON, R. 2013. *ELECTRICALLY RECHARGEABLE, METAL-AIR BATTERY SYSTEMS AND METHODS*. 13/811,013. May 9, 2013.
- AMUNÁTEGUI, B., IBÁÑEZ, A., SIERRA, M. & PÉREZ, M. 2018. Electrochemical energy storage for renewable energy integration: zinc-air flow batteries. *Journal of Applied Electrochemistry*, 48, 627-637.
- APPLEBY, A. J. & JACQUIER, M. 1976. The C.G.E. circulating zinc/air battery: A practical vehicle power source. *Journal of Power Sources*, 1, 17-34.
- ARLT, T., SCHRÖDER, D., KREWER, U. & MANKE, I. 2014. In operando monitoring of the state of charge and species distribution in zinc air batteries using X-ray tomography and model-based simulations. *Physical Chemistry Chemical Physics*, 16, 22273-22280.
- BEVERSKOG, B. & PUIGDOMENECH, I. 1997. Revised pourbaix diagrams for zinc at 25–300 °C. *Corrosion Science*, 39, 107-114.
- BIRD, R. B., STEWART, W. E. & LIGHTFOOT, E. N. 2002. *Transport Phenomena*, Danvers, United States of America, John Wiley & Sons.
- BOCKELMANN, M., BECKER, M., REINING, L., KUNZ, U. & TUREK, T. 2018. Passivation of Zinc Anodes in Alkaline Electrolyte: Part I. Determination of the Starting Point of Passive Film Formation. *Journal of The Electrochemical Society*, 165, A3048-A3055.
- BOCKELMANN, M., KUNZ, U. & TUREK, T. 2016. Electrically rechargeable zinc-oxygen flow battery with high power density. *Electrochemistry Communications*, 69, 24-27.
- BOCKELMANN, M., REINING, L., KUNZ, U. & TUREK, T. 2017. Electrochemical characterization and mathematical modeling of zinc passivation in alkaline solutions: A review. *Electrochimica Acta*, 237, 276-298.
- BOCKRIS, J. O. M. & OTAGAWA, T. 1984. The Electrocatalysis of Oxygen Evolution

- on Perovskites. *Journal of The Electrochemical Society*, 131, 290-302.
- BONNICK, P. & DAHN, J. R. 2012. A Simple Coin Cell Design for Testing Rechargeable Zinc-Air or Alkaline Battery Systems. *Journal of The Electrochemical Society*, 159, A981-A989.
- BULLER, S., THELE, M., KARDEN, E. & DE DONCKER, R. W. 2003. Impedance-based non-linear dynamic battery modeling for automotive applications. *Journal of Power Sources*, 113, 422-430.
- CAI, M., CHEN, W. & TAN, X. 2017. Battery State-Of-Charge Estimation Based on a Dual Unscented Kalman Filter and Fractional Variable-Order Model. *Energies*, 10, 1577.
- CHANG, W.-Y. 2013. The State of Charge Estimating Methods for Battery: A Review. *ISRN Applied Mathematics*, 2013, 7.
- CHEN, D., RUI, X., ZHANG, Q., GENG, H., GAN, L., ZHANG, W., LI, C., HUANG, S. & YU, Y. 2019a. Persistent zinc-ion storage in mass-produced V2O5 architectures. *Nano Energy*, 60, 171-178.
- CHEN, D., TAN, H., RUI, X., ZHANG, Q., FENG, Y., GENG, H., LI, C., HUANG, S. & YU, Y. 2019b. Oxyvanite V3O5: A new intercalation-type anode for lithium-ion battery. *InfoMat*, 1, 251-259.
- CLARK, S., LATZ, A. & HORSTMANN, B. 2017. Rational Development of Neutral Aqueous Electrolytes for Zinc-Air Batteries. *ChemSusChem*, 10, 4735-4747.
- CLARK, S., LATZ, A. & HORSTMANN, B. 2018. A Review of Model-Based Design Tools for Metal-Air Batteries. *Batteries*, 4, 5.
- CLARK, S., MAINAR, A. R., IRUIN, E., COLMENARES, L. C., BLÁZQUEZ, J. A., TOLCHARD, J. R., LATZ, A. & HORSTMANN, B. 2019. Towards rechargeable zinc-air batteries with aqueous chloride electrolytes. *Journal of Materials Chemistry A*, 7, 11387-11399.
- COOPER, J. F. & KRUEGER, R. 2006. The Refuelable Zinc-air Battery: Alternative Techniques for Zinc and Electrolyte Regeneration. ; Lawrence Livermore National Laboratory (LLNL), Livermore, CA.
- DANKO, M., ADAMEC, J., TARABA, M. & DRGONA, P. 2019. Overview of batteries State of Charge estimation methods. *Transportation Research Procedia*, 40, 186-192.
- DEAN, J. A. & LANGE, N. A. 1999. *Lange's handbook of chemistry*, New York :, McGraw-Hill.
- DEISS, E., HOLZER, F. & HAAS, O. 2002. Modeling of an electrically rechargeable alkaline Zn-air battery. *Electrochimica Acta*, 47, 3995-4010.
- DIRKSE, T. P., DE WIT, D. & SHOEMAKER, R. 1968. The Anodic Behavior of Zinc in KOH Solutions. *Journal of The Electrochemical Society*, 115, 442-444.
- DIRKSE, T. P. & HAMPSON, N. A. 1972. The Zn(II)/Zn exchange reaction in KOH solution—I. Exchange current density measurements using the galvanostatic method. *Electrochimica Acta*, 17, 135-141.

- DOCIMO, D., GHANAATPISHE, M., J. ROTHENBERGER, M., RAHN, C. & K. FATHY, H. 2014. *The lithium-ion battery modeling challenge: A dynamic systems and control perspective*.
- DUNDÁLEK, J., ŠNAJDR, I., LIBÁNSKÝ, O., VRÁNA, J., POCEDIČ, J., MAZÚR, P. & KOSEK, J. 2017. Zinc electrodeposition from flowing alkaline zincate solutions: Role of hydrogen evolution reaction. *Journal of Power Sources*, 372, 221-226.
- DUNN, B., KAMATH, H. & TARASCON, J.-M. 2011. Electrical Energy Storage for the Grid: A Battery of Choices. *Science*, 334, 928-935.
- EINERHAND, R. E. F., VISSCHER, W. H. M. & BARENDRECHT, E. 1988. Hydrogen production during zinc deposition from alkaline zincate solutions. *Journal of Applied Electrochemistry*, 18, 799-806.
- EL-SAYED, A.-R., MOHRAN, H. S., ABD EL-LATEEF, H. M. J. M. & A, M. T. 2012. Corrosion Study of Zinc, Nickel, and Zinc-Nickel Alloys in Alkaline Solutions by Tafel Plot and Impedance Techniques. 43, 619-632.
- ENERGIZER Energizer Zinc Air Prismatic Handbook.
- ESCALANTE SOBERANIS, M. A., MITHRUSH, T., BASSAM, A. & MÉRIDA, W. 2018. A sensitivity analysis to determine technical and economic feasibility of energy storage systems implementation: A flow battery case study. *Renewable Energy*, 115, 547-557.
- FU, J., ZHANG, J., SONG, X., ZARRIN, H., TIAN, X., QIAO, J., RASEN, L., LI, K. & CHEN, Z. 2016. A flexible solid-state electrolyte for wide-scale integration of rechargeable zinc-air batteries. *Energy & Environmental Science*, 9, 663-670.
- GARCIA, G., VENTOSA, E. & SCHUHMANN, W. 2017. Complete Prevention of Dendrite Formation in Zn Metal Anodes by Means of Pulsed Charging Protocols. *ACS Applied Materials & Interfaces*, 9, 18691-18698.
- GAVRILOVIĆ-WOHLMUTHER, A., LASKOS, A., ZELGER, C., GOLLAS, B. & WHITEHEAD, A. H. 2015. Effects of Electrolyte Concentration, Temperature, Flow Velocity and Current Density on Zn Deposit Morphology. *Journal of Energy and Power Engineering*, 9, 10.
- GOLDSTEIN, J., BROWN, I. & KORETZ, B. 1999. New developments in the Electric Fuel Ltd. zinc/air system. *Journal of Power Sources*, 80, 171-179.
- GU, P., ZHENG, M., ZHAO, Q., XIAO, X., XUE, H. & PANG, H. 2017. Rechargeable zinc-air batteries: a promising way to green energy. *Journal of Materials Chemistry A*, 5, 7651-7666.
- GUO, J. 2003. *Zn/air cell performance in extreme humidity by controlling hydrophobic layer porosity*. United State of America patent application 09/579,385.
- HARRIS, D. C. 2010. *Quantitative Chemical Analysis*, W. H. Freeman.
- HEISE, G. W. 1933. *Air-depolarized primary battery* United State patent application.
- HONG, W., LI, H. & WANG, B. 2016. Horizontal Three-Electrode Structure for Zinc-

- Air Batteries with Long-Term Cycle Life and High Performance. *International Journal of Electrochemical Science*, 11, 9.
- HOSSEINI, S., ABBASI, A., UGINET, L.-O., HAUSTRAETE, N., PRASERTHDAM, S., YONEZAWA, T. & KHEAWHOM, S. 2019. The Influence of Dimethyl Sulfoxide as Electrolyte Additive on Anodic Dissolution of Alkaline Zinc-Air Flow Battery. *Scientific Reports*, 9, 14958.
- HOSSEINI, S., HAN, S. J., ARPONWICHANOP, A., YONEZAWA, T. & KHEAWHOM, S. 2018a. Ethanol as an electrolyte additive for alkaline zinc-air flow batteries. *Scientific Reports*, 8, 11273.
- HOSSEINI, S., LAO-ATIMAN, W., HAN, S. J., ARPORNWICHANOP, A., YONEZAWA, T. & KHEAWHOM, S. 2018b. Discharge Performance of Zinc-Air Flow Batteries Under the Effects of Sodium Dodecyl Sulfate and Pluronic F-127. *Scientific Reports*, 8, 14909.
- HU, Y. & YURKOVICH, S. 2011. Linear parameter varying battery model identification using subspace methods. *Journal of Power Sources*, 196, 2913-2923.
- HU, Y. & YURKOVICH, S. 2012. Battery cell state-of-charge estimation using linear parameter varying system techniques. *Journal of Power Sources*, 198, 338-350.
- HUH, T., SAVASKAN, G. & EVANS, J. W. 1992. Further studies of a zinc-air cell employing a packed bed anode part II: Regeneration of zinc particles and electrolyte by fluidized bed electrodeposition. *Journal of Applied Electrochemistry*, 22, 916-921.
- HUMMELSHØJ, J. S., BLOMQVIST, J., DATTA, S., VEGGE, T., ROSSMEISL, J., THYGESEN, K. S., LUNTZ, A. C., JACOBSEN, K. W. & NØRSKOV, J. K. 2010. Communications: Elementary oxygen electrode reactions in the aprotic Li-air battery. *The Journal of Chemical Physics*, 132, 071101.
- HUMMELSHØJ, J. S., LUNTZ, A. C. & NØRSKOV, J. K. 2013. Theoretical evidence for low kinetic overpotentials in Li-O₂ electrochemistry. *The Journal of Chemical Physics*, 138, 034703.
- ISAACSON, M. J., MCLARNON, F. R. & CAIRNS, E. J. 1990. Current Density and ZnO Precipitation-Dissolution Distributions in Zn - ZnO Porous Electrodes and Their Effect on Material Redistribution: A Two-Dimensional Mathematical Model. *Journal of The Electrochemical Society*, 137, 2014-2021.
- ITO, Y., WEI, X., DESAI, D., STEINGART, D. & BANERJEE, S. 2012. An indicator of zinc morphology transition in flowing alkaline electrolyte. *Journal of Power Sources*, 211, 119-128.
- JANTHARAMIN, N. & ZHANG, L. A new dynamic model for lead-acid batteries. 2008 4th IET Conference on Power Electronics, Machines and Drives, 2-4 April 2008 2008. 86-90.
- JING, F., PAUL, C. Z., GYU, P. M., AIPING, Y., MICHAEL, F. & ZHONGWEI, C. 2017. Electrically Rechargeable Zinc-Air Batteries: Progress, Challenges, and Perspectives. *Advanced Materials*, 29, 1604685.

- JIRATCHAYAMAETHASAKUL, C., SRIJAROENPRAMONG, N., BUNYANGYUEN, T., ARPAVATE, W., WONGYAO, N., THERDTHIANWONG, A. & THERDTHIANWONG, S. 2014. Effects of anode orientation and flow channel design on performance of refuelable zinc-air fuel cells. *Journal of Applied Electrochemistry*, 44, 1205-1218.
- JIRICNY, V., SIU, S., ROY, A. & EVANS, J. W. 2000. Regeneration of zinc particles for zinc-air fuel cells in a spouted-bed electrode. *Journal of Applied Electrochemistry*, 30, 647-656.
- JULIER, S. J. & UHLMANN, J. K. 2004. Unscented filtering and nonlinear estimation. *Proceedings of the IEEE*, 92, 401-422.
- JUNG, C.-Y., KIM, T.-H., KIM, W.-J. & YI, S.-C. 2016. Computational analysis of the zinc utilization in the primary zinc-air batteries. *Energy*, 102, 694-704.
- KAO-IAN, W., PORNPRASERTSUK, R., THAMYONGKIT, P., MAIYALAGAN, T. & KHEAWHOM, S. 2019. Rechargeable Zinc-Ion Battery Based on Choline Chloride-Urea Deep Eutectic Solvent. *Journal of The Electrochemical Society*, 166, A1063-A1069.
- KHAMSANGA, S., PORNPRASERTSUK, R., YONEZAWA, T., MOHAMAD, A. A. & KHEAWHOM, S. 2019. δ -MnO₂ nanoflower/graphite cathode for rechargeable aqueous zinc ion batteries. *Scientific Reports*, 9, 8441.
- KHEAWHOM, S. 2019. Discharge Performance of Zinc-air Battery. Open Science Framework.
- KIM, H.-I., KIM, E.-J., KIM, S.-J. & SHIN, H.-C. 2015a. Influence of ZnO precipitation on the cycling stability of rechargeable Zn-air batteries. *Journal of Applied Electrochemistry*, 45, 335-342.
- KIM, H. G., SUH, D. J., KIM, C. S., LEE, H. J. & MIN, B. K. 2013. *Zinc air fuel cell with enhanced cell performance*.
- KIM, H. S., JO, Y. N., LEE, W. J., KIM, K. J. & LEE, C. W. 2015b. Coating on Zinc Surface to Improve the Electrochemical Behavior of Zinc Anodes for Zinc-Air Fuel Cells. *Electroanalysis*, 27, 517-523.
- KIMBLE, M. C. & WHITE, R. E. 1991. A Mathematical Model of a Hydrogen/Oxygen Alkaline Fuel Cell. *Journal of The Electrochemical Society*, 138, 3370-3382.
- KREJČÍ, I., VANÝSEK, P. & TROJÁNEK, A. 1993. Transport of Zn(OH)₄²⁻ Ions across a Polyolefin Microporous Membrane. *Journal of The Electrochemical Society*, 140, 2279-2283.
- KREWER, U., RÖDER, F., HARINATH, E., BRAATZ, R. D., BEDÜRFTIG, B. & FINDEISEN, R. 2018. Review—Dynamic Models of Li-Ion Batteries for Diagnosis and Operation: A Review and Perspective. *Journal of The Electrochemical Society*, 165, A3656-A3673.
- LAN, C.-J., CHIN, T.-S., LIN, P. & PERNG, T. 2006. Zn-Al alloy as a new anode-metal of a zinc-air battery. *Journal of New Materials for Electrochemical Systems*, 9.

- LAO-ATIMAN, W., BUMROONGSIL, K., ARPORNWICHANOP, A., BUMROONGSAKULSAWAT, P., OLARU, S. & KHEAWHOM, S. 2019a. Model-Based Analysis of an Integrated Zinc-Air Flow Battery/Zinc Electrolyzer System. *Frontiers in Energy Research*, 7.
- LAO-ATIMAN, W., JULAPHATACHOTE, T., BOONMONGKOLRAS, P. & KHEAWHOM, S. 2017. Printed Transparent Thin Film Zn-MnO₂ Battery. 164, A859-A863.
- LAO-ATIMAN, W., OLARU, S., ARPORNWICHANOP, A. & KHEAWHOM, S. 2019b. Discharge performance and dynamic behavior of refuellable zinc-air battery. *Scientific Data*, 6, 168.
- LAO-ATIMAN, W., OLARU, S., DIOP, S., SKOGESTAD, S., ARPORNWICHANOP, A., CHEACHAROEN, R. & KHEAWHOM, S. 2020. Linear parameter-varying model for a refuellable zinc-air battery. *Royal Society Open Science*, 7, 201107.
- LARSSON, F., RYTINKI, A., AHMED, I., ALBINSSON, I. & MELLANDER, B.-E. 2017. Overcurrent Abuse of Primary Prismatic Zinc-Air Battery Cells Studying Air Supply Effects on Performance and Safety Shut-Down. *Batteries*, 3, 1.
- LECLANCHÉ, G. 1867. Quelques observations sur l'emploi des piles électriques / par Georges Leclanché *Quelques observations sur l'emploi des piles électriques / par Georges Leclanché* Paris.
- LEE, C. W., SATHIYANARAYANAN, K., EOM, S. W., KIM, H. S. & YUN, M. S. 2006a. Effect of additives on the electrochemical behaviour of zinc anodes for zinc/air fuel cells. *Journal of Power Sources*, 160, 161-164.
- LEE, C. W., SATHIYANARAYANAN, K., EOM, S. W., KIM, H. S. & YUN, M. S. 2006b. Novel electrochemical behavior of zinc anodes in zinc/air batteries in the presence of additives. *Journal of Power Sources*, 159, 1474-1477.
- LEE, J.-S., TAI KIM, S., CAO, R., CHOI, N.-S., LIU, M., LEE, K. T. & CHO, J. 2011. Metal-Air Batteries with High Energy Density: Li-Air versus Zn-Air. *Advanced Energy Materials*, 1, 34-50.
- LEE, S.-M., KIM, Y.-J., EOM, S.-W., CHOI, N.-S., KIM, K.-W. & CHO, S.-B. 2013. Improvement in self-discharge of Zn anode by applying surface modification for Zn-air batteries with high energy density. *Journal of Power Sources*, 227, 177-184.
- LEE, T. S. 1971. Hydrogen Over potential on Pure Metals in Alkaline Solution. 118, 1278-1282.
- LI, B., QUAN, J., LOH, A., CHAI, J., CHEN, Y., TAN, C., GE, X., HOR, T. S. A., LIU, Z., ZHANG, H. & ZONG, Y. 2017a. A Robust Hybrid Zn-Battery with Ultralong Cycle Life. *Nano Letters*, 17, 156-163.
- LI, G., MEZAAL, M. A., ZHANG, R., ZHANG, K. & LEI, L. 2016. Electrochemical Performance of MnO₂-based Air Cathodes for Zinc-air Batteries. *Fuel Cells*, 16, 395-400.

- LI, G., ZHANG, K., MEZAAL, M. A., ZHANG, R. & LEI, L. 2015. Effect of Electrolyte Concentration and Depth of Discharge for Zinc-Air Fuel Cell. *International Journal of Electrochemical Science*, 10, 12.
- LI, Y. & DAI, H. 2014. Recent advances in zinc-air batteries. *Chemical Society Reviews*, 43, 5257-5275.
- LI, Y., GONG, M., LIANG, Y., FENG, J., KIM, J.-E., WANG, H., HONG, G., ZHANG, B. & DAI, H. 2013. Advanced zinc-air batteries based on high-performance hybrid electrocatalysts. *Nature Communications*, 4, 1805.
- LI, Y., WONG, M., IP, W., ZHAO, P., WONG, C., CHENG, J. & YOU, Z. Modeling of novel single flow zinc-nickel battery for energy storage system. 2014 9th IEEE Conference on Industrial Electronics and Applications, 9-11 June 2014 2014. 1621-1626.
- LI, Z., HUANG, J., LIAW, B. Y. & ZHANG, J. 2017b. On state-of-charge determination for lithium-ion batteries. *Journal of Power Sources*, 348, 281-301.
- LOVERA, M., BERGAMASCO, M. & CASELLA, F. 2013. *LPV Modelling and Identification: An Overview.*, Springer.
- LUO, X., WANG, J., DOONER, M. & CLARKE, J. 2015. Overview of current development in electrical energy storage technologies and the application potential in power system operation. *Applied Energy*, 137, 511-536.
- MA, H., WANG, B., FAN, Y. & HONG, W. 2014. Development and Characterization of an Electrically Rechargeable Zinc-Air Battery Stack. *Energies*, 7, 6549.
- MADANI, S. S., SCHALTZ, E. & KNUDSEN KÆR, S. 2019. An Electrical Equivalent Circuit Model of a Lithium Titanate Oxide Battery. *Batteries*, 5, 31.
- MAICHE, L. 1878. French patent application.
- MAINAR, A. R., IRUIN, E., COLMENARES, L. C., KVASHA, A., DE MEATZA, I., BENGOCHEA, M., LEONET, O., BOYANO, I., ZHANG, Z. & BLAZQUEZ, J. A. 2018. An overview of progress in electrolytes for secondary zinc-air batteries and other storage systems based on zinc. *Journal of Energy Storage*, 15, 304-328.
- MAO, Z. & WHITE, R. E. 1992. Mathematical Modeling of a Primary Zinc/Air Battery. *Journal of The Electrochemical Society*, 139, 1105-1113.
- MARCUS, Y. 2009. The Standard Partial Molar Volumes of Ions in Solution. Part 4. Ionic Volumes in Water at 0–100 °C. *The Journal of Physical Chemistry B*, 113, 10285-10291.
- MATHIAS, P. M. 2004. Correlation for the density of multicomponent aqueous electrolytes. *Industrial & Engineering Chemistry Research*, 43, 6247-6252.
- MAURACHER, P. & KARDEN, E. 1997. Dynamic modelling of lead/acid batteries using impedance spectroscopy for parameter identification. *Journal of Power Sources*, 67, 69-84.
- MOHAMMADPOUR VELNI, J. & SCHERER, C. 2012. *Control of Linear Parameter*

Varying Systems with Applications.

- MOO, C. S., NG, K. S., CHEN, Y. P. & HSIEH, Y. C. State-of-Charge Estimation with Open-Circuit-Voltage for Lead-Acid Batteries. 2007 Power Conversion Conference - Nagoya, 2-5 April 2007 2007. 758-762.
- MURALIDHARAN, V. S. & RAJAGOPALAN, K. S. 1978. Kinetics and mechanism of corrosion of zinc in sodium hydroxide solutions by steady-state and transient methods. *Journal of Electroanalytical Chemistry and Interfacial Electrochemistry*, 94, 21-36.
- MURNANE, M. & GHAZEL, A. A Closer Look at State of Charge (SOC) and State of Health (SOH) Estimation Techniques for Batteries. Available: <https://www.analog.com/media/en/technical-documentation/technical-articles/a-closer-look-at-state-of-charge-and-state-health-estimation-techniques.pdf>.
- NAM, W., KIM, J.-Y. & OH, K.-Y. 2018. The characterization of dynamic behavior of Li-ion battery packs for enhanced design and states identification. *Energy Conversion and Management*, 162, 264-275.
- NEBURCHILOV, V., WANG, H., MARTIN, J. J. & QU, W. 2010. A review on air cathodes for zinc-air fuel cells. *Journal of Power Sources*, 195, 1271-1291.
- NEWMAN, J. & THOMAS, K. E. 2004. *Electrochemical Systems.*, Hoboken, Wiley-Interscience.
- OH, S.-J., MIN, Y.-J., LEE, M.-H., CHOI, J.-H., KIM, M.-S., JO, N.-J. & EOM, S. 2018. Design and electrochemical characteristics of single-layer cathode for flexible tubular type zinc-air fuel cells. *Journal of Alloys and Compounds*, 740, 895-900.
- PANG, S. C., CHIN, S. F. & LING, C. Y. 2012. Controlled Synthesis of Manganese Dioxide Nanostructures via a Facile Hydrothermal Route. *Journal of Nanomaterials*, 2012, 7.
- PARK, J., PARK, M., NAM, G., LEE, J.-S. & CHO, J. 2015. All-Solid-State Cable-Type Flexible Zinc-Air Battery. 27, 1396-1401.
- PEI, P., MA, Z., WANG, K., WANG, X., SONG, M. & XU, H. 2014a. High performance zinc air fuel cell stack. *Journal of Power Sources*, 249, 13-20.
- PEI, P., WANG, K. & MA, Z. 2014b. Technologies for extending zinc-air battery's cyclife: A review. *Applied Energy*, 128, 315-324.
- PEI, Z., ZHAO, X., YUAN, H., PENG, Z. & WU, L. 2018. An Equivalent Circuit Model for Lithium Battery of Electric Vehicle considering Self-Healing Characteristic. *Journal of Control Science and Engineering*, 2018, 5179758.
- PIERSON, H. O. 1993. 10 - Natural Graphite, Graphite Powders, Particles, and Compounds. *Handbook of Carbon, Graphite, Diamonds and Fullerenes*. Oxford: William Andrew Publishing.
- POOLNAPOL, L., KAO-IAN, W., SOMWANGTHANAROJ, A., MAHLENDORF, F., NGUYEN, M. T., YONEZAWA, T. & KHEAWHOM, S. 2020. Silver Decorated Reduced Graphene Oxide as Electrocatalyst for Zinc-Air Batteries.

Energies, 13, 462.

- POP, V., BERGVELD, H., DANILOV, D., REGTIEN, P. & NOTTEN, P. 2008. *Battery Management Systems: Accurate State-of-Charge Indication for Battery-Powered Applications*.
- POPOV, K. I., KEČA, D. N. & ANDJELIĆ, M. D. 1978. Electrodeposition of zinc on copper from alkaline zincate solutions. *Journal of Applied Electrochemistry*, 8, 19-23.
- PUAPATTANAKUL, A., THERDTHIANWONG, S., THERDTHIANWONG, A. & WONGYAO, N. 2013. Improvement of Zinc-Air Fuel Cell Performance by Gelled KOH. *Energy Procedia*, 34, 173-180.
- R. MAINAR, A., LEONET, O., BENGOCHEA, M., BOYANO, I., DE MEATZA, I., KVASHA, A., GUERFI, A. & ALBERTO BLÁZQUEZ, J. 2016. Alkaline aqueous electrolytes for secondary zinc–air batteries: an overview. *International Journal of Energy Research*, 40, 1032-1049.
- RAVINDRAN, V. & MURALIDHARAN, V. S. 1995. Cathodic processes on zinc in alkaline zincate solutions. *Journal of Power Sources*, 55, 237-241.
- REMMLINGER, J., BUCHHOLZ, M., SOCZKA-GUTH, T. & DIETMAYER, K. 2013. On-board state-of-health monitoring of lithium-ion batteries using linear parameter-varying models. *Journal of Power Sources*, 239, 689-695.
- RIVERA-BARRERA, J. P., MUÑOZ-GALEANO, N. & SARMIENTO-MALDONADO, H. O. 2017. SoC Estimation for Lithium-ion Batteries: Review and Future Challenges. *Electronics*, 6, 102.
- SALEH, M. M., WEIDNER, J. W. & ATEYA, B. G. 1995. Electrowinning of Non-Noble Metals with Simultaneous Hydrogen Evolution at Flow-Through Porous Electrodes: I. Theoretical. *Journal of The Electrochemical Society*, 142, 4113-4121.
- SALEH, M. M., WEIDNER, J. W., EL-ANADOULI, B. E. & ATEYA, B. G. 1997. Electrowinning of Nonnoble Metals with Simultaneous Hydrogen Evolution at Flow-Through Porous Electrodes: III. Time Effects. *Journal of The Electrochemical Society*, 144, 922-927.
- SAMADANI, E., FARHAD, S., SCOTT, W., MASTALI, M., GIMENEZ, L. E., FOWLER, M. & FRASER, R. A. 2015. Empirical Modeling of Lithium-ion Batteries Based on Electrochemical Impedance Spectroscopy Tests. *Electrochimica Acta*, 160, 169-177.
- ŞANAL, E., DOST, P. & SOURKOUNIS, C. Electrotechnical investigation of zinc-air cells for determination of cell-parameters for a battery management system. 2015 International Conference on Renewable Energy Research and Applications (ICRERA), 22-25 Nov. 2015 2015. 1157-1161.
- SAPKOTA, P. & KIM, H. 2009. Zinc–air fuel cell, a potential candidate for alternative energy. *Journal of Industrial and Engineering Chemistry*, 15, 445-450.
- SAPKOTA, P. & KIM, H. 2010. An experimental study on the performance of a zinc air fuel cell with inexpensive metal oxide catalysts and porous organic polymer

- separators. *Journal of Industrial and Engineering Chemistry*, 16, 39-44.
- SAVASKAN, G., HUH, T. & EVANS, J. W. 1992. Further studies of a zinc-air cell employing a packed bed anode part I: Discharge. *Journal of Applied Electrochemistry*, 22, 909-915.
- SCHMITT, T., ARLT, T., MANKE, I., LATZ, A. & HORSTMANN, B. 2019. Zinc electrode shape-change in secondary air batteries: A 2D modeling approach. *Journal of Power Sources*, 432, 119-132.
- SCHOUKENS, M. & TÓTH, R. 2018. From Nonlinear Identification to Linear Parameter Varying Models: Benchmark Examples**This work has received funding from the European Research Council (ERC) under the European Union's Horizon 2020 research and innovation programme (grant agreement nr. 714663). *IFAC-PapersOnLine*, 51, 419-424.
- SCHRÖDER, D. 2016. *Analysis of Reaction and Transport Processes in Zinc Air Batteries*, Springer Fachmedien Wiesbaden.
- SCHRÖDER, D. & KREWER, U. 2014. Model based quantification of air-composition impact on secondary zinc air batteries. *Electrochimica Acta*, 117, 541-553.
- SCHRÖDER, D., LAUE, V. & KREWER, U. 2016. Numerical simulation of gas-diffusion-electrodes with moving gas-liquid interface: A study on pulse-current operation and electrode flooding. *Computers & Chemical Engineering*, 84, 217-225.
- SEE, D. M. & WHITE, R. E. 1997. Temperature and Concentration Dependence of the Specific Conductivity of Concentrated Solutions of Potassium Hydroxide. *Journal of Chemical & Engineering Data*, 42, 1266-1268.
- SHARIFI, B., MOJTAHEDI, M., GOODARZI, M. & VAHDATI KHAKI, J. 2009. Effect of alkaline electrolysis conditions on current efficiency and morphology of zinc powder. *Hydrometallurgy*, 99, 72-76.
- SHIVKUMAR, R., PARUTHIMAL KALAIANAN, G. & VASUDEVAN, T. 1995. Effect of additives on zinc electrodes in alkaline battery systems. *Journal of Power Sources*, 55, 53-62.
- SHOKROLLAHI, E., GOLDENBERG, A. A., DRAKE, J. M., EASTWOOD, K. W. & KANG, M. 2018. Application of a Nonlinear Hammerstein-Wiener Estimator in the Development and Control of a Magnetorheological Fluid Haptic Device for Robotic Bone Biopsy. *Actuators*, 7, 83.
- SHOLL, D. S. & STECKEL, J. A. 2009. *Density Functional Theory: A Practical Introduction*.
- SIMIČIĆ, M. V., POPOV, K. I. & KRSTAJIĆ, N. V. 2000. An experimental study of zinc morphology in alkaline electrolyte at low direct and pulsating overpotentials. *Journal of Electroanalytical Chemistry*, 484, 18-23.
- SMEDLEY, S. & ZHANG, X. G. 2009. SECONDARY BATTERIES – METAL-AIR SYSTEMS | Zinc–Air: Hydraulic Recharge.
- SMEDLEY, S. I. & ZHANG, X. G. 2007. A regenerative zinc–air fuel cell. *Journal of*

- Power Sources*, 165, 897-904.
- SONG, C. & ZHANG, J. 2008. Electrocatalytic Oxygen Reduction Reaction. In: ZHANG, J. (ed.) *PEM Fuel Cell Electrocatalysts and Catalyst Layers: Fundamentals and Applications*. London: Springer London.
- STAMM, J., VARZI, A., LATZ, A. & HORSTMANN, B. 2017. Modeling nucleation and growth of zinc oxide during discharge of primary zinc-air batteries. *Journal of Power Sources*, 360, 136-149.
- STOCK, D., DONGMO, S., JANEK, J. & SCHRÖDER, D. 2019. Benchmarking Anode Concepts: The Future of Electrically Rechargeable Zinc–Air Batteries. *ACS Energy Letters*, 4, 1287-1300.
- STROE, A., STROE, D., SWIERCZYNSKI, M., TEODORESCU, R. & KÆR, S. K. Lithium-ion battery dynamic model for wide range of operating conditions. 2017 International Conference on Optimization of Electrical and Electronic Equipment (OPTIM) & 2017 Intl Aegean Conference on Electrical Machines and Power Electronics (ACEMP), 25-27 May 2017 2017. 660-666.
- SUMBOJA, A., GE, X., ZHENG, G., GOH, F. W. T., HOR, T. S. A., ZONG, Y. & LIU, Z. 2016. Durable rechargeable zinc-air batteries with neutral electrolyte and manganese oxide catalyst. *Journal of Power Sources*, 332, 330-336.
- SUNU, W. G. & BENNION, D. N. 1980. Transient and Failure Analyses of the Porous Zinc Electrode: I . Theoretical. *Journal of The Electrochemical Society*, 127, 2007-2016.
- SUREN, S. & KHEAWHOM, S. 2016. Development of a High Energy Density Flexible Zinc-Air Battery. 163, A846-A850.
- TANG, Q., WANG, L., WU, M., XU, N., JIANG, L. & QIAO, J. 2017. Achieving high-powered Zn/air fuel cell through N and S co-doped hierarchically porous carbons with tunable active-sites as oxygen electrocatalysts. *Journal of Power Sources*, 365, 348-353.
- TANG, X., MAO, X., LIN, J. & KOCH, B. Li-ion battery parameter estimation for state of charge. Proceedings of the 2011 American Control Conference, 29 June-1 July 2011 2011. 941-946.
- TRAN, N.-T., KHAN, A. B. & CHOI, W. 2017. State of Charge and State of Health Estimation of AGM VRLA Batteries by Employing a Dual Extended Kalman Filter and an ARX Model for Online Parameter Estimation. *Energies*, 10, 137.
- WANG, K., PEI, P., MA, Z., CHEN, H., XU, H., CHEN, D. & WANG, X. 2015a. Dendrite growth in the recharging process of zinc-air batteries. *Journal of Materials Chemistry A*, 3, 22648-22655.
- WANG, K., PEI, P., MA, Z., CHEN, H., XU, H., CHEN, D. & XING, H. 2015b. Growth of oxygen bubbles during recharge process in zinc-air battery. *Journal of Power Sources*, 296, 40-45.
- WANG, K., PEI, P., MA, Z., XU, H., LI, P. & WANG, X. 2014. Morphology control of zinc regeneration for zinc–air fuel cell and battery. *Journal of Power Sources*, 271, 65-75.

- WANG, K., PEI, P., WANG, Y., LIAO, C., WANG, W. & HUANG, S. 2018. Advanced rechargeable zinc-air battery with parameter optimization. *Applied Energy*, 225, 848-856.
- WANG, X., SEBASTIAN, P. J., SMIT, M. A., YANG, H. & GAMBOA, S. A. 2003. Studies on the oxygen reduction catalyst for zinc-air battery electrode. *Journal of Power Sources*, 124, 278-284.
- WANG, Z., MENG, X., WU, Z. & MITRA, S. 2017. Development of flexible zinc-air battery with nanocomposite electrodes and a novel separator. *Journal of Energy Chemistry*, 26, 129-138.
- WASSILIADIS, N., ADERMANN, J., FRERICKS, A., PAK, M., REITER, C., LOHMANN, B. & LIENKAMP, M. 2018. Revisiting the dual extended Kalman filter for battery state-of-charge and state-of-health estimation: A use-case life cycle analysis. *Journal of Energy Storage*, 19, 73-87.
- WEI, Z., ZHAO, J., ZOU, C., LIM, T. M. & TSENG, K. J. 2018. Comparative study of methods for integrated model identification and state of charge estimation of lithium-ion battery. *Journal of Power Sources*, 402, 189-197.
- WEN, Y.-H., CHENG, J., NING, S.-Q. & YANG, Y.-S. 2009. Preliminary study on zinc-air battery using zinc regeneration electrolysis with propanol oxidation as a counter electrode reaction. *Journal of Power Sources*, 188, 301-307.
- WILLS, A., SCHÖN, T. B., LJUNG, L. & NINNESS, B. 2013. Identification of Hammerstein-Wiener models. *Automatica*, 49, 70-81.
- WOLFE, D., FRIESEN, C. A. & JOHNSON, P. B. 2012. *Ionic Liquid Containing Sulfonate Ions*. United States patent application 13/448,923.
- WONGRUJIPAIROJ, K., POOLNAPOL, L., ARPORNWICHANOP, A., SUREN, S. & KHEAWHOM, S. 2017. Suppression of zinc anode corrosion for printed flexible zinc-air battery. *physica status solidi (b)*, 254, 1600442.
- WU, M., ZHANG, G., WU, M., PRAKASH, J. & SUN, S. 2019. Rational design of multifunctional air electrodes for rechargeable Zn-Air batteries: Recent progress and future perspectives. *Energy Storage Materials*, 21, 253-286.
- XU, K., LOH, A., WANG, B. & LI, X. 2018. Enhancement of Oxygen Transfer by Design Nickel Foam Electrode for Zinc-Air Battery. *Journal of The Electrochemical Society*, 165, A809-A818.
- XU, M., IVEY, D. G., XIE, Z. & QU, W. 2015. Rechargeable Zn-air batteries: Progress in electrolyte development and cell configuration advancement. *Journal of Power Sources*, 283, 358-371.
- YAN, Z., SUN, H., CHEN, X., FU, X., CHEN, C., CHENG, F. & CHEN, J. 2018. Rapid low-temperature synthesis of perovskite/carbon nanocomposites as superior electrocatalysts for oxygen reduction in Zn-air batteries. *Nano Research*, 11, 3282-3293.
- YANG, D., TAN, H., RUI, X. & YU, Y. 2019. Electrode Materials for Rechargeable Zinc-Ion and Zinc-Air Batteries: Current Status and Future Perspectives.

Electrochemical Energy Reviews, 2, 395-427.

- YAO, S., LIAO, P., XIAO, M., CHENG, J. & HE, K. 2017. Equivalent circuit modeling and simulation of the zinc nickel single flow battery. *AIP Advances*, 7, 055112.
- ZELGER, C., SÜßENBACHER, M., LASKOS, A. & GOLLAS, B. 2019. State of charge indicators for alkaline zinc-air redox flow batteries. *Journal of Power Sources*, 424, 76-81.
- ZHANG, J., ZHOU, Q., TANG, Y., ZHANG, L. & LI, Y. 2019a. Zinc-air batteries: are they ready for prime time? *Chemical Science*, 10, 8924-8929.
- ZHANG, S. 2013. Status, Opportunities, and Challenges of Electrochemical Energy Storage. *Frontiers in Energy Research*, 1.
- ZHANG, X., TSAY, K., FAHLMAN, J. & QU, W. 2019b. Zinc morphology change in pulsating current deposition. *Journal of Energy Storage*, 26, 100966.
- ZHANG, Z., ZUO, C., LIU, Z., YU, Y., ZUO, Y. & SONG, Y. 2014. All-solid-state Al-air batteries with polymer alkaline gel electrolyte. *Journal of Power Sources*, 251, 470-475.
- ZHONG, Y., LIU, B., ZHAO, Z., SHEN, Y., LIU, X. & ZHONG, C. 2021. Influencing Factors of Performance Degradation of Zinc-Air Batteries Exposed to Air. *Energies*, 14, 2607.
- ZHU, A. L., DUCH, D., ROBERTS, G. A., LI, S. X. X., WANG, H., DUCH, K., BAE, E., JUNG, K. S., WILKINSON, D. & KULINICH, S. A. 2015. Increasing the Electrolyte Capacity of Alkaline Zn-Air Fuel Cells by Scavenging Zincate with Ca(OH)₂. *ChemElectroChem*, 2, 134-142.
- ZHU, A. L., WILKINSON, D. P., ZHANG, X., XING, Y., ROZHIN, A. G. & KULINICH, S. A. 2016. Zinc regeneration in rechargeable zinc-air fuel cells—A review. *Journal of Energy Storage*, 8, 35-50.
- ZHU, S., CHEN, Z., LI, B., HIGGINS, D., WANG, H., LI, H. & CHEN, Z. 2011. Nitrogen-doped carbon nanotubes as air cathode catalysts in zinc-air battery. *Electrochimica Acta*, 56, 5080-5084.

Appendix A

Supplementary Material

Model-based Analysis of an Integrated Zinc-Air Flow Battery/ Zinc Electrolyzer System

Table A1 Designed parameters and operating conditions.

Parameter	Value	Unit	Source
a_0	1.4×10^4	dm^2/dm^3	Jung et al. (2016)
a_c	1×10^5	dm^2/dm^3	Mao and White (1992)
A_{zinc}	0.3	dm^2	Given
A_{air}	0.3	dm^2	Given
A_{sep}	0.3	dm^2	Given
$C_{\text{DL}}^{\text{zinc}}$	0.02	F/dm^2	Dirkse et al. (1968)
$C_{\text{DL}}^{\text{air}}$	1.4	F/dm^2	Bockris and Otagawa (1984)
$C_{\text{O}_2, \text{atm}}$	0.008452	mol/dm^3	calculated
$D_{\text{Zn}(\text{OH})_4^{2-}, \text{elec}}$	8.55×10^{-9}	dm^2/s	Krejčí et al. (1993)
$D_{\text{OH}^-, \text{elec}}$	$f(C_{\text{KOH}})$	dm^2/s	Schröder et al. (2016)
$D_{\text{H}_2\text{O}, \text{elec}}$	5.26×10^{-7}	dm^2/s	Newman and Thomas (2004)
$D_{\text{K}^+, \text{elec}}$	1.2×10^{-7}	dm^2/s	Sunu and Bennion (1980)
$D_{\text{O}_2, \text{Air}}$	2.3×10^{-3}	dm^2/s	Bird et al. (2002)
E_0^{zinc}	-1.199	V	Harris (2010)
E_0^{air}	0.401	V	Song and Zhang (2008)
E_0^{H}	-0.828	V	Harris (2010)
F	96,485	C/mol	Dean and Lange (1999)
$i_0^{\text{air}, \text{ref}}$	1.5×10^{-8}	$\text{A} \cdot \text{dm}^{-2}$	Mao and White (1992)
k_s	0.25	$\text{dm}^3 \cdot \text{s}^{-1}$	Schröder and Krewer (2014)
n_e	2	Dimensionless	Given
P_{O_2}	0.2095	atm	Given
R	8.314	$\text{J}/\text{mol} \cdot \text{K}$	Dean and Lange (1999)
T	298.15	K	Given
\bar{V}_{Zn}	9.15×10^{-3}	dm^3/mol	Sunu and Bennion (1980)
\bar{V}_{ZnO}	1.45×10^{-2}	dm^3/mol	Sunu and Bennion (1980)
\bar{V}_{K^+}	3.6×10^{-3}	dm^3/mol	Marcus (2009)
\bar{V}_{OH^-}	7.89×10^{-3}	dm^3/mol	Mathias (2004)

Table A1(cont.) Designed parameters and operating conditions.

Parameter	Value	Unit	Source
$\bar{V}_{\text{Zn(OH)}_4^{2-}}$	1.86×10^{-2}	dm^3/mol	Schröder and Krewer (2014)
$\bar{V}_{\text{H}_2\text{O}}$	1.78×10^{-2}	dm^3/mol	Kimble and White (1991)
$z_{\text{K}^+}^\pm$	+1	dimensionless	Given
$z_{\text{OH}^-}^\pm$	-1	dimensionless	Given
$z_{\text{Zn(OH)}_4^{2-}}^\pm$	-2	dimensionless	Given
α_{zinc}	0.5	dimensionless	Assumed
α_{air}	0.5	dimensionless	Assumed
α_{H}	0.48	dimensionless	Lee (1971)
δ_{Sep}	2×10^{-3}	dm	Given
δ_{anode}	0.0615	dm	Given
δ_{zinc}	0.0115	dm	Given
δ_{GDL}	1.3×10^{-2}	dm	Given
ε_0	0.649	dimensionless	Jung et al. (2016)
ε_{sep}	0.5	dimensionless	Given
σ_{Zn}	2×10^6	S/dm	Sunu and Bennion (1980)
σ_{ZnO}	1×10^{-9}	S/dm	Sunu and Bennion (1980)
σ_{Carbon}	2×10^5	S/dm	Pierson (1993)
$\sigma_{\text{electrolyte}}$	$f(C_{\text{KOH}})$	S/dm	calculated
σ_{Cathode}	5×10^3	S/dm	Given
$\nu_{\text{Zn},1}$	-1	dimensionless	Given
$\nu_{\text{OH}^-,1}$	-4	dimensionless	Given
$\nu_{\text{Zn(OH)}_4^{2-},1}$	+1	dimensionless	Given
$\nu_{\text{Zn(OH)}_4^{2-},2}$	-1	dimensionless	Given
$\nu_{\text{OH}^-,2}$	+2	dimensionless	Given
$\nu_{\text{ZnO},2}$	+1	dimensionless	Given
$\nu_{\text{H}_2\text{O},2}$	+1	dimensionless	Given
$\nu_{\text{O}_2,3}$	-0.5	dimensionless	Given
$\nu_{\text{H}_2\text{O},3}$	-1	dimensionless	Given
$\nu_{\text{OH}^-,2}$	+2	dimensionless	Given

Table A2 Initial conditions at $t = 0$ s used in the simulation.

Parameter	Value	Unit
$C_{Zn(OH)_4^{2-},0}$	0.2, 0.4, 0.6, 0.8, 1.0 for all j	mol/dm ³
$C_{Zn(OH)_4^{2-},b,0}$	$C_{Zn(OH)_4^{2-},0}$ for electrolyzer	mol/dm ³
$C_{Zn(OH)_4^{2-},s,0}$	$C_{Zn(OH)_4^{2-},0}$ for electrolyzer	mol/dm ³
$C_{KOH,0}$	2, 4, 6, 8, 10 for all j	mol/dm ³
$C_{OH^-,0}$	$C_{KOH,0} - 2C_{Zn(OH)_4^{2-},0}$ for all j	mol/dm ³
$C_{H_2O,0}$	54.37, 52.75, 50.73, 48.51, 46.15 for all j	mol/dm ³
$C_{O_2,s,0}$	0.008452	mol/dm ³
$C_{K^+,0}$	$C_{KOH,0}$	mol/dm ³
$N_{Zn,0}$	0.1538 for zinc electrode 0 for electrolyzer	mol
$N_{ZnO,0}$	0	mol
$V_{solid,0}^{zinc}$	$N_{Zn,0} \cdot \bar{V}_{Zn} + N_{ZnO,0} \cdot \bar{V}_{ZnO}$	dm ³
$V_{electrolyte,0}^{zinc}$	$\delta_{anode} \cdot A_{zinc} - V_{solid,0}^{zinc}$	dm ³
$V_{electrolyte,0}^{air}$	0.001075	dm ³
η_{act}^{zinc}	0	V
η_{act}^{air}	0	V

A1 Additional calculations

a. Diffusivity of Hydroxide Ion in Electrolyte

The diffusivity of hydroxide ion in KOH solution electrolyte (dm²/s) is calculated with an empirical expression fitted by Schröder (2016).

$$D_{OH^-,KOH} = \frac{k_B T}{6\pi\mu_{KOH}R_{ion}} \times 10^2 \quad (A.1)$$

$$\mu_{KOH} = 0.799533504 \cdot \exp(0.155921614 \cdot c_{OH^-}) \times 10^{-3} \quad (A.2)$$

Where k_B is the Boltzmann constant, which is equal to 1.3806×10^{-23} m²/kg·s²·K, μ_{KOH} is dynamic viscosity of KOH solution, R_{ion} is Stoke radius of hydroxide ion, which is equal to 4.642×10^{-11} m.

b. Ionic Conductivity of Electrolyte

The ionic conductivity of the electrolyte (S/dm) is determined by the correlation of KOH concentration and temperature (See and White, 1997).

$$\sigma_{electrolyte} = \left(K_9 \cdot T + K_{10} \cdot T^2 + K_{11} \cdot C_{KOH} + K_{12} \cdot C_{KOH}^2 + K_{13} \cdot T \cdot C_{KOH} + K_{14} \cdot \frac{C_{KOH}}{T} + K_{15} \cdot C_{KOH}^3 + K_{16} \cdot T^2 \cdot C_{KOH}^2 \right) \times 10 \quad (A.3)$$

Where	$K_9 = -0.00342000614$	S / cm K
	$K_{10} = 1.19699771 \times 10^{-5}$	S / cm K ²
	$K_{11} = -1.17298091$	S L / cm mol
	$K_{12} = -0.00516794041$	S L / cm ² mol ²
	$K_{13} = 0.00328292638$	S L / cm K mol
	$K_{14} = 119.604837$	S L K / cm mol
	$K_{15} = 0.000624311676$	S L ³ / cm mol ³
	$K_{16} = -1.88320099 \times 10^{-7}$	S L ² / cm mol ² K ²

c. Saturation limit concentration of zincate ion

The saturation limit concentration of zincate ion (mol/dm³) or ZnO solubility is calculated by the correlation fitted from the experiment data of Dyson, Schreier et al. (1968). The correlation expresses as:

$$C_{Zn(OH)_4}^{sat} = 0.007239 \cdot C_{KOH}^2 + 0.056151 \cdot C_{KOH} - 0.03267 \quad (A.4)$$

A2 Validity of Assumption

Temperature variations are negligible: an isothermal operation at 298.15K is assumed. The isothermal assumption is valid in the zinc-air flow batteries because the generated heat from the reaction of the battery is relatively small. Moreover, the flowing electrolyte also enhances the cooling of the batteries.

This assumption is invalid if the generated heat from the reaction is too high, and the cooling rate is inadequate. In many types of batteries, charge or discharge at a very high current density can generate a high amount of heat and make the temperature rise. However, the heat generation depends on the nature of battery types.

Zero-dimensional space: This assumption is valid in the system that the electrode reaction rates are relatively slower than the mass transfer rate. In other words, the assumption is favorable at the sufficiently low current densities. For the zinc-air flow battery, this system includes flow electrolyte which enhances the mass transfer rate therefore this assumption is preferable at the high electrolyte flowrate. The assumption is also valid for the adequately small dimension system because the effect of concentration gradient is relatively insignificant in the small system.

This assumption might be invalid if the current densities and electrolyte flowrate are not appropriate. High current density and low electrolyte flowrate can cause the concentration gradient to occur.

The example works that used this assumption are:

Schröder and Krewer (2014) developed a zero-dimensional zinc-air battery model to investigate the effect of air-composition on cell performance. The system of this work was a zinc-air button cell with sufficiently small electrode thickness (0.13 dm for zinc electrode, 0.01 dm for air electrode). The maximum studied current density was 2.5 A/dm².

Dundálek et al. (2017) proposed a zero-dimensional model of zinc electrodeposition with flowing electrolyte. The system of this work was a zinc electrodeposition electrode with an active area of 2.25 cm². The electrolyte was flowing at 0.04 m/s. The maximum studied current density was about 300 mA/cm².

Negligible distance between the cells: This assumption is justified at a high electrolyte flowrate. At low electrolyte flowrate, this assumption might be invalid because the electrolyte takes a longer time to transfer between the cells.

Constant physical properties, electrode areas and thickness: Because the temperature was assumed to be constant, most physical properties were also constant. The electrode area and thickness were also assumed to be constant. This assumption is valid for the system that the temperature and pressure of the system do not change much.

For the electrode area and thickness, these parameters were assumed to be constant over the whole operation. In fact, the electrode area and thickness are constant except that of the zinc electrode. The area and thickness of the zinc electrode actually change when the operation proceeds. To simplify the simulation, these parameters were assumed to be constant. This assumption is valid for the system that the area and thickness of zinc electrode are small because small electrode area and thickness provide an insignificant effect on the battery. Vice versa, constant electrode area and thickness might be invalid for the cell with high electrode area and thickness since the change in area and thickness provide a high effect on the battery.

The capacitive effects are negligible: a quasi-electroneutrality condition is assumed. The capacitive effects of batteries usually occurred when the batteries immediately switch from charge to discharge or rest. The charge and discharge process occurred in separated cells for the integrated system studied in this work therefore the capacitive effects are absent.

A3 Additional validation information

Table A3 Validation of the ZAFB model (from Fig. 3.3A and 3.3B)

Current density (mA/cm ²)	Cell voltage (V)			Cathode loss (V)			Anode loss (V)		
	Measured	Calculated	Abs Error	Measured	Calculated	Abs Error	Measured	Calculated	Abs Error
0.03	1.363	1.387	0.024	0.240	0.277	0.037	0.016	0.017	0.001
15.92	1.164	1.164	0.000	0.394	0.443	0.049	0.071	0.071	0.000
31.85	1.048	1.054	0.006	0.458	0.496	0.038	0.125	0.126	0.001
47.77	0.944	0.950	0.006	0.510	0.542	0.032	0.175	0.180	0.005
63.69	0.848	0.850	0.002	0.556	0.585	0.029	0.227	0.235	0.008
79.62	0.745	0.757	0.012	0.606	0.624	0.018	0.280	0.286	0.006
95.54	0.654	0.658	0.004	0.647	0.665	0.019	0.329	0.340	0.011
111.46	0.565	0.560	0.005	0.684	0.706	0.023	0.380	0.393	0.013
127.38	0.480	0.461	0.019	0.720	0.748	0.028	0.430	0.447	0.017
132.16	0.460	0.430	0.030	0.724	0.761	0.037	0.442	0.461	0.019
MAE¹	0.0108			0.0311			0.0080		
NMAE²	0.0438			0.1139			0.0138		

¹ MAE expressed as: $\text{mean}|y-\hat{y}|$

² NMAE expressed as: $\frac{\text{mean}|y-\hat{y}|}{\text{mean}|y-\text{mean}(y)|}$

Table A4 Validation of the zinc electrolyzer model (from Fig. 3.3C and 3.3D)

Current density (mA/cm ²)	Cell voltage (V)			Cathode loss (V)			Anode loss (V)		
	Measured	Calculated	Abs Error	Measured	Calculated	Abs Error	Measured	Calculated	Abs Error
0	1.796	1.711	0.085	0.000	0.000	0.000	0.048	0.000	0.048
6.67	2.076	2.122	0.046	-0.015	0.008	0.023	0.353	0.394	0.041
13.33	2.137	2.160	0.023	0.015	0.014	0.001	0.396	0.417	0.021
20	2.186	2.197	0.011	0.017	0.022	0.005	0.431	0.436	0.006
26.67	2.227	2.226	0.001	0.024	0.028	0.004	0.450	0.450	0.001
33.33	2.262	2.258	0.004	0.019	0.036	0.017	0.472	0.465	0.007
40	2.297	2.288	0.009	0.043	0.043	0.000	0.489	0.478	0.011
46.67	2.328	2.318	0.010	0.049	0.051	0.001	0.503	0.491	0.012
53.33	2.359	2.352	0.007	0.056	0.059	0.003	0.517	0.505	0.012
60	2.387	2.372	0.015	0.064	0.065	0.001	0.531	0.513	0.018
66.67	2.413	2.401	0.012	0.071	0.072	0.002	0.543	0.524	0.018
73.33	2.441	2.425	0.016	0.091	0.079	0.012	0.552	0.534	0.019
80	2.468	2.453	0.015	0.084	0.086	0.002	0.564	0.545	0.020

Table A4 (cont.) Validation of the zinc electrolyzer model (from Fig. 3.3C and 3.3D)

Current density (mA/cm ²)	Cell voltage (V)			Cathode loss (V)			Anode loss (V)		
	Measured	Calculated	Abs Error	Measured	Calculated	Abs Error	Measured	Calculated	Abs Error
86.67	2.494	2.477	0.017	0.091	0.093	0.002	0.572	0.554	0.018
93.33	2.521	2.505	0.016	0.101	0.100	0.001	0.583	0.564	0.018
100	2.546	2.533	0.013	0.109	0.108	0.001	0.591	0.575	0.017
106.67	2.569	2.556	0.013	0.116	0.114	0.002	0.599	0.583	0.016
113.33	2.593	2.584	0.009	0.121	0.122	0.001	0.605	0.594	0.011
120	2.639	2.611	0.028	0.129	0.129	0.000	0.614	0.604	0.010
126.67	2.669	2.634	0.035	0.135	0.136	0.001	0.614	0.612	0.002
133.33	2.668	2.661	0.007	0.144	0.143	0.001	0.620	0.622	0.002
MAE¹	0.0187			0.0038			0.0155		
NMAE²	0.1092			0.0935			0.1784		

¹ MAE expressed as: $\text{mean}|y-\hat{y}|$

² NMAE expressed as: $\frac{\text{mean}|y-\hat{y}|}{\text{mean}|y-\text{mean}(y)|}$

Tables A3 and A4 display the validation information related to Fig. 3.3. These tables provide the measured values, calculated values, and absolute errors for the cell voltage and both electrode losses. In addition, mean absolute error (MAE) and normalized mean absolute error (NMAE) are also calculated and displayed.

As regards the ZAFB, the highest error in validation occurred in cathode (air electrode) loss as shown in table A3 and Fig. 3.3B. This error might come from the ohmic loss which has been added to the activation overpotential in order to compare between measured and calculated data. The calculated data of the losses shown in tables A3 and A4 were calculated from the activation overpotential of that electrode and half of the total ohmic loss. The reason for including half of the ohmic loss was that the ohmic loss cannot be measured as separated values. The electrode potentials can only be measured and there are some parts of the ohmic loss involved. Therefore, it was assumed that half of the ohmic loss contributed to the overpotential of cathode and anode, separately. The error might come from this arbitrary adding. Moreover, another reason was the dynamic differentiation of air cathode. When zinc-air battery discharges, some phenomena were happening inside the cathode such as electrolyte flooding. Nevertheless, these phenomena were not included in the model.

Regarding the zinc electrolyzer, the largest error in validation came from anode (charging electrode) loss as shown in table A4 and Fig. 3.3D. This error might come from the same reason about the ohmic loss. Another reason for this error was the oxygen bubble growth at the charging electrode. At the charging electrode, oxygen is generated when the electrolyzer operates. However, the oxygen bubble growth was

not included in the electrolyzer model. Oxygen bubbles can disturb the kinetics of the electrode therefore the measured anode overpotential deviates from the simulation values.

A4 Additional results

The additional example results are the simulation result of the dynamic behavior of the integrated system with initial KOH and zincate ion concentrations of 8 and 0.2 M, respectively. Fig. A1 shows the comparison between the result at a space velocity (SV) of 0.01 and 10 s⁻¹. These results are related to the results shown in Fig.3.10. The SV case of 0.01 s⁻¹ (low flowrate) represents the condition that saturation of zincate ions occurred. Vice versa, the SV case of 10 s⁻¹ (high flowrate) represents the non-saturated case.

As regards cell voltage, the comparison is shown in Fig. A1A. The cell voltages did not differ much between both cases. The low flowrate case provided slightly lower ZAFB voltage and higher electrolyzer voltage than the high flowrate resulting in lower energy efficiency. Regarding the current efficiency of the integrated system, both cases are very different. The high flowrate case provided very high current efficiency while the low flowrate case provided much lower efficiency.

As the current efficiency of the integrated system was dominated by the zinc electrolyzer, the first thing to consider is the zincate ion concentration. The zincate ion concentration was the major factor affecting the performance of the zinc electrolyzer. From Fig. A1D, it was clearly observed that the saturation of zincate ion occurred at the low flowrate case. In the beginning, the zincate ion concentration was increasing but it stopped increasing after reaching the saturation limit. Meanwhile, the high flowrate case was able to maintain the concentration of zincate ions at 0.2 M. Furthermore, the surface concentration of zincate ion of the low flowrate case also reached 0 whilst it remained at the high flowrate case. The zero-surface concentration of zincate ion means that the mass transfer limit of zincate ion occurred. Therefore, the efficiency was relatively low when the mass transfer limit of zincate ion was reached, as observed in Figs. A1E and A1F. From the current efficiency of the electrolyzer at low flowrate case in Fig. A1E (thick red line), the efficiency starts with a sudden drop, Then, it gradually increases until it reaches the steady plain. On the other hand, the efficiency of the electrolyzer at the high flowrate case also decreased but it still maintained at higher efficiency.

Regarding the amount of zinc (Fig. A1B), it was observed that the zinc consumption rates of ZAFB were similar between both flowrates. However, the zinc regeneration rates were different. The regeneration rate of the higher flowrate case was higher than the low flowrate case due to the lower HER. For the hydroxide

concentration (Fig. A1C), the high flowrate case was able to maintain. At the low flowrate, the hydroxide concentration gradually decreased until the saturation of zincate ion occurred. After the saturation of zincate ion, the hydroxide ion concentration remained steady because the zinc oxide precipitation reaction proceeded.

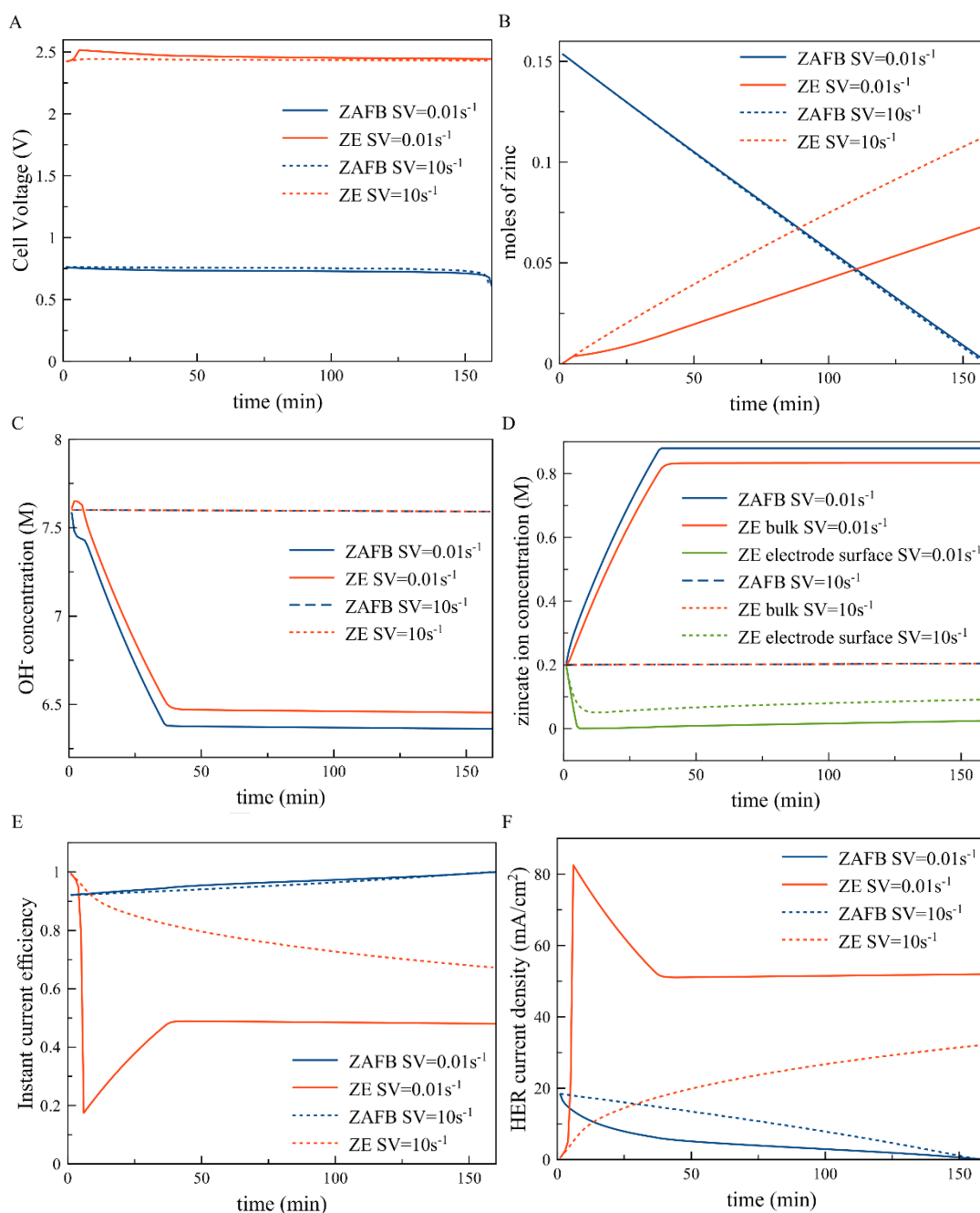


Figure A1 Example of dynamic behavior of ZAFB/ZE integrated system with initial KOH and zincate ion concentration of 8 and 0.2 M, respectively: (A) cell voltage, (B) moles of Zn, (C) hydroxide ion concentration, (D) zincate ion concentration, (E) instant current efficiency and (F) HER current density

The next example is the comparison between initial KOH concentrations of 4 and 8 M as shown in Fig. A2. The initial zincate concentration and SV were fixed at 0.2 M and 0.01 s⁻¹. This example showed the effect of KOH concentration on the saturation limit of zincate ion which significantly affected the efficiency of the system. Fig. A2A showed that the mass transfer limit of zincate ions occurred in both 4 M and 8 M KOH cases, but the 4 M KOH case provided a lower zincate saturation limit. Therefore, the mass transfer rate of zincate ion for the 4 M KOH case was also lower than the 8M KOH case resulting in lower current efficiency as shown in Fig. A2B.

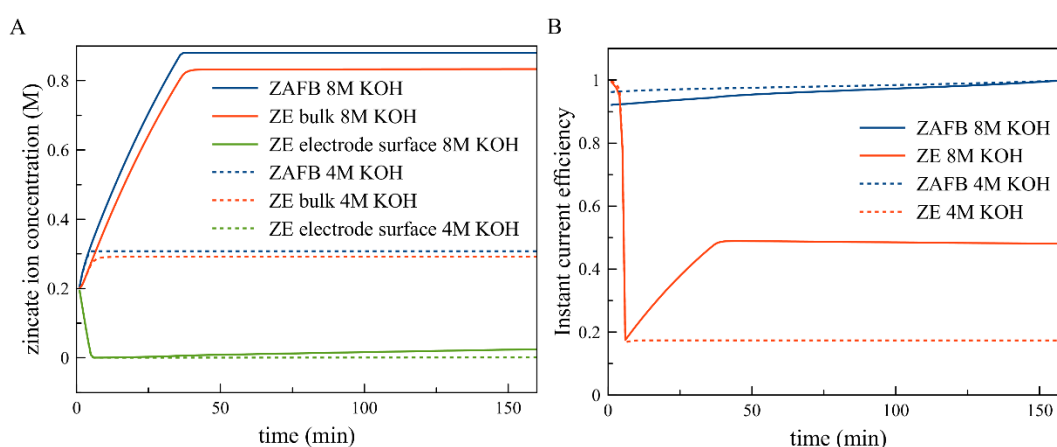


Figure A2 Example of dynamic behavior of ZAFB/ZE integrated system with initial zincate ion concentration and space velocity of 0.2 M and 0.01 s⁻¹, respectively: (A) zincate ion concentration and (B) instant current efficiency

Another interesting example is the inflection that occurred in the current efficiency curve as shown in Fig. A3 (also shown in Fig. 3.10A and 3.10C). In this inflection region, the higher flowrate provided lower current efficiency. To investigate this inflection, the comparison of the dynamic behaviors of the integrated system between the SV of 0.1 and 0.5 s⁻¹ is shown in Fig. A4. The initial KOH and zincate concentrations were fixed at 8 and 0.2 M, respectively. It was found that the higher flowrate case was able to maintain the zincate concentration near the initial concentration while the concentration of the lower flowrate case was increasing. Therefore, the driving force of the zincate ion transfer rate for the lower flowrate case was higher than the higher flowrate case resulting in higher current efficiency. However, this effect only occurred in the inflection region. Increasing flowrate beyond this region led to an increase in current efficiency because higher flowrate also promoted the zincate ion transfer rate.

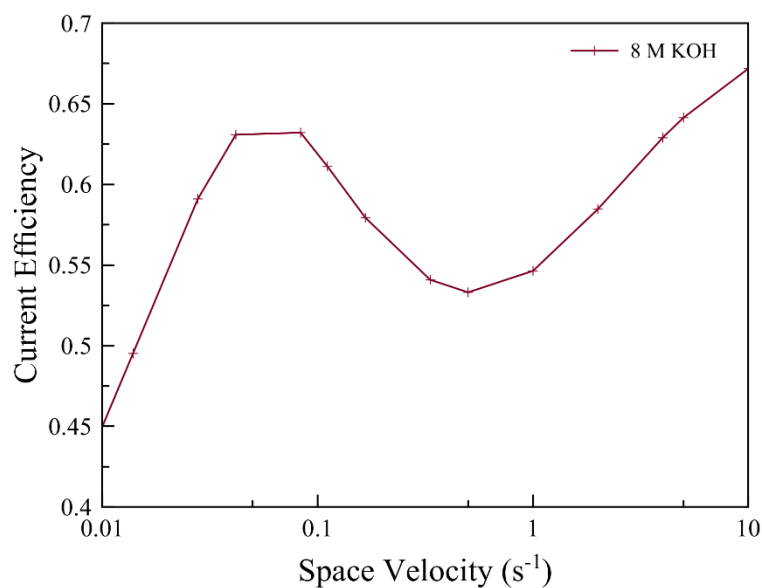


Figure A3 Inflection occurred in the current efficiency curve of ZAFB/ZE integrated system

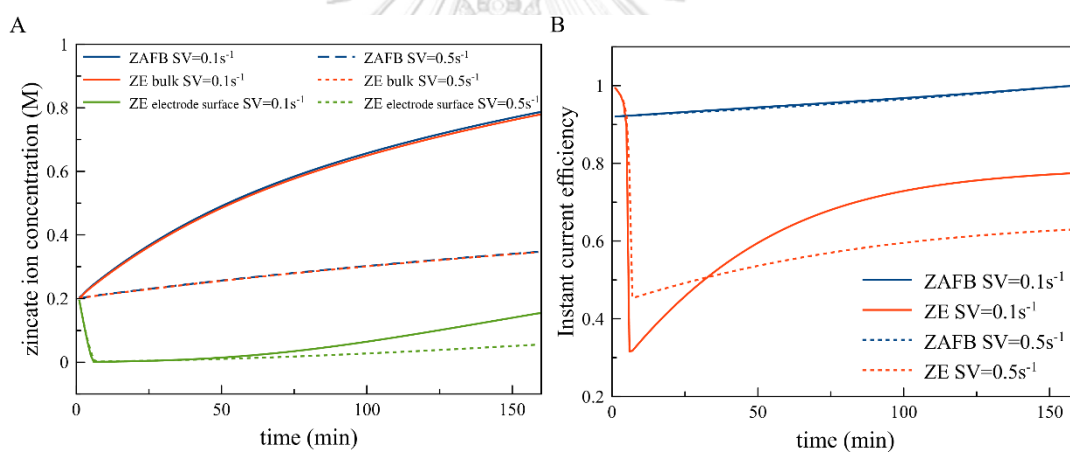


Figure A4 Example of dynamic behavior of ZAFB/ZE integrated system with initial KOH and zincate ion concentration of 8 and 0.2 M, respectively: (A) zincate ion concentration and (B) instant current efficiency

Appendix B
Supplementary Material
Linear Parameter-varying Model for a Refuellable Zinc-air
Battery

Table B1 The location of the data used in this work.

Data name	Data location	
	Data file ^{1,2}	Sheet [time]
0T100A	StepDischarge.xlsx	100STEP0-100-0 [1 s – 302 s]
0T100B	StepDischarge.xlsx	100STEP0-100-0 [585 s – 911 s]
0T100C	StepDischarge.xlsx	100STEP0-100-0 [1185 s – 1502 s]
100T0A	StepDischarge.xlsx	100STEP0-100-0 [291 s – 598 s]
100T0B	StepDischarge.xlsx	100STEP0-100-0 [903 s – 1195 s]
100T0C	StepDischarge.xlsx	100STEP0-100-0 [1491 s – 1801 s]
0T450A	StepDischarge.xlsx	450STEP0-450-0 [1 s - 303 s]
0T450B	StepDischarge.xlsx	450STEP0-450-0 [588 s - 899 s]
0T450C	StepDischarge.xlsx	450STEP0-450-0 [1181 s – 1499 s]
450T0A	StepDischarge.xlsx	450STEP0-450-0 [292 s – 598 s]
450T0B	StepDischarge.xlsx	450STEP0-450-0 [890 s – 1197 s]
450T0C	StepDischarge.xlsx	450STEP0-450-0 [1491 s – 1801 s]
0T900A	StepDischarge.xlsx	900STEP0-900-0 [1 s - 313 s]
0T900B	StepDischarge.xlsx	900STEP0-900-0 [590 s - 901 s]
0T900C	StepDischarge.xlsx	900STEP0-900-0 [1180 s – 1502 s]
900T0A	StepDischarge.xlsx	900STEP0-900-0 [301 s – 601 s]
900T0B	StepDischarge.xlsx	900STEP0-900-0 [889 s – 1193 s]
900T0C	StepDischarge.xlsx	900STEP0-900-0 [1491 s – 1813 s]
400T500R	StepDischarge.xlsx	100STEP400-500
500T1000R	StepDischarge.xlsx	500STEP500-1000-500
MULTI	Supplementary.xlsx	MULTI
VARIOUS	Supplementary.xlsx	VARIOUS

¹'StepDischarge.xlsx' is located in previous published paper (Lao-atiman et al., 2019b).

²'Supplementary.xlsx' is located in supplementary file.

Table B2 Parameter values of linear state space models

Model name	Identification data	A	B	C	D	Fit % ¹
SS0T100A	0T100A	0.8880	0.6476	0.3350	0.1288	97.0686
SS0T100B	0T100B	0.8757	-0.5743	-0.3608	0.4943	98.2905
SS0T100C	0T100C	0.8771	-0.5085	-0.4326	0.4338	98.1266
SS100T0A	100T0A	0.9503	-0.1232	-0.6526	0.4654	97.6896
SS100T0B	100T0B	0.9567	0.0971	0.7602	0.4655	97.6354
SS100T0C	100T0C	0.9583	0.0950	0.7492	0.5061	97.6246
SS0T450A	0T450A	0.6433	-0.5052	-0.3498	0.5296	97.1758
SS0T450B	0T450B	0.7362	0.2783	0.5663	0.4717	98.9290
SS0T450C	0T450C	0.7421	0.2121	0.8703	0.3710	98.6913
SS450T0A	450T0A	0.9132	-0.0505	-1.1848	0.3504	98.2935
SS450T0B	450T0B	0.9349	-0.0357	-1.2178	0.4012	98.2564
SS450T0C	450T0C	0.9421	-0.0313	-1.2382	0.4172	98.3725
SS0T900A	0T900A	0.7885	-0.1840	-0.1394	0.6378	97.5129
SS0T900B	0T900B	0.6926	0.1188	0.9817	0.3954	98.5239
SS0T900C	0T900C	0.7572	0.0947	0.9458	0.4209	98.0704
SS900T0A	900T0A	0.9251	-0.0220	-1.2967	0.3702	98.4046
SS900T0B	900T0B	0.9426	-0.0166	-1.4480	0.3545	98.2246
SS900T0C	900T0C	0.9208	0.0258	1.4074	0.3190	98.1882

¹ Fit % indicates how well the model prediction fits the estimation data and expressed as:
 $100 \left(1 - \frac{\|y - \hat{y}\|}{\|y - \text{mean}(y)\|} \right)$.

Table B3 Parameter values of nonlinear Hammerstein-Wiener model

Model name	nonlinear A	nonlinear B
Identification data	MULTI	VARIOUS
P_1 ¹	0.8617	1.9557
P_2 ¹	-1.4124	-2.8723
P_3 ¹	0.9046	1.6107
P_4 ¹	0.0180	0.0170
b_0 ²	1.0000	1.0000
b_1 ²	-0.5570	-0.9522
f_1 ³	-0.7979	-0.9659
Fit % ⁴	91.9066	91.1311

¹ 3rd degree polynomial: $w = \mu_1 u^3 + \mu_2 u^2 + \mu_3 u + \mu_4$

² $B(z) = b_0 + b_1 z^{-1}$ for $n_b = 2$

³ $F(z) = 1 + f_1 z^{-1}$ for $n_f = 1$

⁴ Fit % indicates how well the model prediction fits the estimation data and expressed as:
 $100 \left(1 - \frac{\|y - \hat{y}\|}{\|y - \text{mean}(y)\|} \right)$

Table B4 Correlations for parameters of LPV model

Parameter	Fitting correlation	Correlation Parameters
A	2 nd degree polynomial ¹	$\mu_1 = 0.6464, \mu_2 = -0.7996, \mu_3 = 0.9411$
B	2 nd degree polynomial	$\mu_1 = 0.1975, \mu_2 = -0.1226, \mu_3 = -0.0308$
C	2 nd degree polynomial	$\mu_1 = -1.535, \mu_2 = 2.533, \mu_3 = -0.4454$
D	Linear function ²	$\mu_1 = 0.1049, \mu_2 = 0.3931$
BC	Two-term exponential ³	$\alpha = 0.3992, \beta = -1.824, \gamma = -0.3485, \delta = -10.84$

¹ 2nd degree Polynomial: $\zeta = \mu_1 p^2 + \mu_2 p + \mu_3$

² Linear function: $\zeta = \mu_1 p + \mu_2$

³ Two-term Exponential: $\zeta = \alpha \exp(\beta p) + \gamma \exp(\delta p)$

Table B5 Fit % values¹ of model predictions relating to Figure 5.4, 5.6 and 5.7

Model name	Validation data					
	0T100A	0T900A	400T500R	500T1000R	MULTI	VARIOUS
SSOT100A	97.0686	-434.8147	-1343.1925	-656.3209	-107.5684	-8.0848
SSOT450A	-97.7554	-29.5903	19.5515	-73.4169	49.7958	48.6385
SSOT900A	-157.3168	97.5129	-344.9635	37.0096	66.1462	21.0252
LPV	86.2316	85.8450	49.6094	65.3644	89.7656	86.8607
Nonlinear A	60.9576	85.9172	50.5309	56.9882	91.9066	87.4859
Nonlinear B	68.5313	53.6687	41.6458	-22.4831	82.3515	91.1311

¹ Fit % indicates how well the model prediction fits the estimation data and expressed as: $100 \left(1 - \frac{\|y - \hat{y}\|}{\|y - \text{mean}(y)\|} \right)$.

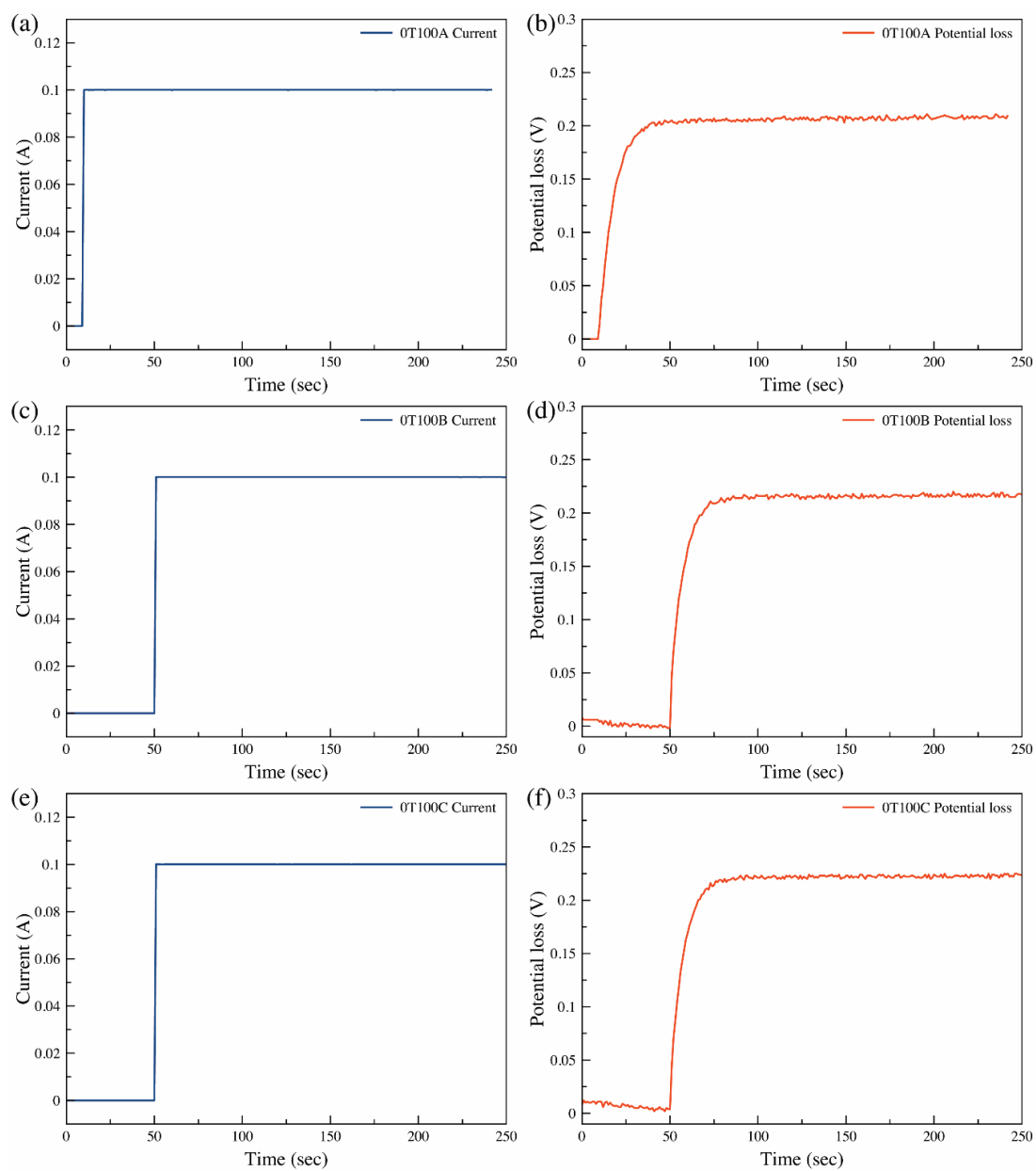


Figure B1 Response signals for data OT100 including (a,c,e) current and (b,d,f) potential loss vs time.

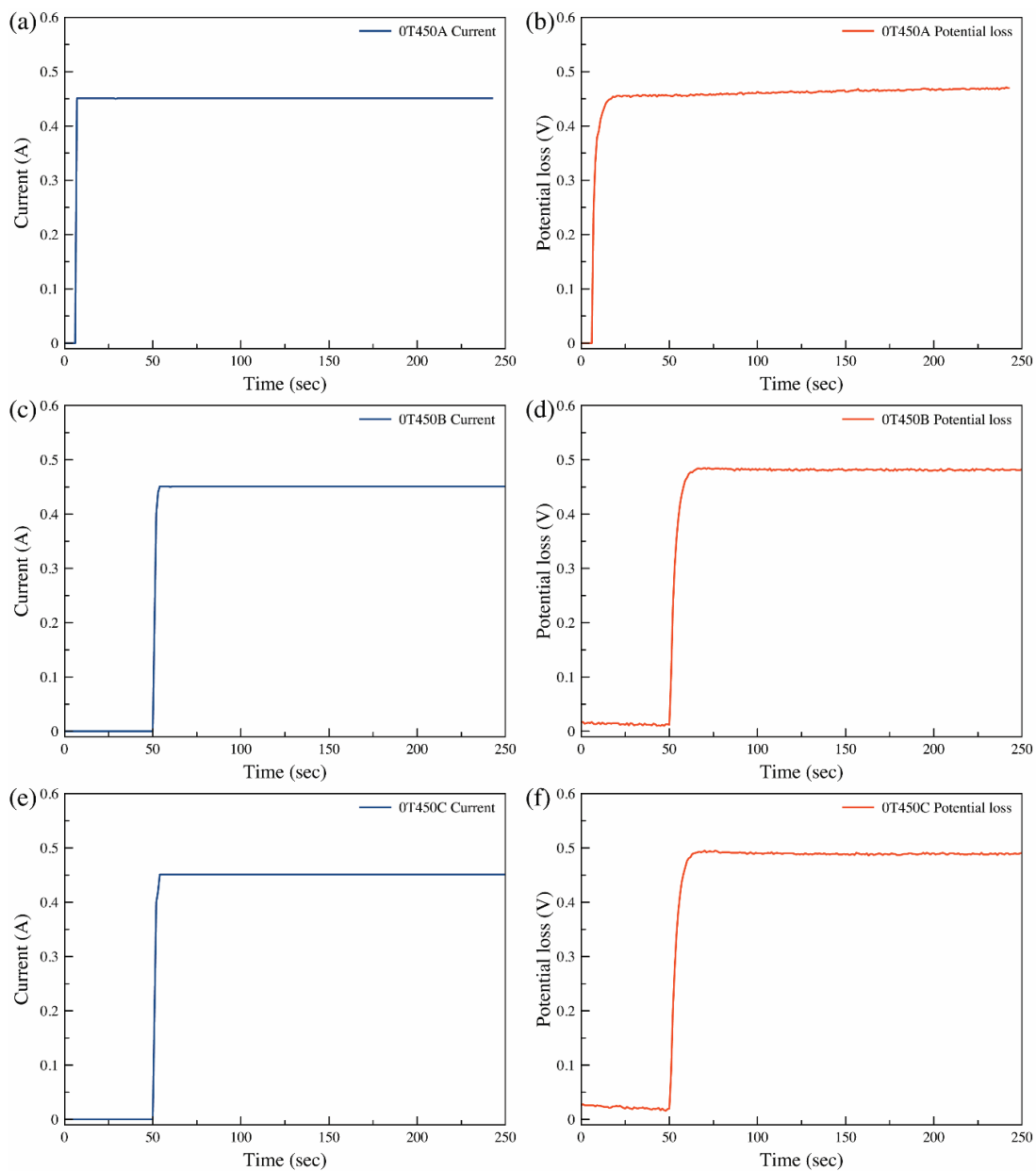


Figure B2 Response signals for data OT450 including (a,c,e) current and (b,d,f) potential loss vs time.

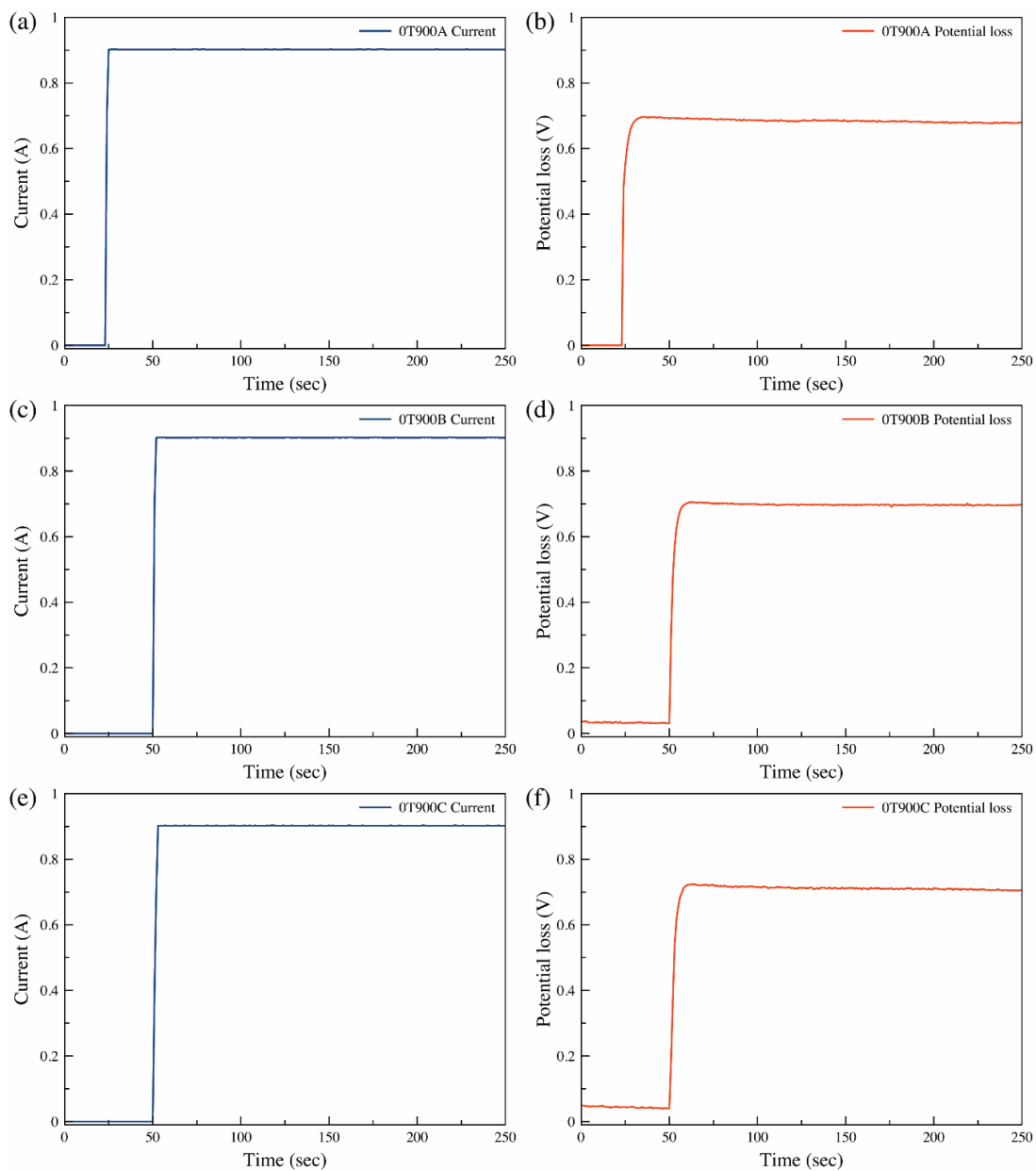


Figure B3 Response signals for data 0T900 including (a,c,e) current and (b,d,f) potential loss vs time.

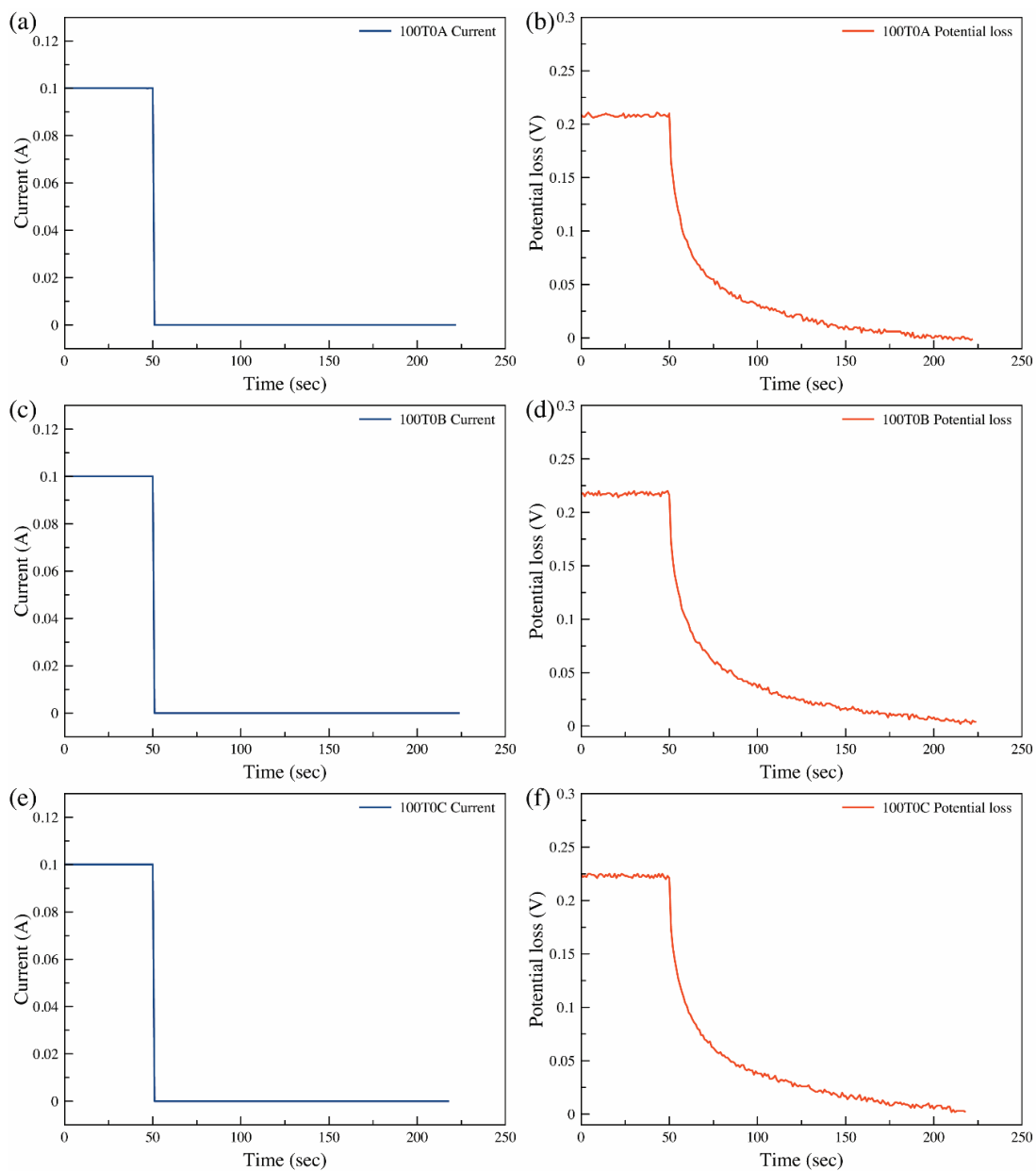


Figure B4 Response signals for data 100T0 including (a,c,e) current and (b,d,f) potential loss vs time.

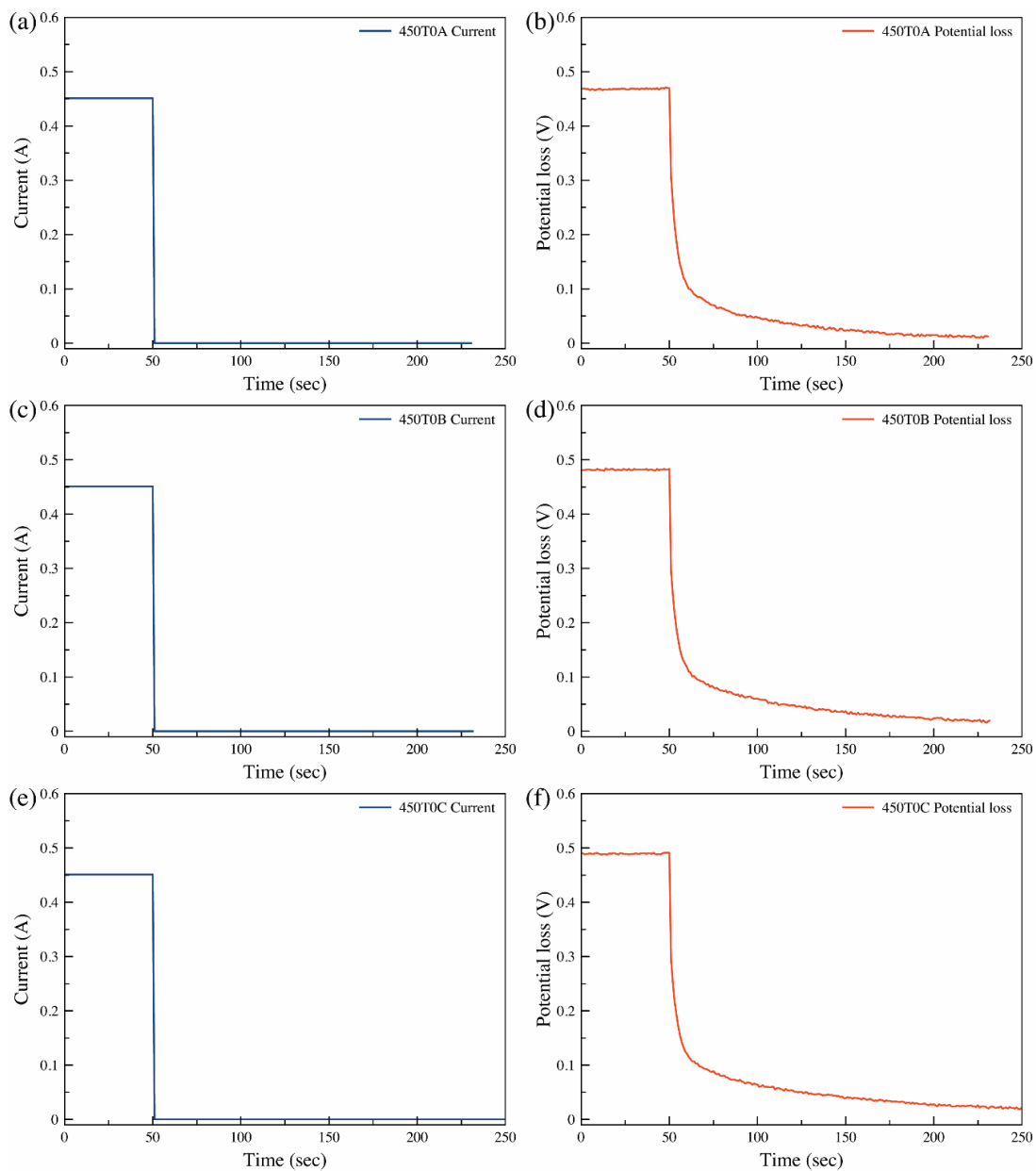


Figure B5 Response signals for data 450T0 including (a,c,e) current and (b,d,f) potential loss vs time.

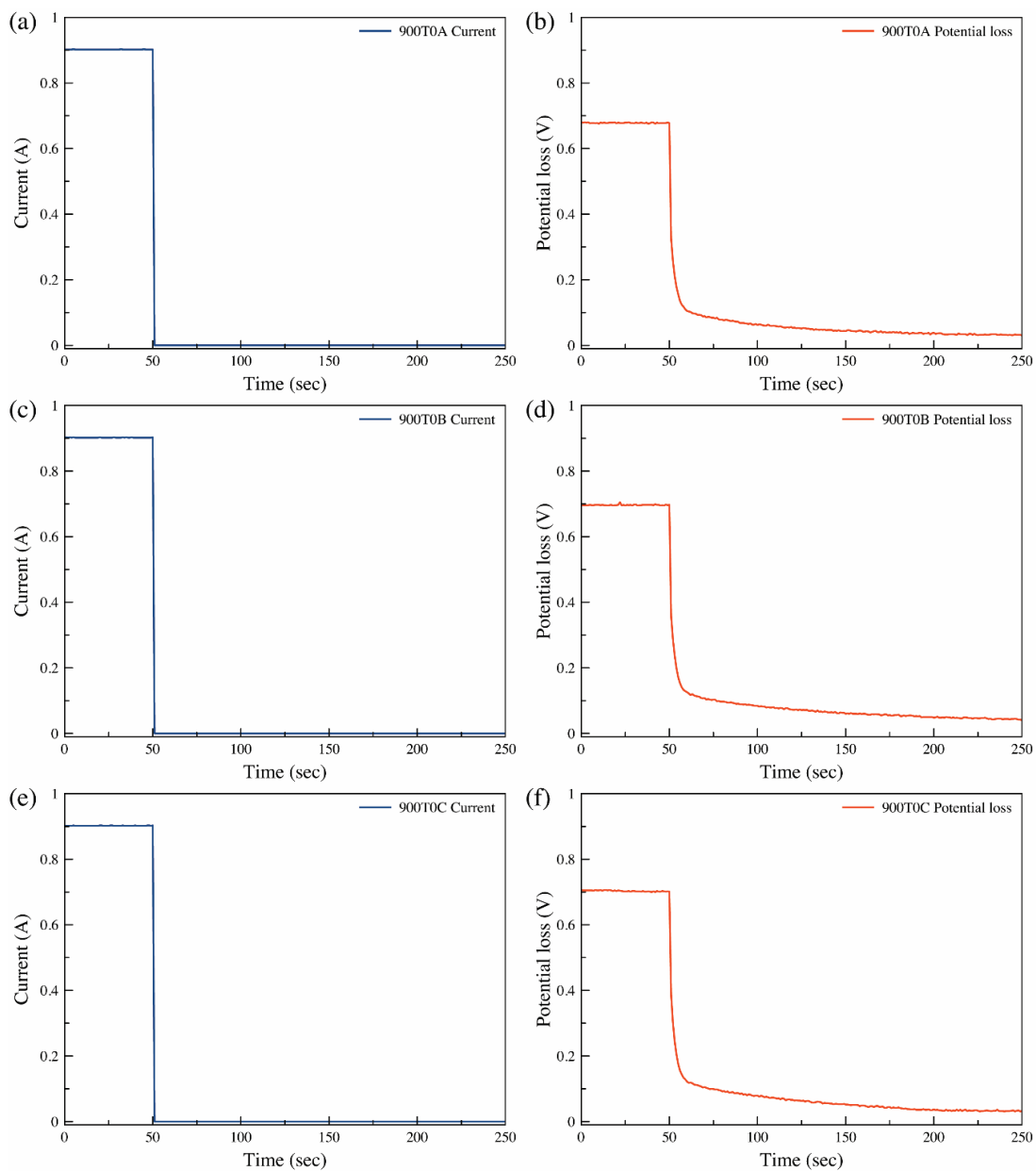


Figure B6 Response signals for data 900T0 including (a,c,e) current and (b,d,f) potential loss vs time.

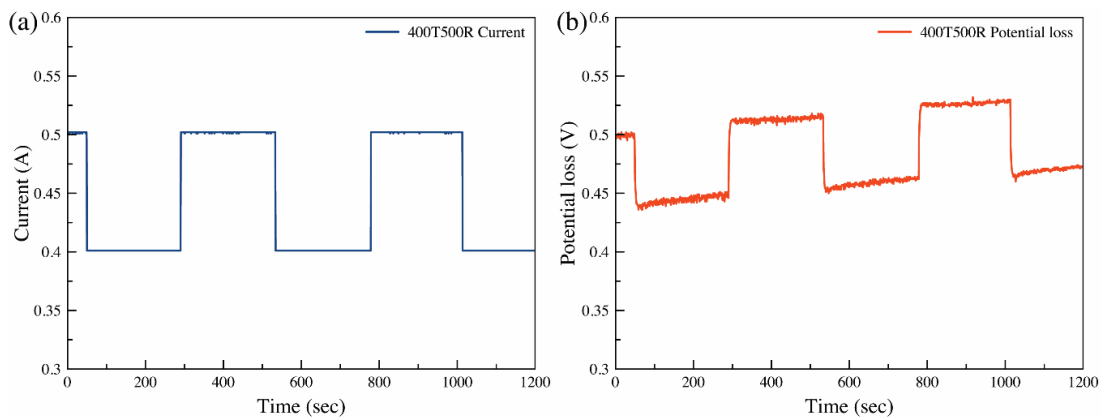


Figure B7 Response signals for data 400T500R including (a) current and (b) potential loss vs time.

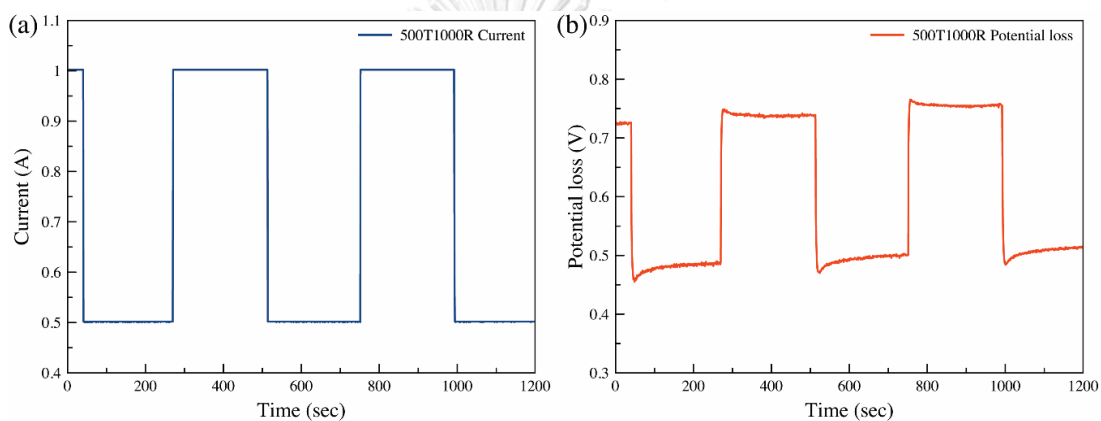


Figure B8 Response signals for data 500T1000R including (a) current and (b) potential loss vs time.

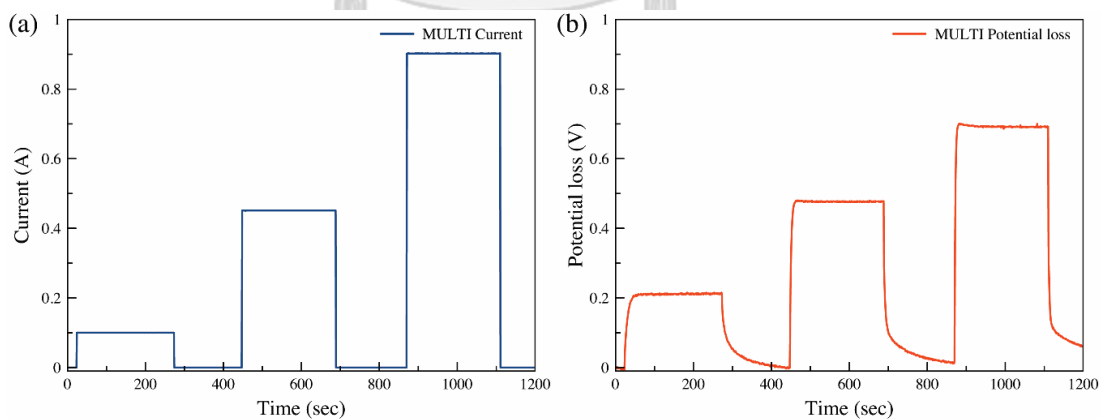


Figure B9 Response signals for data MULTI including (a) current and (b) potential loss vs time.

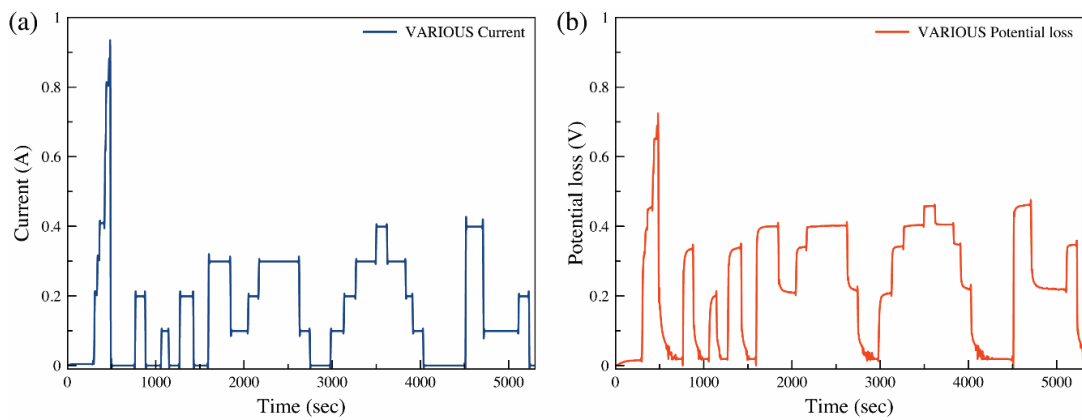


Figure B10 Response signals for data VARIOUS including (a) current and (b) potential loss vs time.



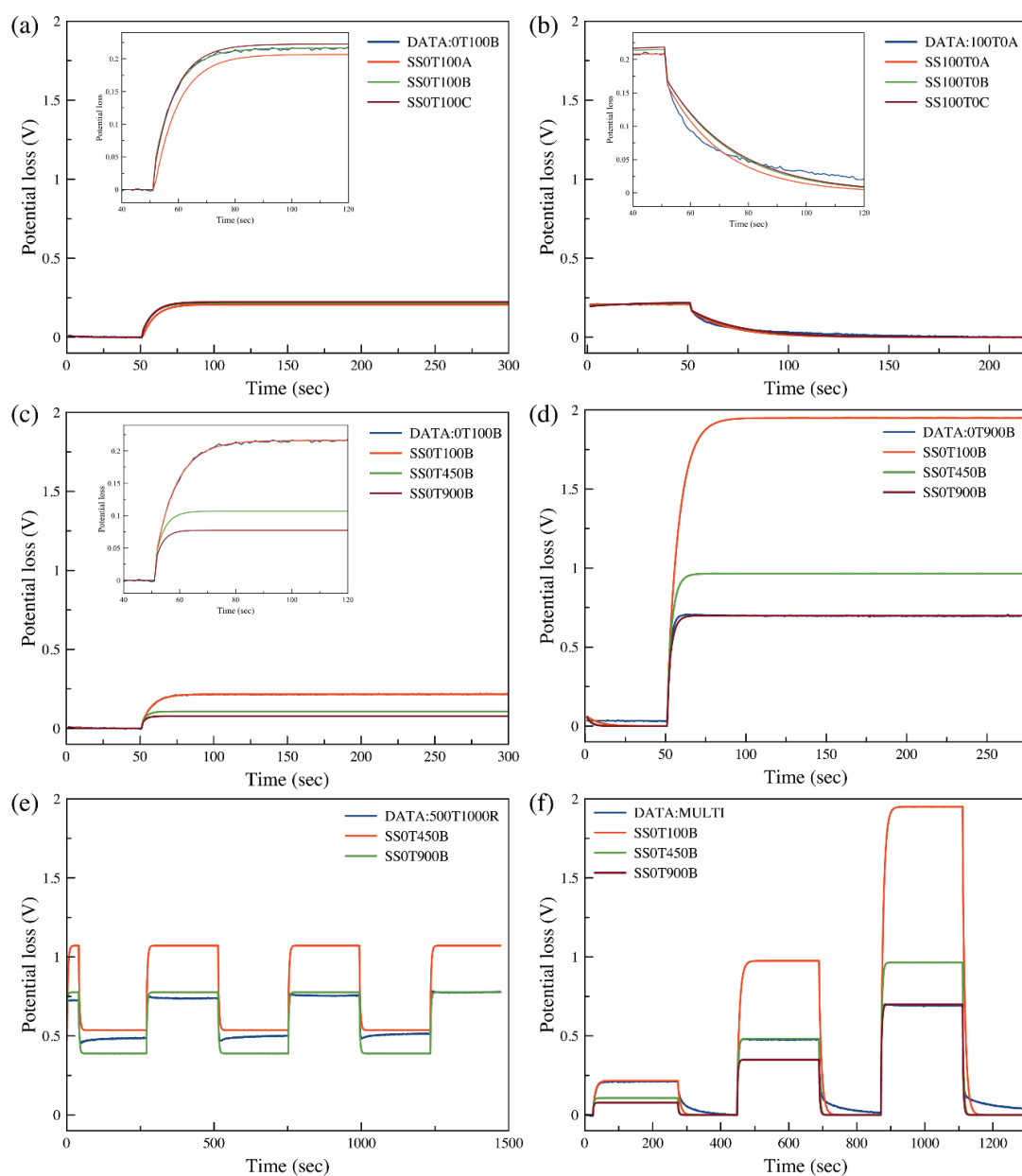


Figure B11 Full graphical comparison of response between measured data (blue lines) and predicted data from linear models: a) Matching conditions with current step from 0 to 100 mA b) Matching condition with current step from 100 to 0 mA c) Different conditions with current step from 0 to 100 mA d) Different conditions with current step of 0 to 900 mA e) Repeating current steps between 500 to 1000 mA and f) Multiple current steps from 0 to 100, 450 and 900 mA

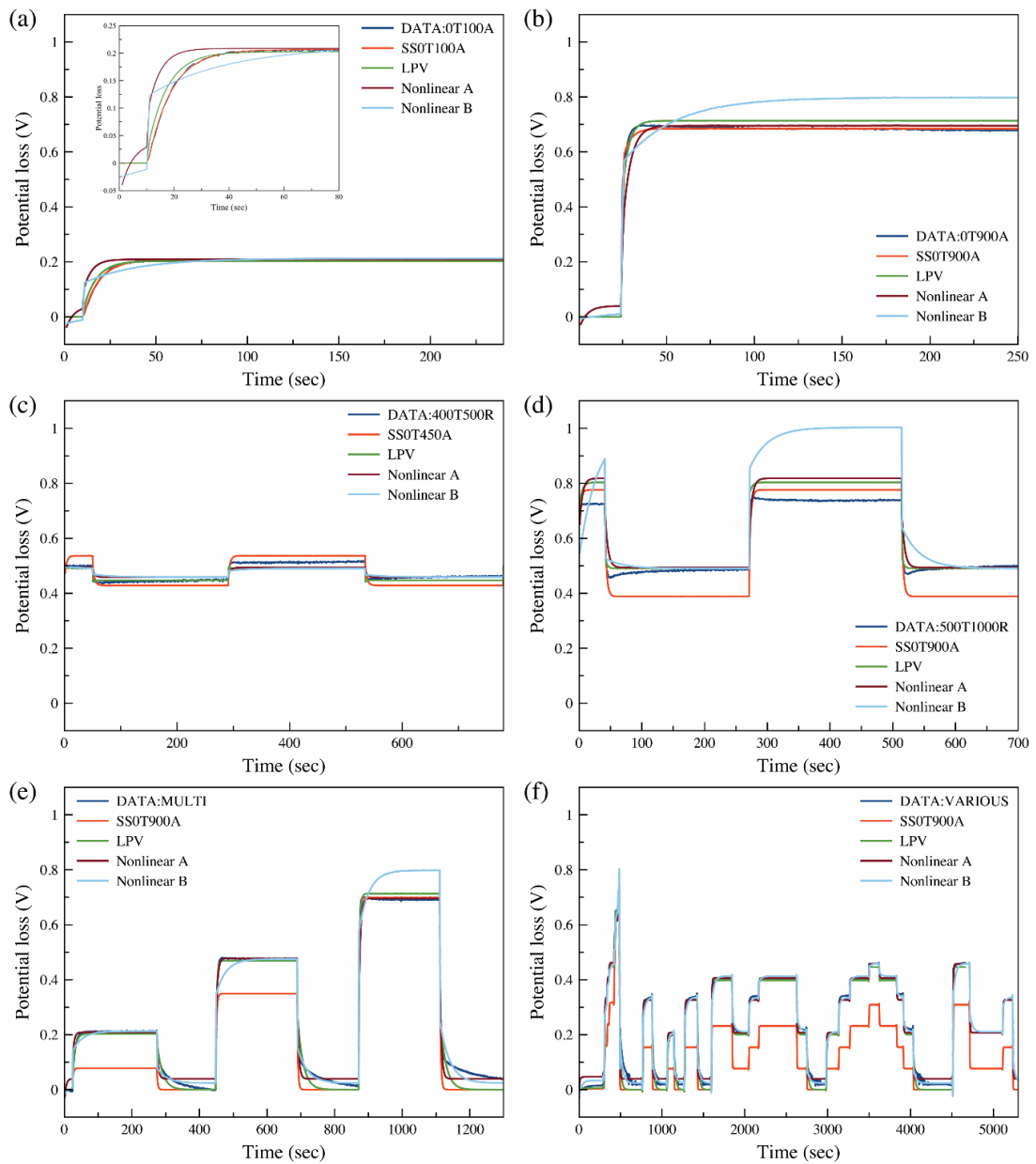


Figure B12 Full graphical comparison of response between measured data (dark blue lines), predicted data from linear model (red line), LPV model (green line) and nonlinear models: a) Current step from 0 to 100 mA b) Current step from 0 to 900 mA c) Repeating current steps between 400 to 500 mA d) Repeating current steps between 500 to 1000 mA e) Multiple current steps from 0 to 100, 450 and 900 mA and f) Various current steps

Appendix C

Supplementary Material

Charge-discharge Behavior Prediction and State of Charge estimation for a Tri-electrode Zinc-air Flow Battery Using Linear Parameter- varying Model integrated with Extended Kalman Filter

Table C1 Correlations for parameters of LPV model

Parameter	Fitting function
Discharging	
A1	$\alpha \exp(\beta(SOC) + \gamma(I_{cell})) + \delta \exp(\varepsilon(I_{cell}) + \theta(SOC)) + \vartheta$
	$\alpha = 0.03873, \beta = -1.854, \gamma = -0.5982$ $\delta = 0.1319, \varepsilon = 1.095, \theta = 0.2778$ $\vartheta = 0.8183$
B1	$\alpha \exp(\beta(SOC) + \gamma(I_{cell})) + \delta \exp(\varepsilon(I_{cell}) + \theta(SOC))$
	$\alpha = 0.0624, \beta = -26.26, \gamma = 1.102$ $\delta = 0.001431, \varepsilon = -0.6444, \theta = -0.4513$
A2	$\alpha \exp(\beta(I_{cell})) + \gamma \exp(\delta(I_{cell}))$
	$\alpha = 4.83 \times 10^{-6}, \beta = -4.653, \gamma = 0.9325$ $\delta = 0.3472$
B2	$\alpha \exp(\beta(I_{cell})) + \gamma \exp(\delta(I_{cell}))$
	$\alpha = -0.00661, \beta = 3.909, \gamma = 0.03438$ $\delta = 0.07753$
D	$\alpha \exp(\beta(SOC)) + \gamma \exp(\delta(SOC))$
	$\alpha = 0.1299, \beta = -17.77, \gamma = 0.1807$ $\delta = -0.1291$
Charging	
A1	$\mu_{00} + \mu_{10}(SOC) + \mu_{01}(I_{cell}) + \mu_{11}(SOC)(I_{cell})$ $+ \mu_{02}(I_{cell})^2$
	$\mu_{00} = 0.9923, \mu_{10} = -0.004831, \mu_{01} = -0.7823$ $\mu_{11} = 0.00005453, \mu_{02} = 0.2045$
A2	$\mu_{00} + \mu_{10}(SOC) + \mu_{01}(I_{cell}) + \mu_{11}(SOC)(I_{cell})$ $+ \mu_{02}(I_{cell})^2$
	$\mu_{00} = 0.8253, \mu_{10} = -0.01581, \mu_{01} = -0.4495$ $\mu_{11} = -0.003726, \mu_{02} = 0.07275$
B1	$\alpha \exp(\beta(I_{cell})) + \gamma \exp(\delta(I_{cell}))$
	$\alpha = -0.06068, \beta = -45.89, \gamma = 0.06152$ $\delta = -0.1717$
B2	$\alpha \exp(\beta(I_{cell})) + \gamma \exp(\delta(I_{cell}))$
	$\alpha = 0.07348, \beta = -0.399, \gamma = -0.05921$ $\delta = -3.857$
D	$\alpha \exp(\beta(SOC)) + \gamma \exp(\delta(SOC))$
	$\alpha = -0.05686, \beta = 0.3054, \gamma = 0.2165$ $\delta = 0.03037$

Table C1(cont.) Correlations for parameters of LPV model

Open Circuit Voltage	
VOC for discharging	$\alpha \exp(\beta(SOC)) + \gamma \exp(\delta(SOC))$
	$\alpha = 1.408, \beta = 0.002382, \gamma = -0.07385$ $\delta = -11.61$
VOC for charging	$\alpha \exp(\beta(SOC)) + \gamma \exp(\delta(SOC))$
	$\alpha = 1.76, \beta = 0.003801, \gamma = -0.1316$ $\delta = -166.1$

Table C2 Fit % values¹ of model predictions according to Figure 6.7

Data	Model		
	LPV model	Linear model	Linear model with VOC change
DSOC500A	77.97405	54.67767	65.09042
DSOC1000A	91.03447	80.3221	86.39993
DSOC1500A	89.18662	76.0557	81.60357
DSOC2000A	85.9723	82.01639	87.83946
MULTI A	82.49611	75.0625	78.32731
MULTI B	80.76646	76.59794	79.03247
CSOC500A	87.6937	77.6334	77.5214
CSOC1000A	94.1808	82.8187	84.1944
CSOC1500A	93.9524	85.9717	87.2975
CSOC2000A	93.8951	81.3498	83.8108
CMULTI	85.60399	68.97507	69.40758

¹ Fit % expressed as: $100 \times \left(1 - \frac{\text{mean}|y-\hat{y}|}{\text{mean}|y-\text{mean}(y)}\right)$.

Table C3 Normalized mean absolute error¹ of SOC estimation according to Figure 6.10

A1	Scenario	LPV model + EKF	Linear model with VOC change + EKF
V_{cell}			
	Reference	0.097695	0.142609
	Q1=10-3	0.017365	0.051288
	Q1=10-9	0.104607	0.143402
	Q3=10-3	0.03252	0.036535
	Q3=10-9	0.167661	0.20773
SOC			
	Reference	0.172974	0.151931
	Q1=10-3	0.067335	0.088736
	Q1=10-9	0.174968	0.152761
	Q3=10-3	1.18968	1.299708
	Q3=10-9	0.015208	0.005044

¹ NMAE expressed as: $\frac{\text{mean}|y-\hat{y}|}{\text{mean}|y-\text{mean}(y)}$

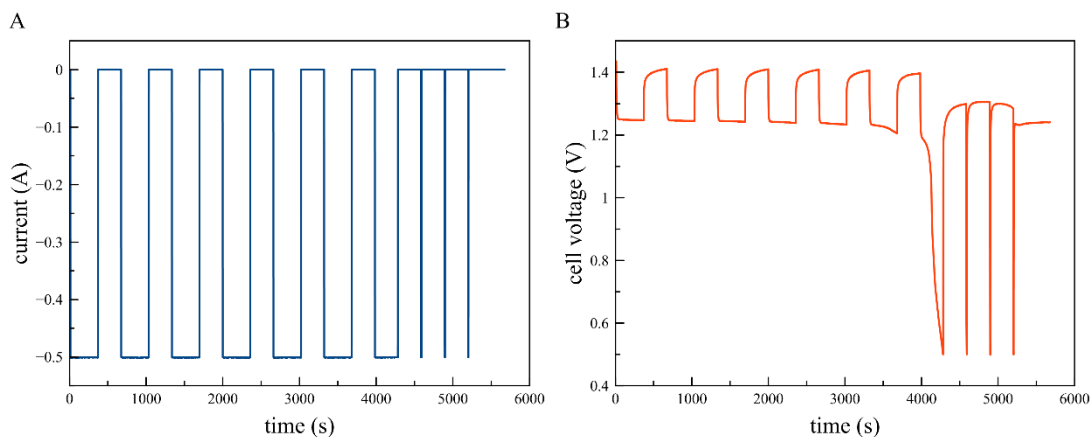


Figure C1 Response signals for data DSOC500A including (A) current and (B) cell voltage vs time.

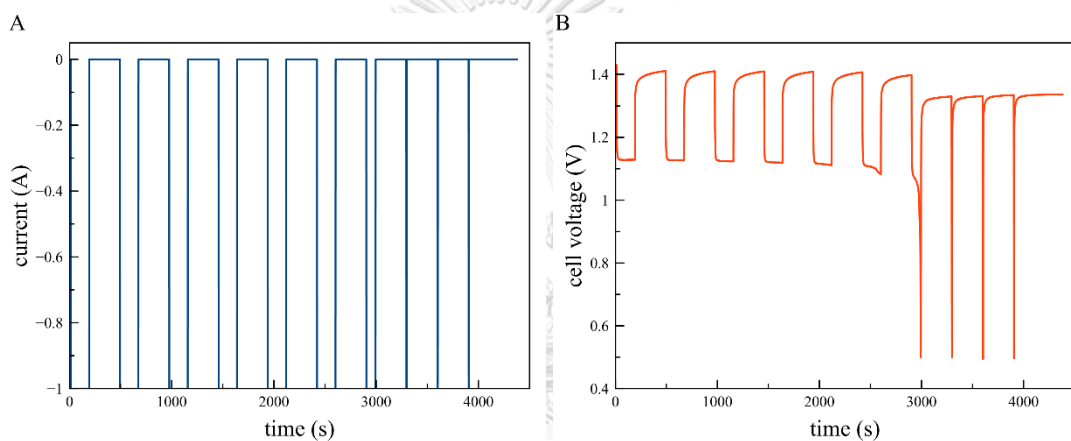


Figure C2 Response signals for data DSOC1000A including (A) current and (B) cell voltage vs time.

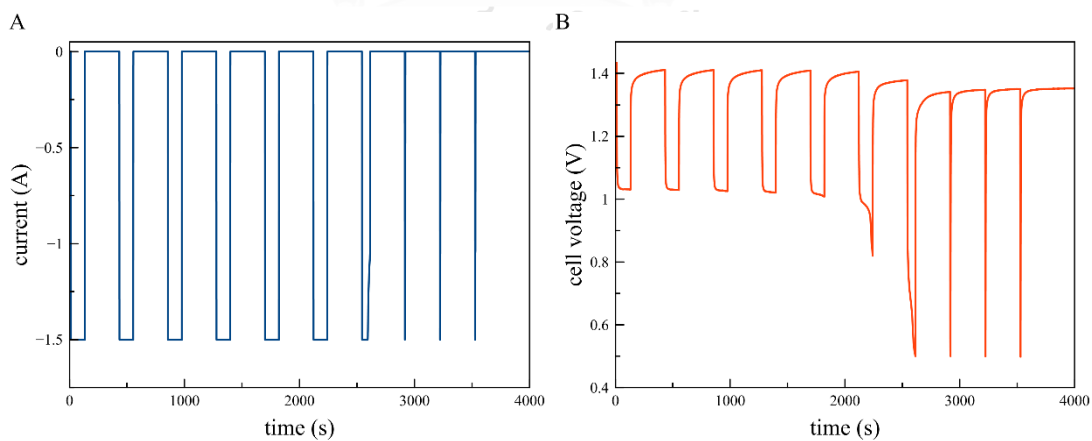


Figure C3 Response signals for data DSOC1500A including (A) current and (B) cell voltage vs time.

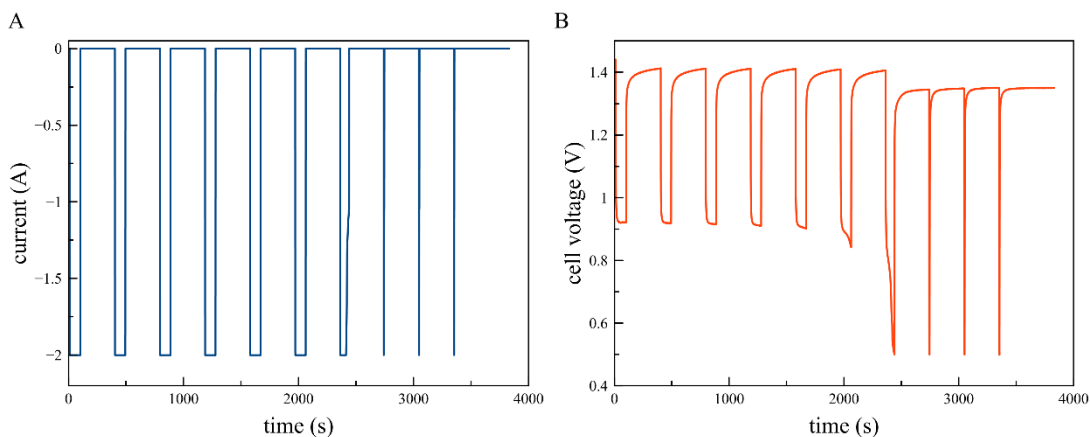


Figure C4 Response signals for data DSOC2000A including (A) current and (B) cell voltage vs time.

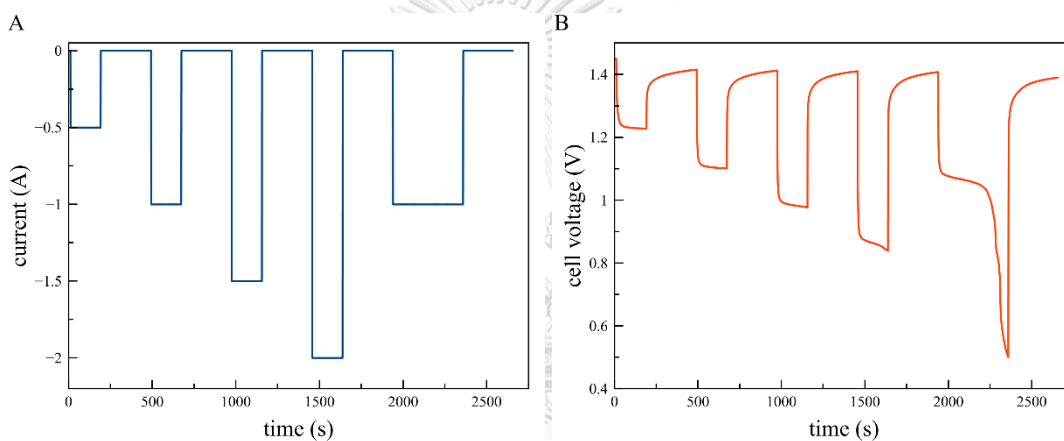


Figure C5 Response signals for data MULTI A including (A) current and (B) cell voltage vs time.

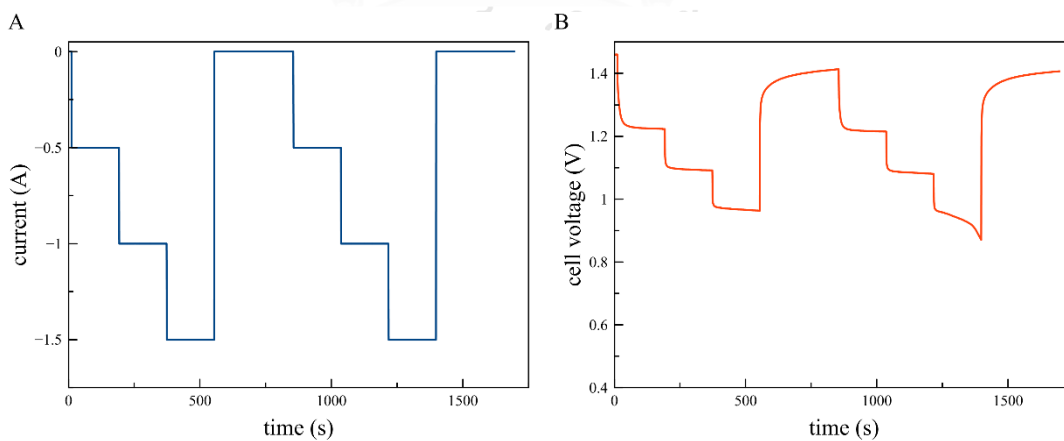


Figure C6 Response signals for data MULTI B including (A) current and (B) cell voltage vs time.

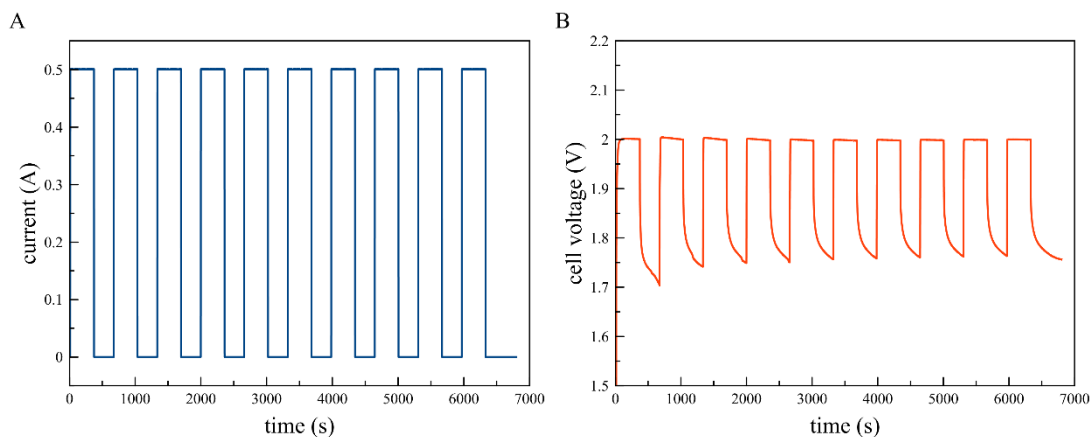


Figure C7 Response signals for data CSOC500A including (A) current and (B) cell voltage vs time.

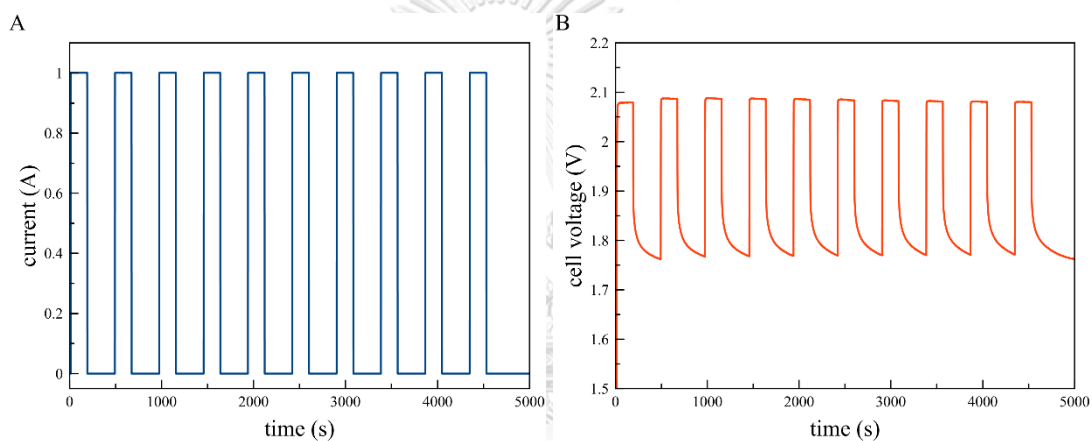


Figure C8 Response signals for data CSOC1000A including (A) current and (B) cell voltage vs time.

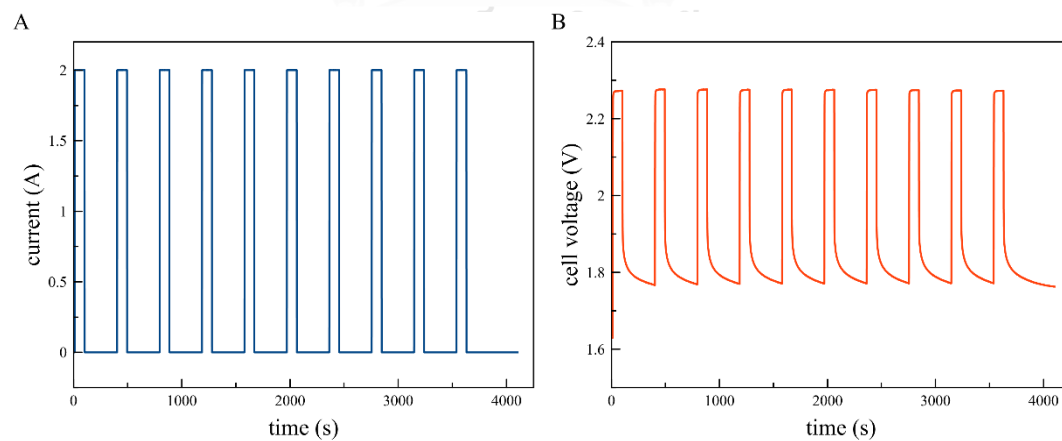


Figure C9 Response signals for data CSOC1500A including (A) current and (B) cell voltage vs time.

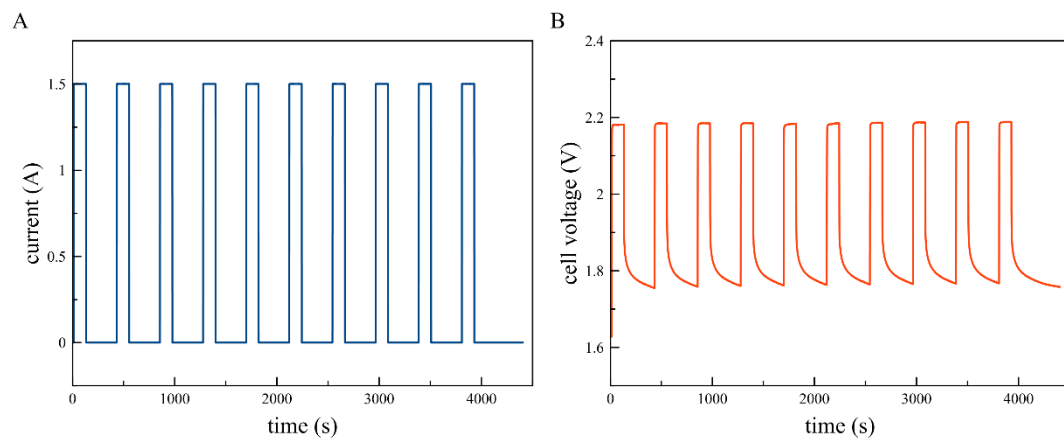


Figure C10 Response signals for data CSOC2000A including (A) current and (B) cell voltage vs time.

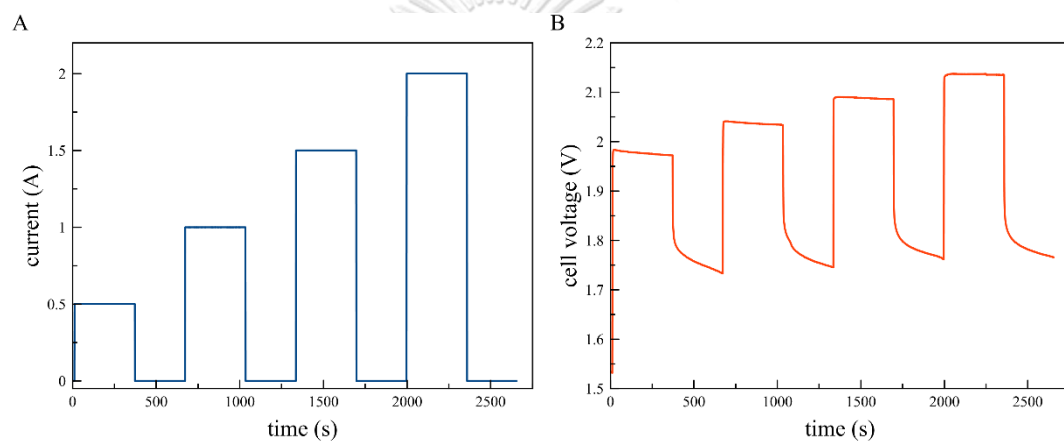


Figure C11 Response signals for data CMULTI including (A) current and (B) cell voltage vs time.

VITA

NAME Woranunt Lao-atiman

DATE OF BIRTH 18 June 1991

PLACE OF BIRTH Chiang Mai, Thailand

INSTITUTIONS ATTENDED Bachelor's Degree in Chemical Engineering from Mahidol University in 2012
Master's Degree in Chemical Engineering from Chulalongkorn University in 2016

HOME ADDRESS 200/26 Village No.5 Nong Phueng, Saraphi, Chiang Mai, Thailand

PUBLICATION W. Lao-atiman, T. Julaphatachote, P. Boonmongkolras, and S. Kheawhom, "Printed Transparent Thin Film Zn-MnO₂ Battery," vol. 164, no. 4, pp. A859-A863, January 1, 2017 %J Journal of The Electrochemical Society 2017.
W. Lao-atiman, K. Bumroongsil, A. Arpornwichanop, P. Bumroongsakulsawat, S. Olaru, and S. Kheawhom, "Model-Based Analysis of an Integrated Zinc-Air Flow Battery/Zinc Electrolyzer System," (in English), Frontiers in Energy Research, Original Research vol. 7, no. 15, 2019-February-22 2019.
Lao-atiman, W., Olaru, S., Arpornwichanop, A. et al. Discharge performance and dynamic behavior of refuellable zinc-air battery. Sci Data 6, 168 (2019). <https://doi.org/10.1038/s41597-019-0178-3>
Lao-atiman Woranunt, Olaru Sorin, Diop Sette, Skogestad Sigurd, Arpornwichanop Amornchai, Cheacharoen Rongrong and Kheawhom Soorathap 2020 Linear parameter-varying model for a refuellable zinc-air battery. R. Soc. open sci. 7: 201107. <http://doi.org/10.1098/rsos.201107>